

# Rare Symmetry Violating Processes

## ‘RSVP’

### A Proposal to the National Science Foundation to Construct the MECO and KOPIO Experiments

#### MECO

Boston University  
Brookhaven National Laboratory  
University of California, Irvine  
Houston University  
INR, Moscow  
New York University  
University of Pennsylvania  
Purdue University  
College of William and Mary

#### KOPIO

University of British Columbia  
Brookhaven National Laboratory  
University of Cincinnati  
Kyoto University  
INR, Moscow  
University of New Mexico  
TJNAF  
TRIUMF  
Virginia Polytechnic Institute  
& State University  
Yale University  
University of Zurich

**Abstract:** Within the Rare Symmetry Violating Processes (RSVP) framework, we propose two experiments that use extremely sensitive measurements of low energy processes to test the *Standard Model* of particle physics and to search for new physics processes. The two experiments comprise a search for coherent, neutrinoless conversion of muons to electrons in the field of a nucleus and a determination of the rate for the CP violating decay of long-lived neutral kaons into a neutral pion, a neutrino and an anti-neutrino. They are proposed to be performed in new, intense muon and kaon beams at the Brookhaven National Laboratory (BNL) Alternating Gradient Synchrotron (AGS). These experiments offer a complementary and, in some theoretical models, more powerful probe for the exploration of new physics phenomena than do experiments at currently operating or proposed high energy particle collider facilities. Both experiments have the potential to change our understanding of the most fundamental constituents of matter and their symmetry properties and interactions.

October 1999

This document is available at <http://pubweb.bnl.gov/people/rsvp/proposal.ps> and at  
<http://meco.ps.uci.edu/RSVP.html>





# Contents

<b>1</b>	<b>Executive Summary</b>	<b>1</b>
<b>2</b>	<b>Introduction</b>	<b>3</b>
2.1	Symmetries and Conservation Laws . . . . .	3
2.2	Rare Muon and Kaon Decays . . . . .	4
2.3	Ultra Rare Muon and Kaon Decays . . . . .	5
<b>3</b>	<b>The MECO <math>\mu^-</math> Beam and <math>\mu^-N \rightarrow e^-N</math> Experiment</b>	<b>7</b>
3.1	Introduction . . . . .	8
3.1.1	Physics Motivation . . . . .	8
3.1.2	Current Limits on Lepton Flavor Violation . . . . .	12
3.1.3	Muon Number Violation – a Brief History . . . . .	12
3.1.4	Muon to Electron Conversion – an Overview . . . . .	14
3.2	Choice of Accelerator for Producing Muon Beam . . . . .	18
3.3	Overview of the MECO Experiment . . . . .	20
3.4	Physics Background Sources . . . . .	22
3.4.1	Electrons from Muon Decay in Orbit . . . . .	23
3.4.2	Radiative $\mu$ Capture . . . . .	24
3.4.3	Beam Electrons . . . . .	25
3.4.4	Muon Decay in Flight . . . . .	26
3.4.5	Pion Decay in Flight . . . . .	26
3.4.6	Radiative $\pi$ Capture . . . . .	27
3.4.7	Anti-proton Induced . . . . .	27
3.4.8	Long Transit Time Backgrounds . . . . .	30
3.4.9	Cosmic Rays . . . . .	32
3.5	Pulsed Proton Beam . . . . .	33
3.6	Muon Beam Design and Performance . . . . .	38
3.6.1	Muon Production . . . . .	39
3.6.2	The Transport Solenoid . . . . .	41
3.6.3	The Muon Stopping Target . . . . .	44
3.6.4	Muon Production Target Cooling . . . . .	46
3.6.5	Solenoid Heat Load . . . . .	48
3.6.6	Preliminary Engineering Design of Super-conducting Solenoids . . . . .	50
3.7	Detector Rates . . . . .	52
3.8	The Tracking Detector . . . . .	57
3.8.1	Prototype Straw Chambers . . . . .	59
3.8.2	Tracking Detector Performance Analysis: Signal Events . . . . .	60
3.8.3	Backgrounds Induced by Pattern Recognition Errors . . . . .	64
3.9	Electron Trigger Calorimeter . . . . .	68
3.9.1	Plastic Scintillation Calorimeter Option . . . . .	68
3.9.2	Crystal Scintillator Calorimeter Option . . . . .	73
3.10	Cosmic Ray Backgrounds and Shield . . . . .	83
3.10.1	Background Rate Calculation . . . . .	83

3.10.2	Hardware Implementation . . . . .	87
3.11	MECO Expected Performance and Sensitivity . . . . .	89
3.12	Estimated Mecos Costs . . . . .	92
3.13	MECO Schedule . . . . .	100
3.14	MECO Appendix 1 – NHMFL Magnet Design . . . . .	107
<b>4</b>	<b>KOPIO - a search for <math>K^0 \rightarrow \pi^0 \nu \bar{\nu}</math></b>	<b>117</b>
4.1	Introduction . . . . .	118
4.2	$K_L^0 \rightarrow \pi^0 \nu \bar{\nu}$ – Theoretical Motivation . . . . .	120
4.2.1	Standard Model . . . . .	120
4.2.2	Non-standard Models . . . . .	123
4.2.3	Theoretical summary . . . . .	124
4.3	Overview of the $K_L^0 \rightarrow \pi^0 \nu \bar{\nu}$ measurement technique . . . . .	125
4.4	AGS . . . . .	132
4.4.1	Primary beam luminosity . . . . .	132
4.4.2	Bunched beam . . . . .	132
4.5	Beam . . . . .	135
4.5.1	Particle production . . . . .	135
4.5.2	Beam design simulation . . . . .	140
4.6	Vacuum and Mechanical considerations. . . . .	148
4.6.1	Vacuum in the decay region. . . . .	148
4.6.2	Vacuum and mechanical downstream of the decay region. . . . .	150
4.7	Preradiator . . . . .	151
4.7.1	Design concept . . . . .	151
4.7.2	Readout . . . . .	152
4.7.3	Performance . . . . .	152
4.8	Calorimeter . . . . .	157
4.8.1	Prototype module . . . . .	157
4.8.2	Experimental study of the prototype module . . . . .	158
4.8.3	Improving the energy resolution . . . . .	161
4.8.4	Time resolution . . . . .	163
4.8.5	Summary . . . . .	163
4.9	Veto detectors . . . . .	164
4.9.1	Decay region veto detectors . . . . .	164
4.9.2	Charged particle and downstream veto detectors . . . . .	167
4.9.3	Beam catcher . . . . .	167
4.10	Trigger . . . . .	172
4.10.1	Trigger scheme . . . . .	172
4.10.2	L0 Trigger rates . . . . .	173
4.10.3	Higher level trigger rates . . . . .	173
4.11	Data Acquisition . . . . .	175
4.12	Simulations . . . . .	177
4.13	Background Rejection . . . . .	179
4.13.1	Photon veto . . . . .	179
4.13.2	Background Estimates . . . . .	182

4.14	Sensitivity and Measurement Precision. . . . .	191
4.15	The KOPIO R&D program and Schedule . . . . .	194
4.16	Costs . . . . .	196
<b>5</b>	<b>RSVP Organization and Management</b>	<b>203</b>
<b>6</b>	<b>AGS Operations to Support RSVP Experiments</b>	<b>207</b>
<b>7</b>	<b>Establishing the RSVP Accelerator Running Plan</b>	<b>211</b>
<b>8</b>	<b>Summary of Educational Outreach Programs</b>	<b>213</b>
8.1	The UCI Program . . . . .	213
8.2	The New York University Program . . . . .	215
8.3	The University of Houston Program . . . . .	215
8.4	The University of New Mexico Program . . . . .	216
8.5	The Virginia Polytechnic Institute and State University Program . . . . .	217
8.6	The Yale Program . . . . .	217
8.7	The Brookhaven National Laboratory Program . . . . .	218
<b>9</b>	<b>Diversity Goals</b>	<b>221</b>



# 1 Executive Summary

We here propose the construction of the Rare Symmetry Violating Processes (RSVP) initiative, consisting of two experiments that study fundamental symmetries of nature. They are a search for coherent conversion of muons to electrons ( $\mu^- N \rightarrow e^- N$ ) proposed by the **MECO Collaboration** and a measurement of the rate for the decay  $K_L^0 \rightarrow \pi^0 \nu \bar{\nu}$  proposed by the **KOPIO Collaboration**. The experiments are coupled by the motivation to study quark and lepton family structure and by the need for intense, low energy beams of protons to produce extremely intense beams of muons or kaons. We propose to build the experiments at the Alternating Gradient Synchrotron (AGS) at Brookhaven National Laboratory.

Observation of muon to electron conversion would be the first evidence for a process that violates muon and electron type lepton number and that cannot be explained by the *Standard Model* of particle physics, extended to include massive neutrinos. It would be direct evidence for previously unknown physics processes involving new forces. This experiment is proposed to achieve a sensitivity 10,000 times that of current experiments. Measurement of the decay rate for  $K_L^0 \rightarrow \pi^0 \nu \bar{\nu}$ , a process that is predicted but not yet seen, would provide the cleanest determination of the fundamental parameter that quantifies the phenomenon of CP violation in the context of the *Standard Model*. This experiment is proposed to achieve a sensitivity 60,000 times that of current limits on  $K_L^0 \rightarrow \pi^0 \nu \bar{\nu}$ . A measured decay rate very different from the precise expectations of the *Standard Model* or one in conflict with CP violation results from the *B* sector would be evidence for startling new physics processes. Both experiments test new physics processes in a way that cannot be done at any of the existing or planned very high energy particle accelerators.

This initiative is proposed by international collaborations with strong U.S. University groups playing leading roles. The Proponents bring to RSVP a record of completing similar experiments of comparable difficulty. Each experiment contains technical elements within the state of the art in particle physics techniques. The required accelerator performance can be extrapolated confidently from current performance and preliminary accelerator R&D.

It is proposed to construct the MECO and KOPIO experiments and the required AGS accelerator and beam-line improvements in fiscal years 2002-04. We propose to begin the detector and accelerator R&D as soon as this Proposal is approved. The capital cost of the MECO and KOPIO Projects are estimated to be \$41M and \$25M (FY00), respectively.

The support for operations of the required running at BNL is estimated at \$7.8M (FY00) per year for 30 weeks of running, 15 weeks for each experiment. Running is anticipated to begin in FY2004; MECO data taking would be completed in 3 years and an additional 1-2 years of running at 30 weeks per year is required to complete KOPIO. We are not requesting support for the running in this proposal.

Construction of the MECO and KOPIO Projects will be undertaken using project management methods modeled on those currently in use for the NSF funding of the ATLAS and CMS Projects. These methods have been used to successfully manage projects that were delivered on-time and on-budget with the proposed capabilities. Oversight of the Projects will be provided by a Joint Oversight Committee containing members from the High Energy Physics Division of the Department of Energy and from the Physics Division of the National Science Foundation and by a Laboratory Oversight Committee consisting of appropriate experts and chaired by the BNL Associate Director for Particle and Nuclear Physics.



## 2 Introduction

The goal of elementary particle physics is to uncover the basic building blocks of matter and understand the fundamental laws that govern our universe. To that end, some of nature's best kept secrets are revealed by examining her rarest phenomena. It has been realized that, special opportunities now exist which allow searches for ultra rare muon and kaon phenomena to be pushed to unprecedented levels of sensitivity by employing techniques and facilities just reaching their full potential. Two particularly compelling new experiments that greatly extend the frontier and that could revolutionize elementary particle physics are the basis of this "Rare Symmetry Violating Processes" (RSVP) Proposal.

### 2.1 Symmetries and Conservation Laws

Symmetries and conservation laws are the guiding principles of elementary particle physics. Local gauge symmetries, labeled by  $SU(3)_C \times SU(2)_L \times U(1)_Y$ , constitute the underlying framework of the "Standard Model." They dictate the dynamics of strong and electroweak interactions. Poincaré invariance, the symmetry of space-time translations, rotations, and Einstein's velocity boosts, is also fundamental to the laws of physics. It provides a classification basis for elementary particles as either bosons (integer spin) or fermions (half-integer spin). Supersymmetry (SUSY), the leading candidate for new physics beyond the Standard Model, changes bosons into fermions and vice-versa. Its existence would radically alter our understanding of space-time and imply that superpartners of all the currently known elementary particles must exist and await discovery.

Symmetry breaking can also provide important insights regarding nature's intricacies. Parity (P) violation shocked the scientific world and forever changed our perception of weak interactions. Today, we accommodate parity violation by treating left and right-handed chiral components of fermions differently. However, it is likely that parity violation implies even deeper more profound short-distance properties of space-time than have so far been realized.

Electroweak symmetry breaking is responsible for the unusually diverse mass spectrum of elementary particles. We parameterize those effects by the so-called Higgs mechanism and expect confirmation of its validity by the eventual discovery of a Higgs scalar particle. Uncovering the Higgs particle or some alternative source of electroweak symmetry breaking along with searching for superparticles implied by supersymmetry, are the primary motivations for constructing high energy collider facilities such as the LHC (Large Hadron Collider). They are designed to elucidate physics at the TeV (1000 GeV) scale or, equivalently, to explore distances of order  $2 \times 10^{-17}$  cm.

Even null results in the search for symmetry breaking can be illuminating. For example, conservation of baryon number ensures the stability of matter. However, it is quite likely that at some level the global symmetry connected with baryon number is violated. Indeed, the observed matter-antimatter asymmetry of our universe suggests that baryon number violation was important during its early evolution (baryogenesis). However, attempts to find such violation via proton decay experiments have failed to uncover evidence. Instead, they provide the impressive lower bound of  $10^{33}$  years on the proton's lifetime. That null result implies, within the framework of grand unification, that strong and electroweak interactions

can be unified only at extremely high mass scales ( $\geq 10^{15}$  GeV). Accommodating such a high unification scale in these theories also indirectly suggests the exciting prospect of discovery in the next decade of low energy supersymmetry's existence.

## 2.2 Rare Muon and Kaon Decays

Ever since the discovery of the muon and the kaon more than 50 years ago, experiments with these particles have been at the forefront of attempts to uncover new symmetries and their breaking. In fact, they have played very similar leading roles in revealing the respective properties of leptons and quarks.

Discovery of the muon was completely unexpected. It was the harbinger of more 2nd and 3rd generation fermions to follow. Early attempts to understand the muon's role often focused on global lepton flavor symmetries. The muon was assigned a quantum unit called 'muon number' while the electron and its partner neutrino,  $\nu_e$ , carried 'electron number'. The FCNC (flavor changing neutral current) decay mode  $\mu \rightarrow e\gamma$  was sought as a means of testing the conservation of those quantities. Failure to observe that decay implied that the muon was not an excited electron, but a distinct fundamental particle. As those searches became more sensitive, they were used to suggest the existence of a second distinct neutrino,  $\nu_\mu$ , which also carried muon number. In that scheme, the muon decays via  $\mu \rightarrow e\bar{\nu}_e\nu_\mu$  and thus conserves muon and electron number. Follow-up efforts to find the proposed second neutrino gave birth to the field of accelerator-based neutrino studies. Its discovery at Brookhaven was later awarded a Nobel prize. Today, we have three species of neutrinos  $\nu_e$ ,  $\nu_\mu$  and  $\nu_\tau$  and major experimental programs designed to study lepton flavor violation via oscillations due to neutrino mass and mixing effects. Atmospheric neutrino studies indicate a large violation of muon number in  $\nu_\mu \rightarrow \nu_\tau$  oscillations. All those efforts have their roots in the search for and failure to observe the rare decay  $\mu \rightarrow e\gamma$ .

Kaon physics has an even richer history. The long kaon lifetime and its associated production with other 'strange' particles gave rise to the concept of hadronic flavor and  $SU(3)_F$  unitary symmetry. In time, that finding led to the quark model in which the strange quark is the hadronic analog of the muon. Kaon studies gave rise to many other important discoveries. Parity violation had its roots in the  $\Theta - \tau$  puzzle of K decays to 2 or 3 pions. Lack of observation of the rare FCNC decay  $K_L^0 \rightarrow \mu^+\mu^-$  led to the introduction of charm, analogous to the second neutrino. The existence of charmed quarks was later confirmed in near-simultaneous Nobel prize winning J/ $\Psi$  discoveries at Brookhaven and SLAC. CP (charge conjugation-parity) non-conservation, another Brookhaven Nobel prize experiment, was also first observed in the K decays. In fact, to this point in time CP violation has only been observed in K decays.

To explain the origin of CP violation, Kobayashi and Maskawa (KM) introduced a third generation of fermions. The small degree of flavor changing quark mixing and large top quark mass appear to be the source of CP violation via quantum loops. However, the KM model of CP violation must be confirmed by corroborating studies in the K and B decays. Baryogenesis suggests that other sources of CP violation are also likely. Extensive CP violation studies in B decays are planned and now underway worldwide.



## 2.3 Ultra Rare Muon and Kaon Decays

Muon and kaon studies have had a glorious history, but can their rare decays program be pushed much further? If so, how much more can we hope to learn from them? Are such studies competitive with other ways to search for new physics? The answers are all yes.

Because of the high intensity of the AGS and its pulsed structure, clean, copious, well-engineered muon and kaon secondary beams are possible. They allow the sensitivity of several important rare muon and kaon decays to be extended by 4 or more orders of magnitude. Such a large improvement is generally unheard of in such a mature field. In addition, the discovery potential of those decays is extremely rich, covering a wide range of new physics scenarios which extend all the way into the 1000 TeV (PeV) regime. These ultra-rate decays can effectively explore energy scales a thousand times beyond the direct discovery potential of the LHC. In that capacity, they could revolutionize elementary particle physics.

The RSVP initiative would study with unprecedented sensitivity what are generally acknowledged to be the two most compelling rare muon and kaon decays. They are linked because both rely on the unique capabilities of the AGS accelerator complex and both are capable of uncovering new physics up to the PeV scale, *i.e.*, they explore down to distances of  $\mathcal{O}(10^{-20} \text{ cm})$ . Here, we briefly outline the goals of these experiments. Details are given in subsequent sections.

The MECO (muon-electron conversion) experiment is designed to search for coherent muon-electron conversion in the field of a nucleus,  $\mu^- N \rightarrow e^- N$  with a  $5 \times 10^{-17}$  branching ratio sensitivity. That represents 4 orders of magnitude improvement over the current experimental bound  $B(\mu^- Ti \rightarrow e^- Ti) < 6 \times 10^{-13}$ , which is already the best bound on any muon number violating reaction (*e.g.*, currently  $B(\mu \rightarrow e \gamma) < 1.2 \times 10^{-11}$ ). Coherent muon conversion alone can be pushed to that incredible level of sensitivity because of its extremely clean signature, a monoenergetic final state electron with energy  $\sim m_\mu \sim 105 \text{ MeV}$ . Rare decays with several final state particles such as  $\mu \rightarrow e \gamma$  are generally limited by accidentals from two distinct muon decays, well above the  $5 \times 10^{-17}$  level.

The physics discovery potential of MECO is extremely robust. A positive signal of this process could have a number of possible explanations, ranging from flavor changing quantum loops containing mixed superparticles with masses in the hundreds of GeV to lepton compositeness at the multi-PeV scale. In between are scenarios that could involve heavy lepton mixing, leptoquarks, multi-Higgs models, off-diagonal  $Z'$  couplings etc. As with other revolutionary low-energy discoveries, a positive finding, along with follow-up studies and other rare decay constraints would likely single out the most viable new physics explanation rather definitively.

In the case of rare kaon decays, the process  $K_L^0 \rightarrow \pi^0 \nu \bar{\nu}$  stands out as the most compelling. Indeed, it is sometimes called the “Golden Mode” because of its theoretically pristine underpinnings. It is a highly suppressed FCNC decay that violates strangeness and CP. However, unlike purely hadronic CP violating K decays, this semileptonic decay can be very accurately computed in terms of Standard Model parameters with only 1 or 2% theoretical uncertainty. Roughly, one expects  $B(K_L^0 \rightarrow \pi^0 \nu \bar{\nu}) \sim 3 \times 10^{-11}$  if no new physics enters. Measuring such a small branching ratio by detecting only the  $\pi^0$  is extremely challenging, but it appears to be possible. In fact, the KOPIO experiment will aim for a  $\pm 20\%$  measurement. Reaching this goal represents an improvement of more than 5 orders of magnitude in

sensitivity beyond the current bound  $B(K_L^0 \rightarrow \pi^0 \nu \bar{\nu}) < 5.9 \times 10^{-7}$ .

Such a precise determination of  $B(K_L^0 \rightarrow \pi^0 \nu \bar{\nu})$  will have a dual utility. It tests the Standard Model while at the same time probing for new physics. Within the Standard Model framework it will yield a clean precise value of the important CP invariant Jarlskog parameter  $J_{CP} = 5.6(B(K_L^0 \rightarrow \pi^0 \nu \bar{\nu}))^{1/2}$ , to about  $\pm 10\%$ . No other experiment is capable of determining  $J_{CP}$  so directly or with such precision. Indeed, combining the worldwide results from B factories and the Fermilab Tevatron B program will likely yield  $J_{CP}$  (twice the area of the unitarity triangle) to about  $\pm 15\%$ . So,  $B(K_L^0 \rightarrow \pi^0 \nu \bar{\nu})$  will set the standard for CP violation. To search for new physics, one can compare  $J_{CP}$  values obtained independently in K and B experiments. Disagreement would signal new physics due to supersymmetry loops, leptoquarks, multi-Higgs models, etc. in one or both systems. Because the B is heavier, it might more likely be the locus of new physics. However, because the  $K_L^0 \rightarrow \pi^0 \nu \bar{\nu}$  branching ratio is so small, in some cases it is more sensitive to new high scale physics. In fact, a disagreement could be due to an additional source of CP violation in the K system at scales as high as several PeV. The power of that comparison illustrates the complementarity of K and B studies. It doesn't make sense to invest exclusively in one at the expense of the other. *Instead, both K and B experiments should strive for similar levels of precision in CP violation studies.*

We see that the RSVP initiative provides a pair of unique experiments that, together, are capable of searching for muon number non-conservation and testing CP violation at unprecedented sensitivity levels. They are designed to explore new physics possibilities to the PeV scale. Only a handful of potential experiments have such high-scale sensitivity and RSVP represents two of the most compelling. If the field of elementary particle physics is to move forward, all such well motivated efforts must be pursued.

### 3 The MECO $\mu^-$ Beam and $\mu^-N \rightarrow e^-N$ Experiment

J. Miller, O. Rind, B.L. Roberts  
Boston University

M. Brennan, W. Morse, Y. Semertzidis  
Brookhaven National Laboratory

T. J. Liu, W. Molzon <sup>1</sup>, V. Tumakov  
University of California, Irvine

E. Hungerford, K. Lan, B. Mayes, L. Pinsky, J. Wilson  
University of Houston

R. Djilkibaev, V. Lobashev, A.N. Toropin  
INR, Moscow

A. Mincer, P. Nemethy, J. Popp, J. Sculli  
New York University

W. Wales  
University of Pennsylvania

D. Koltick  
Purdue University

M. Eckhause, J. Kane, R. Welsh  
College of William and Mary

---

<sup>1</sup>Spokesperson

### 3.1 Introduction

We propose to search for the rare process  $\mu^- N \rightarrow e^- N$  with far greater sensitivity than in any past experiment. Muon to electron conversion does not conserve the additive quantum numbers,  $L_e$  and  $L_\mu$ , associated with the electron and muon and their corresponding neutrinos. Non-conservation of these quantum numbers, and that of the third lepton,  $L_\tau$ , is commonly referred to as lepton flavor violation (LFV). The observation of this process provides direct evidence for lepton flavor violation and requires new physics, beyond the usual Standard Model and the minimal extension to include massive neutrinos.

The experiment, dubbed MECO for Muon to Electron Conversion, will be conducted in a new  $\mu^-$  beam-line at the Brookhaven National Laboratory (BNL) Alternating Gradient Synchrotron (AGS), produced using a pulsed proton beam. The proton energy will be  $\sim 8$  GeV for a variety of reasons discussed at length in the proposal. The expected sensitivity, normalized to the rate for the kinematically similar process of muon capture, is one event for a branching fraction of  $2 \times 10^{-17}$  for a data taking period of 30 weeks at full design intensity. Current calculations of the expected background rates indicate that increased running time would result in even better sensitivity.

In this proposal, we review the physics motivation for such a search, discuss the present status and expected results of other experiments with related goals, outline the basic ideas of the experiment, and discuss the status and results of studies of the important experimental issues.

We believe that this experiment has a real chance of making a discovery of profound importance. This physics cannot be addressed at the *high energy frontier*. In many theoretical models there is no particular reason to believe that lepton flavor violation is more likely in the  $\tau$  lepton sector, and making significant improvements in that sector will be quite difficult. It is very unlikely that lepton flavor violating interactions of high energy hadrons or leptons can be detected directly, and even if this were possible, LFV decays of light particles are a more sensitive probe for any conceivable interaction luminosity at a high energy machine. The largest flux of  $\mu$ 's is produced at existing low energy accelerators and no facility is foreseen at which this experiment could be done better and or on a comparable time scale.

The remainder of the proposal is organized as follows. We first discuss the motivation for and experimental status of muon and electron number violation. We then give an overview of the experimental technique, followed by a discussion of physics backgrounds and signal rates. We discuss the reasons for choosing BNL as the facility at which to do the experiment, and then discuss the new pulsed muon beam and describe in detail the experimental apparatus. We conclude by summarizing the expected results of the experiment, estimating its cost, describing an R & D plan that will allow us to refine the cost estimate and answer the remaining technical questions about the beam and detector, and describing a construction and running schedule that will allow us to obtain physics results by 2006.

#### 3.1.1 Physics Motivation

Apart from the searches for the Standard Model Higgs particle, at LEP II if its mass is less than about 105 GeV/ $c^2$ , at Fermilab for masses up to 150-180 GeV/ $c^2$  [1, 2], and up to

and beyond the limit set by precision electroweak measurements at the LHC, the principal thrust of particle physics research for the foreseeable future is the search for new phenomena, beyond the Standard Model. Precision measurements have verified the predictions of the Standard Model and determined many of its parameters, but the unification of all of the forces, including gravity, will ultimately require departures from the Model. The Standard Model is incomplete, and the theoretical arguments for extensions to the Model are compelling.

A major search for new phenomena is being mounted at the LHC where, for example, weak scale supersymmetry will be either observed or rejected. The high energy community has invested heavily in the two general purpose detectors, ATLAS and CMS, that will begin taking data after 2005. There is also a good chance for discovery at the Tevatron in run II and beyond, where the integrated luminosity will reach  $2 \text{ fb}^{-1}$  by 2002-2003 and approach  $10 \text{ fb}^{-1}$  by the scheduled time for turn on of the LHC[3]. In addition to much improved searches for supersymmetry, the study of the dynamics of the production and decay of 1000 top quark events (in run II) may reveal new physics, perhaps even a dynamical mechanism for electroweak symmetry breaking.

In addition to these fundamentally high energy experiments that search for new phenomena at the energy frontier, a host of interesting ‘low energy’ and non-accelerator experiments provide important tests of the Standard Model, and could also reveal departures. Among these are measurements of CP violation in the neutral kaon system, the search for CP violation in B decays, measurements of neutrino mass and mixing in oscillation experiments, precision measurements of electric dipole moments and the g-2 of the muon, measurements of flavor changing neutral currents, searches for proton decay, and searches for lepton flavor violating processes— i.e., those that do not conserve  $L_e$ ,  $L_\mu$ , or  $L_\tau$  but do preserve their sum, L, —in the decays of mesons and muons, and in muon to electron conversion.

These low energy experiments also address fundamental questions, most often related to the replication of leptons and quarks in generations: the quark and lepton mass spectra, the mixing of flavors, and the CP violation induced by the mixing. They test interesting predictions based on extensions of the Standard Model, most notably those involving supersymmetry and quark-lepton unification.

Some of the ‘low energy’ experiments are being done at high energy for technical reasons. Thus, copious B production and the advantages of high energy for B-tagging make the CDF and DØ collider experiments competitive in studies of the B system. Not all of the experiments are being pursued with equal vigor. Some have reached limits that are currently difficult to improve upon. Others, such as experiments on B physics and neutrino oscillations, are generally regarded as holding so much potential for discovery that they will be pursued world-wide with enormous energy and resources over the next decade.

The  $SU(3)_C \times SU(2)_L \times U(1)_Y$  structure of the Standard Model includes in each generation a color triplet of left-handed u and d states in a weak isodoublet, color triplets of right-handed  $u_R$  and  $d_R$  quarks, a left-handed weak isodoublet of leptons and a right-handed lepton singlet; fifteen states in all. In the absence of the Yukawa couplings to the Higgs, the three generation states in each of the five configurations cannot be distinguished by the known gauge interactions, and each possesses a U(3) global symmetry corresponding to unitary transformations in generation space. In the Standard Model, the quark masses and mixing introduced through the Yukawa couplings break this symmetry down to  $U(1)^4$ ,

the four exact global symmetries of the Standard Model that lead to the empirically well established conserved quantum numbers:  $B$ ,  $L_e$ ,  $L_\mu$ , and  $L_\tau$ . These symmetries, together with the local gauge symmetries,  $SU(3)_C$  and  $U(1)_{EM}$ , are the exact internal symmetries of the Standard Model.

Lepton flavor is conserved at the charged  $W$  vertex, unlike quark flavor, because the neutrinos in the theory are assumed massless. The lepton and neutrino mass matrices can be simultaneously diagonalized (trivially). Many of the questions of particle physics come down to understanding what symmetry replaces this very large  $U(3)^5$  global invariance in the inevitable extension of the Standard Model and, ultimately, in nature[4]. Which of the horizontal symmetries, those mixing generations, remain and which of these are gauged? The Standard Model is silent on the replication of generations and on the relationship between quarks and leptons within a generation. It is silent too on the mass spectrum of the fermions and on the size of the flavor mixing parameters. Not all of the answers to these questions will come from experiments at the high energy frontier. The limit on the proton lifetime, which rules out the simplest grand unified extensions, provides input, as do studies of CP violation, directly related to generation mixing, and the observation of neutrino oscillations, implying both non-zero neutrino mass and lepton flavor violation. Limits on flavor changing neutral currents strongly constrain most extensions of the Standard Model, as do limits from the lepton flavor violating processes  $\mu \rightarrow e + \gamma$  and muon to electron conversion. Substantial improvements in these measurements could lead to a breakthrough, or to further restrictions on theoretical models.

In the Super-Kamiokande neutrino experiment[5, 6, 7, 8], strong evidence for a flavor symmetry breaking transition, most likely  $\nu_\mu \rightarrow \nu_\tau$ , has been observed. The inescapable conclusion is that neutrinos have non-zero mass and mix. A small, but significant, extension of the Standard Model can be made to accommodate this result. While this minimal extension does not conserve lepton flavor, the experimental consequences away from oscillation experiments appear to be small. For example, the process  $\tau \rightarrow \mu + \gamma$  proceeds at a rate  $\sim (\delta m_\nu^2/M_W^2)^2$ , too small to be observed. In extensions of the Standard Model, including supersymmetric theories that unify quarks and leptons, the analogous processes  $\mu^+ \rightarrow e^+ \gamma$  and  $\mu^- N \rightarrow e^- N$  can occur at small but observable rates. The distinguishing feature of these super-unified models is that the slepton (supersymmetric partners of the leptons) masses of different generations are different, the degeneracy being split by radiative corrections induced by the large top Yukawa coupling. No longer a multiple of the unit matrix, the slepton and lepton matrices cannot then be simultaneously diagonalized, and the mismatch between the rotations will result in lepton flavor and, in general, CP violation. For example, the lepton-slepton coupling to the neutralino will change lepton flavor. The lepton mixing angles in these models are related to the quark mixing angles. The calculated rates for  $\mu \rightarrow e + \gamma$  and muon to electron conversion are still model dependent— they vary with  $\tan \beta$ , the ratio of the vacuum expectation values of the two Higgs doublets, the masses of the scalar leptons, and other parameters as well – and are generally 2-3 orders of magnitude below the current experimental limits[9, 10]. For muon to electron conversion, the ratio

$$R_{\mu e} \equiv \frac{\mu^- + (Z, A) \rightarrow e^- + (Z, A)}{\mu^- + (Z, A) \rightarrow \nu + (Z - 1, A)} \quad (1)$$

falls in the range  $10^{-14}$  to  $10^{-17}$  over the entire parameter space (see Figure 1).

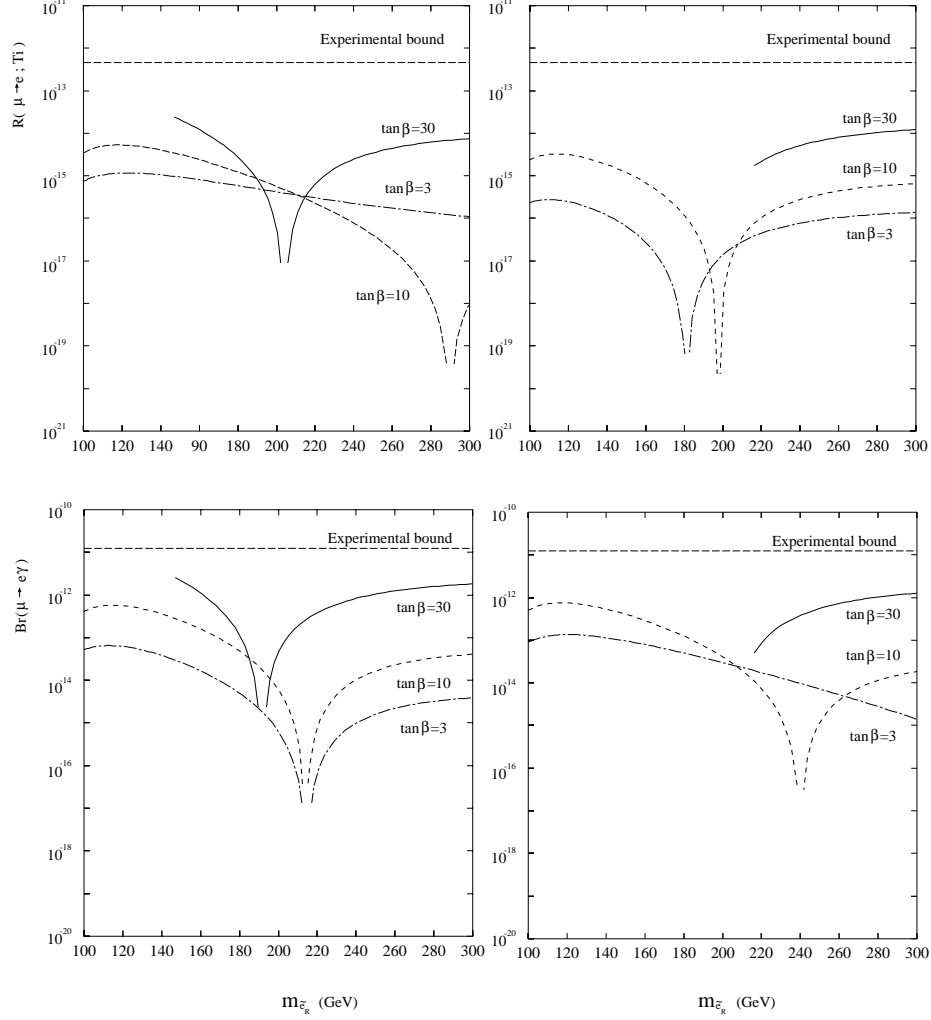


Figure 1: Expected rates for  $\mu^- N \rightarrow e^- N$  and  $\mu^+ \rightarrow e^+ \gamma$  in a minimal supersymmetric SU(5) model [11] for different values of the ratio of the vacuum expectation values of the Higgs particles,  $\tan \beta$ , and the slepton mass. The plots shown are for the parameter  $\mu > 0$  (left) and  $\mu < 0$  (right). The experimental limits have been updated from the reference to account for recently reported results.

As just described, these models also provide a new source of CP violation, induced by the phase in the lepton mixing matrix. In SO(10) an electric dipole moment of the electron is predicted, whose magnitude is related directly to the amplitude for the  $\mu \rightarrow e$  transition with the initial state muon replaced by an electron.

$$d_e = 1.3 \times 10^{-21} \sqrt{B(\mu^+ \rightarrow e^+ \gamma)} \sin \phi [e \cdot cm] \simeq 18.0 \times 10^{-21} \sqrt{R_{\mu e}} \sin \phi [e \cdot cm]$$

where the CP violating phase  $\phi$ , analogous to the phase in the CKM matrix, need not be small[10, 12]. An experiment at  $R_{\mu e} \sim 10^{-17}$  would limit the contribution to the electric dipole moment of the electron from this source to  $d_e < 6 \times 10^{-29}$ , two orders of magnitude below the current limit [13].

An experiment with this sensitivity would provide a significant test of supersymmetric quark-lepton unification. It would probe many other models as well: those with induced non-diagonal  $Z\mu e$  or  $H\mu e$  couplings, horizontal gauge bosons, or heavy neutrino mixing. Such an enormously sensitive experiment, improving upon the most recent experiments at the PSI and TRIUMF by three or more orders of magnitude, requires an entirely new and significantly scaled up approach to the measurement. In section 3.3 an overview of just how this will be accomplished in the proposed experiment is presented. Details of the experimental design are provided in the remaining sections.

### 3.1.2 Current Limits on Lepton Flavor Violation

Limits on lepton flavor violation have been lowered by recent experiments searching for rare decays of kaons and muons. The limits obtained from these experiments are listed in Table 1. They are compared in columns 3-5 using the toy model of Cahn and Harari [14], in which a horizontal gauge symmetry  $SU(2)_H$  is mediated by three neutral gauge bosons that are in general non-degenerate in mass and of mass  $\sim m_H$  and mass difference  $\sim \Delta$ . In this two generation model, the *generation number*  $G$  is an isospin,  $-1/2$  and  $+1/2$  for the first and second generations of charged and neutral fermions (leptons and quarks), respectively. Generation number conservation is violated by mixing, and explicitly by the mass splittings among the bosons. Columns 3 and 4 of Table 1 list  $\Delta G$  and the combination of mixing angles, boson mass and boson coupling measured by the reaction, expressed as a mass. The measured rates depend on the inverse fourth power of this mass. Column five lists the limit on this mass obtained from each reaction. In the model, reactions that separately violate lepton flavor and quark flavor but conserve total generation number ( $\Delta G = 0$ ) are not ‘Cabbibo’ suppressed. The generation number may have significance in some models where mixing in the quark and lepton sectors are related; in any event it serves as a means of classifying related processes.

### 3.1.3 Muon Number Violation – a Brief History

Accelerator searches [23, 24, 25, 26, 27, 28, 29, 30, 31] for the muon number violating processes  $\mu^+ \rightarrow e^+ \gamma$  and  $\mu^- N \rightarrow e^- N$  began 45 years ago with the experiments of Lokanathan and Steinberger ( $\mu^+ \rightarrow e^+ \gamma$ ) and Steinberger and Wolfe ( $\mu^- N \rightarrow e^- N$ ). The  $\mu^- N \rightarrow e^- N$  neutrinoless transitions were studied theoretically by Feinberg [32] (1958) and the phenomenology was developed in 1959 by Feinberg and Weinberg [33], several years before the two neutrino experiment. Two observations in that 1959 paper are of special relevance here. First, the conversion of a muon to an electron in the field of the nucleus occurs coherently, implying a two body final state and a monochromatic electron with energy approximately equal to the muon mass. It is this distinctive signature that makes the process attractive experimentally. Second, because of the “chiral character” of the weak interactions of the leptons, it is easy to imagine processes in which the muon to electron transition occurs through chirality conserving processes (e.g., four fermion interactions) while  $\mu^+ \rightarrow e^+ + \gamma$ , which requires a chirality change, is forbidden.

The subject was re-examined within the framework of gauge theories in 1977 by Marciano and Sanda [34] who studied  $\mu^+ \rightarrow e^+ \gamma$ ,  $\mu^- N \rightarrow e^- N$  and  $\mu^+ \rightarrow e^+ e^+ e^-$  in a variety of gauge



models. They pointed out the potential for these processes as probes of extensions to the Standard Model and emphasized that muon to electron conversion was the more probable reaction in many of the models.

In 1994, Barbieri and Hall [9] proposed these same lepton flavor violating transitions as a way to test super-unified theories. In supersymmetric extensions of the Standard Model, stringent theoretical constraints are imposed on the squark and slepton mass spectra; both are required to be nearly degenerate to avoid flavor changing neutral currents and lepton flavor violation [35]. In their proposed super-unified theory, the slepton mass degeneracy is broken, leading to flavor and CP-violating transitions. The results of the specific calculation and those of Hisano et al. [11] presented in Figure 1 are model dependent, but the physical mechanisms that lead to  $L_e$ ,  $L_\mu$ , and  $L_\tau$  non-conservation are generic to supersymmetric quark-lepton unification.

On the experimental side, an excellent starting point is provided by the knowledge and experience obtained from the two most recent experiments at TRIUMF and the PSI, and from the MELC proposal [36, 37] to the Moscow Meson Factory. In the MELC proposal, a large increase in muon flux is predicted with a solenoidal collection scheme at the front end, as was adopted by the muon collider proponents, and many of the backgrounds that accompany this large flux were studied.

A collaborative effort, with the participation of groups from the University of California Irvine, Houston University, the Institute for Nuclear Research Moscow, New York University, Purdue University, and the University of Pennsylvania, resulted in a proposal to the

Table 1: Experiments on lepton flavor violation: the current experimental limits, the change in generation number in the model of Cahn and Harari, the effective mass measured and the inferred limits on the mass (updated from the reference for new experimental results).

Process	limit	$\Delta G$ [14]	measured	mass limit (TeV)
$K_L^0 \rightarrow \mu^\pm e^\mp$ [15, 16, 17]	$4.7 \times 10^{-12}$	0,2	$m_H \frac{(\frac{g_W}{g_H})}{\cos \beta_{LU}}$	150
$K_L^0 \rightarrow \pi^0 \mu^\pm e^\mp$ [18]	$3.2 \times 10^{-10}$	0,2	$m_H \frac{(\frac{g_W}{g_H})}{\cos \beta_{LU}}$	37
$K^+ \rightarrow \pi^+ \mu^+ e^-$ [19]	$2.1 \times 10^{-10}$	0	$m_H \frac{(\frac{g_W}{g_H})}{\cos \beta_{LU}}$	21
$\mu^+ \rightarrow e^+ e^+ e^-$ [20]	$1.0 \times 10^{-12}$	1	$\frac{\Delta(\frac{g_W}{g_H})}{(\cos \beta_{LL} \sin \beta_{LL})^{1/2}}$	80
$\mu^+ \rightarrow e^+ \gamma$ [21]	$1.2 \times 10^{-11}$	1	$\frac{\Delta(\frac{g_W}{g_H})}{(\cos \beta_{LL} \sin \beta_{LL})^{1/2}}$	21
$\mu^- N \rightarrow e^- N$ [22]	$7.8 \times 10^{-13}$	1	$\frac{m_H (\frac{g_W}{g_H})}{(\sin \beta_{LQ})^{1/2}}$	340

Brookhaven National Laboratory, MECO, for a  $\mu^-N \rightarrow e^-N$  conversion experiment with a sensitivity of  $R_{\mu e} < 10^{-16}$ [38]. The experiment received scientific approval in October of 1997 from the BNL Program Advisory Committee, who were enthusiastic in their support:

*The search for coherent muon-electron conversion at  $10^{-16}$  sensitivity is an extremely powerful probe of lepton flavor violation and physics beyond the Standard Model. Such an experiment has the potential to become a flagship effort for AGS-2000 and could make a major discovery.*

Since that time we have been joined by groups from Boston University, Brookhaven National Laboratory, and The College of William and Mary.

### 3.1.4 Muon to Electron Conversion – an Overview

Sensitive searches have been made for the two lepton flavor violating processes  $\mu^+ \rightarrow e^+\gamma$  and  $\mu^-N \rightarrow e^-N$ . The reactions are complementary, both theoretically and experimentally. On the theoretical side, if the  $\mu^-N \rightarrow e^-N$  conversion is not Coulombic, e.g., if it is mediated by a heavy Z or non-standard Higgs, or proceeds through an effective four-fermion interaction (box diagrams), it has clear advantages over the decay process. In the supersymmetric grand unified theory of Ref. [10], on the other hand, both processes occur predominantly through effective chirality changing couplings ( $\sim \sigma_{\mu\nu}q^\nu \times [1, \gamma_5]$ ), and the branching ratio for  $\mu^+ \rightarrow e^+\gamma$  is approximately 200 times larger than  $R_{\mu e}$  in aluminum. The two experiments are different:  $\mu^+ \rightarrow e^+\gamma$  is limited by accidental backgrounds from radiative muon decay in which the photon and electron can come from either the same or different muon decays in a necessarily intense muon beam. A significant advantage for  $\mu^-N \rightarrow e^-N$  is the absence of accidental coincidences of this kind; there is only one mono-energetic electron in the final state. Furthermore, the energy distribution of the background electrons from  $\mu^+ \rightarrow e^+\nu\bar{\nu}$  is peaked at the energy of the electron in  $\mu^+ \rightarrow e^+\gamma$ , while background from muon decay electrons at the conversion electron energy, approximately the muon rest mass energy, are strongly suppressed. The current best experimental limit for  $\mu^+ \rightarrow e^+\gamma$  comes from the MEGA experiment at Los Alamos; that collaboration recently reported [21] their final result,  $B(\mu^+ \rightarrow e^+\gamma) < 1.2 \times 10^{-11}$  at 90% confidence level, limited by background. There currently exists an approved experiment [39] at the PSI with the goal of reaching a sensitivity of  $10^{-14}$ . Muon to electron conversion experiments have reached a sensitivity of  $6 \times 10^{-13}$ . The sensitivity is expected to improve to  $\sim 2 \times 10^{-14}$  in the next few years.

### Kinematics and Backgrounds

The backgrounds in  $\mu^-N \rightarrow e^-N$  result principally from four sources: muon decay in orbit (DIO), radiative muon capture (RMC), prompt processes where the detected putative conversion electron is nearly coincident in time with a beam particle arriving at the stopping target, and cosmic ray induced electrons. Muon to electron conversion,  $\mu^-N \rightarrow e^-N$  occurs coherently in the field of the nucleus, the electron recoiling against the nucleus with energy  $\approx m_\mu c^2$ ,  $E_0 \simeq E_\mu - \frac{E_\mu^2}{2M_A}$ , where  $E_\mu$  is the muon energy, mass plus binding energy, before capture. An electron of this energy, detected in a time window delayed with respect to the muon stop, signals the conversion. While a free muon decaying at rest can produce an electron whose energy is at most  $m_\mu c^2/2$ , the decay of a bound muon can result in an

electron with energy approaching that of a conversion electron. At the kinematic limit in bound decay, the two neutrinos carry away no momentum and the electron recoils against the nucleus, simulating the two-body final state of  $\mu \rightarrow e$  conversion. The differential spectrum falls rapidly near the endpoint, proportional to  $(E_0 - E_e)^5$ . In aluminum, our choice for the target material, the fraction of all muon decays that produce electrons within 3 MeV of the endpoint is about  $5 \times 10^{-15}$ .

Radiative muon capture will sometimes produce photons with energy approaching that of the muon rest mass but falling short because of the difference in mass of the initial and final nuclear states and the nuclear recoil energy. For capture on aluminum, the maximum photon energy is 102.5 MeV. The photon can convert in the target to an asymmetric electron-positron pair, resulting in an electron within 3.5 MeV of the conversion energy.

The above are the dominant physics backgrounds if prompt processes can be rejected. Pions stopping in the target are the major source of prompt background, and can produce photons with energy up to 140 MeV. Electrons in the beam that scatter in the target are another such prompt background, as is the decay in flight of a muon in the region of the target in which the muons stop. In addition, a cosmic ray muon or a photon that enters the detector region and produces an electron of 105 MeV can fake a muon conversion if the electron trajectory appears to originate in the stopping target.

### **Previous $\mu^- N \rightarrow e^- N$ Experiments**

There is a long history of muon to electron conversion experiments [23, 24, 25, 26, 27, 28, 40, 30, 31] dating from the 1955 experiment of Steinberger and Wolfe. The techniques employed in the more recent experiments provide important input in our effort to reach the levels prescribed by supersymmetric grand unification. We focus on the last two, whose properties and results are listed in the first two columns of Table 2.

In the 1993 SINDRUM2 experiment, electrons with transverse momenta below 112 MeV/c were trapped in helical trajectories in the 1.2 T field of a super-conducting solenoid, 1.35 m in diameter and 1.8 m long. Those with sufficient momentum to reach cylindrical Cerenkov hodoscopes at the ends of the solenoid triggered the system and their momenta were measured in cylindrical tracking chambers. The beam,  $1.2 \times 10^7 \mu^-/\text{s}$ , was brought in along the axis of the solenoid; 28% stopped in a titanium target. The ratio of  $\pi^-$  to  $\mu^-$  stops was  $10^{-4}$ .

The 1988 TRIUMF experiment was similar; it used a hexagonal time projection chamber situated in an 0.9 T axial field. About  $1.0 \times 10^6 \mu^-/\text{s}$  were stopped in a titanium target; the ratio of  $\pi^-$  to  $\mu^-$  stops was  $10^{-4}$ .

In both the the 1988 TRIUMF experiment and the 1993 SINDRUM2 experiment, the beam intensity was low enough to use scintillation counters in the beam to veto events coincident with the arrival of a particle at the stopping target. Figure 2 shows graphically the events in the region 85-120 MeV in the SINDRUM2 experiment. The plot shows the data (i) before suppression of any backgrounds, (ii) after suppression of prompt backgrounds and (iii) after suppression of prompt and cosmic backgrounds. The remaining events are consistent with having come entirely from muon decay in orbit. The highest energy electron detected had an energy of 100.6 MeV. In the earlier TRIUMF experiment, there were no events in the window  $96.5 \leq P_e \leq 106 \text{ MeV}/c$ , where 85 % of all  $\mu - e$  conversion electrons were expected. Nine events with momenta  $> 106 \text{ MeV}/c$  were observed; the source of most

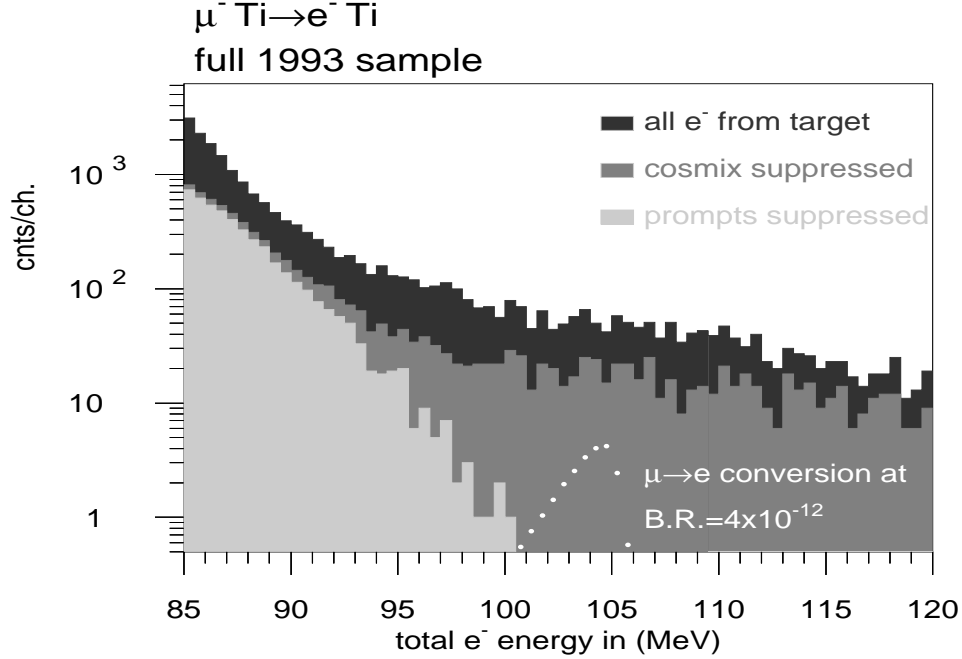


Figure 2: Electron energy spectrum from SINDRUM2 experiment. There is no background above 101 MeV after suppression of cosmics and prompts.

of these events was thought to be cosmic rays. This cosmic ray leakage through the shield was confirmed in a separate experiment in which the cosmic ray induced background was measured with the beam turned off. These two experiments achieved similar sensitivities,  $R_{\mu e} < 4 \times 10^{-12}$ . The limit from the SINDRUM2 experiment has since been lowered by a factor of six in a fifty day exposure ( $3 \times 10^{13}$  stopped muons) to  $6.1 \times 10^{-13}$  and should reach  $2 \times 10^{-14}$  in two years. To get to this level, the beam intensity will be raised an order of magnitude or more from the value given in Table 2. At this intensity, beam counters can no longer be used to reject prompts. A new high flux beam line and a pion to muon converter situated inside an 8.5 meter long super-conducting solenoid has been commissioned. It is calculated that this will reduce prompt backgrounds to a negligible level, and data are currently being collected.

### Choice of Muon Conversion Target

For coherent  $\mu^- N \rightarrow e^- N$  conversion in the nuclear Coulomb field the ratio  $R_{\mu e}$  was found in reference [33] to increase with  $Z$ , as  $Z|F_p|^2$ , where  $F_p$  is the form factor that describes the nuclear charge distribution, as measured for example in low energy  $e - N$  scattering. Relativistic calculations have been done by Shankar [41] and, more recently, by Czarnecki, Marciano, and Melnikov [42], that take into account the Coulomb distortion of the outgoing electron's wave function in addition to the effect of the finite nuclear size. While these results do not differ dramatically from the earlier one, they do decrease the conversion rate at high  $Z$ , where the effects considered are expected to have an impact. The result is that  $R_{\mu e}$  increases with  $Z$  between aluminum ( $Z=13$ ) and titanium ( $Z=22$ ) but saturates and then falls, the value of  $R_{\mu e}$  for lead ( $Z=82$ ) only 15

Table 2: The table gives the main features of the two most recent  $\mu^- N \rightarrow e^- N$  searches in columns 2 and 3, and for the MECO experiment proposed for BNL in column 4.

Features	TRIUMF [30]	SINDRUM2 [31]	MECO [38]
Principal detector	TPC, 0.9 T	Drift Chamber, 1.2 T	Straw tubes, 1.0 T
Target material	Titanium	Titanium	Aluminum
$\mu^-$ in/stopped [Hz]	$1.3/1.0 \times 10^6$	$12/3.3 \times 10^6$	$2.5/1 \times 10^{11}$
$\pi/\mu$ stops	$10^{-4}$	$10^{-7}$	$10^{-11}$
Prompt rejection	beam counters	beam counters	pulsed beam
FWHM Resolution [MeV]	4.5	2.3	0.78
Exposure time	100 days	25 days	150 days
Cosmic ray background	$\sim 0.15$ / MeV	Negligible	Negligible
90 % CL Limit	$4.6 \times 10^{-12}$	$6.1 \times 10^{-13}$	$5 \times 10^{-17}$

The factor of 1.7 improvement in going from aluminum to titanium is outweighed by the difficulty in dealing with prompt backgrounds that result from the much shorter muon lifetime in titanium. The longer lifetime in aluminum ( $\tau = 0.88 \mu s$ ) permits using a pulsed proton beam to produce muons, delaying the detection time window for the conversion electron by 600-700 ns, well beyond the arrival time at the stopping target of nearly all particles, without a significant loss in sensitivity. An added advantage is that very pure targets of aluminum are available and the endpoint is close to the muon mass. A muon decaying in orbit around a low Z impurity in a high Z target, on the other hand, can produce an electron with energy beyond the nominal endpoint.

### 3.2 Choice of Accelerator for Producing Muon Beam

Experiments using low energy  $\mu$  beams have until now been done at low energy accelerators (PSI, LAMPF, TRIUMF) that produce very intense beams of protons with kinetic energy below 1 GeV. Typically, the ratio of usable produced muons to targeted protons was of order  $10^{-8}$ . Djilkibaev and Lobashev [36, 37] proposed placing the pion production target in a graded solenoidal field and collecting pions over essentially  $4\pi$  solid angle. They calculated it should be possible to produce up to  $\sim 10^{-4}$  muons per proton with such a scheme. Coupled with the very high currents possible at these machines, significant improvements in sensitivity could be contemplated. The Moscow Meson Factory, for which the MELC muon conversion experiment was proposed, will not be able to operate enough to execute a sensitive experiment.

The TRIUMF cyclotron could accelerate sufficient protons to produce the necessary muon flux. A preliminary design for a means of making a pulsed beam with intensity close to that required has been produced. For reasons of scheduling and resources at TRIUMF, we cannot foresee doing the experiment there in the near future.

PSI has a planned program to reach sensitivity below  $10^{-13}$  for  $R_{\mu e}$ , after which the focus of LFV physics at PSI will shift to  $\mu^+ \rightarrow e^+ \gamma$  experiments. There is now an approved experiment with a goal of a branching fraction sensitivity for this mode of  $10^{-14}$ . In principal, a pulsed beam could be produced at PSI by chopping the essentially continuous beam they now have. We have not explored whether a sufficiently good extinction could be achieved at PSI. It appears to us that scheduling difficulties and programmatic decisions at that laboratory preclude doing MECO there.

We now know that a significantly larger ratio of usable muons to targeted protons can be achieved using higher energy (e.g. 8 GeV) protons. The choice of beam energy is driven by background from anti-protons, the flux of which rises rapidly with energy in the region around  $\bar{p}$  production threshold. Our estimate of the muon flux that can be achieved is now tied rather closely to experimental measurements of pion production; this is also discussed below.

One possibility that was considered was to use the Fermilab 8 GeV Booster. In principle, with modifications, the accelerator can produce  $5 \times 10^{12}$  protons per spill at 7.5 Hz and 50% duty cycle. This meets our requirements, and reduced intensity could be had while simultaneously operating the  $\bar{p}$  source and the 120 GeV program. As we understand things, the following modifications would be needed at the Booster:

- The magnet now have an activation that varies sinusoidally in time; the power supplies would have to be modified to run with a flat top, allowing a slow beam extraction with  $\sim 50\%$  duty factor.
- A slow beam extraction would need to be implemented.
- The beam would need to be rebunched, with 2 bunches in the revolution time of the machine.
- A suitable area would be needed to which the beam would be extracted, and sufficient space for the experiment and a secondary pulsing device would be needed.

- A suitable “super-cycle” incorporating fast extraction for  $\bar{p}$  production and the 120 GeV program interleaved with slow extraction for MECO would have to be devised.
- Radiation shielding to accommodate the increased intensity would be needed.

The above set of design modifications were studied by Fermilab accelerator physicists. Most design criteria could be met for some cost. The most problematic of the MECO requirements is the bunch structure. Simulations of the Fermilab design showed that rebunching the beam from the 53 MHz accelerating RF structure to an RF structure with 2 buckets would result in significant losses and would not achieve the desired narrow bunch structure.

We have settled on the AGS as the accelerator proposed to produce the intense pulsed muon beam required. The natural way to pulse the beam is to use the accelerating RF structure. The AGS currently accelerates  $\sim 10^{13}$  protons in each RF bucket. Our proposed mode of operation would accelerate two RF buckets, each containing  $2 \times 10^{13}$  protons. The cycle time would be 1 s and the macro duty factor would be 50% (500 ms acceleration and 500 ms spill). The AGS would operate below transition (the energy at which the derivative of the revolution frequency with beam energy is zero). This simplifies its operation, since accelerating through transition results in instabilities that limit the bunch intensity. A number of modifications to the AGS operation will be required to meet our intensity goals. They involve the following:

- Extracting a beam just below transition energy.
- Operating the accelerator with 2 filled bunches and 4 empty bunches to get the appropriate time structure ( $1.35 \mu\text{s}$  pulse spacing).
- Implementing a means of reducing the background protons in nominally unfilled RF buckets in the AGS. This would involve kickers in the ring.
- Constructing a secondary means of beam pulsing to remove protons extracted from the AGS at times between the filled RF buckets.
- Increasing the maximum proton intensity per RF bucket to  $2.0 \times 10^{13}$  protons.

With these changes, the AGS would deliver a proton beam that is capable of producing a muon beam of unprecedented intensity. In subsequent sections we discuss the technical means of achieving each of these design requirements and describe the muon beam and how its energy, charge, and time structure can be varied to produce not only a beam for the MECO experiment, but also for other applications requiring very intense muon beams.

### 3.3 Overview of the MECO Experiment

Except for the cosmic-ray induced events in the TRIUMF experiment, which were later understood, neither of the experiments described in the previous section was background limited. The incident muon flux is sufficiently high in all these experiments that the cosmic ray background scales with exposure time and not the beam intensity. In the SINDRUM2 experiment, there was no background at all in the  $\pm 2\sigma$  region ( $\pm 2$  MeV) about 104.3 MeV, the muon conversion energy in titanium. The highest energy electron detected was 100.6 MeV, almost  $4\sigma$  from the conversion energy, and this electron and those observed at lower momenta appear to come from muon decay in orbit, an irreducible source of electrons that can only be isolated by energy resolution. The SINDRUM2 authors conclude that this experiment demonstrates the feasibility of reaching their goal of  $\sim 2 \times 10^{-14}$  if they can produce a  $\mu^-$  beam sufficiently free of  $\pi^-$  and electrons.

We expect to improve on these experiments by a factor of 1000-10000 in the MECO experiment at BNL. The parameters of the MECO experiment are listed in column four of Table 2, and the differences that lead us to believe that such an improvement is possible are highlighted below.

- The muon beam intensity will be increased to  $10^{11}$  Hz. The high intensity is achieved in the same way it would be in the proposed muon collider. A graded solenoidal field would be used, but with field varying only from 2.3 to 5.0 T. The proton beam enters the production solenoid moving in the direction of increasing field, opposite the outgoing muon beam direction and away from the detectors. Pions and decay muons moving in the forward direction but outside the graded magnet's loss cone ( $\sim 30^\circ$ ) will be reflected back by the higher field and will join the backward produced pions following helical trajectories, those with  $p_T$  less than 180 MeV/c confined within the 30 cm inner radius of the magnet's shielding. A large fraction of the confined pions decay, producing muons which accelerate out of the low field region into the transport solenoid. The resulting efficiency is  $\sim .0025$  stopped muons per incident proton.
- The beam will be pulsed to avoid prompt background, one bunch approximately every microsecond to match the negative muon lifetime in aluminum. The conversion electron is detected in a  $\sim 700$  ns time window between bunches when, ideally, there is no beam in the detector region. The AGS will be run with two of six RF-buckets filled.
- The target in which the muons are stopped is situated in a graded solenoidal field and the detector is displaced several meters downstream of the target to a region of uniform field. The graded field varies from 2 T at the entrance to 1 T about 2 m downstream of the entrance. The increasing field encountered by electrons initially moving upstream reflects electrons back towards the detectors, resulting in large acceptance. Conversion electrons emitted at  $90^\circ \pm 30^\circ$  with respect to the axis of the solenoid (with  $p_T > 90$  MeV/c for conversion electrons) are projected forward in helical trajectories of large radii that intercept the cylindrical tracking detector. Beam particles and decay electrons at smaller  $p_T$  pass undisturbed down the center of the solenoid. The conversion electrons with  $p_T > 90$  MeV/c reach the detector with  $75 < p_t < 86$  MeV/c as a consequence of the graded field. Electrons with 105 MeV/c total momentum that are made



in the beam upstream of the graded field cannot have transverse momentum greater than 75 MeV/c in the detector region, thereby eliminating many potential sources of background. By displacing the detector downstream of the stopping target, the solid angle for neutrons and photons produced in the target to reach the detector is greatly reduced. Further, protons produced in the stopping target can be attenuated with absorbers placed between the stopping target and detectors.

- The energy of the electron will be measured to better than 1 MeV (FWHM). Rejection of the background from muon DIO improves rapidly with the resolution because of the steeply falling energy spectrum. With 900 keV resolution, studies using GEANT predict this background in the region above 103.6 MeV to be one twentieth the signal for  $R_{\mu e} = 10^{-16}$  (see Fig. 26).

Figure 3 is a schematic drawing of the proposed MECO experiment showing the production, transport and detector solenoids. The S-shaped transport solenoid transmits low energy  $\mu^-$  from the production solenoid to the detector solenoid. High energy negatively charged particles and nearly all positively charged particles are absorbed in the collimators. The tracking detector shown here would be made from straw tubes oriented along the axis of the solenoid. A cylindrical (or octagonal) detector with 8 vanes extending radially outward has been shown using GEANT to provide good acceptance. The electron energy resolution determined from the same GEANT simulation is  $\sim 900$  keV (FWHM), the uncertainty coming largely from fluctuations in the energy lost in the target and from multiple scattering. The simulation of the signal shape and the background from muon DIO are shown in Fig. 26.

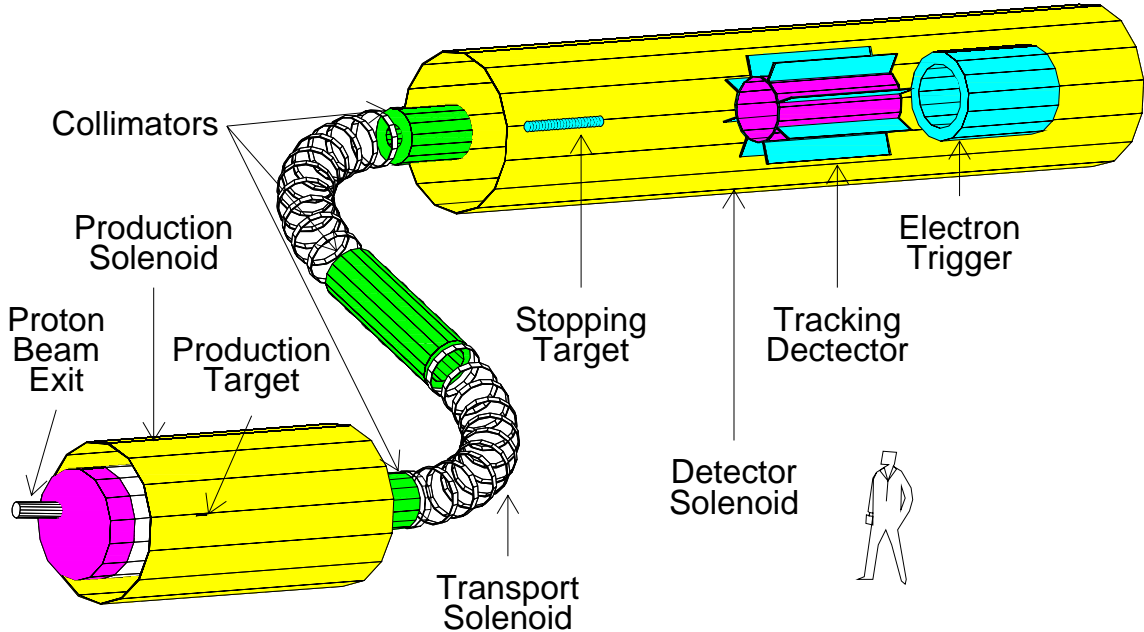


Figure 3: The MECO muon beam and detector system. The proton beam enters the production solenoid from the right side. The region of the interior of the solenoid system is evacuated; a thin beryllium window at the location of the second collimator separates the production and detection region vacuum and serves as a  $\bar{p}$  absorber.

### 3.4 Physics Background Sources

We next discuss the backgrounds to the  $\mu^- N \rightarrow e^- N$  signal in some detail; eliminating them motivates many of the basic ideas of our experiment. We give in this section the results of calculations of the expected background levels based on the performance of the baseline beam and detector. Details of the beam and detector and of the method by which the background calculations were done are in many cases deferred to later sections. The primary sources of physics backgrounds are:

1. Muon decay in a Coulomb bound orbit (DIO).
2. Radiative muon capture on a nucleus (RMC).
3. Beam electrons that scatter in the stopping target.
4. Muon decay in flight.
5. Pion decay in flight.
6. Radiative pion capture on a nucleus.
7. Backgrounds induced by anti-protons.
8. Backgrounds induced by other late arriving particles.
9. Cosmic ray induced electrons.

Backgrounds 1 and 2 are intrinsic to muons stopped in the target. Hence, the source (stopped muons) cannot be eliminated. The endpoint of the spectrum of DIO electrons is equal to the energy of conversion electrons when the neutrinos have zero kinetic energy; energy and momentum are conserved by nuclear recoil. The spectrum falls very steeply near the endpoint (proportional to  $(E_0 - E)^5$ ) and the number of DIO electrons that have an energy consistent with that of conversion electrons can be made negligible by a sufficiently precise measurement of the energy. The situation with RMC is similar; the spectrum of RMC electrons has an endpoint well below the signal and this background is also eliminated with a precise energy measurement.

Backgrounds 3-6 derive from prompt processes, with the electron detected close in time to the arrival of a secondary beam particle at the stopping target. We conclude that a pulsed beam is necessary to eliminate this background. The idea is that conversion electrons are detected only during periods when the flux of particles in the secondary muon beam is extremely low. A similar technique was used in an earlier conversion experiment [29]. A first estimate of the degree to which secondary beam particles must be suppressed during the measurement time can be obtained by reference to the SINDRUM2 data. Without the beam veto there is one prompt background at a sensitivity of about  $10^{-10}$ . To get an expected background below 0.01 events at a branching fraction of  $10^{-16}$  requires a reduction in the particle flux during the conversion detection time by a factor of  $10^{-8}$  with respect to that in the SINDRUM2 experiment. A detailed simulation of prompt background processes leads us to conclude that a beam extinction (defined as the fraction of the total proton flux that hits the production target during the detection time) of  $\leq 10^{-9}$  is required.

Even with a pulsed beam, background may result from particles that spend a very long time in the muon transport system and hence arrive at the stopping target late, even though they are produced by protons in the main pulse. These backgrounds have been calculated with a variety of Monte Carlo and semi-analytic techniques.

Background from anti-protons is a special case in that the background is from prompt processes for which the ultimate source is not reduced by a pulsed beam. It results from very slow  $\bar{p}$ 's that have a transit time in the muon beam-line that is long compared to the time between pulses. The  $\bar{p}$ 's eventually annihilate and the resulting electrons and pions produce background. Hence, to eliminate this background,  $\bar{p}$ 's must not reach the stopping target and the transport of their annihilation products to the stopping target must be heavily suppressed.

Finally, cosmic ray background arises from a variety of processes. This background is unique in that it scales with running time, not sensitivity. Only modest improvement in the cosmic ray background rejection with respect to that of earlier experiments is required, appropriate to the somewhat longer running time proposed.

At the proposal stage, we show by calculation that backgrounds can be reduced to a level such that the detection of even a small number of events (perhaps 1 event) would be compelling evidence for  $\mu^- N \rightarrow e^- N$ . When analyzing the data, it will be essential to demonstrate that the backgrounds are understood and the expected level of background can be predicted with a high degree of certainty from direct measurement. An example of the degree to which that can be done is the E871 experiment that searched for  $K_L^0 \rightarrow \mu^\pm e^\mp$ . The number and kinematic distributions of events near the signal region were calculated and compared to data with good agreement [15], allowing a precise prediction of the expected number of background events directly from the data. Similar techniques will be used in the analysis of MECO data, and we discuss how this can be done for each background source.

### 3.4.1 Electrons from Muon Decay in Orbit

The rate for production of electrons from  $\mu$  decay in Coulomb bound orbit is approximately proportional to  $(E_0 - E_e)^5$  near the endpoint, where  $E_0$  is the endpoint energy. Both the absolute normalization and energy spectrum have been calculated [43, 44] and these calculations agree with a precision of about 25%. The small discrepancy in the calculations can be traced to different approximations for nuclear recoil effects and relativistic corrections to the muon wave function.

Because the spectrum rises very steeply from the endpoint, the signal/background ratio is extremely sensitive to electron energy resolution. To reduce the background, the central part of the resolution function must be minimized and high energy tails in it must be highly suppressed. The main contributions to the central part of the resolution function are energy loss in the stopping target and multiple scattering in the magnetic spectrometer, with smaller contributions from energy loss in the spectrometer and spatial resolution in the spectrometer detectors. The largest potential contribution to high energy tails is pattern recognition errors (associating noise hits in the tracking detector with a putative particle trajectory) in the noisy environment around the stopping target and spectrometer. Straggling (large energy loss) in the stopping target and detector reduces acceptance when energy loss is sufficiently large that the event cannot be distinguished from background (typically more than 1.4 MeV loss),

but does not contribute to background.

A simulation of all processes contributing to energy mismeasurement and an analysis that includes selection criteria designed to remove badly measured events was done and is discussed in section 3.8 and reference [45]. The most probable detected energy is less than 105 MeV due to energy loss in the target, the proton absorbers, and the tracking detector. By accepting events between 103.6 MeV and 105.1 MeV, the noise to signal ratio is below 0.05 for  $R_{\mu e} = 10^{-16}$  with selection criteria that give  $\sim 20\%$  acceptance. The resolution function has FWHM of about 900 keV and very little high energy tail. There are additional potential backgrounds resulting from pattern recognition errors; these are discussed in detail in section 3.8.3. The background level depends sensitively on the detector accidental rates. It is calculated to be 0.006 events at the expected detector rates.

The resolution function can eventually be verified from the data in a number of ways. Positive pions can be stopped and the spectrum of electrons from  $\pi^+ \rightarrow e^+ \nu$  decay measured with reduced magnetic field. The spectrum of electrons near the endpoint can be predicted and compared to the measured distribution. Tails in the resolution function that arise from pattern recognition errors can be studied by relaxing selection criteria. For example, the requirement that the fitted trajectory project to the energy deposited in the trigger calorimeter can be removed and the number and energy distribution of background excluded by that cut compared to simulations. Other examples of essentially independent selection criteria that can be relaxed are the requirement that there be no missing hits on the fitted trajectory and the requirement that no low energy track be reconstructed in the same event. In this way, the efficacy of each selection criterion can be measured from the data and compared with the calculated efficacy. Finally, tails in the resolution function are extremely sensitive to detector rates, and the background rate with relaxed selection criteria will be studied as a function of the muon stopping rate.

### 3.4.2 Radiative $\mu$ Capture

Electrons result from radiative muon capture (RMC),  $\mu^- \text{Al} \rightarrow \gamma \nu_\mu \text{Mg}$ . The  $\gamma$  endpoint energy is 102.5 MeV and the probability (per  $\mu$  capture) of producing a photon with energy exceeding 100.5 MeV is  $\sim 4 \times 10^{-9}$  [46]. The conversion probability in the target is  $\sim 0.005$ , and the probability that the electron energy exceeds 100 MeV is  $\sim 0.005$ . The probability of producing an electron above 100 MeV is then  $\sim 10^{-13}$ .

These electrons are all less than 102 MeV (most are near 100 MeV), and for an electron to be considered as signal, its measured energy must exceed 103.6 MeV. The integral of the high energy tail in the resolution function above 1.6 MeV is less than  $10^{-6}$  (limited by statistics). Hence, the probability of getting an electron above 103.6 from radiative  $\mu$  capture is less than  $10^{-19}$  or a background/signal ratio of below 0.001 for  $R_{\mu e} = 10^{-16}$ .

This background is not distinguished from DIO electrons. However, the measured energy distribution near the endpoint can be fit to a combination of DIO and RMC electrons to verify the respective contributions.

### 3.4.3 Beam Electrons

Beam electrons may cause background if they are produced in the production or transport solenoid region and then scatter in the stopping target. Independent of the transverse momentum of the electron as it exits the transport solenoid, the transverse momentum at the tracking detector is below 75 MeV/c unless it scatters in the stopping target, by design of the detector solenoid field.

The rate for electrons scattering at  $\sim 100$  MeV is defined by the Mott cross section multiplied by a nuclear form factor for the target material. The experimentally determined [47] form factor for aluminum is shown in Figure 4. Figure 4 also shows the scattering cross section on aluminum for Mott scattering with and without the form factor included.

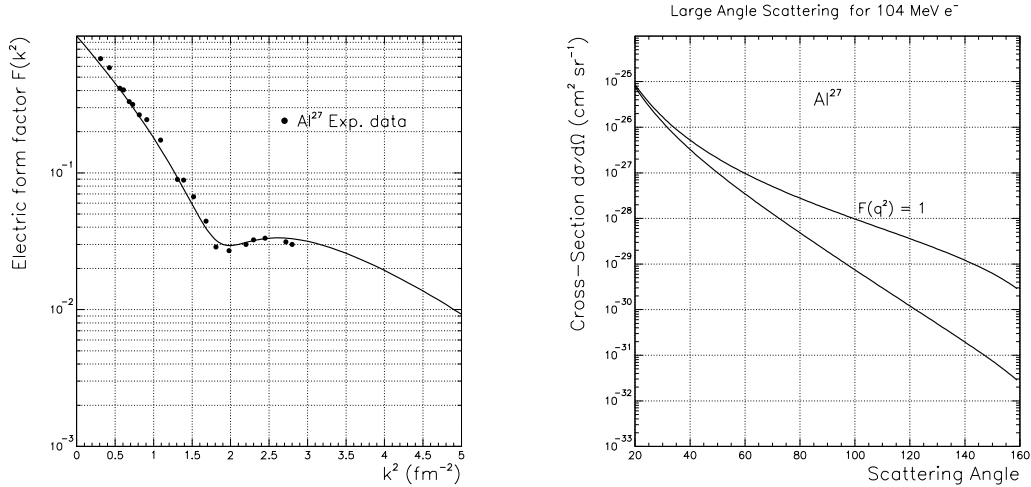


Figure 4: The form factor for electrons scattering on aluminum is shown on the left. The plot on the right shows the electron scattering cross section as a function of scattering angle for 100 MeV electrons. Cross sections are shown for the Mott formula, and with the inclusion of the nuclear form factor.

The collimator system is designed to suppress high energy electrons. A GEANT simulation of the production of electrons and their transport to the detector solenoid yielded no transmitted electrons above 100 MeV for  $10^7$  incident protons. We approximate the expected number of events above 100 MeV by fitting the energy spectrum between 70 and 90 MeV to an exponential and extrapolating to the region above 100 MeV. We take the transverse momentum distribution of the events to be that of electrons with energy in the interval 70–90 MeV (essentially flat from 0–20 MeV/c), and use that distribution to calculate the probability of scattering in the target to a transverse momentum exceeding 90 MeV/c. Including the solid angle acceptance, the probability that electrons of 100 MeV scatter to  $p_t > 90$  MeV/c is about  $10^{-5}$ . With a run time of  $10^7$  sec, a proton intensity of  $4 \times 10^{13}$  p/s, and a beam extinction of  $10^{-9}$ , the expected background is 0.04 events in a 1.5 MeV region around the signal.

Background from beam electrons can be distinguished from other prompt backgrounds by the energy distribution of these events, which is falling very steeply with energy due to the beam acceptance, and by their transverse momentum distribution, which is also strongly forward peaked. This is contrasted with the transverse momentum distribution of electrons

from muon DIO and radiative pion capture. The energy distribution is also very different from that of electrons from radiative pion capture. These events will also have a very different time distribution than those from muon DIO, following the time distribution of out of time protons hitting the production target, which will be monitored.

#### 3.4.4 Muon Decay in Flight

Muons decaying in flight can produce energetic electrons that either have sufficient transverse momentum to fake signal or that scatter in the stopping target and fake signal. In order for the electron to have energy above 102 MeV, the  $\mu^-$  momentum must exceed 77 MeV/c. Electrons produced by  $\mu^-$  decays before and within the transport solenoid are included in the beam electron background calculation. Background from decays in the detector solenoid are calculated using a GEANT beam simulation. The yield of  $\mu$ 's with  $p_\mu > 77$  MeV/c passing the transport solenoid is  $\sim 0.5 \times 10^{-4}$  per incident proton, the decay probability upstream of the tracking detector is  $1.2 \times 10^{-2}$ , and the probability of having  $103 \text{ MeV} < E_e < 105 \text{ MeV}$  and  $p_T > 90 \text{ MeV/c}$  is less than  $1.2 \times 10^{-7}$  with no events seen in a larger energy interval. With a beam extinction of  $10^{-9}$ , the total background in a one year run is less than 0.03. This estimate can be better refined with increased statistics in the simulation.

A second background source is electrons from  $\mu^-$  decay that scatter in the stopping target. A GEANT simulation was used to calculate the energy distribution of electrons from muons that passed the transport solenoid and decayed in the region between the entrance to the production solenoid and the tracking detector. The kinematic distribution of these electrons was then used as input to a simple simulation of the probability that an electron of the appropriate energy scattered in the stopping target with a resulting transverse momentum exceeding 90 MeV/c. The probability per proton of getting an electron with  $103 \text{ MeV} < E_e < 105 \text{ MeV}$  from a  $\mu^-$  decay is  $0.5 \times 10^{-8}$  and the probability of scattering to  $p_t > 90 \text{ MeV/c}$  is  $2 \times 10^{-5}$ , resulting in an expected background of 0.04 events for an extinction of  $10^{-9}$ .

This background is very similar in kinematic and time distributions to that from beam electrons and can be distinguished from muon DIO and radiative pion decay in the same way.

#### 3.4.5 Pion Decay in Flight

Beam pions decaying to electrons with  $E_e > 102 \text{ MeV}$  and  $p_T > 90 \text{ MeV/c}$  are also a potential source of background. The  $\pi$  momentum must exceed 60 MeV/c for this background process. A GEANT simulation was used to calculate the probability of a proton producing a beam  $\pi$  with  $p_\pi > 54 \text{ MeV/c}$  passing the transport solenoid; it is  $2.0 \times 10^{-6}$ . The probability for a  $\pi$  to decay into an electron after the transport solenoid and before the tracking detector is  $1 \times 10^{-4}$  and the probability of the decay electron to have  $E_e > 102 \text{ MeV}$  and  $p_T > 90 \text{ MeV/c}$  is  $5 \times 10^{-6}$ . The background from this source is below  $10^{-3}$  events for an extinction of  $10^{-9}$ .

A second background mechanism is  $\pi$  decay electrons that scatter in the stopping target. This background was calculated in much the same way as the similar process for  $\mu^-$  decay. The number of electrons from  $\pi$  decay with  $103 \text{ MeV} < E_e < 105 \text{ MeV}$  per proton is  $0.8 \times$

$10^{-11}$  and the probability of scattering to  $p_T > 90$  MeV/c is  $4 \times 10^{-5}$ , also resulting in an expected background of less than  $10^{-3}$  events for an extinction of  $10^{-9}$ .

### 3.4.6 Radiative $\pi$ Capture

Pions are immediately captured by a nucleus after they stop in the target; about 2% of the captures result in the emission of a photon [48] without significant nuclear excitation. The photon energy spectrum has a peak at 110 MeV and endpoint at 140 MeV. The probability of photon conversion in the Al target, with a conversion electron in a 1.5 MeV energy interval around 104 MeV is  $3.5 \times 10^{-5}$ , as calculated in a GEANT simulation. The acceptance for electrons from photon conversion is large ( $\sim 0.8$ ), since the path length for conversion is largest for photons emitted at  $90^\circ$ . The yield of  $\pi$ 's that pass the transport solenoid and stop in the target is  $\sim 3 \times 10^{-7}$  per proton. With a beam extinction of  $10^{-9}$ , the background is estimated to be 0.07 events from pions produced by protons impinging on the target between beam pulses.

The energy spectrum of these events extends to above 130 MeV. They are distinguished from beam electrons and muon decay in flight backgrounds by this spectrum. They also are more strongly peaked to higher transverse momentum and can be distinguished in this way. As with all prompt processes, the fluxes of these can be increased by orders of magnitude by decreasing the extinction.

A second contribution to radiative pion capture is that due to pions that take a very long time to traverse the production and transport solenoid and arrive at the stopping target. For these events, the suppression factor from the beam extinction is absent. However, since our detection window starts 700 ns after the proton pulse, the pions must live approximately 700 ns and must either move slowly or follow a trajectory in the transport solenoid that results in a flight time of 700 ns in order to be a source of background. This background is estimated as follows. Protons are caused to impinge on the production target. The momentum, position, and time coordinates are recorded for  $\pi$ 's that reach the entrance of the transport solenoid. These events are then transported to the stopping target without allowing them to decay. Figure 5 shows the distribution in the arrival time at the stopping target, weighted by the survival probability. Based on the time distribution in Figure 5, we take an accepted time window starting 700 ns after the proton pulse (the minimum flight time to the target is  $\sim 50$  ns), giving a ratio of late arriving pions per proton of  $0.4 \times 10^{-17}$ . The probability of making a background electron is  $5.6 \times 10^{-7}$  (see the preceding paragraph). Hence, the expected background is 0.001 events.

This background is easily calibrated from the data due to the very strong time dependence. By measuring the number of energetic electrons as a function of time during the pulse, this source can be directly normalized and an appropriate starting time for the detection window chosen.

### 3.4.7 Anti-proton Induced

Another potential source of background is due to anti-protons. Only low momentum ( $< 100$  MeV/c)  $\bar{p}$ 's can propagate down the transport solenoid; they have very low kinetic energy and velocity and will take a very long time to transit the transport solenoid. For this reason,

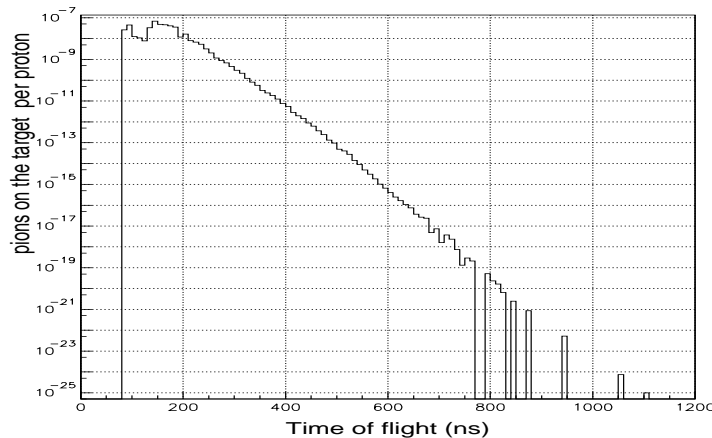


Figure 5: The distribution in the  $\pi$  arrival time for late arriving  $\pi$ 's, weighted by the survival probability in the transport solenoid.

they are not suppressed by the beam extinction and arrive at the stopping target essentially continuously. Since the proton energy is near  $\bar{p}$  production threshold, the production cross section is small and strongly depends on the Fermi momentum in the nucleus, particularly for low momentum  $\bar{p}$ 's. This cross section is not well measured, nor is it well modeled in the GEANT code.

In general, the backgrounds can be suppressed in the following ways:

- Reduce the rate of production by decreasing the proton beam momentum below  $\bar{p}$  production threshold.
- Absorb the  $\bar{p}$ 's in a thin absorber somewhere in the muon transport.
- Sweep the  $\bar{p}$ 's from the beam with crossed E and B fields.

We have studied the backgrounds arising from  $\bar{p}$ 's produced at the production target for proton beam momenta in the interval 5-8 GeV/c. The studies included the appropriate nuclear model for nucleon momentum and energy distributions, the  $\bar{p}$  production mechanisms, and the  $\bar{p}$  annihilation mechanisms. The  $\bar{p}$  flux was calculated as was the flux of pions and electrons resulting from their annihilation. It is found that a thin absorber in the transport system is required to reduce the background to below  $10^{-3}$  events. This is accomplished without introducing additional sources of backgrounds or changing the muon yield. The calculations are discussed in reference [49].

Figure 6 shows the differential cross section for  $\bar{p}$  production at several angles for 7 GeV/c protons incident on W, calculated using a phase space model. The kinematics of nucleons in the heavy nucleus were modeled [50] including a dispersion relationship between energy and momentum. At low momentum,  $\bar{p}$ 's are produced isotropically as expected from phase space consideration. At high momentum, the production cross section is strongly forward peaked. Recall that for  $\bar{p}$  production on a proton at threshold, the momentum of each of the four (anti)baryons is one fourth the beam momentum. The  $\bar{p}$  momentum is peaked and slow-varying between 1-2 GeV/c, and the production is suppressed for momenta below 100 MeV/c.



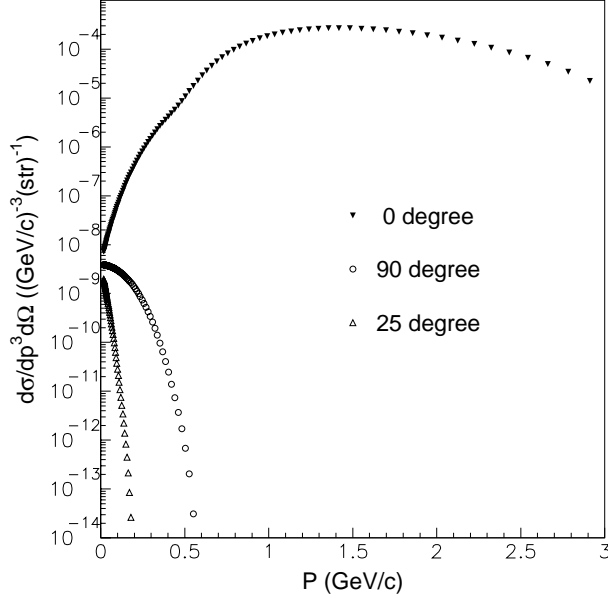


Figure 6:  $\bar{p}$  differential cross section at production angles of 0, 90 and 180 degrees respectively.

The differential cross section was normalized to the measurements of Cork, et al. [51], for incident proton kinetic energy of 6 GeV on a beryllium target and  $\bar{p}$  momentum of 1.41 GeV/c at 6 degrees exit angle, corrected for the A dependence of the production cross section [52, 53]. This is essentially at the peak of the differential cross section. Other measurements [54] (also on Be) give similar normalization. There is also differential production cross section data for 12.3 GeV protons incident on copper at  $\bar{p}$  momenta around 1 GeV/c in the forward direction [55]. As a comparison, the production cross section was also calculated using the same phase space method for 12.3 GeV incident protons. The calculated values were smaller than the measurements by a factor of 4, presumably because the phase space method underestimates the production at higher energy where more production channels open up. Even if the discrepancy between data and theory persisted near threshold for heavy targets, the  $\bar{p}$  induced background would not be limiting.

The calculated production cross sections were used to generate  $\bar{p}$ 's within the MECO production target; their motion and interactions were then studied using GEANT. It was found that most of the low energy  $\bar{p}$ 's that entered the transport system were produced at the peak of the production cross section (forward and with about 1.5 GeV/c momentum) and were shifted down in momentum by dE/dx energy loss and nuclear interactions in the target. Hence, the predicted  $\bar{p}$  flux is reliably normalized to experimentally determined production cross sections in the relevant kinematic region.

These simulations showed that an unacceptable flux of  $\bar{p}$ 's reached the stopping target with the nominal transport. The typical kinetic energy was very low, and they could be completely absorbed with a 120  $\mu\text{m}$  beryllium window at the center of the transport solenoid. Figure 7 shows the  $\bar{p}$  annihilation positions in the transport with the absorber in place. The horizontal line at the position (0,0) is formed by the many annihilations in the absorber.

To calculate expected fluxes of electrons and pions in the detector solenoid from  $\bar{p}$  annihilations, experimentally determined annihilation cross sections were used to generate appropriate numbers and kinematic distributions of charged and neutral pions at the  $\bar{p}$  annihilation positions. These annihilation products were then tracked with GEANT and particle fluxes at the stopping target determined. Using previously determined probabilities that pions and electrons produce background, the expected  $\bar{p}$  induced background was calculated. The re-

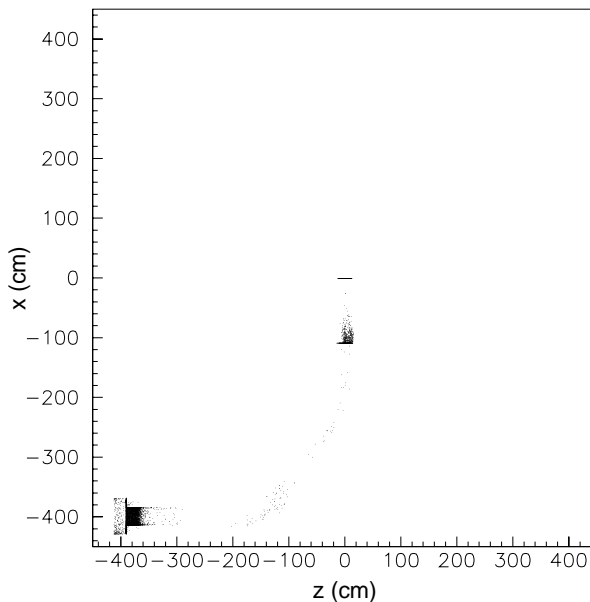


Figure 7: A scatter plot of the  $\bar{p}$  annihilation positions in the transport system. Outlines of the production solenoid, the first  $90^\circ$  bend in the transport solenoid and the thin beryllium window that stops all  $\bar{p}$ 's that would otherwise reach the detector solenoid are formed by the dense accumulation of annihilation positions.

sulting low level of background primarily resulted from radiative pion capture with a smaller contribution from electrons that scatter in the stopping target. Table 3 summarizes results of  $\bar{p}$  induced backgrounds for different incident proton momenta; the details of the calculations are discussed in reference [49].

Anti-proton induced backgrounds are very sensitive to the incident proton energy and in principle can be studied by changing proton beam energy. They are also the only beam associated background that has a time distribution with no correlation with the RF structure in the beam. Backgrounds without time structure above the level of that due to cosmic rays would indicate  $\bar{p}$  contamination.

### 3.4.8 Long Transit Time Backgrounds

We have discussed two sources of backgrounds from late arriving particles: pions that arrive at the stopping target with long transport times and anti-protons. Late arriving pions are easily calculated with high sensitivity because we can turn off decays and study them with

high effective luminosity and then multiply by the very small probability that they have not decayed. Anti-proton induced backgrounds can be calculated because we can independently calculate the stopping probability at different places in the transport and the probability that annihilation product produced at the stopping position causes background. Both are small numbers, and they can be multiplied to give the total background probability.

Backgrounds from other processes with long transit times are not so easily calculated because large suppression factors cannot be independently calculated and then multiplied to give a total suppression. The largest contribution to this category is pions that decay in a region of nearly uniform field (in the first straight section of the transport solenoid, for example) yielding a trajectory with very little longitudinal momentum. Without a muon decay, such a particle would be swept out of the beam acceptance as it traversed the first curved section. However, with a muon decay and the electron subsequently scattering, it could in principle reach the detector solenoid. There is no simple set of multiplicative suppression factors that can be calculated to describe this situation.

To study those backgrounds in a complete Monte Carlo technique to the level of  $10^{-3}$  events would require simulating about  $10^{17}$  protons. Simulating that many events is not possible given available computing resources. We have adopted a semi-analytic technique that breaks this generic type of background into many classes (depending, for example, on where the pion and muon decay) and then calculating either multiplicative suppression factors for these many classes or showing that a particular class cannot result in a particle surviving the transport.

A full discussion of the calculations is given in reference [56]. The potential for long transit time in both the production and the transport region is considered. In the transport region, maximum possible transit times in each of the straight and curved sections is calculated. We considered all possible decay modes of  $\mu \rightarrow e$ ,  $\pi \rightarrow e$  and  $\pi \rightarrow \mu \rightarrow e$ . We also take into account the effects of scattering on the collimators and the production target.

Some important features of the MECO design allows significant suppression of the late arriving particle backgrounds. First an axially graded B field tends to increase the longitudinal momentum of charged particles moving through it in helical orbits. As a result of these background calculations, we have removed all constant field regions of the transport, introducing gradients in each of the three straight sections of the transport solenoid and removing the constant field region in the production solenoid. Another important feature is that particles moving in helical orbits in a torus drift in a direction perpendicular to the

Table 3: The table gives the total  $\bar{p}$  induced backgrounds for different incident proton momenta.

Proton momentum (GeV/c)	Number of $\bar{p}/p$ produced	Number of $\bar{p}/p$ entering transport	Background events
5	$3.9 \times 10^{-10}$	$7.4 \times 10^{-15}$	$7 \times 10^{-7}$
6	$5.3 \times 10^{-8}$	$8.0 \times 10^{-13}$	$8 \times 10^{-5}$
7	$1.4 \times 10^{-6}$	$1.2 \times 10^{-11}$	$1.2 \times 10^{-3}$
8	$8.5 \times 10^{-6}$	$6.8 \times 10^{-11}$	$7 \times 10^{-3}$

plane of the torus. The amount of drift is approximately proportional to the inverse of longitudinal momentum. Therefore, a charged particle with longitudinal momentum small enough to have a long transit time in the curved portion of the solenoid (produced with that trajectory by either scattering or decay) will drift to the wall and be absorbed in the curved section.

With the changes to the transport discussed above, it is found[56] that the number of muons or electrons with sufficient energy to cause backgrounds is negligible.

### 3.4.9 Cosmic Rays

Cosmic ray induced electrons are potentially a limiting background and we have studied it using a GEANT simulation [57] of the detector and shielding. The details of the simulation and the shielding required to reduce the background to a negligible level are discussed in a later section. The conclusion of these studies is that cosmic ray background can be reduced to a negligible level with a combination of active and passive shielding and detection of extra particles in the tracking detector. The rejection techniques consist of the following:

- A passive shield of modest thickness (2 m of concrete and 0.5 m of steel).
- Two layers of scintillator veto counter surrounding the detector, with a combined efficiency for charged particles of 99.99% (1% inefficiency per layer).
- Selection criteria that eliminate events having significant evidence of extra particles in either the tracking or calorimetric trigger detector in time with the electron candidate.

With this suppression, the expected background from cosmic rays in a  $10^7$  second run is estimated to be  $\sim 0.004$  events.

### 3.5 Pulsed Proton Beam

As discussed in Section 3.4, a pulsed beam is required to reduce prompt backgrounds to an acceptable level. The required time structure has short (much less than  $\tau_\mu$ ) pulses of muons separated by approximately  $\tau_\mu$ . A natural way to do this with the AGS is to fill two RF buckets, separated by half the circumference of the machine (corresponding to  $1.35 \mu\text{s}$ ), and then extract the beam while still bunched. Figure 8 shows schematically the various time structures in the proposed beam.

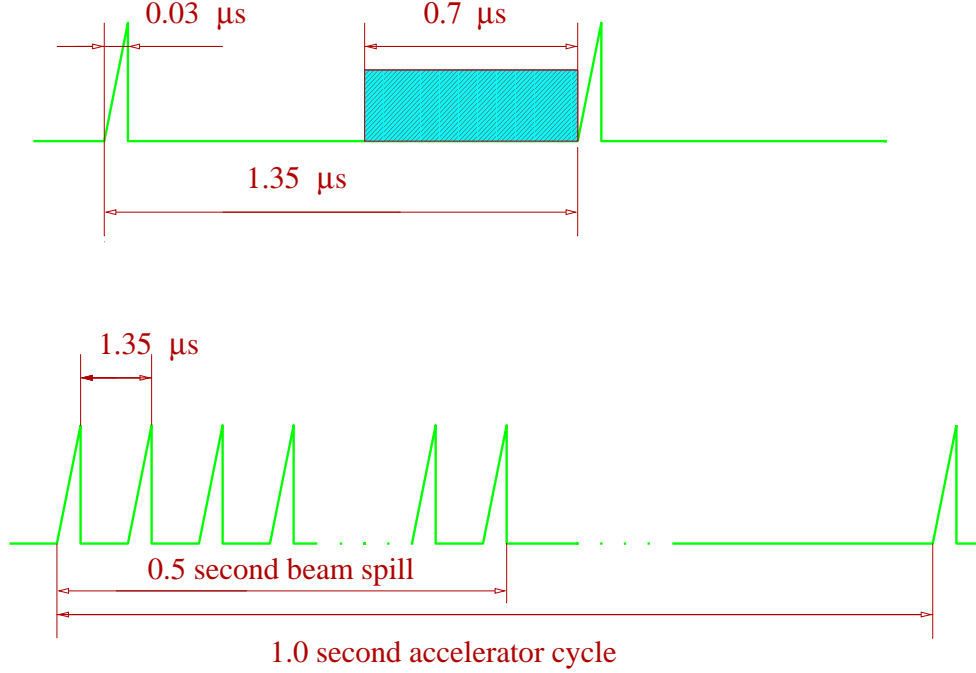


Figure 8: A schematic picture of the beam time structure is shown. The top drawing shows the micro-structure, with 30 ns long proton pulses separated by  $1.35 \mu\text{s}$ . The shaded region is the time during which conversion electrons are detected. The bottom drawing shows the macro-structure with a 0.5 s long train of pulses separated by  $1.35 \mu\text{s}$  in a 1.0 second long accelerator cycle.

Two machine operating parameters are affected by the pulsed beam requirement. The first is the amount of beam that exists and is extracted between the filled bunches; we call this the extinction, defined as the ratio of the proton flux in a time interval of 700 ns just before the filled bucket (the time during which the conversion signal would be detected) to that in the filled bucket. The second is the intensity in the filled buckets required to reach the MECO intensity goal. We believe that acceptable values of both operating parameters can be achieved, based on extrapolation of current operating parameters.

The AGS has operated with 6, 8 and 12 buckets in the  $2.7 \mu\text{s}$  revolution time. Minimizing the number of unfilled RF buckets is an advantage, since only particles in RF buckets can remain in stable orbits during acceleration. We propose that the AGS would run with harmonic number 6 (6 RF buckets in the revolution time) with a total of  $4 \times 10^{13}$  protons per cycle ( $2 \times 10^{13}$  protons in each filled RF bucket). Currently, the maximum intensity that has

been demonstrated is  $\sim 10^{13}$  protons per RF bucket. AGS accelerator physicists believe that doubling the density is possible. The optimism stems largely from two differences in MECO vs. standard running conditions. First, only two transfers from the booster to the AGS will be required. Hence, beam will be stored at transfer energy, where space charge effects are most severe, for only 160 ms. Second, the beam will not be accelerated through transition. Beam instabilities at transition restrict the bucket density during normal operations and this limitation will not exist. No tests have yet been done of operation at design bucket intensity.

Since only two transfers from the booster are required and we only accelerate to 8 GeV, the cycle time is short. Table 4 summarizes the cycle. It consists of two transfers from the booster to the AGS, each filling two buckets. Each of the two pairs of bunches are then coalesced into a single bucket with a VHF cavity. The bunches are then accelerated to between 7 and 8 GeV/c and extracted over a period of 0.5 s.

Table 4: The table shows the times required for the various stages in injection, acceleration and extraction for the MECO operating mode of the AGS.

Operation	Cumulative time [ms]
First booster transfer	0
Second booster transfer	130
Coalesce bunches	160
Accelerate	320
Slow extraction	820
Ramp down and settle	980

There may be advantages to producing a pulsed beam with spacing  $2.7 \mu\text{s}$ . This could be achieved by running the AGS at higher harmonic number (12, for example) and filling two adjacent buckets. The two filled buckets would then be coalesced just before extraction, resulting in a single bunch in the  $2.7 \mu\text{s}$  revolution time. This running mode is particularly advantageous if a calorimeter with long collection time (i.e. one made of BGO) is used. It would allow a longer detection time (up to  $1.8 \mu\text{s}$  out of  $2.7 \mu\text{s}$ ), resulting in a gain in sensitivity per unit running time. The disadvantage is the higher instantaneous intensity, since all beam is now in one bunch rather than two. Accelerator physicists in CAD have said that either mode of operation could be achieved, and the operating mode would not have to be decided until rather late and could be changed during the experiment. It is likely that the second mode of operation will be required if a BGO calorimeter is used.

Some tests have been done [58, 59] of the extinction with the help of AGS personnel. One RF bucket was filled and accelerated to 24 GeV, and extracted bunched. We measured the trigger rate in a neutral kaon decay experiment at various times with respect to the RF bucket. That trigger is known to have unmeasurably small rate when high energy protons are not hitting the production target in which kaons are made and the rate is proportional to the rate of protons hitting the target. Figure 9 shows the relative intensity as a function of time with respect to the filled bucket. The extinction between buckets is below  $10^{-6}$  and in unfilled buckets is of order  $10^{-3}$ . The solid histogram and dots are result from measurements

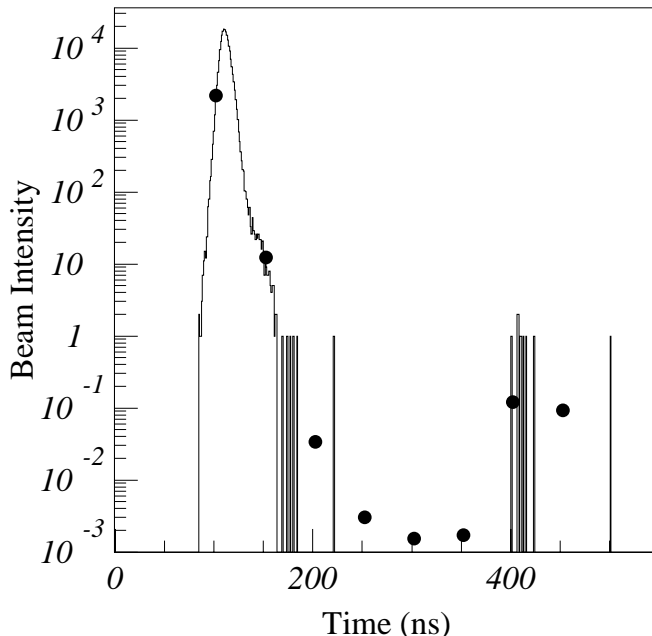


Figure 9: Plot of the beam intensity as a function of time with respect to pulses in the bunched beam extracted from the AGS.

with a QVT and scalars, respectively; both were used in order to get both a good measure of the main pulse shape and a good dynamic range. The extracted pulse has a width of about 30 ns. During these tests, no time was available to understand the source of beam in unfilled buckets nor was any tuning done to reduce beam in unfilled buckets.

A second study was carried out using the E787 detector. That experiment uses 24 GeV proton interactions incident on a platinum target to produce a secondary beam of 720 MeV/c  $K^+$ . The beam is defined by a series of counters including a Cerenkov counter and Pb glass counter. For the test, the proton beam was extracted at 7.4 GeV/c and the secondary beam tuned to 200 MeV/c. Pions of momentum 200 MeV/c have approximately the same beta as 720 MeV/c kaons and will trigger the Cerenkov counter. The pion rate was measured by a coincidence between an upstream scintillation counter and the Cerenkov counter.

One RF bucket was filled, producing bunches separated by  $2.7 \mu\text{s}$ . Approximately  $10^5$  pions per 0.3 s spill were counted. The measurement consisted of determining the total pion rate and comparing it to the rate between bunches. The total rate used a coincidence with a signal 900 ns long centered on the extracted RF bucket. The background was in a 1800 ns interval between the filled bunches. The extinction (defined as the ratio of these count rates, corrected by about a factor of 2 for saturation) was measured to be  $\sim 1.0 \times 10^{-7}$ . Again, the test time did not allow significant tuning to improve the spill quality.

It is possible, but unlikely, that by appropriate tuning of the AGS a pulsed beam with extinction below  $10^{-9}$  can be achieved. If that is not the case, a means of improving it is required. Two possibilities have been explored. The first involves a system of kickers in the AGS ring. This method of improving the extinction has the advantage that the kickers will run continuously during acceleration and require relatively small field since the beam is

kicked many times. The basic idea of the system is to use two magnets in the AGS ring. One magnet produces a field modulated at 60kHz. This would serve to destabilize the beam, and only low field is required for this purpose. To preserve the stability of the beam in the filled RF buckets, a kicker is operated at the frequency of the filled RF buckets, about 740 kHz in the case of two filled buckets in the  $2.7 \mu\text{s}$  revolution time of the machine. The field integral in this kicker is adjusted to be equal and opposite in magnitude to that of the sinusoidally modulated magnet, and it fires only when the filled buckets pass through it. Hence, the net momentum transfer to protons in the filled RF buckets is zero.

A second solution is a pulsed electric or magnetic kicker [60] in the proton transport line. A kicker could, for example, divert an 8 GeV beam by 2 mrad. The beam would then be focused onto a septum magnet at the end of a drift path following the kicker, such that the beam could then be transported to the  $\mu$  production target during the active part of the duty cycle and dumped during the rest of the duty cycle. By measuring the diverted flux during the off cycle in a short secondary beam, the extinction of the beam as it exits the AGS would also be monitored.

An efficient way of producing a rectangular pulse train that achieves this goal is described in reference [60]. The idea is to develop the appropriate time structure (rectangular, for example) by driving magnets at the harmonics of the pulse frequencies at amplitudes that correspond to the Fourier decomposition of the desired time structure. Since these devices can have relatively high Q, significant power savings can be achieved, and the driving electronics can be rather straightforward. The currently preferred solution is a magnetic device, basically a series of strip-line magnets.

With the expectation that the internal AGS kicker described above will achieve the desired extinction, we currently propose to build a single device running at 740 kHz. This kicker would be run with the beam pulses synchronized with the maxima of the magnetic field, and would divert unfilled bunches in the opposite direction. This mode of operation requires more careful control of the amplitude of the field and gives better separation of filled and unfilled bunches (compared with synchronizing the pulses with the zero crossing). A peak magnetic field of 0.0075 T in a magnet of 5 m length would result in a separation of filled and unfilled bunches by  $\sim 21$  mrad. A bare copper magnet with those parameters running with a Q of 300 and having a field volume of  $10 \times 10 \times 500 \text{ cm}^3$  would require 35 kW of delivered power at 740 kHz. Returning the field in ferrite would reduce the stored power by a factor of two, but would have a somewhat lower Q due to losses in the ferrite; the required RF power is about 24 kW.

The simplified external kicker would provide some additional extinction and would also allow a measurement of the beam extinction as it leaves the AGS and allow early detection of problems with the internal kicker operation. This is done by measuring the intensity and time structure of the diverted beam between pulses. This intensity is rather low and easily measured with a simple counter system.

We note that developing the operating parameters of the accelerator could begin as soon as the MECO Project is approved. Indeed, some test have already been done. We propose that both kickers be built early in the construction phase to allow the machine performance to be optimized prior to finishing the construction and beginning the commissioning of the experiment.

Both the internal and external kickers have been costed by CAD personnel, albeit with



different levels of sophistication. A rather reliable costing of the internal device is based on a specific design. A conceptual design is used for the costing of the external device. The current estimated cost is dominated by the cost of commercially available broad band RF amplifiers plus significant personnel costs due to the uncertainty in the final design. We anticipate significant savings in the final cost of the external device.

### 3.6 Muon Beam Design and Performance

A new muon beam with intensity a factor of 1000 greater than that of any previously constructed is crucial to achieve the goals of this experiment. Further, for reasons discussed previously, the beam must be pulsed, and having it sign and momentum selected is a significant advantage in terms of reducing rates and backgrounds. It must have low contamination by pions and energetic electrons and muons. In meeting these performance goals, we have come upon a design that is extremely flexible; it can be reconfigured for positive or negative muons and as a “surface” muon beam. Simple modifications to the primary proton beam that is used to produce the muons can be made that will allow different time structures to be made. Figure 3 shows the full set of solenoids with production and stopping targets and the detectors.

Protons impinge on a heavy target in a *production solenoid* that has a graded axial field. The use of a production target in a graded solenoid was first discussed by Djilkibaev, Lobashev and collaborators [36, 37]. Their ideas were subsequently adopted by proponents of the muon collider [61, 62]. Pions produced in the target with transverse momentum below some value (about 180 MeV/c) travel in helical trajectories within the clear bore of the solenoid and decay to muons. The graded axial field results in a magnetic bottle open in the direction of the muon beam. Invariance of the quantity  $p_T^2/B$  and energy conservation imply that particles originating at the target are reflected from the closed (upstream) end of the bottle if  $\tan(\theta) > \sqrt{B_{target}/B_{max}}$ , where  $B_{max}$  and  $B_{target}$  are the values of the axial component of the magnetic field at the target and the upstream end, respectively, and  $\theta$  is the angle of the pion with respect to the solenoid axis at the target. For the MECO case, the *loss cone*, where particles are not reflected, has a half angle of about  $30^\circ$  and hence the solid angle acceptance for pion capture is  $\sim 93\%$ .

A fraction of the muons resulting from pion decay are captured in the *transport solenoid* that guides them to the experiment. They are transported with high efficiency by maintaining a solenoid field from the production target to the detector region. So long as the field varies slowly with respect to the Larmour radius of the helical orbit, particles will follow field lines in helical orbits. The radius of the clear bore of the transport solenoid is chosen to provide good acceptance for muons that would eventually hit and stop in the stopping target. Minimizing long transit times requires a field with monotonically decreasing axial component so that particles are not reflected from local field maxima. Particles that scatter in a region of constant field such that the resulting axial component of the momentum is very small could spend a long time in the constant field region. By introducing even a small gradient, long transit times are heavily suppressed. The beam is sign and momentum selected by using two curved sections and appropriate collimators at three positions along the transport solenoid.

Muons arrive at the *detector solenoid* where a significant fraction are brought to rest in a *stopping target* where conversion electrons may be produced and detected in a series of particle detectors. Here the muon beam is integrated with the detection apparatus. In the region of the stopping target and detector, the goal of the field design is to transport electrons from the stopping target to the magnetic spectrometer, which is downstream of the target. The purpose of having the spectrometer displaced from the axial position of the target is to reduce rates in it due to photons and protons originating from  $\mu$  capture. Good

detection efficiency is achieved by placing the target in a region of graded field. Since  $B/p_T^2$  is conserved, 105 MeV/c particles with  $p_T$  exceeding some value (whether initially moving towards or away from the stopping target) will arrive at the region of the spectrometer with a restricted range of  $p_T$ . For the MECO geometry, 105 MeV/c electrons emitted at  $90^\circ \pm 30^\circ$  with respect to the magnet axis are accepted with high efficiency if the B field decreases from 2 T at the entrance of the detector solenoid to  $\sim 1.4$  T at the target and then to 1.0 T before the spectrometer.

In the following sections, we describe in detail the components of the muon beam-line, the results of calculations of the particle content in the beam, and the calculations of the effects of the intense flux of particles that originate from the production target. In general, these calculations have been done using the GEANT package of particle interaction codes. The beam-line and detector elements were modeled in detail appropriate to the calculation. Results from different hadron interaction codes were compared and, when possible, compared with data. In some cases, analytic calculations were used to augment the numerical calculations. We end with a description of the technical implementation of the super-conducting magnet system, based on a preliminary design by the NSF supported National High Magnetic Field Laboratory (NHMFL).

### 3.6.1 Muon Production

The basic principle of the production region is illustrated in Figure 10, which shows a schematic view of the production solenoid and beginning of the transport solenoid. The result of the GEANT simulation of a typical event containing a  $\mu^-$  produced by the interac-

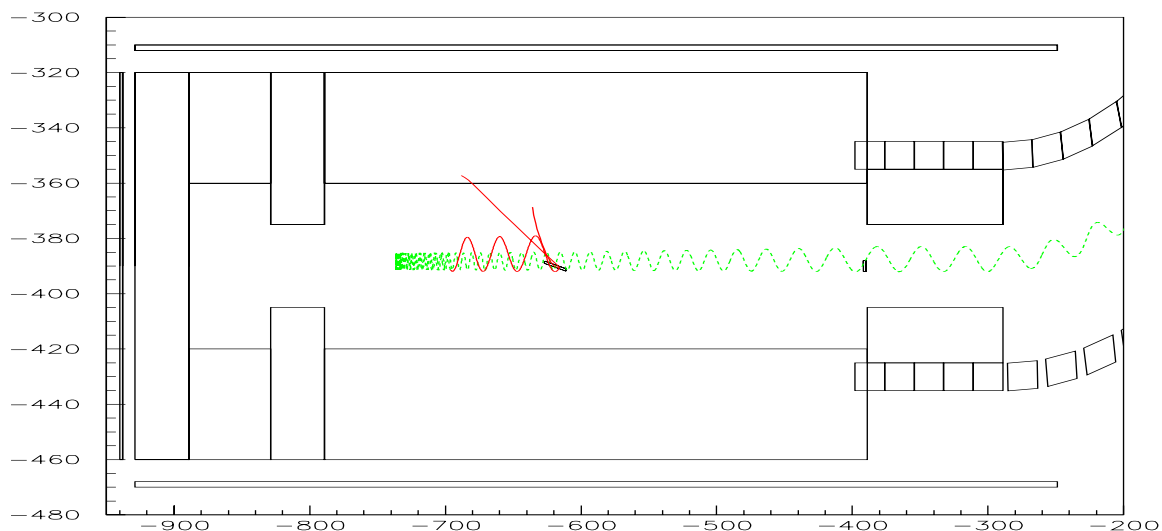


Figure 10: Schematic drawing of the production solenoid with a proton interaction producing a  $\mu$  superimposed. The incident proton beam enters from the right.

tion of a proton in the target is superimposed. The proton beam enters from a hole in the downstream wall of the solenoid (-400 cm in Figure 10); non-interacting protons exit through a larger hole in the upstream wall (-800 cm). The direction of the proton beam is opposite

that of the muon beam in order to reduce the fluence of low energy photons and neutrons into the muon channel and eliminate complications associated with the interactions of the diffuse exiting proton beam and the beginning of the muon transport.

The calculated values of particle fluxes in the beam are based on GEANT simulations of proton interactions in the Tungsten target. GEANT has a variety of hadron interaction codes, and we have primarily used GHEISHA. However, there is significant variation between different codes for the total  $\pi^-$  production cross sections and kinematic distributions. For example, the GHEISHA and FLUKA codes differ by a factor of about 4 in the muon yield at 8 GeV incident proton energy; the variations with model were discussed extensively in the original MECO proposal [38]. In order to reduce the uncertainty in the muon yield (and hence the sensitivity of the experiment) due to the uncertainty in the hadronic models of low energy hadron production, we have scaled the results from GEANT (with GHEISHA) to agree with measured  $\pi^-$  production cross sections. The effect of this scaling is to reduce yields by a factor of  $\sim 2$  with respect to the GEANT + GHEISHA prediction. The backgrounds that depend directly on pion production rates have also been scaled in the same way.

The data to which we compare our simulation are from measurements [63] of invariant cross sections for  $\pi^-$  production as a function of kinetic energy ( $T$ ) and production angle ( $\theta$ ) measured in the reaction  $p + Ta \rightarrow \pi^- + X$  over the full angular production range and for  $p_\pi > 80$  MeV/c. Tantalum is adjacent to Tungsten in the periodic chart. One mm thick Ta plates with spacing of 93 mm were placed in a 2 m propane bubble chamber that was operated under a magnetic field of 1.5 T. Pion trajectories were confidently identified with minimum momentum of 80 MeV/c ( $T = 21$  MeV). The measured average  $\pi^-$  multiplicity at 10 GeV/c is  $1.51 \pm 0.03$ . The experimental  $\pi^-$  inclusive differential cross section measurements, together with a phenomenological fit, are shown in Figure 11. The dependence of the invariant cross sections on the  $\pi^-$  kinetic energy ( $T$ ) is well approximated by an exponential function:  $f = C \cdot \exp(-T/T_0)$ . The total pion production cross section for Ta at 10 GeV/c found by integrating this formula with fitted values of  $C$  and  $T_0$  is 2.36 barn. With a nuclear inelastic cross section for Ta of 1.56 barn, there is good agreement with the measured pion multiplicity of 1.51.

To compare the MECO muon flux simulation using the hadron codes with the experimental data, a Ta proton target ( $\rho=16.6$  g/cm<sup>3</sup>) with length 19.34 cm (1.67 nuclear lengths) and radius 0.4 cm was studied. For the muon flux calculations, the GEANT 3.21 code with the GHEISHA hadronic model was used. A proton beam with Gaussian shape and  $\sigma_x = \sigma_y = 0.2$  cm was caused to impinge on the target. The proton interaction point was chosen using GEANT, and then  $\pi^-$  were produced at that point according to the measured production cross sections. The  $\pi^-$  were then tracked using the GEANT code and the resulting  $\mu^-$  yield calculated. The ratio of this  $\mu^-$  yield based on measured production cross sections to that based on GHEISHA is 0.54. We scale all results that depend on pion yield down by a factor of 2 to account for this difference and the energy dependence of the production cross section, the latter taken from a GEANT calculation.

The yield of muons depends on the target shape, the proton energy, the value of the field in the production and transport solenoids, the clear bore of the production solenoid and the size of the collimators which ultimately define the muon beam size. The yield was optimized [64, 65] with respect to variations in these parameters. It is relatively insensitive to small variations in target position and to the target length in the range of 12-20 cm. The

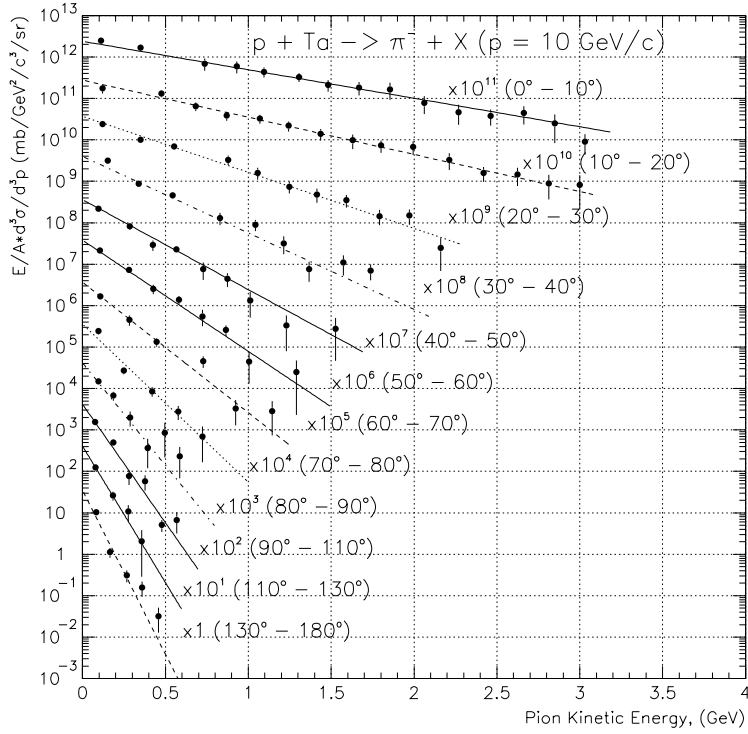


Figure 11: The plot shows the  $\pi^-$  inclusive differential production cross section in different angle intervals for 10 GeV/c protons incident on Ta. The lines are the result of a fit to an exponential form  $f = C \cdot \exp(-T/T_0)$ .

yield decreases by about a factor of two with target radius variations between 3 mm to 9 mm due to absorption as the pion exits the target and as it passes through it again while moving in a helical trajectory in the production solenoid. We currently use a target radius of 4 mm. This has some implications on target heating, as discussed below.

Figures 12 shows the a scatter plot of  $\mu^-$  and  $\mu^+$  production positions in the region of the production solenoid. Most  $\mu^-$  are produced in vacuum around the production target, while many  $\mu^+$  are produced in the walls of the production solenoid and in the target from stopped  $\pi^+$ .

The current design of the production solenoid region calls for a graded magnetic field with maximum value of the axial component between 3.3 and 5 T at the upstream end of the production solenoid, decreasing linearly to 2.3 T at the downstream end. The target is 16 cm long and 0.8 cm diameter, made of tungsten, rotated at  $10^\circ$  with respect to the solenoid axis. The entrance to the transport solenoid is defined by a collimator of radius 15 cm.

### 3.6.2 The Transport Solenoid

Muons are transported from the production solenoid to the detector solenoid using a curved solenoid bent first by  $90^\circ$  in one direction, and then  $90^\circ$  in the opposite direction. The

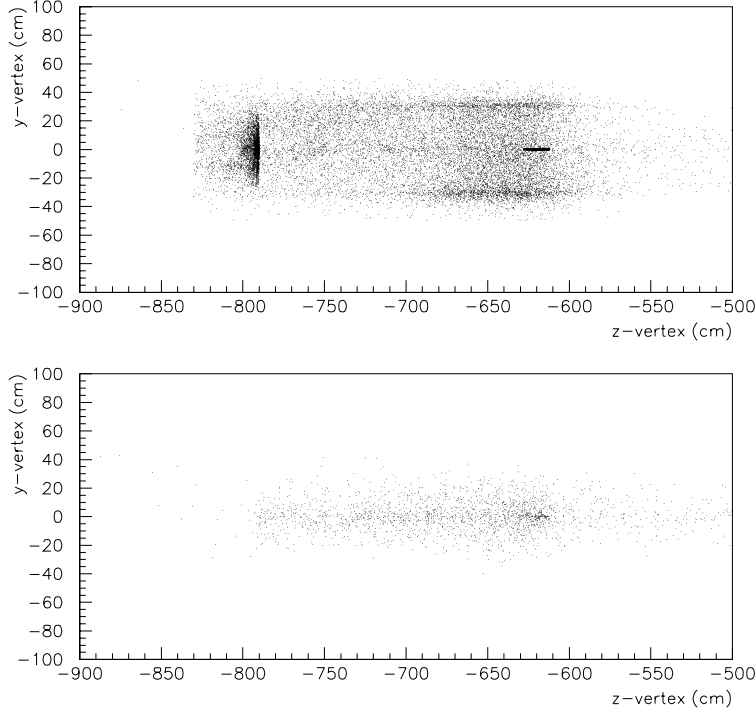


Figure 12: The plots show the location of  $\mu^+$  (top) and  $\mu^-$  creation points in the production solenoid. Most  $\mu^+$  are generated in the walls of the solenoid (“surface muons”), whereas the  $\mu^-$  come largeley from  $\pi^-$  decay in flight.

purpose of the bends is to decrease the transmission of both high momentum particles and positive particles. Unwanted particles are absorbed in appropriately shaped collimators at the ends of the transport and at the center.

The simulation of the beam transport is based on an initial design [66] of the solenoid that used 54 “coil packs” to produce a field with axial component of approximately 2 T. The packs are arranged in the curved configuration with appropriate gaps for mechanical considerations. The magnetic field was calculated exactly using the law of Biot and Savart, then used in GEANT simulations to accurately integrate the trajectories including effects of field inhomogeneities, etc.

Charged particles of sufficiently low momentum follow helical trajectories centered on magnetic field lines. In a torus, they drift in a direction perpendicular to the plane of the torus, by an amount given by  $D = \frac{1}{0.3B} \times \frac{s}{R} \times \frac{p_s^2 + \frac{1}{2}p_t^2}{p_s}$ , where  $D$  is the drift distance,  $B$  is the magnetic field,  $s/R$  is the bend angle of the solenoid, and  $p_t$  and  $p_s$  are the perpendicular and parallel momentum components. For  $s/R = \pi/2$ ,  $p_t = 0.09$  GeV/c,  $p_s = 0.12$  GeV/c, and  $B = 2$  T, the drift of the center of the helix is 49 cm. The drift direction depends on the charge. Hence, by putting appropriate collimators in the straight sections, positive particles can be absorbed as can negative particles of high momentum. The drift effect in the trajectory is illustrated in Figure 13.

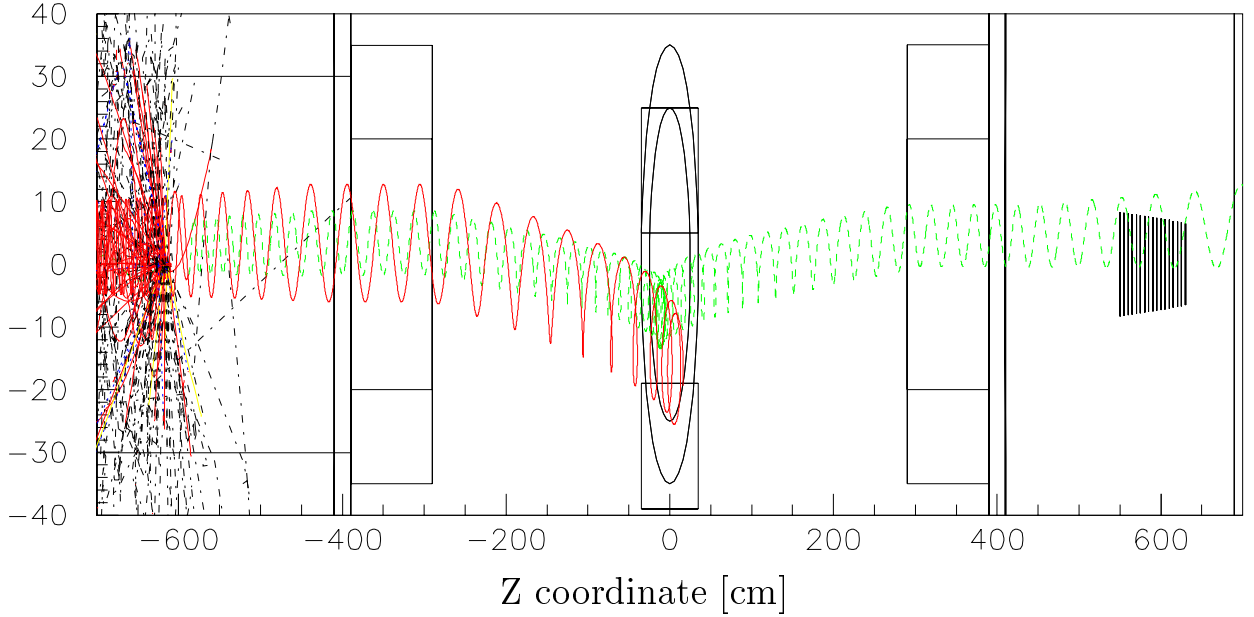


Figure 13: The plot shows a few simulated trajectories in the production and transport solenoids. A downward drift in the first curved portion of the transport solenoid (-400 to 0 in the figure) is apparent; the amount of drift depends on the momentum. Both particles are negative.

Cylindrical collimators are placed in the first and last straight sections (regions 1 and 5 with inner radii  $r_1$  and  $r_5$ ) and in the center straight section (region 3 with inner radius  $r_3$ ). In addition, collimators in region 3 restrict the coordinate perpendicular to the plane of the transport to be in the range  $y_{min} < y < y_{max}$  so as to absorb positive particles and high energy negative particles. The collimator sizes were optimized to remove heavily suppress electrons above 100 MeV, which are a potential source of background. To determine these parameters, a GEANT simulation of  $10^7$  protons was used. Values of  $r_1 = r_5 = 15$  cm,  $r_3 = 25$  cm,  $y_{min} = -19$  cm and  $y_{max} = 5$  cm completely eliminated 100 MeV electrons at this level of statistical precision.

The net yield of  $\mu^-$  with this beam is  $0.0046 \mu^-$  per proton at the entrance to the detector solenoid, after scaling the GEANT yield down by a factor of two to account for the measured  $\pi^-$  production cross section. The stopping probability in a set of thin target disks is 56%. Figure 14 shows the momentum distribution of the full  $\mu^-$  flux and the stopping flux from the GEANT simulation.

The fluence of pions and electrons is also important, as these are a potential cause of background. The  $\pi^-$  flux is a negligible contribution to the total flux of particles exiting the transport solenoid and their effect on backgrounds was discussed in Section 3.4. Electrons form the major component of the beam, and they potentially are a significant contribution to detector rates. We have minimized the electron flux by two modifications to the transport. First, it was found that many electrons were produced in the upstream (proton exit) end of the production solenoid due to interactions in the magnet pole. The current magnet

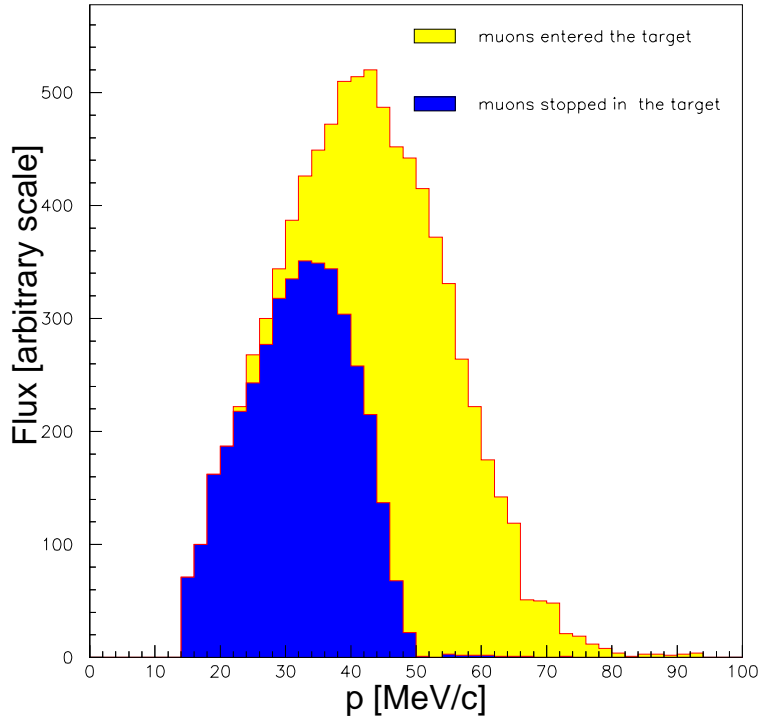


Figure 14: The full histogram is the energy distribution of muons which reach the stopping target. The inner shaded region is the momentum distribution of muons that stop in the target disks. Results are based on the GHEISHA production model for  $\pi$ 's.

design does not have a pole piece, and we have extended the vacuum farther upstream to a low field region, and inserted low Z material on the axis of the magnet system to minimize electron production. Second, a small absorber (radius 2 cm and length 2 cm) is placed at the transition between the production and transport solenoids. It significantly attenuates electrons made in the production target. Figure 15 shows the fluxes of electrons and muons at the exit of the transport solenoid. The time and momentum distributions are shown. The very high flux of particles within 100 ns of the proton pulse will require that detector gains be reduced during this pulse. We are continuing studies to reduce this flux. The electrons and muons that arrive at the detector solenoid at times longer than 700 ns are predominantly very low energy and are not a source of physics background.

### 3.6.3 The Muon Stopping Target

The goal of the stopping target design is to maximize the probability for beam muons to stop and the probability for conversion electrons to be detected in the tracking detector and calorimeter. At the same time, the target should be designed to minimize the energy loss of conversion electrons as they exit the target and to minimize the number of electrons from muon DIO that reach the tracking detector. Further, detector rates (for example from beam



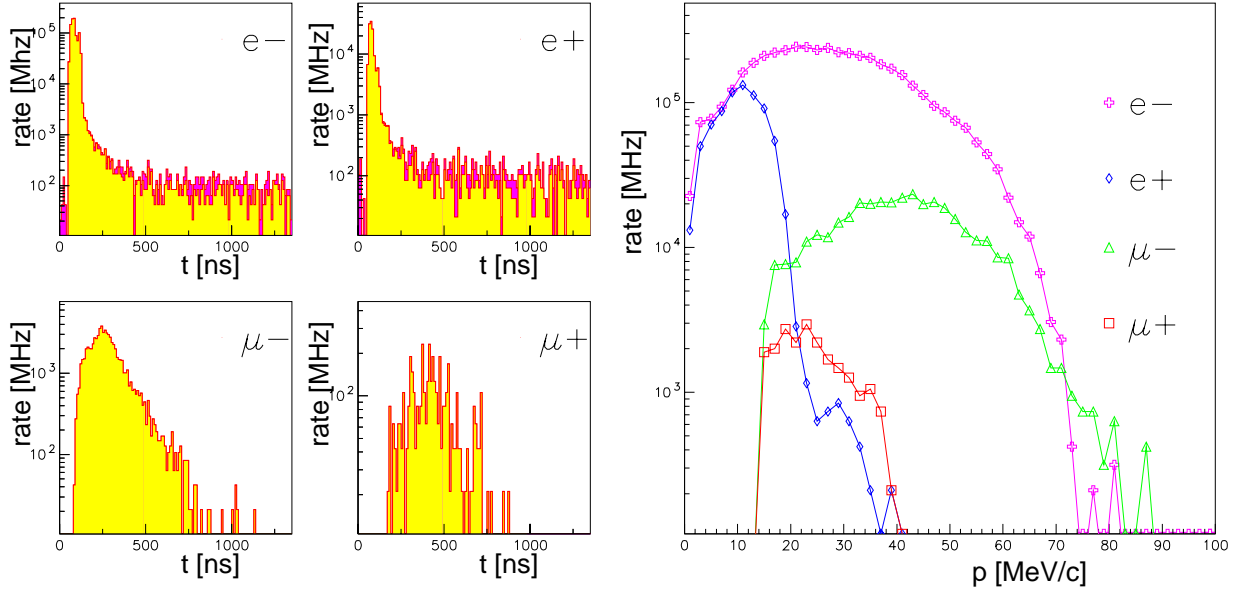


Figure 15: Time and momentum distributions for particles that exit the transport solenoid. The plots on the left show the time distribution, folded about the pulse spacing. The plot on the right shows the momentum distribution of each particle type. The effect of the asymmetric collimator on the flux of negative and positive particles is apparent, as is the effect on the momentum distribution, particularly for positives.

electron bremsstrahlung) and backgrounds (for example from cosmic ray interactions in the target) are minimized with the smallest possible target mass. The transverse size, thickness and number of thin disks that comprise the target were optimized to best achieve these goals.

It was found that a design with 17-25 thin disks, each with radius 6-8 cm and thickness 0.02 cm, separated by 5 cm yielded high stopping probability, relatively small energy loss for conversion electrons, and resulted in relatively low probability of muon DIO electrons intercepting the detectors. The target is situated in a region of the field that varies from 1.7 T to 1.3 T over its axial extent.

Within this general parameter range it is possible to minimize the probability of electrons from muon DIO hitting the tracking detector while maximizing the acceptance for conversion electrons by varying the disk radii. In an axially graded magnetic field the transverse momentum varies with axial coordinate, with  $p_T^2/B$  being constant. The distance  $R$  from the helix center to the axis of the solenoid also varies with axial coordinate, with  $R^2 \times B$  constant. The energy below which no electron reaches the tracking detector increases with increasing  $B$  field value at the target for a given target radius and detector inner diameter. For a target radius of 6.53 cm, this energy is 56 MeV for electrons originating in the most downstream target layer at 1.3 T. Increased stop rate is achieved by increasing the target radius at higher  $B$  field to maintain the same cut-off energy. This criterion gives a target radius of 6.53 cm at 1.3 T and 8.3 cm at 1.57 T.

We take the baseline target to be 17 layers extending between 1.57 T and 1.30 T with target radius between 8.3 and 6.53 cm. The electron cut-off energy for hitting the tracking detector is 56 MeV. Figure 16 shows the distribution of the stopped  $\mu$ 's along z for this optimal target setting, showing that more  $\mu$ 's are stopped upstream than downstream. Depending on operational experience and measurements of muon and electron fluxes, further optimization of the target may be achieved.

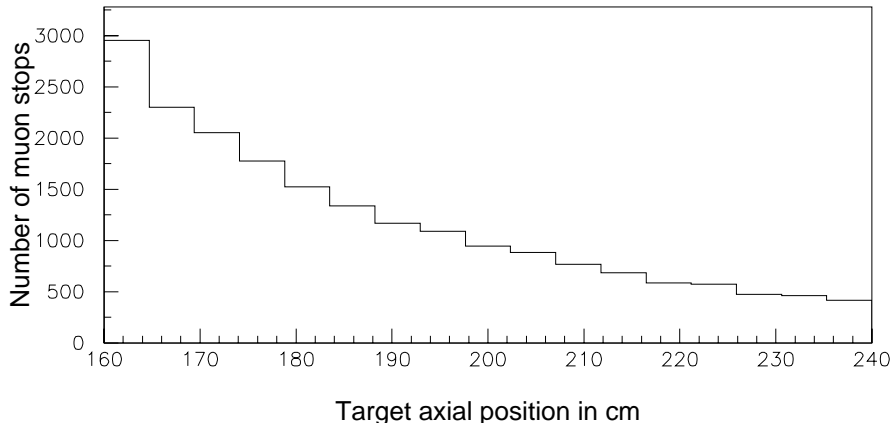


Figure 16: The distribution in the axial stopping position of  $\mu$ 's for the optimal target setting with 17 layers between 1.57 T and 1.3 T, with target radii of 8.3 cm at 1.57 T and 6.53 cm at 1.3 T. The z coordinate is referenced to 0 at the beginning of the detector solenoid.

### 3.6.4 Muon Production Target Cooling

Two technical issues involving the use of a very intense proton beam incident on a heavy target in a super-conducting magnet are important. The first of these is the issue of target heating. To minimize absorption of  $\pi^-$  in support material in the production solenoid, we propose to use a radiation cooled target, suspended in position with very low mass supports. Tungsten's high melting temperature (3722 K) makes a radiation cooled target possible even with the very high proton flux and resulting energy deposition.

The target temperature is calculated in a straightforward way, accounting for heating by the energy deposited by the beam and radiative cooling. It depends on the duty cycle of the beam and the geometry and materials properties of the target. The macro duty cycle of the proton beam is 50%, with 0.5 s bursts and a 1 Hz repetition rate. The total surface area of the target is about 42 cm<sup>2</sup> and the mass is approximately 156 g. To estimate target temperature, we assume that the heat conduction is sufficiently high that the temperature is independent of radius and that it does not follow the micro time structure ( $\sim 1$  MHz) of the beam. The steady state average temperature is set by equating the average energy deposition with the radiated energy, the latter given by  $\epsilon\sigma T^4$ , where  $\epsilon$  is the emissivity,  $\sigma$  is the Stefan-Boltzmann constant, and T is the temperature in Kelvin.

Table 5: Average energy loss per proton and heat power release in the tungsten target by 8 GeV/c proton beam with emittance  $6 \pi$ -mm-mrad.

Hadron Code	Average Current [p/s]	Target Radius [cm]	Target Length [cm]	Average Loss [GeV]	Peak Power [kW]	Average Power [kW]
GHEISHA	$4 \times 10^{13}$	0.4	16	0.7	9.4	4.7
GHEISHA	-	-	20	0.8	10.2	5.1
FLUKA	-	-	16	0.7	9.4	4.7
FLUKA	-	-	20	0.8	10.2	5.1
GHEISHA	-	0.6	16	1.0	12.8	6.4
GHEISHA	-	-	20	1.1	14.0	7.0
FLUKA	-	-	16	1.0	9.4	6.4
FLUKA	-	-	20	1.1	10.2	7.0

The power deposited in the target is determined from GEANT simulation; it is not very sensitive to the hadronic code used. Table 5 shows the GEANT [67] simulation results for average energy loss per proton and heat power release in the tungsten target for 8 GeV/c protons. The calculated average energy loss per proton is equal to  $\sim 0.7$  GeV/proton and  $\sim 0.8$  GeV/proton for target lengths 16 cm and 20 cm, respectively, equivalent to a peak power of 9.4 kW and 10.2 kW. The longitudinal distribution of the average energy loss per primary 8 GeV/c proton is shown in Figure 17.

Figure 18 shows the target temperature rise in both 0.4 and 0.6 cm radius targets, assuming the emissivity is independent of temperature and equal to 0.4. The target reaches

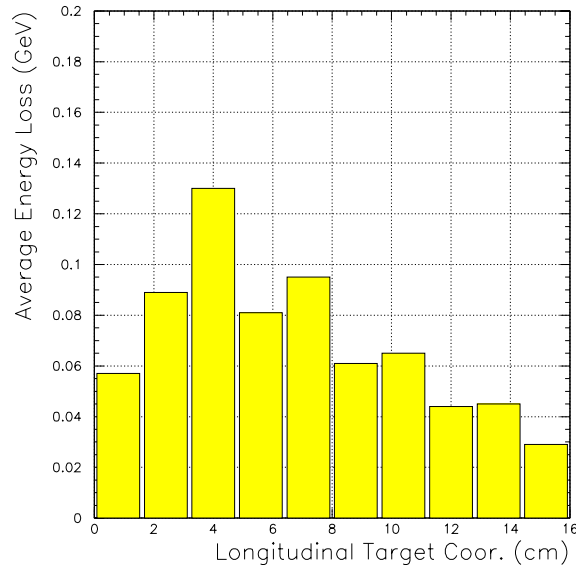


Figure 17: The longitudinal distribution of average energy loss per primary 8 GeV/c proton in the tungsten target ( $L = 16$  cm,  $r = 0.6$  cm). The profile is similar for a target of 4 cm diameter.

an average temperature of 2660 K after 25 seconds. It fluctuates about the mean by  $\pm 60$  K.

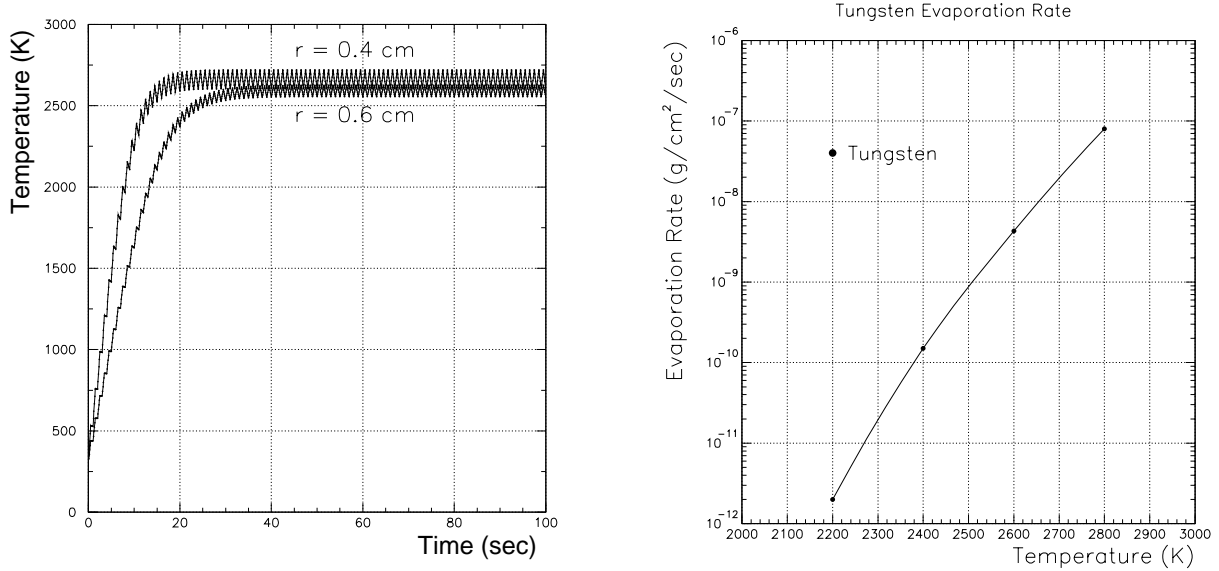


Figure 18: The plot on the left shows the target temperature rise in targets of radius 0.4 and 0.6 cm when irradiated by an 8 GeV/c beam of  $4 \times 10^{13}$  protons per 0.5 s pulse and 1.0 s repetition cycle. The plot on the right shows the evaporation rate as a function of the target temperature, from reference [68].

Even though the temperature is well below Tungsten's melting point, material will evaporate from the surface. Figure 18 shows the evaporation rate as a function of temperature. At  $\sim 2650$  K, the rate is  $\sim 10^{-8} g cm^{-2} s^{-1}$ . For a target of mass 156 g, surface area  $42 cm^2$ , and running time of  $10^7$  seconds, this corresponds to 2.6% material loss over the course of the experiment.

Significant reduction of target temperature can be achieved in two ways. First, tungsten surfaces with higher emissivity (of order 0.9) have been made by chemical vapor deposition of tungsten on various materials. If this emissivity could be achieved, the temperature would decrease to 2160 K, where the evaporation rate is negligible. We are exploring with materials scientists at the College of William and Mary whether this type of surface can be prepared on a solid tungsten cylinder. Another possibility they have suggested is to use rhenium as the surface coating; it also has a very high melting temperature. Alternatively, the geometry of the target could be changed (adding thin fins or making it elliptical) to increase the surface area and hence reduce the operating temperature.

### 3.6.5 Solenoid Heat Load

The heat and radiation load from the particle spray on the super-conducting solenoid surrounding the production target could cause the magnet to quench or fail due to radiation damage, and in any case will represent a heat load on the refrigeration system. Simulations using GEANT have shown that a combination of copper and/or tungsten shielding in a

cylindrical shell surrounding the 30 cm radius clear bore can reduce the local instantaneous heat load, the average heat load, and the radiation load integrated over the lifetime of the experiment to a manageable level.

To estimate the heat load on the super-conducting coils, a GEANT simulation was run for 8 GeV protons hitting the tungsten target inside the super-conducting solenoid [69]. Copper and/or tungsten shields of different thicknesses were studied. In preliminary calculations, the solenoid cold mass was approximated by a 6 cm thick aluminum shell immediately outside the shield. These studies were done with different hadronic codes: GHEISHA, FLUKA, SHIELD. Figure 19 shows the energy deposited in the cylindrical shell corresponding to the cold mass is insensitive to the hadronic model chosen. For subsequent studies only GHEISHA, the GEANT default model, was used.

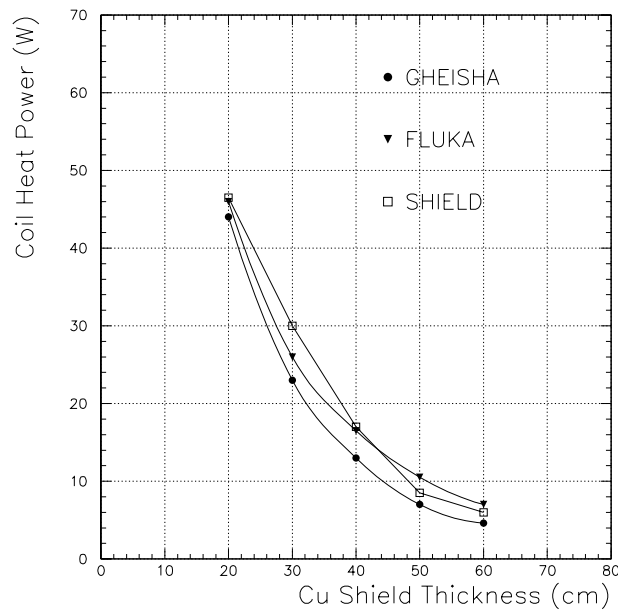


Figure 19: Power deposited in a 6 cm thick cylindrical aluminum shell surrounding copper shields of different thickness for different hadrons codes. All codes give approximately the same result.

Following a conceptual engineering design of the solenoids by the NHMFL, calculations were done for a cold mass consistent with that design (a radial thickness of  $\sim 24$  gm/cm<sup>2</sup>), again for different shield thicknesses of copper or tungsten. Table 6 gives results for the total heat load, the maximum instantaneous local heat load and the maximum radiation load in the lifetime of the experiment. Figure 20 shows the distribution of average heat load as a function of azimuthal angle and axial position. It is apparent that the heat load is concentrated in a relatively small region upstream (in the direction that the protons are moving) of the production target. Even for the case of a shield of 30 cm of copper, all three parameters are acceptable from the point of view of reliable operation of the magnet and longterm radiation damage. We anticipate that we will use a mostly copper shield with some heavy inserts in the region of most intense particle spray in order to reduce the heat load to below 50 W.

Table 6: The table gives the energy deposited in a model of the production solenoid cold mass for different heat shield configurations. In all cases, the shield has an internal radius of 30 cm and a length of 440 cm.

Configuration	Average total power (W)	maximum power $\mu\text{W/g}$	max. radiation load MRad
30 cm copper	108	151	146
40 cm copper	52	65	62
30 cm tungsten	28	43	41
40 cm tungsten	10	14	14

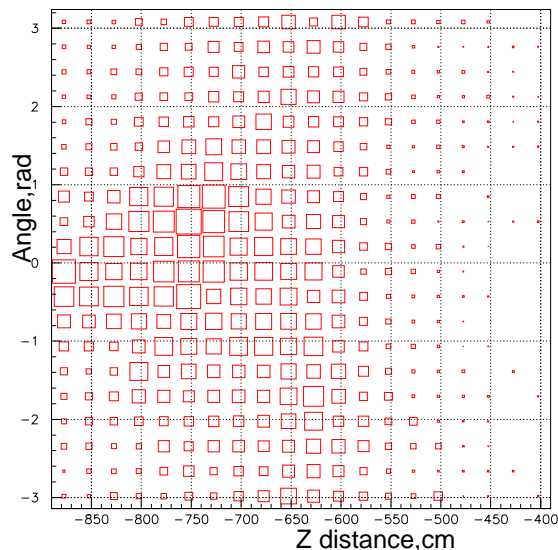


Figure 20: Angular and axial dependence of power deposited in solenoid cold mass for a 30 cm thick copper shield. The area of the boxes is proportional to the power, and the largest box corresponds to  $165 \mu\text{W/gm}$ .

### 3.6.6 Preliminary Engineering Design of Super-conducting Solenoids

We have commissioned and received the results of a preliminary design of the system of three magnets that comprise the MECO muon beam-line. The design was done by the National High Magnetic Field Laboratory (NHMFL) at Florida State University. That group has experience in design and construction of high field, typically small bore super-conducting and copper magnets. They magnets are illustrated in Figure 3. The production solenoid has a bore of length 4 m and radius of  $\sim 0.7$  m. The maximum field (at the upstream end) will be between 3.3 and 5.0 T. The final choice of these parameters will follow the engineering design and a more precise estimate of the variation of cost with these parameters. The bore radius is based on a clear bore of  $\sim 30$  cm radius and a heat shield of thickness 30 cm. The

field decreases uniformly from the maximum field to 2.3 T at the downstream end where it matches with the transport solenoid.

The transport solenoid consists of two curved sections (each 1/4 of a toroid) with straight matching sections at each end and a straight section between them. The curved sections bend in opposite directions, have a major radius of  $\sim 2.7$  m and a minor radius of  $\sim 0.35$  m. The bore has space for collimators in each of the three straight sections. The maximum extent of the particle transport region corresponds to a minor radius of 20 cm. Non-uniformities in the field due to gaps between coils are significant only at larger radii. Each of the straight sections has a small gradient ( $\sim 0.1$  T/m) in the axial field component.

The detector solenoid has a clear bore of length  $\sim 10$  m and radius  $\sim 0.9$  m. The axial component of the field grades from  $\sim 2.0$  T at the entrance to 1.0 T at axial position 2.5 m from the entrance and is then constant until after all detector elements.

The NHMFL design follows initial calculations of the field in the production solenoid and the matching region in the transition to the transport solenoid [70] and of the transport region [66]. The goal of the NHMFL study was a conceptual design of the complete magnet system that addressed the major design issues, that would form the basis for an engineering design, and that would allow a cost estimate one step beyond estimates based on scaling laws for large magnets. The result of that design study [71, 72] is contained in a report attached as Appendix 1.

The design address the major issues, including a calculation of the current density required to achieve the desired field, the means to achieve the varying current density, the mechanical support of the heat shield, the means of reacting the magnetic forces on the coils, the way of getting the proton beam into the interior of the production solenoid, the radiative and conductive heat loads, etc.

The design contains 101 coil elements. The current density is similar to that of earlier calculations that were used to produce the field used in simulations of the muon yield. The axial and radial forces on the coils have also been calculated in both design studies and are consistent. The heat load from the dominant sources (exclusive of energy resulting from interactions in the production target) is  $\sim 120$  W at 4.2 K and is dominated by radiation. Calculations of the particle spray load have been done by the MECO collaboration; they showed that using a shield of copper and tungsten will reduce the heat load to  $\sim 50$  W, with a maximum local heat load of  $\sim 50$   $\mu$ W/g. The total radiation load in the proposed running time is  $\sim 50$  MRad in the region of highest radiation. These values are within the acceptable range for operation of the magnet.

Various options are considered for establishing the appropriate currents in the coils while minimizing the number of power supplies and current leads, maximizing the flexibility in tuning the fields, and minimizing production costs. The current design has all coils activated with the same current. We anticipate using either small trim coils or persistent mode switches to do fine-tuning of the field gradient.

The magnet system has been costed in two ways with essentially consistent results. Substantial contingency is still carried and a precise cost estimate will be made only after full engineering design. The costs are discussed in section 3.12.

### 3.7 Detector Rates

High rates in the detector may limit the experimental sensitivity in several ways. First detector occupancy might be sufficiently high that the detection efficiency is reduced by corrupting signals from candidate electrons. This problem is addressed by making finely segmented detectors with short integration times. Second, signals in the detectors may fake those of a real electron. For example, by combining noise hits with those from a low energy ( $< 100$  MeV) electron, the momentum as measured in the tracking detector could be consistent with that of a conversion electron (105 MeV). This is a problem common to many high rate experiments that look for rare events; it is addressed by having short resolving times, sufficient redundancy in particle position measurements in the tracking detector, and means of discriminating against signals caused by particles other than the electron of interest. Third, there may be contributions to the trigger rate due to pile-up of many low energy particles in the trigger detector. This possibility may be reduced by segmentation and geometric design of the trigger device.

In this section, we discuss the principal contributions to the rate environment and discuss the calculations of the rates in the tracking detectors. How these rates affect the physics backgrounds is discussed in Sections 3.4 and 3.8. The effects of the rate environment on the trigger detector are discussed in Section 3.9.

The time structure of the beam helps mitigate the effects of the high stopping rate. Since we only detect electrons when (in principle) no protons are hitting the production target, the particle flux in the beam channel is very low when detectors must be active. For a period of about 200 ns following the proton pulse, when there is a very high flux of charged particles in the muon beam channel, detector rates are sufficiently high that it will probably be necessary to decrease the tracking detector gain by a factor of 10-100 during that time. The time structure of the total particle flux in the beam is discussed in Section 3.5.

We also note that the magnetic field is designed in such a way that it does not trap charged particles. The field is monotonically decreasing in magnitude in the beam direction, and low energy particles will not be trapped to make multiple passes through the detector.

During the detection time window, significant detector rates potentially arise from four main sources:

- Muon DIO electrons potentially produce high detector rates. The detector is designed so that the majority of these are restricted by the magnetic field to radii less than 38 cm; only those with momenta above  $\sim 60$  MeV/c will reach detectors.
- Roughly 60% of the stopped muons are eventually captured on nuclei and produce photons, neutrons, and protons from de-excitation of the magnesium nucleus that is produced. Approximately 2  $\gamma$ 's, 2 neutrons, and 0.1 protons are emitted on average for each capture.
- Beam electrons emit bremsstrahlung radiation as they traverse the stopping target, and the resulting  $\gamma$ 's may Compton scatter or pair produce in the detectors. The muon beam-line is designed to reduce the flux of low energy electrons that can reach the stopping target. This is the dominant contribution to the detector rates during the time immediately following the arrival of the proton pulse at the production target.



- Detector rates may result from albedo from the muon beam stop; this device has been designed to reduce these rates to a negligible level. The rates from each of the sources above include that from secondary interactions in the dump. An additional source of rates arises from muons that stop in the dump. This is less than half of the total flux of beam muons, and the probability that a muon decaying in the dump causes hits in one of the detectors is significantly less than that of a muon decaying in the stopping target.

Rates have been calculated using a full GEANT simulation of the interior of the detector solenoid. The spatial distribution of stopped muons was first calculated using GEANT. The source distribution of particles that potentially cause detector hits was then chosen from this distribution. Energy spectra of particles emitted from nuclei following muon capture and of electrons from muon decay in orbit (DIO) have been taken from the literature, as discussed below. These particles were then generated with the appropriate energy distribution and isotropic angular distribution and tracked using GEANT, including the effects of magnetic field and incorporating all physical processes in the materials in the detector solenoid, muon beam dump, and the solenoid itself. Some of the rates depend on the amount of material in the tracking detector, and this has been modeled in some detail, including the structure supporting the straws, the cabling, etc. One limitation of the GEANT code is that neutrons are tracked only down to 40 keV, at which point they deposit that energy locally. We have recently started using codes that track neutrons to lower energies and account in detail for the nuclear properties of detector materials; results of studies using these codes are not yet available.

The detector design is driven by the need to be insensitive to the majority of the approximately  $10^{11}$  muon decays per second. This is an advantage of  $\mu^- N \rightarrow e^- N$  experiments with respect to  $\mu \rightarrow e \gamma$  experiments, since the signal electrons have twice the maximum energy of electrons from  $\mu^-$  decay in vacuum. For muon DIO, the spectrum extends to 105 MeV; it is shown in Figure 21. To simulate the detector rates from this source, electrons were generated with this spectrum according to the previously determined stopping distribution in the target and the hit rate in the tracking detector calculated by GEANT simulation. The rate comes both from the DIO electron traversing the detector, and from bremsstrahlung photons that then pair produce or Compton scatter in the tracking detector, often after first scattering somewhere else in the detector solenoid. The total contribution is significant only in the octagon part of the detector and in any case is not a dominant contribution. This and other contributions to the rate are tabulated in Table 7.

There is an unavoidable flux of  $\gamma$ 's, protons and neutrons resulting from nuclear de-excitation following muon capture on nuclei. Every  $\mu$  capture results in the production of excited nuclear states, radioactive nuclei, and/or neutron emission with the possibility of subsequent neutron induced nuclear gamma rays. This results in photons originating from various places in the detector solenoid, some fraction of which are not even time associated with the beam gating. Almost all of these photons are less than a few MeV (the binding energies of the most probable excited nuclei after  $\mu$  capture are less than 4 MeV). To proceed we analyze the effects of a flat energy spectrum out to 10 MeV at a rate of 1.8  $\gamma$ 's per  $\mu^-$  capture.

Neutrons are produced during the  $\mu^-$  capture process. A neutron spectrum, typical for

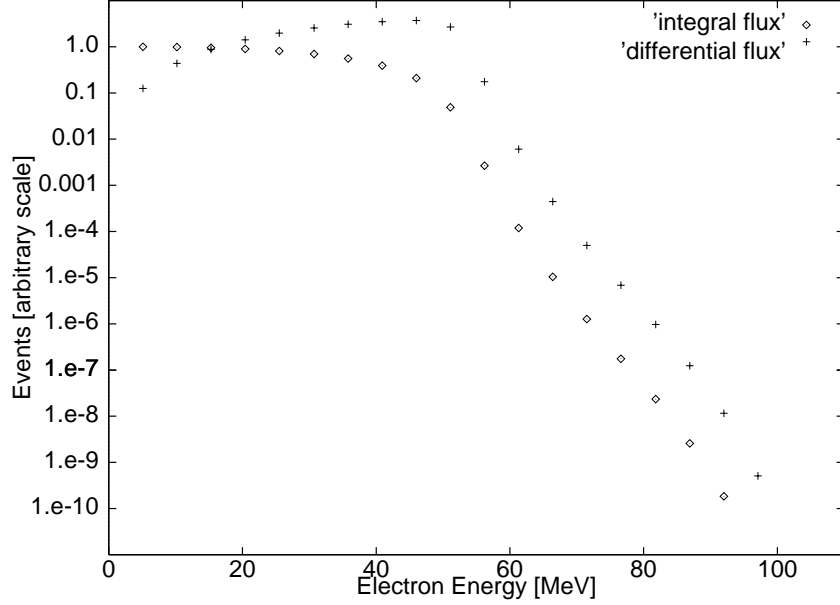


Figure 21: Plot of the differential and integral electron energy distributions for  $\mu$  decay in orbit. The circles are the integral of the distribution for energies above the abscissa value, and the crosses are the differential distribution.

our target, can be created from experimental data [73, 74]. Neutrons below 10 MeV are produced by a thermal distribution and there is an exponential tail above 10 MeV. Detector rates have been calculated assuming 2 neutrons are emitted per  $\mu^-$  capture.

Protons are also emitted during the  $\mu^-$  capture process. The proton spectrum shape, which is predominately due to protons below 15 MeV, was taken from an experiment [75] using  $\mu$ 's stopping in emulsion. The shape is almost Gaussian, centered at a proton energy of  $\sim 7.5$  MeV with a width of  $\sim 5.5$  MeV a high energy tail extending to above 50 MeV. The normalization is somewhat uncertain and depends strongly on the nuclear size. The best available data on the normalization is from Budyashov et al. [76]; other experiments [77, 78, 79, 80] also report measurements on different nuclei. We have taken the conservative approach and use the largest reported flux, 0.15 protons per  $\mu^-$  capture. The proton spectrum we use is shown in Figure 22. The protons are relatively high momentum, but low kinetic energy and are easily absorbed in even thin absorbers.

The largest potential contribution to the rate is from protons; the total instantaneous flux of protons exiting the stopping target is  $\sim 1.6 \times 10^{10}$ . Without shielding, the average rate in individual tracking detector elements is well above 1 MHz. However, the protons can be attenuated significantly by a set of absorbers. One is a cylindrical conical shell of thickness 1.0 mm surrounding the stopping target at large radii. The geometry of this upstream absorber is chosen so that it is not hit by 105 MeV electrons originating in the stopping target. A second absorber consists of a cylindrical shell of thickness 0.5 mm and with radius slightly smaller than the inner radius of the tracker and extending from just downstream of the stopping target to the beginning of the tracker. Both absorbers are made of polyethylene. The effect of proton absorption in the stopping target and the absorbers is shown in Figure 22. The lowest momentum protons are fully absorbed; the remaining protons

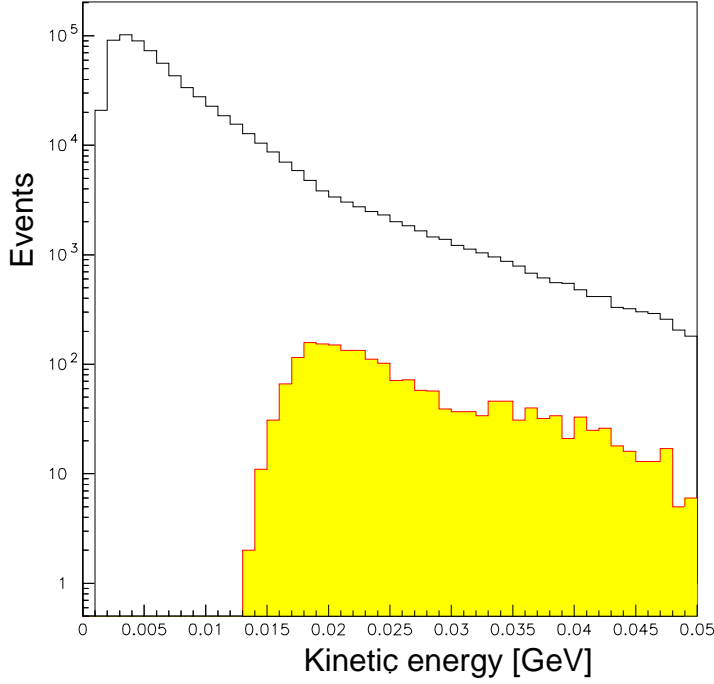


Figure 22: The distribution of the energy of protons originating from  $\mu$  capture on aluminum. The shape is from a fit to the data of reference [75]. Also shown (shaded) is the distribution of the kinetic energy of protons which cause hits in the tracking detector, showing the attenuation of low energy protons in the proton absorbers described in the text.

are still low energy and typically have a mean ionization rate  $\sim 10 \times$  minimum ionizing. The resulting rates are given in Table 7.

Table 7: Contributions of various sources to the tracking detector rates, from  $\gamma$ 's, protons and neutrons from muon capture, from muon DIO electrons, and from beam electrons that arrive during the detection time window.

Source	capture $\gamma$	capture proton	capture neutron	decay e (0 – 55 MeV)	decay e > 55 MeV	beam e
Rate [Hz]	$1.9 * 10^{11}$	$1.6 * 10^{10}$	$2.1 * 10^{11}$	$7.2 * 10^{10}$	$1.1 * 10^8$	$4.6 * 10^{10}$
Tracker hit probability	0.00043	0.0038	0.0009	0.00029	0.0017	0.00066
<straw hits / event>	5.0	4.0	2.1	4.1	4.0	5.5
<straw hit rate> [kHz]	163	97	159	100	2	67

A similar calculation was done for photons. Many of the photons interact in the tracker after scattering in other material. The tracker hits are caused by low momentum electrons from Compton scattering or pair production; they typically make multiple passes through a given straw within a very short time. These resulting rates are given in Table 7.

The rate of hits from neutrons also follows a GEANT simulation. It is sensitive to the details of the geometry of the detector solenoid. The current simulation suffers from the lack of sophistication in the neutron tracking codes implemented in GEANT and particularly from the fact that the code does not track below 40 keV. We have recently started using the GCALOR code to do what should be more reliable calculations. In addition, it should be possible to reduce the flux of neutrons that intercept the tracker by using appropriate neutron absorbers, for example in the region upstream and around the stopping target and outside the conical proton absorber. In any event, neutron induced signals in the tracker often do not have three straws hit in a cluster and can often be identified and hence not used in pattern recognition. The tracker rates from neutrons are given in column 3 of Table 7.

Additional rate derives from late arriving beam electrons. These are calculated in a GEANT simulation using the time and energy distribution of beam electrons as discussed in section 3.6. They are caused by bremsstrahlung in the stopping target, with the  $\gamma$  subsequently Compton scattering or producing  $e^+e^-$  pairs in the tracker. This contribution is given in column 7 of Table 7. We note that this contribution may be reduced by improved design of the muon beam to reduce the electron content in the beam.

The total rate per detector element is  $\sim 500$  kHz. These rates are lower than those in the BNL E871 straw chambers detectors of similar construction. In a 30 ns gate, typical of the drift time in the straw detectors operated with a  $100 \mu\text{m}/\text{ns}$  drift velocity gas, the average occupancy is under 2%. Many of the signals induced by these particles may be distinguished from those induced by conversion electrons. For examples, hits caused by protons will have large pulse height. Hits caused by electrons from Compton scattering and pair production will also typically have high pulse height since the electrons will make multiple turns through a single straw. They will be distinguished both by pulse height and by the fact that the time structure of the straw hits will not be consistent with that of a through-going 105 MeV electron. Neutron induced hits will also have high energy deposition and will typically not have all three layers of the straw detectors hit.

### 3.8 The Tracking Detector

As discussed earlier, the limiting background in the MECO experiment is from muon decay in orbit (DIO) with the endpoint of the DIO electron energy spectrum at the energy of electrons from coherent muon conversion. The level of background is related directly to the precision with which the electron energy can be measured; in principle the background can be made arbitrarily small if the electron energy resolution is arbitrarily good. Because the DIO spectrum rises as the fifth power of the difference of the endpoint energy and the energy of the DIO electron, the background level is very sensitive to the resolution.

The goal for the tracking detector is to measure with good efficiency the parameters of the helix trajectory of electrons in the uniform magnetic field in which the tracking detector is located. Uncertainty in the measurement of these parameters is dominated by multiple scattering in the tracking detector. A second source of error in the energy determination comes from pattern recognition errors. It does not reduce the acceptance significantly, but is a potential source of backgrounds because it generates high energy tails in the resolution function. With even modest position resolution in the tracking detectors, spatial resolution in the measurement is not a significant contribution to the energy resolution.

Inferring the energy of the emitted electron depends, in addition, on knowing the energy loss in the stopping target and in any material between the target and the tracking detector. Energy loss has two effects. One is to broaden the central part of the resolution function and introduce a small mean energy loss. The second is to introduce a low energy tail. This latter effect is essentially equivalent to a loss of acceptance and does not introduce backgrounds.

A “good geometry” spectrometer to measure helical trajectories has detectors placed at three points along the helix, with the first and last separated by  $180^\circ$ . A minimum of three position measurements is required to measure the radius, and more are needed to provide constraints on the fit and reduce backgrounds from badly measured positions. This is particularly important in the instance of extra signals (noise) in the detectors, which can be combined with signals from a low energy electron to yield a trajectory that appears to be from a high energy (105 MeV) electron.

These general design considerations lead to a detector geometry consisting of an octagonal array of planes of tracking detectors placed symmetrically around the axis of the detector solenoid plus 8 planes of tracking detectors (referred to as vanes) projecting radially outward from each vertex of the octagon. In some studies, the octagonal array has been modeled as a cylindrical array. All individual detector elements are oriented approximately in the axial direction. A feature of helical trajectories is that they return to the same  $r - \phi$  point at each turn of the helix. We have found that more than one turn must be measured to reduce backgrounds to an acceptable level. To eliminate the situation that the same tracking detector element is struck by the particle in two successive turns of the helix, the planes (both in the octagon and vanes) are rotated by a small angle (typically 15 mrad) about an axis perpendicular to the plane. The detector length will be in the range 2.4-2.9 m. Extensive studies have been done for 2.4 m and 2.9 m long detectors. For a 2.4 m detector, 39% of conversion electrons emitted with  $p_T > 91$  MeV/c have at least 6 hits in the tracking detector; a 2.9 m detector guarantees that two full helical turns are measured for the same class of events. This is discussed further in section 3.8.2.

The minimum radial position of the octagon planes is chosen to be 38 cm so as to make

the rates from DIO electrons small compared to those from photons and protons. With this geometry, a typical trajectory has one half of the helix inside the octagon. Either one or two vanes are intercepted by a conversion electron in a single helix turn – we refer to these as 3 and 4 hit turns. To set the scale of the trajectories, Figure 23 shows a cross section of the detector with three circular trajectories superposed. The transverse momenta of

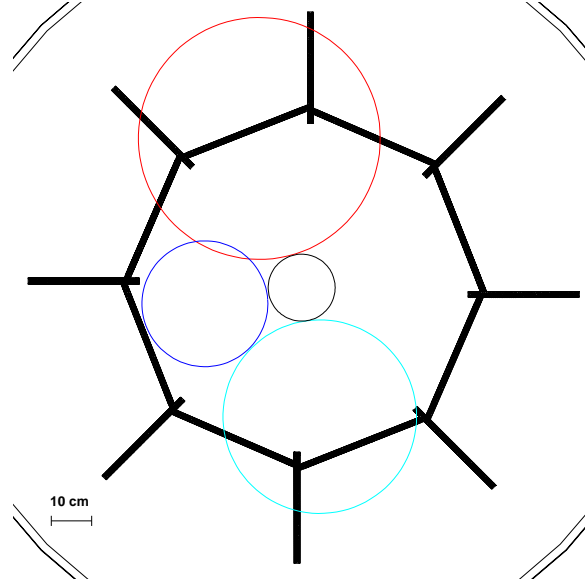


Figure 23: The figure shows a cross section of the tracking detector, the stopping target, and trajectories for electrons created in the target with transverse momentum of 55, 91, and 105 MeV/c. The trajectories are shown in the region of the detector and are positioned to show the minimum allowed detector radius that keeps rates from muon DIO manageable.

these trajectories (referenced to the stopping target position) are 55 MeV/c (the momentum exceeded by only 0.3% of decay in orbit electrons), 91 MeV/c (the transverse momentum of a conversion electron emitted at  $60^\circ$ ), and 105 MeV/c. The radius of a circle inscribed inside the octagon is 38 cm, the vanes extend radially for 30 cm, and the physical target radius shown is 6.5 cm.

The tracking detector will be made of 5 mm diameter straw tubes. Both the octagon and the vanes will have detector planes with three layers of nearly axially oriented straws. The straws will be  $25\ \mu\text{m}$  thick and made of carbon loaded kapton. The axial coordinate will be measured by capacitive coupling to foils on both sides of the octagon and vane detector planes. The foils will be made of  $25\ \mu\text{m}$  kapton with 5 mm pitch copper strips etched on them perpendicular to the wire direction. The pad signals from the octagon will be carried on  $25\ \mu\text{m}$  kapton foils near the surface of the vanes. With straws of length 2.4 m, one intermediate wire support will be required. The straws and wires will be fixed at the end to manifolds that also provide for gas flow and electrical connections. The manifold and straw mounting fixtures on each end of the straws will be made of beryllium with a total of  $2\ \text{gm}/\text{cm}^2$  thickness in the axial direction and a width perpendicular to the straws of 2.0 cm.

The position resolution requirements of this experiment are not severe, and well within what has been demonstrated in a number of experiments. We have assumed a Gaussian po-

sition resolution of 200  $\mu\text{m}$  for the  $\phi$  (drift) coordinate and 1.5 mm for the  $z$  axial coordinate, both for the mean coordinate of a cluster of hits (3-4 drift coordinates and 2  $z$  coordinates). Typical drift resolution in detectors of this type is 160  $\mu\text{m}$  for each drift coordinate [81] and  $\sim 10\%$  of the pad width for capacitive strip readout. Simulations have shown that position resolution tails at the few percent level extending out to a straw diameter do not adversely affect the momentum resolution.

Straws similar to these but shorter have been successfully used in BNL experiments E871 [15]. Low density straw tube systems of 2.7 m, 2.6 m, and 2.4 m have been successfully built and tested by several groups [82, 83, 84]. Straws have also been built and operated in vacuum [85], and coordinates along the wire direction have been measured with capacitive pad readout [86, 87].

### 3.8.1 Prototype Straw Chambers

We have begun a straw detector R&D project to test some of the required properties of the detector. One test was of the ability to operate the straws in vacuum with sufficiently small leak rates. Our tracking simulations have assumed we would use straws similar to those used in E871. They are made of two layers of kapton, each .0005 inch thick, spiral wound with a half strip overlap. The inner layer has  $\sim 1000$  Angstroms of copper deposited on the interior. We tested the leak rate of both the bulk straw material and the end fittings by measuring the rate of rise of pressure in an evacuated tube in which sample straws with 1 atmosphere pressure were placed. The rate of rise of the chamber pressure was measured (with the pump valved off) as a function of pumping time. It decreased with pumping time, indicating the rise was due to out-gassing of the exterior of the straw. The residual rise after 5 days of pumping corresponded to a leak rate of  $\sim 2 \times 10^{-8} \text{ l min}^{-1} \text{ m}^{-1}$  for the bulk straw, and a leak rate of  $\sim 3 \times 10^{-9} \text{ l min}^{-1}$  per end. These leak rates, when scaled to the full spectrometer, are well within pumping rates easily achievable. We have also constructed prototype low-mass gas and electrical manifolds with which a fraction of a “vane” module has been assembled.

A second test was done of the deformation of straws when loaded by gas pressure and wire tension. If treated as a cylinder under tension due to the internal gas pressure, the tension is  $\sim 2.0$  N per straw. This exceeds the wire tension of  $\sim 0.5$  N. At issue is the extent to which the straw stretches due to this loading, which would cause them to bow if the length was constrained, or over-tension the wires and complicate the construction if the length were allowed to change. We tested the fractional stretch by increasing the pressure in a sealed straw with one end fixed and the other free. The typical fractional change in length is 0.04% for 1 atmosphere overpressure. This would not over-tension the wires, and will likely require a mounting system in which one end of the tracking detector can move axially as the interior pressure is increased.

A second significant feature of the straw chamber spectrometer is the use of pad readout for determining the coordinate along the straw. This technique has been demonstrated [86, 87]. The straws are constructed of carbon loaded kapton, which allows an electrical signal to be induced on copper pads deposited on a thin film of kapton that is glued to the exterior of the straw assembly. We envision layers of pads on either side of a three layer straw assembly, with charge readout of the pads. By interpolating the position based on the charge deposited

on the pads, we anticipate a resolution of under 1 mm can be achieved with pads a few mm wide. In our simulations of resolution, we have used a resolution of 1.5 mm, significantly larger than what has been achieved. We view the development of this straw system as the highest priority of the detector system R&D plan.

### 3.8.2 Tracking Detector Performance Analysis: Signal Events

In this section, we discuss the tracking detector performance for signal events for the detector length of 2.4 m. A full GEANT simulation of the target and detectors was done [88, 45]. It incorporated the full Moliere scattering formalism and Landau fluctuations in the energy loss. It also incorporates Gaussian measurement errors with  $\sigma_x$ ,  $\sigma_y$  and  $\sigma_z$  to be 0.2 mm, 0.2 mm and 1.5 mm, respectively, as an approximation to the position resolution of clusters of straw tube hits. This simulation generated electrons originating in the target with the appropriate distribution of  $\mu$  stopping positions, and exiting the target isotropically.

The simulation reported here does not use a full model of the tracking detector down to drift times in the straw cells. Rather, positions of the electron hits in the detector were recorded; we refer to this as the *cluster* position, and it was randomized according to the resolutions given above. We have not incorporated straw chamber inefficiencies. By allowing up to two of the six or more clusters on each trajectory to have one of the three straw signals missing, a single cell efficiency of 97.5% would result in a 3% loss of events due to straw chamber inefficiency.

In addition to generating simulated cluster positions from the DIO or conversion electrons, clusters induced by the high ambient flux of protons, neutrons and photons emitted following muon capture were superimposed on events. This was done by using a GEANT simulation to produce events in which these background particles produced hits in the tracking detectors. A large sample of such events was produced and stored, and these were randomly sampled at an appropriate rate. In the studies we describe in this section, the average number of noise clusters is 8, corresponding to the estimated flux of background particles in a 15 ns time window around the electron time. This time window corresponds to the time window outside of which we can confidently reject a cluster as not originating from an in-time particle track.

It is assumed in the analysis that the two coordinates for a given particle traversal are not correlated in the hardware. Some correlation could be implemented, for example by comparing pulse heights in the two coordinate measurements. In all the studies we have done, we have assumed no correlations as a worst case scenario.

Since we do not simulate individual straw signals, many of the tools that could be used to reject noise clusters have either not been incorporated into the analysis or have been incorporated only in an approximate and typically rather conservative way. One example is the time interval that is used to calculate the number of noise hits to superimpose on signal events. Other such background rejection techniques are discussed in the following section on backgrounds from pattern recognition errors.

About 60% of all conversion electrons hit the detector. Figure 24 shows a typical event in the simulation. The number of times the electron helix trajectory turns within the detector region is determined by its pitch angle (  $\theta_P \equiv \text{atan}(p_T/p_L)$  ) and the detector length. Figure 25 shows the distribution in the number of clusters in the tracking detector for conversion electrons that hit the detector. A small tail extends beyond 14 clusters from



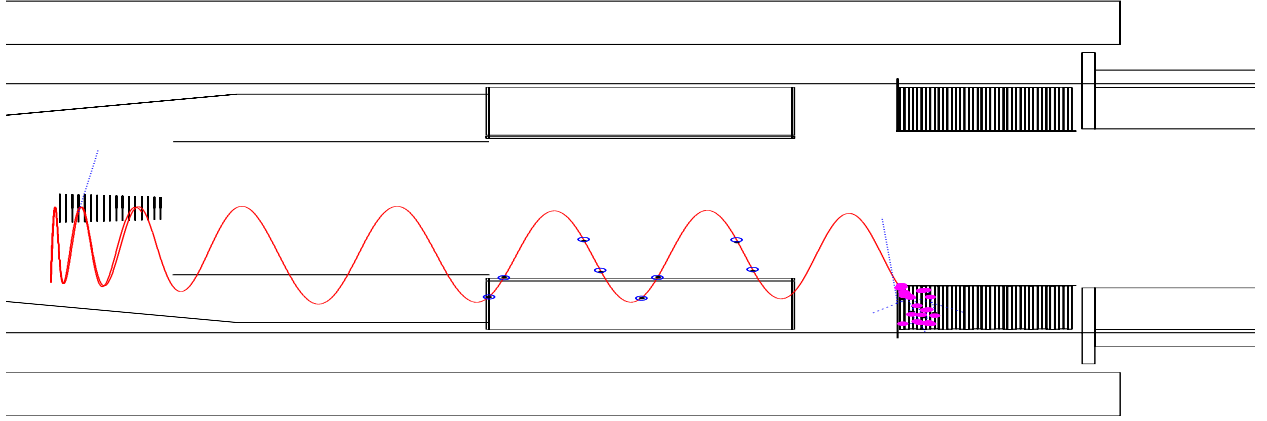


Figure 24: One sample trajectory from the GEANT simulation.

electrons that lose significant energy in the tracking detector and then make many turns in it. Figure 25 also shows the distribution in the pitch angle at the detector entrance for the same electrons. We require that signal events have measured value of  $\theta_P$  in the range

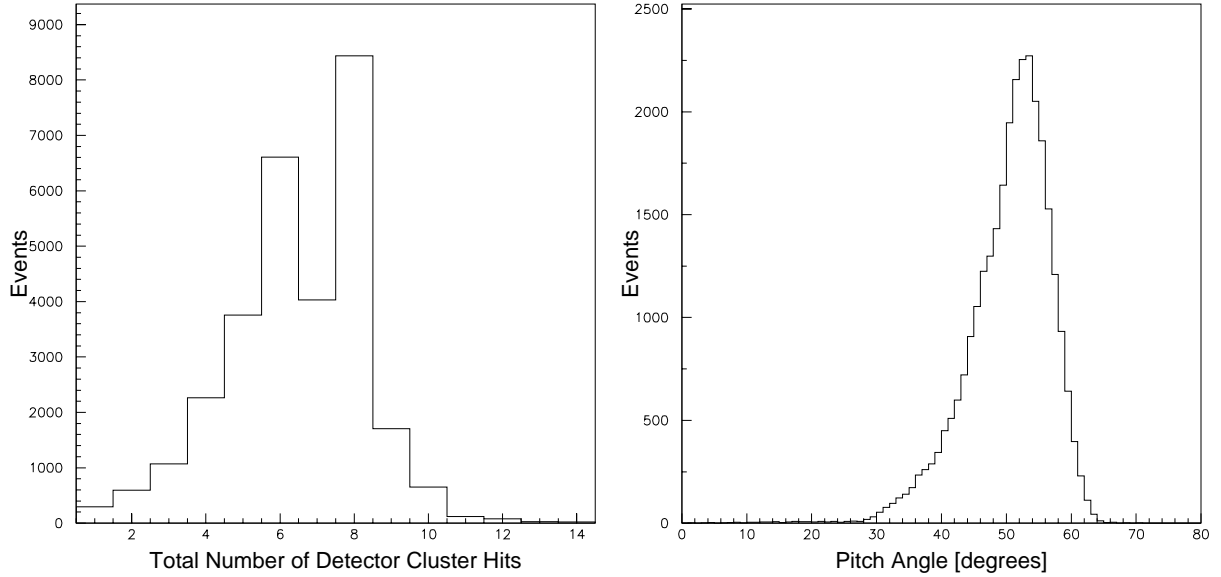


Figure 25: The plot on the left shows the distribution in the number of clusters in the tracking detector for the  $\sim 60\%$  of the conversion electrons that hit the detector. The plot on the right shows the pitch angle distribution for the same set of events.

$45^\circ < \theta_P < 60^\circ$ . The lower limit on  $\theta_P$  eliminates electrons originating in regions with magnetic field of 2 T or larger (for example, in the transport solenoid or in the final collimator), as a consequence of the graded field in the detector solenoid. This also minimizes backgrounds from beam electrons that scatter in the target, as discussed in section 3.4. The upper limit on the pitch angle helps in reducing backgrounds from cosmic rays or events

produced in the proton absorber. It is equivalent to a requirement that the electron could propagate upstream to the target without being reflected in the increasing magnetic field.

The pattern recognition procedure is to first select clusters that form circles in the  $xy$  (transverse) projection and then match them with the  $z$  (axial) clusters to look for good helix tracks. All possible combinations of clusters are tried including combining all  $xy$  clusters with all  $z$  clusters in a given vane or segment of the octagon. The momentum value for the particle track is then determined by a fitting algorithm (*fitter*) that uses a likelihood method described below. The fitter returns the most probable momentum and a corresponding likelihood at this momentum. Because this fitter is very CPU intensive, preliminary selection criteria are used to select potentially good circles in the transverse plane and full helices so that the number of possible trajectories analyzed in the fitter is minimized. Those selection criteria have been chosen to reduce computing time while causing negligible loss in acceptance for signal events.

We briefly describe the fitter, which works on the principle of the maximum likelihood method that determines the most likely momentum of a particle that made the helix trajectory. The trajectory deviates from a helix, mainly due to multiple scattering in the detector elements; nonetheless, the individual segments between adjacent hits are helical. The fitter exploits this to determine the trajectory of each segment between detector crossings as a function of the electron momentum ( $p_e$ ) and then calculates a likelihood value  $L(p_e)$  for the full trajectory as a function of  $p_e$ . This likelihood value is simply the product of the scattering probability at each detector position:

$$L(P_e) = f_2(\theta_2)f_3(\theta_3)...f_{n-1}(\theta_{n-1}) \quad (2)$$

where  $n$  is the total number of hits and  $f_i(\theta)d\Omega$  is the probability that the particle scattered into the solid angle  $d\Omega$  at  $\theta_i$  in the detector element where the  $i$ th hit was recorded. The parameter  $f(\theta)$  takes Gaussian form for small angles and has Moliere tails for large scattering. It is also possible to incorporate energy loss and the detector spatial resolutions in equation 2. This is discussed in detail in reference [88].

The most probable value of  $p_e$  is that which maximizes the likelihood. To estimate the error on the value of  $p_e$  from the fitter, the distribution in the likelihood vs.  $p_e$  in the region of the peak is fitted with a Gaussian form. The  $\sigma$  of this fit is denoted  $\sigma_{p_e}$  and it gives a good estimate of the uncertainty in the measured value of  $p_e$ . The parameter  $\sigma_{p_e}$  and the maximum likelihood value are found to be powerful discriminants against events with badly fit trajectories. The above algorithm is derived assuming the hits that are used are those actually made by the particle track (i.e. no pattern recognition errors). The same algorithm is found to work well even with noise after applying additional selection criteria as discussed below.

The following are the selection criteria imposed to select well measured particle trajectories following the track fitting:

1. The value of the likelihood is required to be greater than some value.
2. The scattering angle at each detector element is required to be less than 0.08 radian.
3. The fitting uncertainty  $\sigma_{p_e}$  is required to be less than 600 keV.

4. The total number of clusters is required to be at least 6 for the 2.4 meter detector. This requirement varies with the detector length. It significantly reduces high energy tails in the resolution function, primarily coming from pattern recognition errors.
5. The fitted trajectory is required to have a hit cluster at each place that it intercepts a plane of the tracking detector.
6. The projection of the fitted track's trajectory to the point where it intercepts the electron calorimeter is required to agree with the position at which the GEANT simulated electron entered the calorimeter to within 20 cm. For well fit trajectories, this cut corresponds to many standard deviations in the distribution between projected track position and the position that can be deduced from either of the potential calorimeter implementations.
7. The energy of the GEANT primary electron at the entrance of the electron calorimeter is required to be at least 75 MeV.
8. An event is rejected if a lower momentum track is found with a suitably relaxed set of selection criteria. This significantly reduces background from pattern recognition errors with essentially no loss of acceptance for the signal events.

The intrinsic energy resolution (excluding the effects of energy loss in the target, but including spatial resolution in the tracking detector and the effect of noise) is found to be  $\sigma_{RMS} = 150$  keV. Including the effect of energy loss straggling in the target causes the resolution function to deviate from a Gaussian shape at low energies without introducing high energy tails in the resolution function. The FWHM of the response function is 900 keV. The resolution function, including all the above effects, is shown in Figure 26. The figure has curves for signal and DIO background, normalized to a value of  $R_{\mu e} = 10^{-16}$  and a running time of  $10^7$  seconds. The distribution for DIO electrons is calculated by convolving the response function with the theoretical DIO spectrum [88], which is proportional to  $(E_{max} - E_e)^5$  near the endpoint [44]. The signal to background ratio is 20 for  $E_e > 103.6$  MeV, and the acceptance is 19%. The right plot in Figure 26 is a parametric plot of acceptance versus background to signal ratio as the lower limit on the electron energy is varied. This plot demonstrates that the background to signal ratio can be further reduced below 0.05 with little loss of acceptance; for example, the acceptance is 18% for background to signal ratio of 0.025. We summarize the efficiencies of the critical selection criteria in Table 8. Further suppression of some backgrounds can be gained by restricting the upper limit on the electron energy; for example, restricting the electron energy to have  $103.6 < E_e < 105.1$  introduces negligible additional acceptance loss.

We next turn to a discussion of backgrounds due to very high energy tails in the resolution function of the spectrometer; these have been shown to be due primarily to combining signals from a low energy electron with noise signals and thereby forming a trajectory with momentum higher than that of the electron. We refer to this as *pattern recognition errors*.

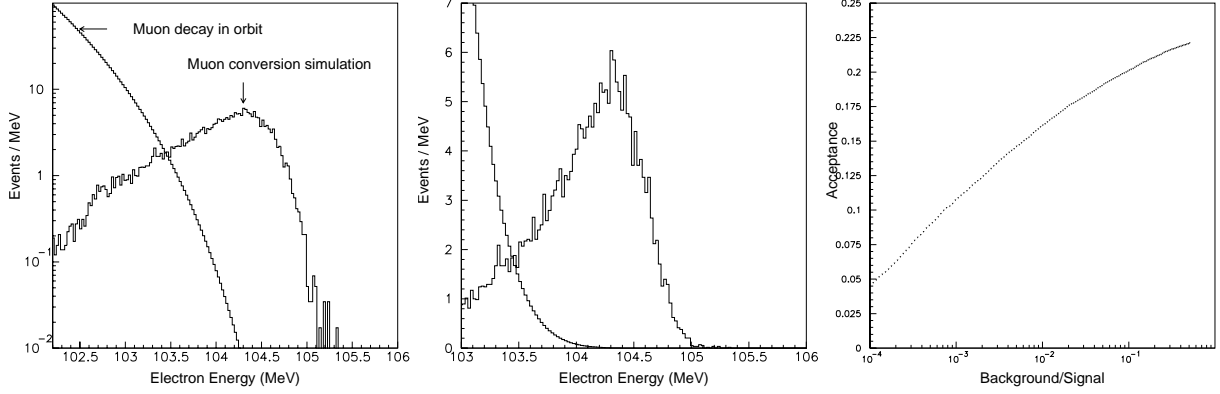


Figure 26: The left and center plots are the response function of the detector for 105 MeV electrons generated in the stopping target on log and linear scale respectively. Also shown is the expected DIO background, calculated by convolving the response function with the theoretical DIO distribution. The normalization is to a data taking period of  $10^7$  seconds and a value of  $R_{\mu e} = 10^{-16}$ . The right plot shows a parametric plot of acceptance versus background/signal ratio as the lower limit on the electron energy is varied. The plots shown are generated for  $10^5$  simulated conversion electrons. The background/signal curve has been calculated for a sample corresponding to  $10^7$  events and is essentially identical to that shown.

Table 8: A summary of the critical selection criteria used in the electron momentum measurement for the MECO detector

Selection criterion	Efficiency
At least 6 hits in tracking detector	0.44
Detected energy above $\sim 103.6$ MeV	0.62
Required pitch angle at the detector	0.88
Requirements on fitting quality	0.83
Position match in electron calorimeter	0.97
Overall acceptance	0.19

### 3.8.3 Backgrounds Induced by Pattern Recognition Errors

While the preceding discussion of backgrounds explicitly includes the possibility of background due to pattern recognition errors, it is limited due to the finite statistics of the calculation, consisting of  $10^7$  events fully simulated using GEANT, including superimposing appropriate noise. The statistical level of this simulation is sufficient to calculate the background arising from DIO electrons with energy above 100 MeV, of which there are  $\sim 10^5$  in the sensitivity of the experiment. For DIO events below 100 MeV, of which there are many more, additional calculations are required in order to estimate the expected level of background. These calculations are described in detail in reference [45]. The background could in principle arise from a variety of sources (multiple scattering, large tails in position resolution,

etc.) We have found that DIO electrons in this energy range primarily produce potential background by pattern recognition errors [45], but at a level well below the sensitivity of the experiment. We briefly describe those calculations here. In this discussion, we define a background event to be a reconstructed track with momentum above 103.6 MeV. The pattern recognition and fitting code imposes an upper limit of 120 MeV on the reconstructed energy; hence the background is in the interval  $103.6 \text{ MeV} < E_e < 120 \text{ MeV}$ .

Table 9 gives integral fluxes for DIO electrons during the nominal  $10^7$  seconds data collection period for the experiment. The integral flux rises steeply as the lower energy limit is decreased, and the energy range that is likely to contribute background can be deduced only by a calculation of the relative likelihood of events of different energies being mis-measured at 105 MeV.

Table 9: The table gives the integral number of DIO electrons above various energies.

Lower energy limit (MeV)	Total DIO events
100	$1 \times 10^5$
95	$5 \times 10^6$
90	$1 \times 10^8$
85	$1 \times 10^9$
80	$9 \times 10^9$
75	$6 \times 10^{10}$

Two independent studies to determine the number of mis-reconstructed events were performed, for detector lengths in the range 2-3 m. Both studies used GEANT simulations of the detector; they used different pattern recognition and background rejection strategies. The calculations proceeded by determining the cluster positions of the DIO electrons and superimposing, on average, an additional 24 noise clusters. This is larger than the expected noise rate and allows an efficient determination of the most probable topology of background events.

The more powerful of the two pattern recognition strategies applied to the DIO events the same reconstruction procedure as was described in the previous section. Results for two different detector lengths and several intervals of the energy of DIO electrons windows are given in Table 10. For the 2.0 m detector, a minimum of 5 clusters was required for each track instead of the 6 required for the 2.4 m detector.

It was possible to generate sufficient statistics for DIO electrons with  $E_e > 95 \text{ MeV}$  to show by direct simulation that the background rate is negligible. For lower energy, it is not possible, given available computing power, to generate the full sensitivity of the experiment. Hence, we rely on a study of a sample of events with somewhat looser selection criteria to infer the properties of events that are likely to cause background. The basic procedure is to relax selection criteria and study the number of noise hits necessary to make background events. It is found that the background events typically use a large number of noise hits; the high energy part of the resolution function is dominated by events with many noise hits. To study a sample of events with higher probability to produce background, we generate events

Table 10: Pattern recognition results for two different detector lengths and several production windows. A background event is an electron reconstructing with momentum exceeding 103.6 MeV and satisfying the selection criteria listed in the preceding section.

Detector length	DIO energy window	Events thrown	Background events
2.4 m	95-100 MeV	$5 \times 10^7$	0
2.4 m	80-95 MeV	$1 \times 10^8$	0
2.4 m	75-80 MeV	$4 \times 10^7$	0
2.0 m	95-100 MeV	$4 \times 10^7$	2

with higher than expected noise rates and weight the events appropriately. The specific procedure we use to calculate the expected level of background is to weight each event by suppression factors corresponding to the random probability that the particular event with a certain number of noise hits would occur if we did the simulation with the expected noise rate rather than an inflated noise rate.

There are several suppression factors to apply. We have used a mean noise rate a factor of 3 higher than that expected, so there is an event suppression factor of  $f_t = (1/3)^{n_t}$  where  $n_t$  is the total number of  $xy$  and  $z$  noise clusters used in the fitted trajectory. Further, the helix track angle in the transverse plane is determined to high precision, and the track angle can also be inferred locally with a precision of about 50 mrad from the straw hits in the cluster, using the full drift information. These angles can be compared, and hits rejected if they are not consistent. We estimate that a conservative (high efficiency) cut on the agreement would result in a suppression factor of  $f_\theta = (1/8)^{n_{xy}}$ , where  $n_{xy}$  is the number of  $xy$  noise clusters. This is equivalent to the statement that only 1 noise cluster in 8 would have local cluster information consistent with being due to a particle with a well known trajectory inducing the hits. An event suppression factor is taken as the product  $f_t \times f_\theta$ , and this is then averaged over the background event sample; we denote this average factor as  $f_s$ .

For electrons between 95 and 100 MeV,  $f_s$  is estimated to be 0.005 for a larger sample of backgrounds satisfying relaxed cuts. Since there is no background found after the final cuts, we calculate  $P_b$ , the probability of producing a background per DIO electron if the sample corresponded to one background:  $P_b = 0.005 \times \frac{1}{5 \times 10^7} = 10^{-10}$ . Multiplying this probability by the total number of DIO electrons in this energy window, we expect 0.0005 background events.

Similarly, for electrons between 80 and 95 MeV,  $f_s$  is calculated to be 0.00006 for a relaxed sample of background. For this sample, we have  $P_b = 0.00006 \times \frac{1}{10^8} = 6 \times 10^{-13}$ , and we estimate the background from DIO electrons between 80 and 95 MeV to be  $6 \times 10^{-13} \times 9 \times 10^9 = 0.005$ . For electrons between 75 and 80 MeV, no background was found even when the fitting criteria were considerably relaxed. Since  $P_b$  is smaller for lower energy electrons, we use the value of  $P_b$  for 80-95 MeV electrons and multiply by the total DIO electron number; this overestimates the expected background. Taking into account the triggering efficiency of 0.6 for an 80 MeV electron, we find the background from DIO electrons in the energy range 75-80 MeV to be  $6 \times 10^{-13} \times 0.6 \times 5 \times 10^{10} = 0.02$  events.

In this study, only events with 4 hits per helical turn were accepted. Other studies have shown that the background level for reconstructed events with 3 hits per helical turn have approximately the same background level, and we assume that would be the case. Summing all backgrounds and accounting for the exponential dependence of the detector rate during the 700 ns detection time, the total expected background is 0.067 events. Doing the same analysis, but assuming a noise rate twice higher than expected results in an expected background of 1 event.

These background events are consistent with being uniformly distributed in the energy interval searched,  $103.6 \text{ MeV} < E_e < 120 \text{ MeV}$ . Hence, the number of events expected in the signal window size ( $103.6 \text{ MeV} < E_e < 105.1 \text{ MeV}$ ) is about a factor of 10 less, or 0.006 events at nominal noise rates.

We further note that this calculation is conservative in a number of ways. First, we have used essentially no energy matching in the calorimeter and only very loose position matching requirements. Second, additional rejection against noise hits will derive from pulse height information. Protons are heavily ionizing and hits caused by them will be rejected with high probability. Photons cause hits by Compton scattering or pair production; in both cases the electrons make helical orbits within a drift tube and will also be distinguished by their high apparent ionization. Further, we have assumed that we have no means of correlating  $xy$  and  $z$  clusters, and pulse height matching can be used to reject incorrect pairings. Finally, one powerful rejection technique is rejecting events with a low momentum track. Currently only low momentum tracks with 4 hits per helical turn are found; finding 3 hits per turn low momentum tracks will further reduce background.

A more straightforward strategy, employing helical roads, was used in an independent simulation and analysis of background from DIO events. This algorithm reconstructed events with both 3 and 4 hits per turn and used similar noise rates. It also used energy matching and tighter space matching in the electron calorimeter, but did not use local track angle information. Although it achieved background rejection a few times worse than in the strategy described above, it did give another set of direct simulation results on the sensitivity of the background rate to factors like the noise rates, local track angle information, and detector length. The dependence of the expected background level on the noise rate is similar to that of the other analysis, as is the dependence on the energy of the muon DIO electron.

We conclude that the expected muon DIO background from event mis-reconstruction would be  $< 1$  event with a 2 m detector and is significantly under one event for a 2.4 m detector, if accidental rates are as expected. This will not be a limiting background. Making a longer detector will provide significant further rejection that provides insurance in the event that detector noise rates are higher than calculated. Some additional background rejection tools not currently used provide further rejection possibilities. We propose a tracking detector length in the range 2.4 - 2.9 m. The actual length will be chosen by balancing construction constraints against the desire for redundancy in event reconstruction.

### 3.9 Electron Trigger Calorimeter

The electron trigger calorimeter serves two purposes in the MECO experiment. First, it is used as a trigger device, selecting events to be recorded for further analysis. For this purpose, the design goal is to provide a signal that selects conversion events with high efficiency while minimizing the rate of triggers from lower energy electrons or other processes, for example pile-up of energy from the many neutrons, photons, and protons that are produced following muon capture. Second, this device provides an independent measure of the energy of putative conversion electrons and a measurement of the position of the electron that can be compared with the position determined by projecting the fitted helix to the calorimeter. These latter tools provide powerful discrimination against pattern recognition errors, as has been discussed in the preceding section.

We discuss below two possible implementations of the trigger device. Each provides an efficient trigger signal that reduces the total trigger rate to a very manageable level. Each is a highly segmented device, limiting the contribution from pile-up. Each has advantages and disadvantages and the choice of which to construct will be based on considerations of cost and performance. Our estimate of the background rate from pattern recognition errors is based on the rejection provided by the lower performance (plastic scintillator) device. The project cost given is for the more expensive of the two options (the crystal scintillator).

#### 3.9.1 Plastic Scintillation Calorimeter Option

We describe here the design and performance of a simple calorimetric trigger device consisting of a highly segmented, in principle fully absorbing plastic scintillator that uses construction techniques previously used in such devices. Driving the design, in addition to the high rates, is the need to operate the detector in a 1 T magnetic field. The scintillation light is transported out of the high field region with the use of optical waveguides, cladded fibers, whose small diameter makes possible the consideration also of specialized higher quantum efficiency devices, e.g., VLPC's (visible light photon counters), in place of conventional photo-multiplier tubes to produce signals of higher quality.

##### Detector Description

The proposed detector [89] is a conical shell of scintillator that extends radially from 45 cm to 75 cm at its upstream end and from 45 cm to 85 cm at its furthest point downstream. The detector is 136 cm in length and centered on the axis of the solenoid (the z-axis). It is divided into 40 segments in azimuth and 40 along the z-axis. The 1600 segments, or tiles, are 7.1 cm and 11.8-13.3 cm across at the inner and outer radii, 30-40 cm along a radial edge and 3.4 cm thick. Light from each tile is absorbed in a wavelength shifting fiber embedded in the tile that mates to a waveguide fiber at the outer edge of the cylinder. The waveguide fiber transmits the light to the rear of the cylinder and on to the readout system. The tiles in each successive layer in z are rotated through an angle of 0.03 radians, following the helical trajectory of the conversion electron. The detector is shown in Fig. 27.

The light output of each tile can be estimated from recent thorough studies of light yields in similar geometries. In reference [90] eight photoelectrons were detected in a photo-multiplier tube (Q.E.  $\sim 0.18$ ) when a minimum ionizing particle traversed a 0.4 cm thick tile,



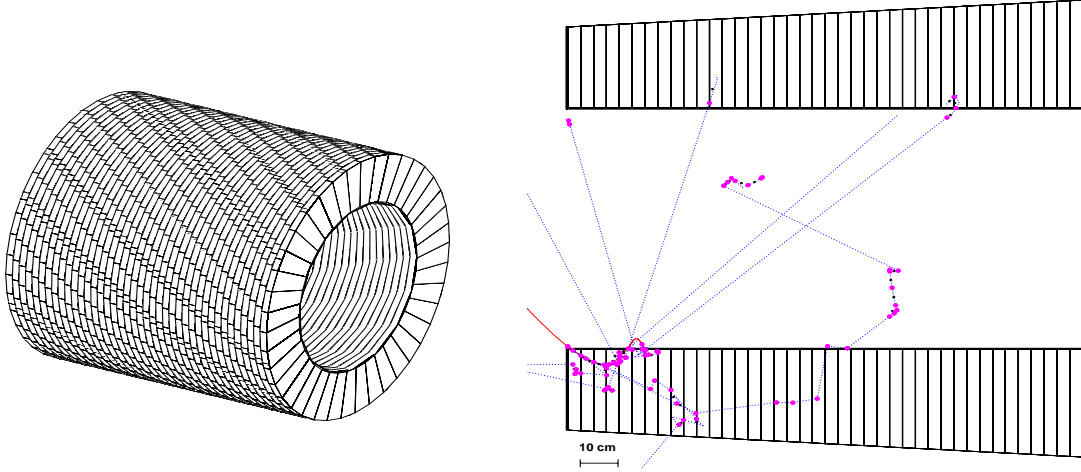


Figure 27: Two views of the MECO scintillating tile trigger detector are shown. It contains 1600 tiles, 3.4 cm thick. Each tile is 7.1 cm across at the inner radius, 11.8-13.3 cm at the outer radius, and 30-40 cm along a radial edge.

approximately one photo-electron per 100 keV of energy deposition. The result varied only slightly with tile shape. Four meters of waveguide fiber with couplings at three connectors were used to bring the light to the photo-multiplier tube. The loss at each connection was approximately 10%. In the proposed detector only one thermally fused connection is required, which should result in a photo-electron yield about 20% higher.

Two options for the photo-transducer are being considered. Multi-anode photo-multiplier tubes give light yields as just described. VLPC's are more troublesome to use but have a quantum efficiency of approximately 70%. Using the above results, the 105 MeV conversion electron should produce a signal of 1200 photoelectrons in the photo-multiplier tube and three to four times that in the VLPC, if all the energy is deposited in the detector. The photo-electron statistics contribution to the energy measurement is expected to be  $\sim 1.5 - 3$  MeV for conversion electrons, which is small compared to the energy uncertainty resulting from fluctuations in the deposited energy and from fluctuations in the energy under the electron produced by low energy particles coincident in time with the electron.

### **Performance and Trigger Rates**

The performance of the trigger detector was studied using MECO's implementation of the GEANT package. The trigger rate is dominated by muon DIO electrons in which the measured energy is modified by the substantial flux of low energy particles produced following muon capture and by bremsstrahlung photons emitted by late arriving beam electrons.

Table 11 summarizes the sources of background and the energy deposition from each source in the detector, integrated over a 30 ns time window. To suppress the rate from protons produced following muon capture, the calorimeter is shielded by a 0.3 cm layer of  $CH_2$ . The mean energy deposited in the entire calorimeter is 150 MeV. The distribution is plotted in Figure 28.

While the energy deposited in the entire detector is large, the trigger is built around trigger towers, 100 in all, that extend just 27 cm in z and covers 5% of the azimuth. The

Table 11: Contributions to the energy deposited in the plastic scintillator trigger calorimeter from  $\gamma$ 's, protons and neutrons from muon capture, from muon DIO electrons in two energy ranges, and from beam electrons that arrive during the detection time window. Particularly in the case of DIO electrons with  $E > 55$  MeV, the value of the mean energy deposited is somewhat misleading, since the trigger rate derives from the high energy tail in this distribution.

	capture $\gamma$	capture proton	capture neutron	decay electron $E < 55$ MeV	decay electron $E > 55$ MeV	beam electron
Rate [Hz]	$1.9 \times 10^{11}$	$1.6 \times 10^{10}$	$2.1 \times 10^{11}$	$7.2 \times 10^{10}$	$1.1 \times 10^8$	$4.6 \times 10^{10}$
Calorimeter hit probability	0.0032	0.00026	0.0065	0.0032	0.0045	0.0055
Events in 30 ns	18.24	0.125	40.95	6.9	0.0148	7.6
$\langle \text{Energy} \rangle$ deposited [MeV]	1.5	12.8	2.0	1.1	1.0	1.07

tower size was chosen to minimize the trigger rate while still providing an efficient trigger for conversion electrons. The energy deposited in a trigger tower by the background sources is plotted in 28. The energy deposition averages 14 MeV and falls exponentially above 25 MeV.

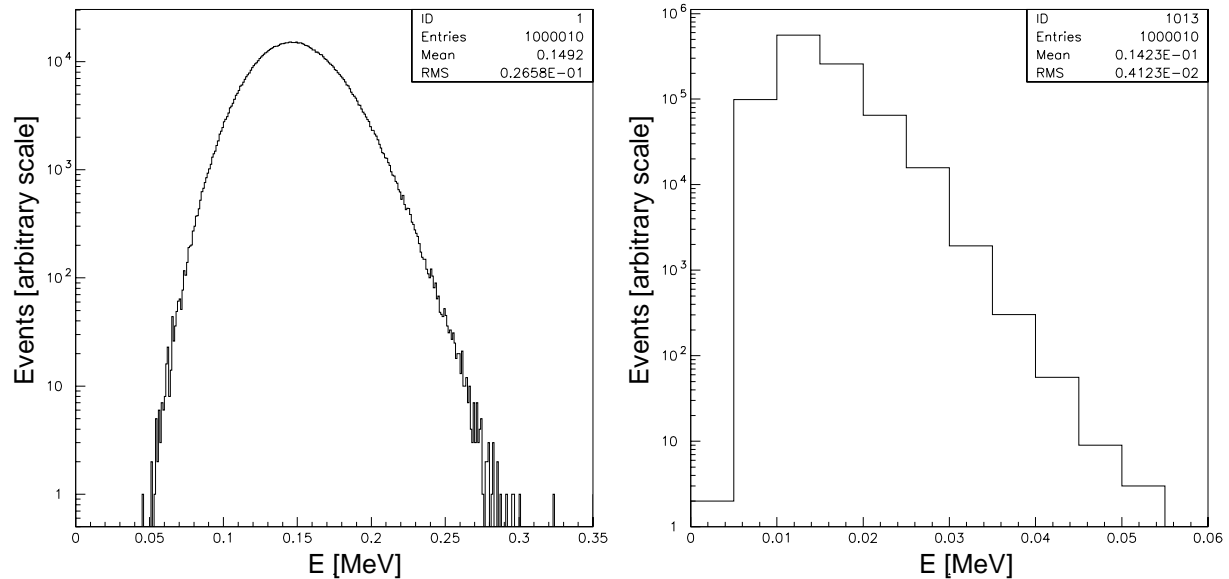


Figure 28: The plots show the total energy deposited in the whole detector (left) and in a trigger tower (right) in a 30 ns integration time from all sources: protons,  $\gamma$ 's, and neutrons from capture processes, beam electrons and DIO electrons.

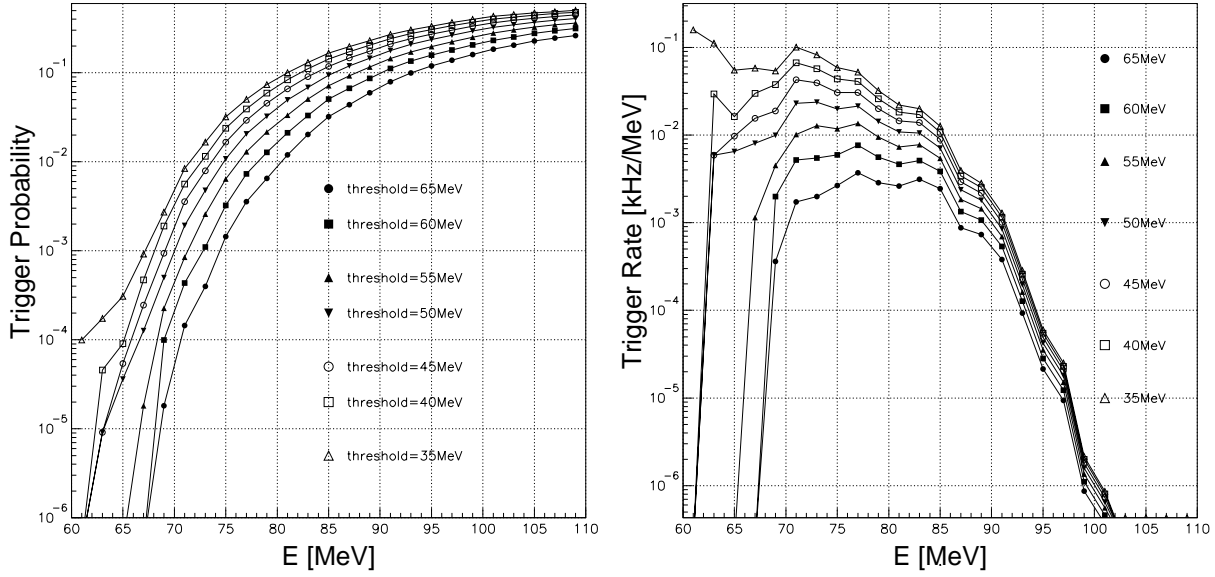


Figure 29: The probability to have energy deposition in any trigger cell above threshold as a function of electron energy, for different values of the trigger threshold is shown in the leftmost plot. The plot on the right shows the result of convolving the distribution on the left with the spectrum of DIO electrons to give the instantaneous trigger rate as a function of the electron energy, again for different thresholds. The integral of this curve, plus a contribution from pure noise pile-up, the size of which depends on the threshold, gives the total instantaneous trigger rate.

The majority of the triggers occur when this energy is superimposed upon the energy deposited by an electron from muon DIO. The probability that total energy exceeds a preset threshold in any of the towers determines the trigger rate. This probability is shown as a function of the electron energy in the plot on the left in Figure 29. This probability rises rapidly with electron energy, as expected. When convolved with the steeply falling spectrum of electrons from muon DIO (see Figure 21), the trigger rate as a function of DIO electron energy is obtained. This is shown in the plot on the right in Figure 29. An additional small contribution to the trigger rate results from pure noise pile-up. Table 12 gives the expected trigger rate from all sources as a function of the trigger threshold. A value of 40 MeV for the threshold gives an instantaneous trigger rate in the 700 ns active time each pulse of 2.4 kHz. This corresponds to approximately 600 triggers for each AGS cycle of 1 second. The trigger efficiency for conversion electrons is 89% at this threshold.

Fig. 30 shows the energy deposited in the trigger tower by conversion electrons with and without background energy superimposed. It contains in mean about 70% of the conversion electron's energy.

Table 12: The table gives the trigger efficiency for conversion electrons and the total trigger rate for different values of the trigger threshold. The trigger rate given is the instantaneous trigger rate during the 700 ns live period during each  $1.35 \mu\text{s}$  pulse.

Energy threshold [MeV]	Efficiency	Trigger Rate [kHz]
65	0.54	0.05
60	0.63	0.10
55	0.71	0.17
50	0.77	0.3
45	0.83	0.5
40	0.89	2.4
35	0.92	14.5

### Position Measurement

The calorimeter entry point of the conversion electron can be either at the face of the calorimeter or downstream in  $z$  if the electron enters from the inner cylindrical surface. The entry point,  $(z_{ent}, \phi_{ent})$ , is estimated using a simple algorithm that first finds the scintillator cell containing the most energy and then searches for a cell in the upstream two  $z$ -layers and in the same or adjacent  $\phi$  sectors with energy exceeding a third of that in the segment of maximum energy. The full space distance  $D$  between this point and the true (GEANT)

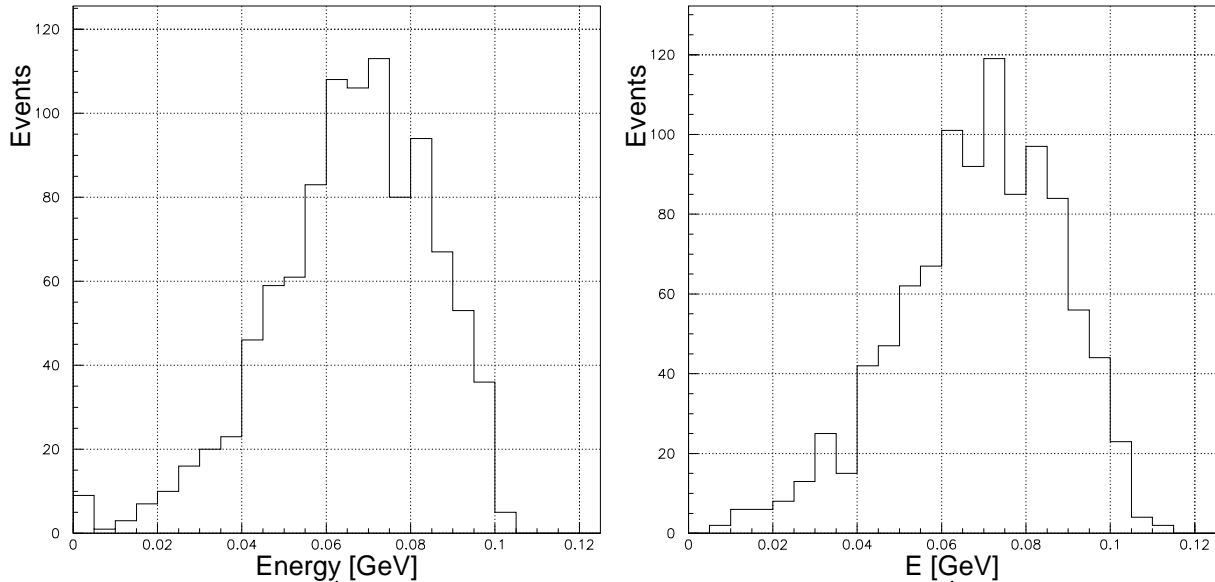


Figure 30: The left(right) plot shows the energy deposited in a trigger tower of the scintillation trigger detector by a conversion with(without) background energy superimposed.

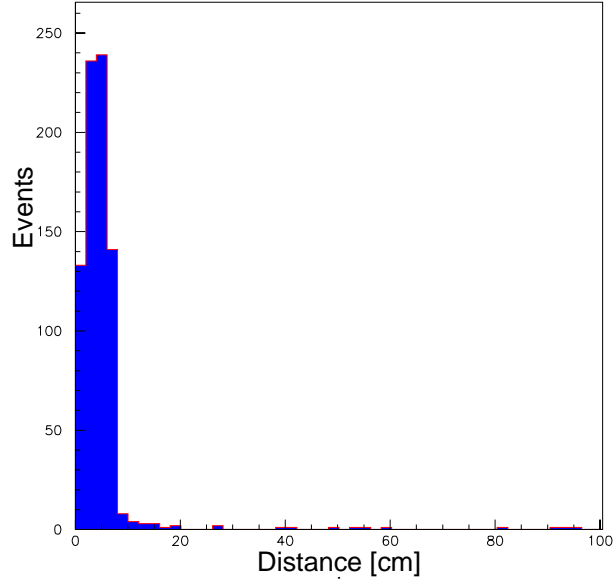


Figure 31: The plot shows the distribution in the distance between the calorimeter entry point derived from the distribution of deposited energy and the true entry point from the GEANT simulation.

entry point of the electron is plotted in Fig.31. For three-quarters of the events the distance between the estimated and true entry points is less than 10 cm. The tails in the distribution arise from events that barely strike the calorimeter at the upstream end, and then enter it after a significant fraction of a helix turn. A more sophisticated algorithm could identify these events and deduce a better match. This position determination, correlated with the deposited energy, provides a useful constraint on the electron’s trajectory measured in the tracking detector.

### 3.9.2 Crystal Scintillator Calorimeter Option

The plastic scintillation detector provides an adequate trigger for the experiment but suffers ultimately because it responds primarily to the ionization loss of the incident electron, and the range of the conversion electron, 54 cm, exceeds the radiation length in the plastic, 42 cm. Photons radiated by the incident electron often either escape the calorimeter or their energy is deposited far from the main shower. The energy that escapes the primary cluster leads to a significant tail in the resolution that forces the trigger threshold to be rather low to be efficient.

It is possible to reduce the data sample substantially by using a high density crystal calorimeter that provides at the same time additional meaningful constraints on the event. The energy resolution expected is  $\pm 5\%$  (RMS) and an energy correlated (x,y,z) coordinate on the trajectory can be determined to  $\pm 1$  cm (RMS). The solid angle subtended by the detector is 14% of that subtended by the scintillation counter, reducing the rate from neutrals—gammas and neutrons—reaching the detector directly from the target. Most of these are

absorbed harmlessly in the front face of the detector.

### **Detector Description**

The proposed detector geometry uses vanes as in the MECO tracking detector, but differs in that each vane is a high density bar that functions as a total absorption calorimeter. Detectors with 4 and 6 bars have been studied. The 4 bar arrangement is shown in Figure 32. Each bar extends radially from  $r = 39$  cm to  $r = 69$  cm and 150 cm along the axis of the solenoid. The bar height, typically 12-16 cm, depends on the calorimeter material. Electrons

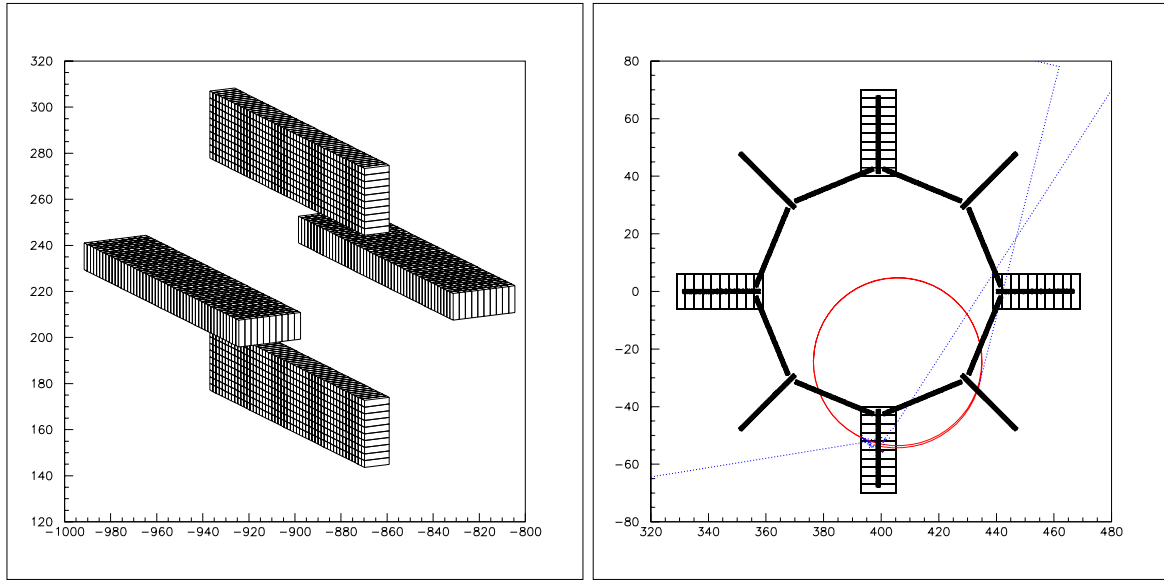


Figure 32: Two views of the proposed crystal calorimeter are shown. Four bars consisting of crystals  $3 \times 3$  cm on a side and 12 cm in depth are shown. The drawing on the right shows the tracking detector and the calorimeter bars, looking along the  $z$ -axis from the muon target. The trajectory of a typical 105 MeV electron is superimposed.

strike only one of the  $150 \text{ cm} \times 30 \text{ cm}$  surfaces and are absorbed in the calorimeter. The geometry works best for detectors with short radiation length; twelve centimeter long BGO crystals with  $X_0 = 1.1$  cm have been studied in detail. Crystals made from GSO are more suited to our application. They have shorter decay time by an order of magnitude and 3-4 times the light output. Their use would result in considerably better resolution, but they are at the moment too costly by a factor two. Several large collaborations are interested in using GSO and could well motivate a price reduction.

Lead scintillating-fiber calorimeters can also be used in this geometry and provide a solution intermediate between the scintillation detector proposed above and the crystal calorimeter discussed in this section. An energy resolution of  $4.4\%/\sqrt{E(\text{GeV})}$  and a time resolution of  $34\text{ps}/\sqrt{E(\text{GeV})}$  were achieved in KLOE prototypes that match fairly well our geometry [91]. The radiation length of 1.6 cm would require bars thicker than the 12 cm required with the crystal.

In what follows, we study a BGO crystal calorimeter with 2000 crystals of 3 x 3 cm lateral dimension and 12 cm long. A calorimeter made from 4 x 4 cm crystals meets all of the physics requirements of the experiment. The channel count reduces to 1152, and the cost of the photo-detectors and readout electronics is 40% less. Various lengths of crystals also have been studied. Fourteen centimeter long detectors give a small improvement in resolution; no further improvement is obtained with 16 cm long detectors and some fall-off in efficiency is observed because of electrons striking the sides of the bars.

### **Performance and Trigger Rates**

The crystal calorimeter was studied using a full GEANT simulation of the detector. Electrons of 105 MeV were generated in the aluminum target and traced through the tracking detector to the electron calorimeter, which extends 6 to 7.5 meters from the end of the muon target. Only ‘good’ electrons, those producing quality tracks in the tracking detector, were retained for the calorimeter study. Figure 33 shows the efficiency of the BGO detector as a function of the threshold imposed on the reconstructed energy. In the studies of the

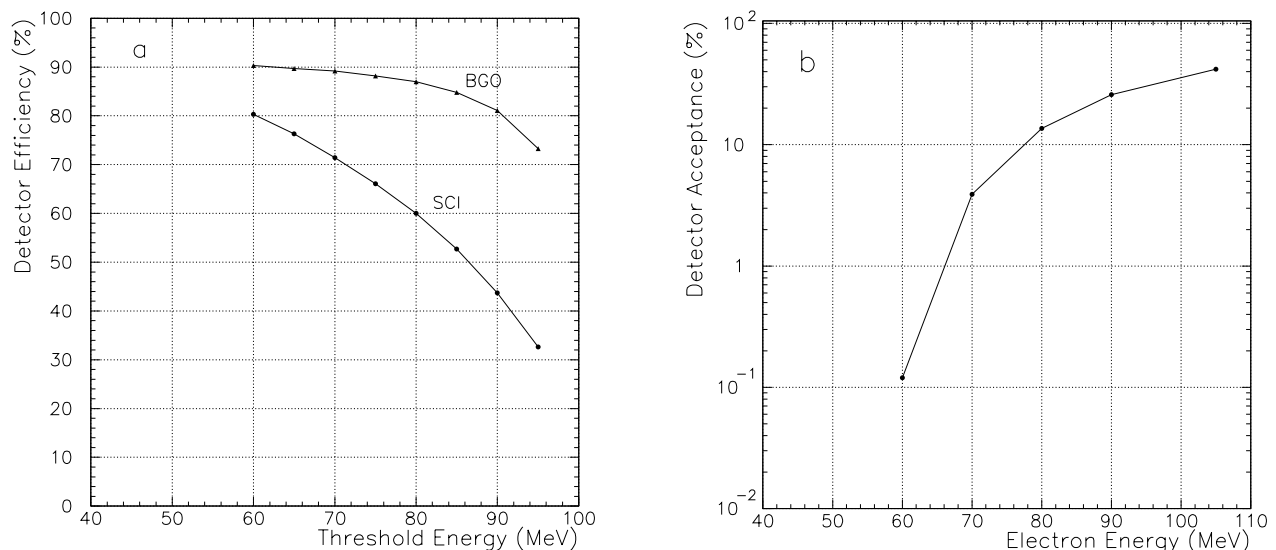


Figure 33: The plot on the left shows the reconstruction efficiency of the BGO crystal calorimeter. The second curve (labeled SCI) is for a somewhat different implementation of a plastic scintillator than the one described in the preceding subsection. The plot on the right shows the geometrical acceptance versus electron energy.

crystal detector, electrons are accepted only if they strike the 30 x 150 cm electron sensitive surface. Figure 33 also shows the rapid fall off of the geometrical acceptance with decreasing electron energy, required to avoid the large flux of decay electrons below 52.8 MeV. The energy reconstructed in the calorimeter is compared to the energy of the electron leaving the tracker in Figure 34. The difference is plotted for the electrons that strike the calorimeter on the electron sensitive surface. The low energy tail in this plot comes mostly from hits near the edges of the bar. Figure 34 also shows the impact of neutrons from muon capture, produced either directly or as a result of nuclear de-excitation, on the measured energy.

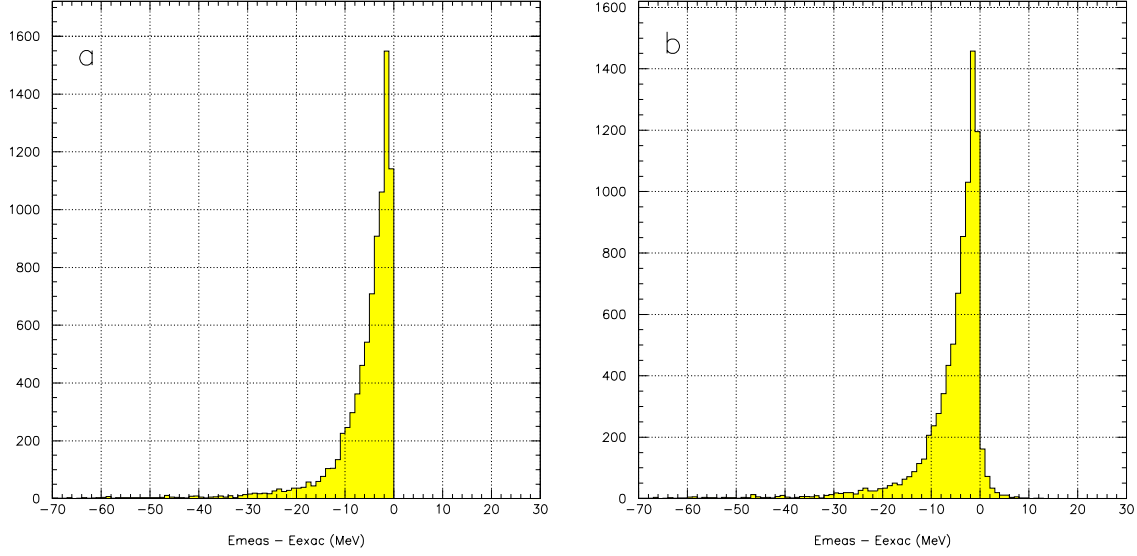


Figure 34: The plot on the left shows the difference between the incident energy and the energy deposited in a 12 cm long BGO crystal calorimeter for conversion electrons in a GEANT simulation. The bin size is 1 MeV. The plot on the right shows the same quantity, with broadening due to noise, primarily neutrons from muon capture processes.

The neutrons were tracked through the detector, the solenoid coils, and the surrounding 35 cm iron return yoke using the hadron code GCALOR in GEANT. Re-scattering in the 35 cm thick return yoke increases the flux reaching the detector by a factor of 20. Still the impact on the resolution is small. The angle between the electron's trajectory and the  $z$ -axis, is typically 50 degrees, implying that the electron encounters on average 15.7 radiation lengths.

The crystal calorimeter geometry permits the reconstruction of three independent coordinates of the particle position. To estimate simply the detector coordinate resolution, the cell energies obtained from a GEANT simulation were projected onto the radial,  $x$  or  $y$ , and  $z$  axes. An energy weighted sum of the coordinates of the centers of the struck cells was used to estimate the impact coordinate of the electron at the surface of the calorimeter. Figure 35 shows the difference between the real and reconstructed coordinates, plotted in 0.5 cm bins, in the BGO crystal calorimeter with 3 x 3 cm elements. The RMS resolution in the radial coordinate is worse because of shower leakage from hits near the edges of the bar, which is not as significant in the measurement of the  $z$ -coordinate. The resolution in the radial coordinate can be improved using the shower profile. This well measured position, correlated with the energy deposition in the trigger calorimeter, provides a valuable constraint on the event.

### Detector Energy Resolution

The location of the trigger calorimeter in a 1 T magnetic field and the severe time constraint imposed by the beam micro-structure provide the major challenges to obtaining good energy resolution in the calorimeter. The magnetic field makes it difficult to take



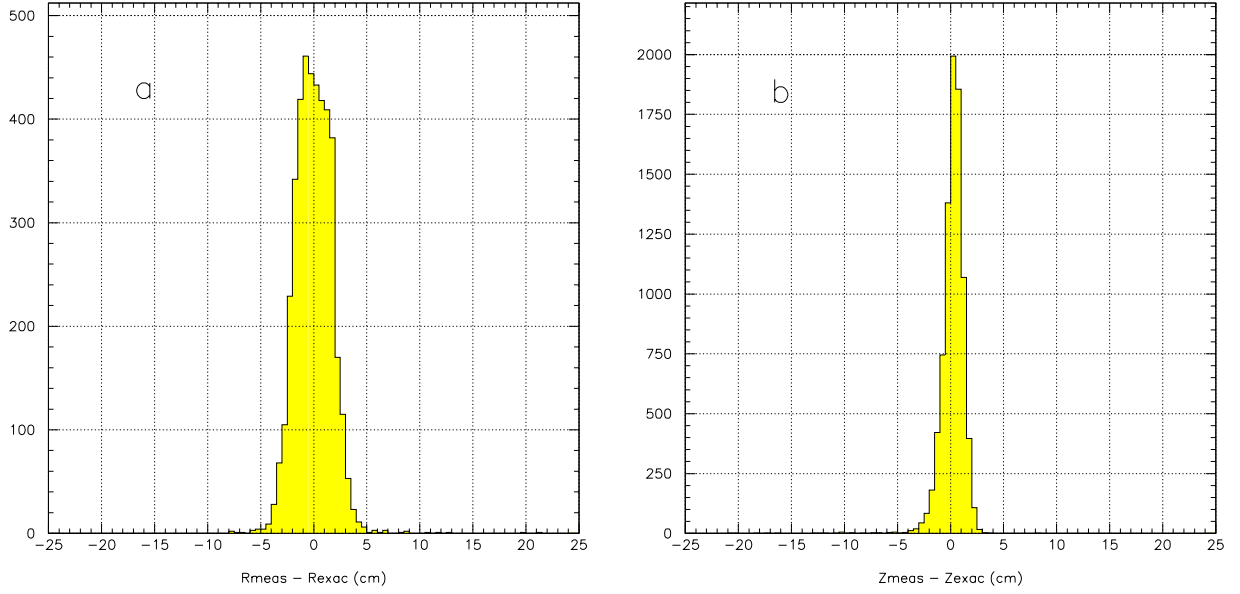


Figure 35: The plots show the difference between the reconstructed coordinate in the calorimeter and the electron coordinate at impact (from GEANT) in the radial direction on the left and along the z-axis on the right. The bin size is 0.5 cm.

advantage of the broad-bandwidth, high gain and low noise of photo-multiplier tubes in this application. To overcome the magnetic field problem, many experiments have turned to sensing the light from the crystal using photodiodes, sometimes coupled in a creative fashion to the crystal [92]. The high quantum efficiency of these devices and the stability achieved when coupled to a charge sensitive amplifier are advantages not shared by photo-multiplier tubes. The down side is that in sensing and amplifying the diode photo-current electronic noise is introduced, due primarily to the thermal noise associated with the channel resistance of the field effect transistor commonly used at the input stage of the amplifier. This energy independent contribution to the resolution becomes particularly important at low energy and is largest when time constraints force short shaping times in the amplifier-filter network. Despite these drawbacks, great progress has been made recently in using crystal calorimeters at low energy. The development of large area photodiodes with large depletion depths, and therefore small capacitance, has been important in improving the signal-to-noise ratio at low energy [93, 94].

The energy spectra shown in Figure 34 have a full width at half maximum of 4 MeV and a low energy tail from energy leakage, particularly for hits near the radial edge of the detector. To this width must be added the contributions from other sources. The resolution is usually described by the quadrature sum of three contributions:

$$\sigma(E) = A \oplus B \cdot \sqrt{E} \oplus C \cdot E$$

in which the first term is the contribution from electronic noise, the second is due to photon statistics, and the third term, proportional to the energy, includes an assortment of ills: inter-calibration errors; non-uniform light collection over the crystal; fluctuations due to

Table 13: The table gives the parameters used in the calculation of the electronic noise.

Parameter	Device	Value	reference
$e_n$ (nV/ $\sqrt{\text{Hz}}$ )	FET:2SK147,2SK190	0.48	Hitachi
$C_{gs}$ (pf)	FET:2SK190	75	Hitachi
$C_d$ (pf)	PD:S2744-08	85pf@ $V_R = 70\text{V}$	Hamamatsu [95]
$I_d$ (namps)	PD:S27744-08	5namps@ $V_R = 70\text{V}$	Hamamatsu [95]
$L$ (pe/MeV)		370/diode	(see text)
Scint. Decay (ns)		300 ns	[96]

energy leakage; and, if not monitored effectively with time, collective temperature and gain drifts. Sometimes a fourth empirically observed term proportional to  $^4\sqrt{E}$  and of order 1% is included.

The first term in this equation is the most difficult to limit at low energy when using photodiodes. The quantity  $A$  is called the equivalent noise energy and is the ratio of the equivalent noise charge, expressed in units of the electron's charge, to the light collected,  $L$ , in photoelectrons per MeV:

$$ENE = \frac{1}{e \cdot L \cdot F(t_{max})} \left[ \frac{e_n}{\sqrt{\tau_1}} (C_{gs} + C_d) \oplus \sqrt{2eI_d\sqrt{\tau_2}} \right]$$

In this equation, the times  $\tau_1$  and  $\tau_2$  are obtained from the filter transfer function,  $g(\omega)$ , through the series and parallel noise integrals  $\tau_1 = \left[ \int_0^\infty |g(\omega)|^2 \frac{d\omega}{2\pi} \right]^{-1}$  and  $\tau_2 = \left[ \int_0^\infty \frac{|g(\omega)|^2}{\omega^2} \frac{d\omega}{2\pi} \right]$ . The quantities  $C_d$  and  $I_d$  are the diode capacitance and reverse bias leakage current, and  $e_n$  and  $C_{gs}$  are properties of the FET at the input to the charge sensitive amplifier:  $e_n$  is the thermal noise due to the FET channel resistance in nanovolts/ $\sqrt{\text{Hz}}$  and  $C_{gs}$  is the gate-source capacitance. The output voltage of the filter rises to a maximum  $F(t_{max}) \cdot Q/C_F$  at  $t = t_{max}$ , where  $Q/C_F$  is the output voltage of the preamplifier with feedback capacitance  $C_F$ . If the duration of the input current pulse from the diode is short compared to the RC time constant of the filter,  $F(t_{max})$  is independent of the time constant. The decay time of the BGO scintillator, 300 ns, leads to a dependence on the shaping time. Figure 36 shows the equivalent noise energy and the dependence of  $F(t_{max})$  and  $t_{max}$  on the RC time constant for a CR – (RC)<sup>2</sup> filter with the parameters given in Table 13. The rise at small times is due to the series noise while the parallel noise gives rise to the increase at large values of the shaping time. For RC = 300 ns and a scintillation decay time of 300 ns, the peak is at 900 ns. The calculation assumes two diodes that are each of area 2 cm<sup>2</sup> and together cover 44% of the face of the crystal. They have the properties given in the Table 13. A large number are being used in the BaBar electromagnetic calorimeter.

The signal to noise improves directly with the collected light, the quantity  $L$  in the expression for the equivalent noise energy. The value of  $L$  given in the table was estimated as follows. A Monte Carlo simulation was made of the light collection from a polished, unwrapped 3 x 3 x 12 cm crystal of index of refraction 2.15 coupled at one end to a detector of

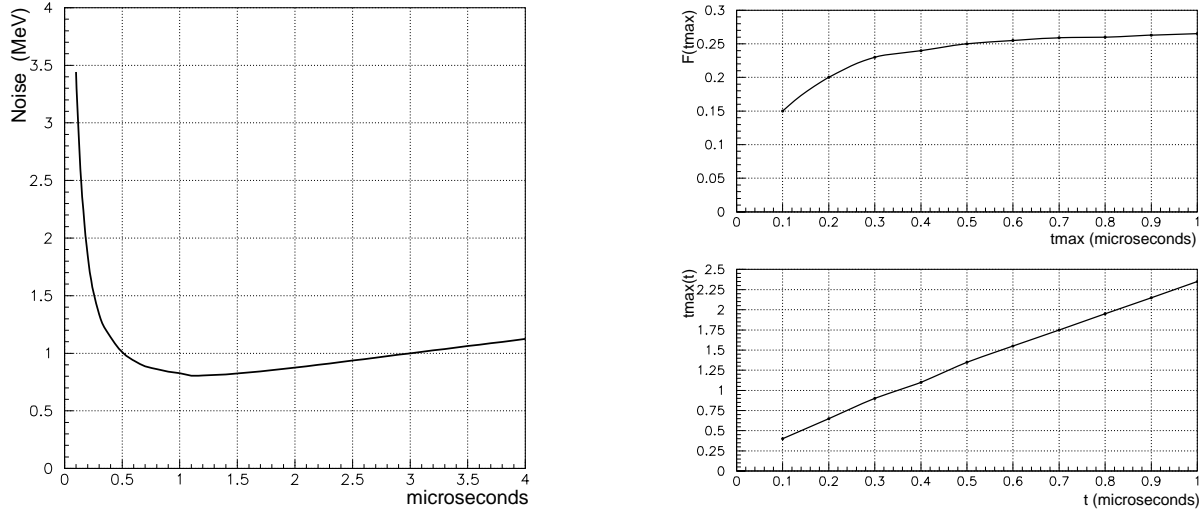


Figure 36: The plot on the left gives the equivalent noise energy vs RC-time constant for  $CR - (RC)^2$ . The plots on the right give the time  $t_{\max}$  at which output peaks (in the lower plot) and the peak amplitude (in the upper plot) in units  $Q/C_F$  vs RC.

refractive index 1.5. The light passing through the detector face originating from a source at the far end is 22.5% of the total. The mean distance traveled by the light is 20.4 centimeters, far less than the attenuation length in the crystal above 400 nm [97]. This collection improves to 28.4% if the end opposite the detector is made reflective. It is well known that the light collection improves substantially if the crystal is wrapped with a white, diffuse-reflecting material, e.g., several layers of teflon [98]. Precisely the right measurement was made in reference [99] for us to complete the calculation. The light collection from a wrapped BGO crystal was compared to that from a bare, polished crystal. A 30% improvement was found if the far end was capped, in agreement with the result given above, and an 85% increase in the light collected was found if the entire crystal was wrapped. Using this result we calculate the light yield of the wrapped crystal:

$$L = 5 \times 10^3 \text{ (photons/MeV)} \times 0.225 \times 1.85 \times 4/9 \times 0.8 = 740 \text{ e-h pairs.}$$

where the last two numbers on the left are the fraction of the area covered by the diodes and the diode quantum efficiency at 480 nm. The number calculated is somewhat less than numbers reported in the literature: 850 e-h pairs/MeV obtained in reference [100] with a  $4.4 \times 2.0 \times 15$  cm crystal and diodes covering a third of the face area, and the 1200 e-h pairs/MeV obtained in reference [97], in which a fraction 0.36 of the end of a  $2.5 \times 2.5 \times 18$  cm crystal was covered. Notice that the wrapping makes the choice of diode size more complicated (pleasantly so) because light that misses the diode can be reflected away and return to strike the diode on another try (see reference [100]). The capacitance and therefore the noise charge is reduced if a diode of smaller area can be used.

Beam constraints force a less than optimum value for the filter time-constant. For  $RC=300$  ns, the signal peaks at 900 ns and the equivalent noise energy is 1.3 MeV/crystal.

At this value of the time constant, the contribution to the resolution from electron – hole statistics is 0.4%. Figure 37 shows the GEANT generated energy spectrum, including neutron pile-up, smeared by the electronic noise. The resolution obtained from the upper half of the curve is  $\sigma = 5.5\text{MeV}$ .

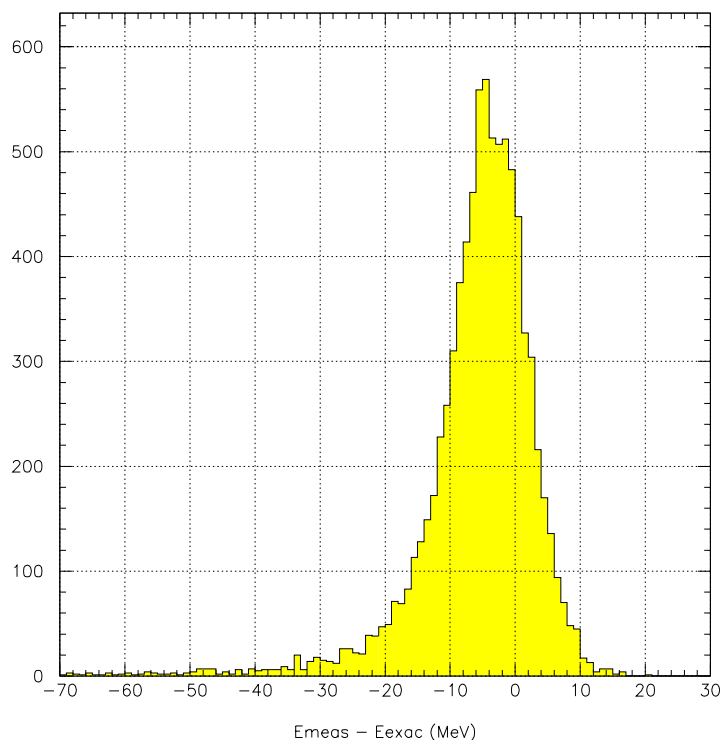


Figure 37: The plot shows the the distribution in the measured electron energy minus the incident energy. Pile-up and electronic noise are included.

An alternative approach to the light collection is to attach a wavelength-shifting plate of the same area as the crystal to the read-out end, spaced a 1 mm or so off the end of the crystal. The WLS plate absorbs the light from the crystal and re-emits it, shifting it in wavelength to a more sensitive region of the diode response (at larger wavelengths) and, more importantly in this case, concentrating the flux. The light is sensed from the edge of the plate, typically 3-4 mm thick, with smaller area photodiodes. This technique was first used with BaF crystals to shift the fast component of the light at 250 nm to higher wavelengths. A factor of 24 improvement was achieved in this case, as measured by moving a small diode from the surface of the crystal to the WLS edge; a fourfold gain was obtained from the improvement in QE and another factor of six from the concentration of the flux [92]. The technique was used also by the Crystal Barrel Collaboration at LEAR in a CsI(Tl) calorimeter. More modest results are reported in tests by the BaBar collaboration of their CsI(Tl) calorimeter; 75% of the light collected at the crystal surface is collected in less expensive diodes of half the area attached to the edge of the WLS plate. The noise level is about the same.

This approach would have to be explored and compared to the more conventional method.

Even with equal performance in light collection, there can be advantages in light collection uniformity, cost, and implementation in the geometrical arrangement of the planned detector.

### Readout, Trigger Rates

The beam structure imposes severe constraints on the readout if there is a flash produced when the protons strike the production target. The readout scheme described below assumes that such a flash does occur, and that all of the analog signals have to be held before the next beam micro-pulse. Two possible timing schemes have been considered. For most of our studies, the structure assumed consisted of one pulse of 100 ns duration every 1.35 microseconds filled by one booster cycle to an intensity  $\leq 2 \times 10^{13}$  protons. This is accomplished by filling two of six equally spaced buckets around the ring. The gate for detecting the conversion electron extends from 700 ns to 1350 ns, 50 ns before the arrival of particles produced by the next beam pulse. A conversion electron coming near the end of the gate has to be held before the next pulse. Fifty nanoseconds should be sufficient for the scintillation detector. The fraction of  $\mu$  captures during the gate is 47%.

For the crystal calorimeter, a longer time is required, partly because of the longer decay time of the scintillator but primarily because of the need to reduce the noise. A better mode of operation for both detectors is to fill two adjacent buckets 335 ns apart with two booster cycles, and extract the beam in one micro-pulse spread over 200 ns every 2.7 microseconds. The pulse would be filled by the two booster cycles to an intensity of  $\leq 4 \times 10^{13}$  protons. In this mode, the gate extends from 0.8  $\mu$ s to 1.8  $\mu$ s if the crystal calorimeter is used and from 0.8  $\mu$ s to 2.6  $\mu$ s using the scintillation detector. The fraction of  $\mu$  captures during the gate is larger in this mode, by 7% for the crystal detector and by 38% for the scintillation detector.

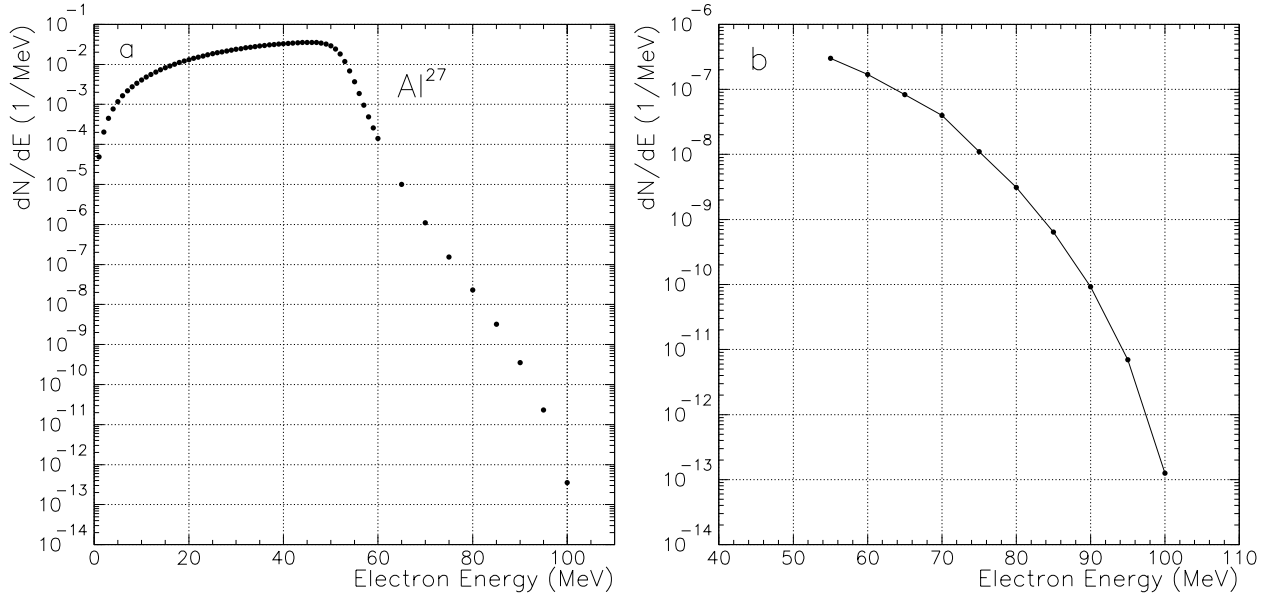


Figure 38: (a) Differential energy spectrum for muon DIO in Al. (b) Spectrum multiplied by calorimeter acceptance.

With the longer gate, the crystal calorimeter becomes tractable even in the presence of beam flash. The trigger is formed by dividing each bar of the calorimeter into 48 overlapping super-cells. Each super-cell is obtained by summing signals, after filtering, from  $5 \times 5$  arrays of crystals. The sums from the 48 channels are encoded with FADC's, 8 bits are more than sufficient, every  $\sim 132$  ns and fed to a pipeline processor. At the same time the signals from the 500 crystals, 1000 diodes, (288, 576 for  $4 \times 4$  cm crystals) are sampled every 132 ns and stored in an analog pipeline, e.g., a switched-capacitor pipeline, 64 channels deep. The sample clock can be gated to store signals only during the interval from  $0.8 \mu\text{s}$  to  $2.7 \mu\text{s}$  after a micro-pulse. When the energy in a super-cell is greater than a preset threshold, the sampling clock is stopped and the analogue data is digitized and read out. The rate is low enough that a high level of multiplexing is possible. This readout scheme is similar to many used in previous experiments and we would hope to borrow from this experience.

An energy deposition of  $\sim 80$  MeV that triggers the detector comes principally from muon DIO. Beam electrons would have to survive the beam collimators that limit the momenta to  $< 50$  MeV, and the 30% reduction in transverse momentum when passing through the graded field at the muon target. The rate is discussed in previous sections and contributes insignificantly to the trigger. Cosmic ray muons that might trigger the detector are reduced to a negligible level by the shield.

The differential spectrum of the decay electrons for muons stopping in aluminum is presented in tabular form in reference [101] and plotted in Fig. 38(a). Plotted in Fig. 38(b) is the spectrum of electrons that actually strike the detector.

A GEANT simulation determines the energy deposited in each cell of the detector, which is then smeared by electronic noise and pile-up from neutrons. Table 14 gives the trigger rates as a function of the energy threshold in a super-cell, and the expected detector efficiency for conversion electrons, are presented. An efficient trigger at an entirely manageable rate is achievable.

Table 14: Trigger rate and efficiency vs threshold energy in super-cell.

$E_{th}(\text{MeV})$	Trigger Rate (kHz)	Efficiency
60	14	0.903
65	6.3	0.896
70	2.0	0.892
75	0.57	0.882
80	0.2	0.870

To summarize, the crystal calorimeter option sharpens the event signature by adding to the high resolution measurement of the electron momentum provided by the tracker a 5 MeV energy measurement and an improved energy correlated full space coordinate measurement. In addition, the data rate is reduced substantially.

### 3.10 Cosmic Ray Backgrounds and Shield

Cosmic ray induced electrons (or muons mistaken as electrons) may induce backgrounds. Previous experiments have been close to being limited in sensitivity due to cosmic ray backgrounds. Since this source of background scales not with sensitivity but with running time, only modest improvement in rejection with respect to that achieved by earlier experiments is needed. Detailed calculation of the sources of backgrounds and the shielding requirements have been done and are described in this section.

Cosmic ray background is already reduced by placing the target and detector in a graded solenoidal field. Most importantly, there is a restricted range of  $p_T$  of electrons produced in the stopping target and detected in the spectrometer. All electrons produced upstream of the stopping target, for example at the interface between the transport and detector solenoids, are identified as background since their transverse momentum is below 75 MeV. Some electrons resulting from  $\mu$  decay or interactions in the detector will also be eliminated by restricting the allowed  $p_T$  range. The use of active and passive shielding, in combination with these intrinsic rejection techniques, will reduce backgrounds to a negligible level.

The cosmic ray background rate will be monitored during the 0.5 s each cycle when beam is not delivered to the target. Hence, we will have a direct measure of the effectiveness of the shield and the expected level of background. Additionally, cosmic ray background rates can be measured as soon as the detector and detector solenoid are in place, allowing modifications to the shield if necessary.

#### 3.10.1 Background Rate Calculation

The calculation is based on measured cosmic  $\mu$  fluxes from the literature [102] and a GEANT simulation of the shielding and detector. Muons dominate the flux of particles penetrating any significant amount of shielding. Their energy spectrum at sea level is essentially flat below 1 GeV, and then falls with a power law approximately given by  $E_\mu^{-2.5}$ ,  $E_\mu$  in GeV. The angular distribution is approximated by  $dN/d\theta \propto e^{-1.43\theta}$ . The muon flux is about 60% positive. For decays and incident muons mistaken as electrons, only  $\mu^-$  contribute. For delta rays and pair production in materials in the target and detector region, both  $\mu^+$  and  $\mu^-$  contribute.

The calculation accounts for the following sources:

- Muons penetrating the shielding and decaying in the detector solenoid.
- Muons penetrating the shielding, interacting in the target, detector and other material, and making electrons.
- Muons penetrating the shielding, scattering in the target or other material, and the muon being mistaken for an electron.
- Muons interacting in the shielding and producing other particles (photons or hadrons) which then interact in the detector to produce electrons. These events may not deposit energy in a veto counter.

The shield configuration consists of 0.5 m of steel surrounding the detector solenoid, followed by a double layer of scintillation counter detectors, and 2.0 m of concrete. A thicker

shield (1 m of steel and 3 m of concrete) was also studied. The effect of the magnetic field in the steel shielding has not been included in the background calculation; it should reduce the particle flux inside the solenoid by curling up low energy muons.

The probability of particles penetrating the shielding was calculated by simulating muons incident on the shielding normal to the surface. This underestimates the attenuation since it underestimates the average path-length. The flux of particles exiting the shielding consists of photons, muons, electrons, positrons and lesser numbers of low energy hadrons. Figure 39 shows the distribution in the type of particles that penetrate the shield. The thicker shield

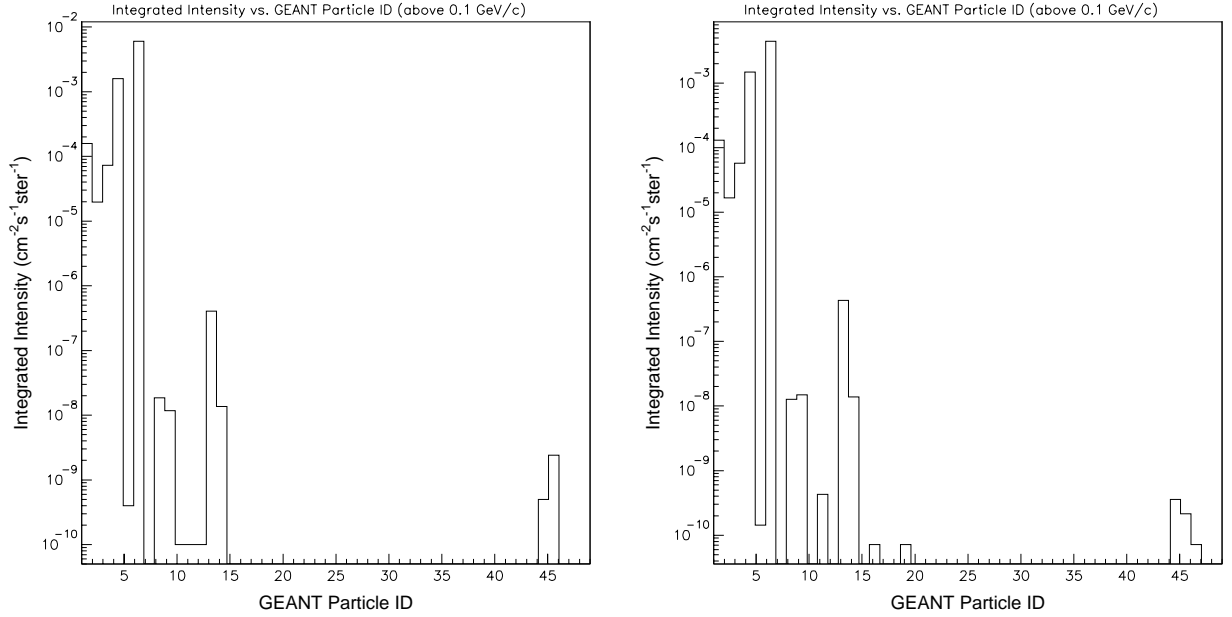


Figure 39: The distribution in particle types emerging from two shielding configurations, the nominal version on the left and a thicker shield on the right. The particle codes are  $\gamma$  (1),  $e^+$  and  $e^-$  (2,3),  $\nu$  (4),  $\mu^+$  and  $\mu^-$  (5,6),  $\pi^+$  and  $\pi^-$  (8,9), neutrons and protons (13,14), and other hadrons ( $>15$ ).

reduces the penetrating particles by about a factor of 2. Figure 40 shows the differential intensities for  $\gamma$ ,  $e^\pm$  and  $\mu^-$  fluxes emerging from the nominal shielding. These fluxes were used as input to the calculation of the probability of producing a 100 MeV electron from cosmic rays.

Essentially all particles penetrating the shielding resulted from processes that deposited energy in the scintillation counter between the concrete and steel. A small flux of photons emerged without depositing energy in the scintillator. They resulted from bremsstrahlung by a  $\mu$  which then ranged out before passing through the scintillator. The probability of getting a photon with energy exceeding 100 MeV is  $\simeq 2 \times 10^{-6}$ . This contributes a negligible amount to the potential background from photons caused by processes that did deposit energy in the scintillator, assuming an inefficiency in the scintillator for detecting a penetrating charged particle is  $10^{-4}$ .

To estimate the total background, the penetrating flux of  $\gamma$ 's,  $e^\pm$ , and  $\mu^\pm$  was caused to impinge on the volume inside the detector solenoid. Particles were generated on the



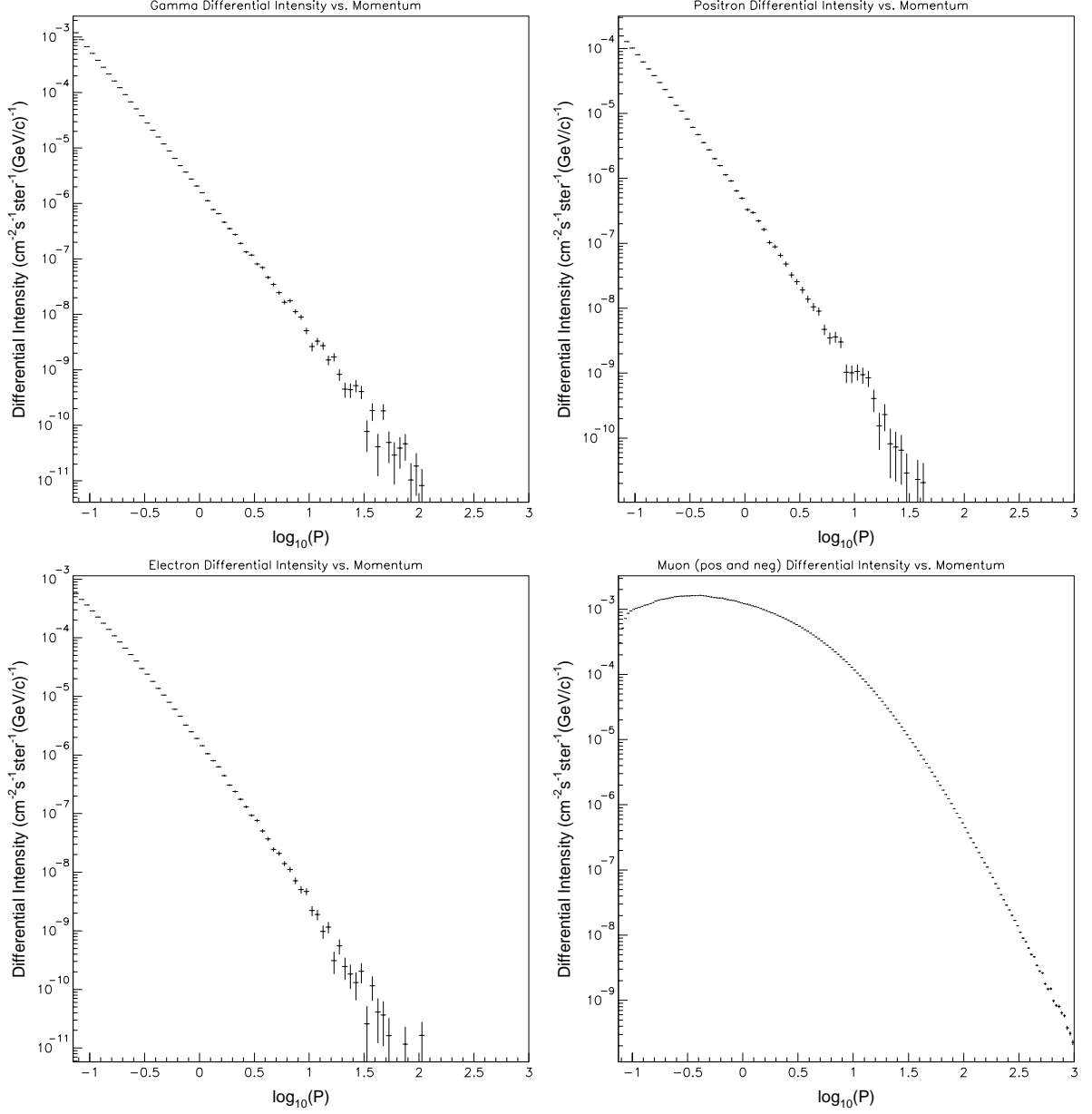


Figure 40: The plot shows the momentum distribution of particles that penetrate the nominal shielding configuration, for the four background particle types with highest flux: upper left –  $\gamma$ , upper right –  $e^+$ , lower left –  $e^-$ , and lower right –  $\mu^-$ .

interior of a cylindrical shell (the magnet coil) according to the calculated flux of particles penetrating the shielding, and weighted by the cosmic ray flux as a function of zenith angle. The simulation of the resulting propagation and interactions was done including the effect of the magnetic field. All kinematic properties of all particles which intersected any part of the tracking detector were recorded, and the following selection criteria imposed:

- The particle charge is negative.
- The particle momentum is in the range  $100 \text{ MeV}/c < p < 110 \text{ MeV}/c$ .

- The number of hits in the tracking detector is more than 3.
- The pitch angle is in the range  $45^\circ < \theta_P < 62^\circ$ .
- The closest distance to the solenoid axis at the stopping target less than 10 cm.
- The track has less than 3 missing hits in the fitted trajectory.

The selection on the pitch angle accounts for the fact that electrons produced in the stopping target have allowed values in this range. The last selection criterion eliminates electrons originating in the middle of the detector, for which the fitted trajectory is predicted to pass through an octagon or vane detector 3 or more times without it having done so. The current event selection criteria are more stringent than these.

A total of  $9 \times 10^7$  particles was generated, distributed according to the particle type and momentum distributions calculated as described above. Taking the duty cycle of the accelerator to be 50%, the detection time for conversion electrons to be 700 ns each  $1.35 \mu\text{s}$ , assuming that we veto cosmic ray induced events using the veto scintillation counter with an efficiency of 0.9999, and accounting for the illumination area, this corresponds to  $\sim 200$  times the nominal MECO running time of  $10^7$  s.

A total of  $\sim 24$  (weighted as described above) particles satisfying the above selection criteria was found. Most of these events were caused by particles produced downstream of the tracking detector (in the electron trigger detector, for example), moving upstream through the tracking detector, reflecting off the B field, and then moving downstream through the tracking detector a second time. Figure 41 shows the distribution in the number of hits in the tracking detector caused by particles moving upstream, for the 24 (weighted) background

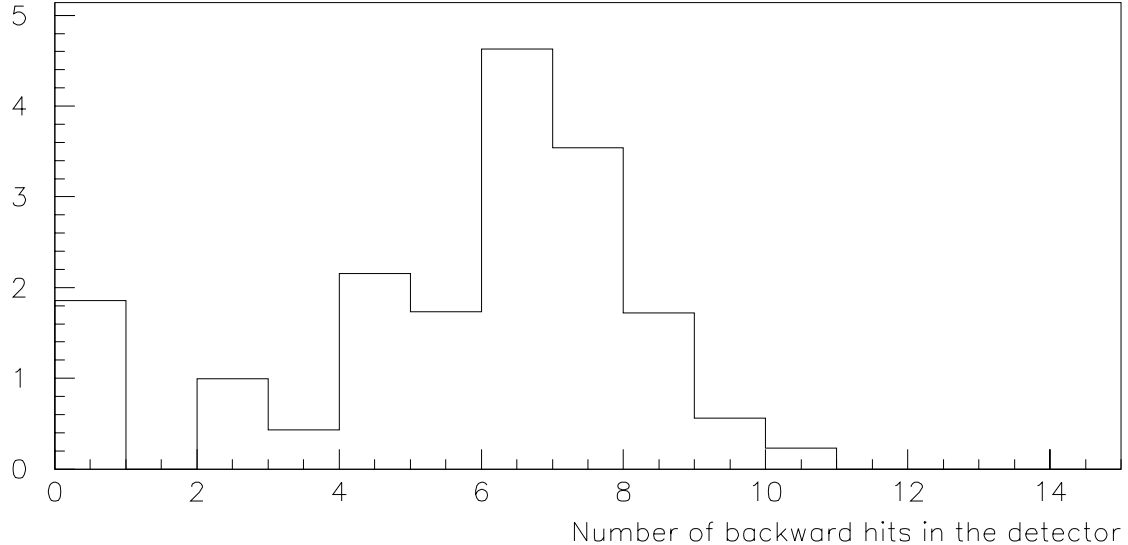


Figure 41: The distribution in the number of hits caused by a particle as it moved upstream through the detector. The entries are weighted by the zenith angle dependence of the cosmic ray  $\mu$  flux.

events. All but 3 (weighted) events have at least 4 clusters in the tracking detector caused by the backward moving particle.

This background is suppressed since we will detect and reconstruct the backward moving track, out of time in the tracking detector. Additionally, events produced in the electron trigger detector will have energy deposited at a time and position which can be deduced from the tracking information. We assume that these events will be vetoed with high efficiency. Of the particles with less than four clusters produced by the backward moving track, three (1.2 weighted) were  $\mu$ 's and can be eliminated by a time of flight requirement between the tracking detector and electron trigger counter. Three (1.2 weighted) others had more than 200 MeV deposited in the electron trigger counter, and can be eliminated by a cleanliness requirement in a small time and position window. One (0.1 weighted) had only 27 MeV deposited in the electron trigger counter. The three (0.7 weighted) remaining events were a  $\mu$  decay upstream of the tracking detector and two delta rays, one produced in the target and one in the straw detector. Figure 42 shows GEANT event displays of a sample of background events.

The cosmic ray background is predicted to be 0.7 events at  $200 \times$  the nominal  $10^7$  running time, or a background of 0.0035 events.

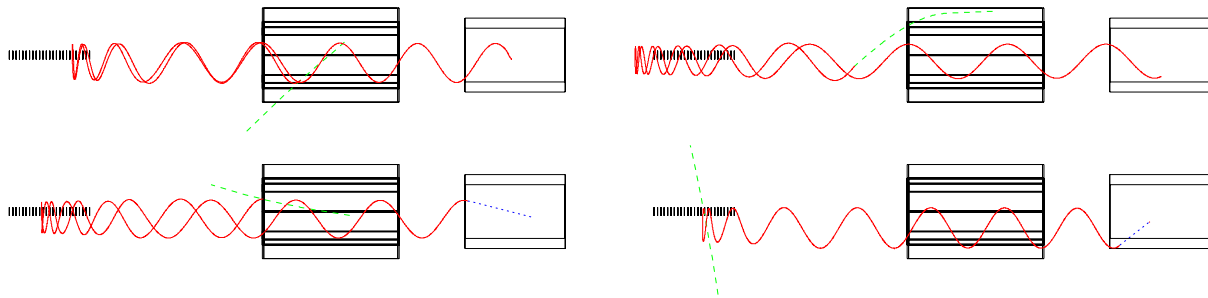


Figure 42: Sample CR induced background events. The event on the top-left is a delta ray produced in the straw material; that on the top-right is a  $\mu$  decay that cannot be eliminated; that on the bottom-left is a delta ray produced in the straw chamber gas manifold (eliminated because it deposited too little energy in the electron trigger detector); that on the bottom-right is a delta ray produced in the stopping target.

### 3.10.2 Hardware Implementation

The cosmic ray shield completely surrounds the detector solenoid. Assuming a length of 12 m and appropriate end-walls, the total volume is  $\sim 200 \text{ m}^3$  of concrete, and  $\sim 65 \text{ m}^3$  of steel. The active shield will consist of  $\sim 260 \text{ m}^2$  of plastic scintillator. To achieve an inefficiency below  $10^{-4}$ , we assume a double layer of detectors will be required.

The active detectors are modeled on those for the MINOS detector. We anticipate that we will be able to use essentially the same technology, reducing design costs and possibly resulting in cost savings if identical scintillator can be used. The veto scintillator will be arranged in a box made of 1500 rectangular extruded scintillator bars 6.5 m in length and 4 cm wide and 1 cm thick. The end bars will be 4 m in length by 4 cm wide by 1 cm thick. The scintillator bars will be co-extruded with a titanium oxide outer coating to improve the

light output. The narrow bars will allow for dense placement around support structures. The light generated in the bar will be brought out to photo-tubes using wave-shifting scintillating fibers.

Two wave-shifting fibers will pass through the entire length of each bar. Each end of these fibers will be read out by a separate photo-tube, to assure redundancy. A single photo-tube will detect the light from 20 fibers, resulting in only 300 photo-tubes in the entire system. Failure of a single photo-tube will not cause a hole in the veto system. Fibers from the top layer of bars will not share photo-tubes with fibers from the lower layer.

The MINOS group has made light yield measurements on a system similar to the one proposed. Measurements using 8 m long by 4 cm wide by 1 cm thick scintillator bars have achieved 7 photoelectrons for minimum ionizing particles passing through the center of the bar. The signal consisted of the sum of the photo-tube (Q.E.=12%) signals readout using 1 mm scintillating fibers readout from each end of the bar. The signal reached 12 photoelectrons at the end of the bar. Because MECO will use shorter scintillating bars, the average signal from the center of the bar is expected to be 8 photo-electrons. Other improvements, such as the use of the titanium oxide coating on the bar and the use of extended range photo-tubes (Q.E.=18%) can further improve the worst case signal to about 10 photoelectrons. However, in either case the photo-electron yield is more than adequate. With the goal of a system wide inefficiency of  $10^{-4}$ , a single layer inefficiency of  $10^{-2}$  is acceptable. A worse case signal level of 8 photoelectrons means the contribution of the scintillator inefficiency to the system inefficiency is less than  $10^{-3}$  per layer. Gaps between scintillating bars will be the dominant contribution to the inefficiency of a single layer if the bars in a given layer are not overlapped. Assuming gaps of 0.5mm, the single layer inefficiency will be  $\sim 10^{-2}$ . By staggering the gaps in the two layers the system inefficiency should be less than  $10^{-5}$ .

The cost estimate for this device has been based on that of the MINOS detectors. We have inflated individual item costs by 50% to account for higher prices due to the smaller quantity to be purchased.

### 3.11 MECO Expected Performance and Sensitivity

We first discuss the fraction of  $\mu$  captures in the timing window, to which the sensitivity is directly proportional. This fraction depends on the specific choice of the time structure of the pulsed beam as well as the distribution of  $\mu$  stopping times. We estimate this fraction for the scenario in which the pulse spacing is 1350 ns, corresponding to 2 bunches in the AGS revolution time. The accepted time window starts at 700 ns after the proton pulse hits the production target, or 650 ns after the time a particle moving at velocity  $c$  and traveling axially along the solenoids arrives at the stopping target. We assume the signal time window ends just before the arrival at the stopping target of velocity  $c$  particles from the next pulse moving with momentum along the transport solenoid axis. Figure 43 shows the  $\mu$  stopping time distribution relative to the proton arrival time at the production target. The average

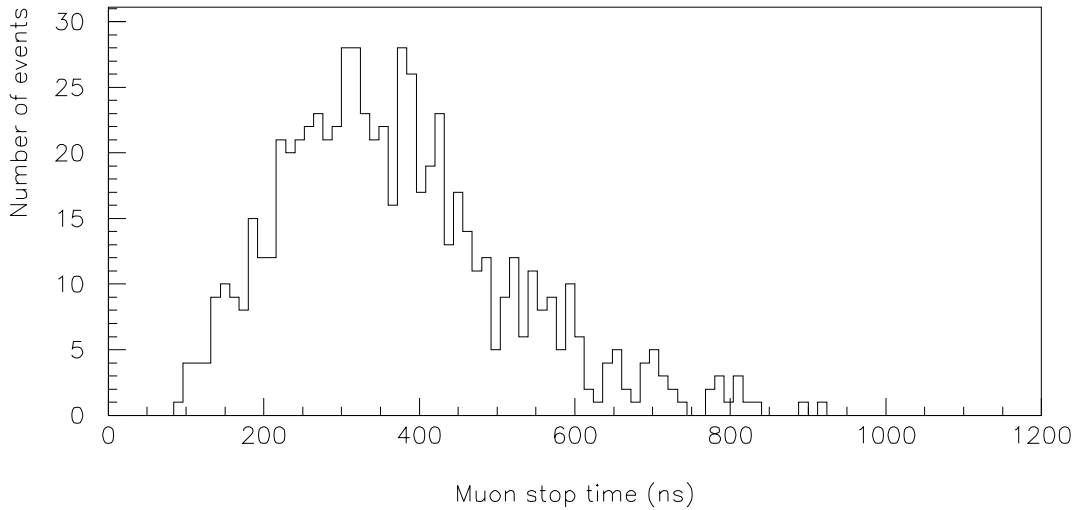


Figure 43: The distribution in the  $\mu^-$  stop time relative to the time when the proton beam impinges on the production target.

stop time is 370 ns. Using this distribution and a  $\mu^-$  lifetime in aluminum of 880 ns, we calculate the fraction of  $\mu^-$  captures in the detection time window to be 49%.

Other factors entering into the sensitivity are the running time, the proton intensity, the probability per proton that a  $\mu$  is produced, transported and stopped in the stopping target, the fraction of stops which capture (as opposed to decay), the trigger efficiency and the tracking acceptance. We have not included in this table loss of events due to accidental cosmic ray vetos, dead-time losses and losses due to straw chamber inefficiencies, all of which are expected to be small. The numerical values of the factors entering the sensitivity are given in Table 15. With one year ( $10^7$  s) running time with the AGS and experiment working,  $\sim 5$  events would be detected if  $R_{\mu e} = 10^{-16}$ .

Table 16 summarizes the expected background rates for the sensitivity quoted above. The backgrounds scale in different ways. We tabulate the backgrounds with the following assumptions. For  $\mu^-$  DIO and radiative  $\mu^-$  capture, the background scales with the number of captured  $\mu$ 's, and hence is directly proportional to the sensitivity. The background from pattern recognition errors is a strong function of the noise rate, which is most sensitive to

Table 15: The table summarizes the factors entering into the calculation of the expected MECO sensitivity for a one year ( $10^7$  s) run.

Running time [s]	$10^7$
Proton flux [Hz]	$4 \times 10^{13}$
Probability of $\mu/p$ transported and stopped in target	0.0025
$\mu$ capture probability	0.60
Fraction of $\mu$ which capture in time window	0.49
Electron trigger efficiency	0.90
Fitting and selection criteria (see table 8)	0.19
Detected events for $R_{\mu e} = 10^{-16}$	5.0

the rate of muon capture. It decreases rapidly with lower proton beam intensity. For cosmic ray backgrounds, we assume the sensitivity can be achieved in  $10^7$  seconds of data collection. This background is proportional to the total data collection time.

The background is dominated by electrons from muon DIO, which contribute a background/signal of 0.05 assuming  $R_{\mu e} = 10^{-16}$ . Substantial improvements in discrimination against this source of background can be made with modest loss in acceptance, as shown in Figure 26. For example, the background/signal ratio can be decreased from 0.05 to 0.02 with a relative loss in sensitivity of less than 10%.

The next three largest contributions are due to radiative  $\pi^-$  capture, beam electrons, and  $\mu^-$  decay in flight. These sources (and others identified with a \* in Table 16) are proportional

Table 16: A summary of the level of background from various sources, calculated for the sensitivity given in the previous table, and with scaling as discussed in the text. Backgrounds identified with a \* are proportional to the beam extinction and the numbers in the table assume  $10^{-9}$  extinction. The number of background events corresponds to a  $10^7$  second data collection period, yielding a sensitivity of 5 events for  $R_{\mu E} = 10^{-16}$ .

Source	Events	Comment
$\mu$ decay in orbit	0.25	signal/noise = 20 for $R_{\mu e} = 10^{-16}$
Pattern recognition errors	$< 0.006$	
Radiative $\mu$ capture	$< 0.005$	
Beam electrons*	0.04	
$\mu$ decay in flight*	$< 0.03$	without scatter in target
$\mu$ decay in flight*	0.04	with scatter in target
$\pi$ decay in flight*	$< 0.001$	
Radiative $\pi^-$ capture*	0.07	from protons during detection time
Radiative $\pi^-$ capture	0.001	from late arriving $\pi^-$
Anti-proton induced	0.007	
Cosmic ray induced	0.004	assuming $10^{-4}$ CR veto inefficiency
Total background	0.45	

to the proton beam extinction and we have assumed a value of  $10^{-9}$  for this parameter in calculating the backgrounds shown.

We conclude this section with some general comments about the proposed sensitivity. First, the muon yield is now rather closely tied to experimental measurements of pion production cross sections. The technical issues involved in getting the design beam intensity have not been proved by example, but involve relatively modest extrapolations in accelerator performance. We rely on calculations of the muon beam parameters, and to the extent possible, these use realistic beam parameters. Nonetheless, there is always the possibility that the design intensity may not be realized. The consequence of not reaching the design beam intensity is that we would achieve a worse sensitivity or we would run longer to achieve the proposal goals. The backgrounds scale with the sensitivity and are independent of the rate of data collection, with two exceptions. Backgrounds from pattern recognition errors scale as a power of the instantaneous intensity and will be smaller if beam fluxes are lower and the data are collected over a longer time. Cosmic ray backgrounds are proportional to the running time and are the only background source that would be adversely affected by longer running time to achieve the design sensitivity.

At the proposed sensitivity, the experiment is not expected to be limited by background. In addition, if backgrounds are higher than expected, many of them will be learned about early in the running when time is available to react. For example, if the detector rates are higher than expected, the background that is most sensitive to this (that from pattern recognition errors) can be substantially reduced with small changes in beam intensity since they scale as a power of the intensity.

Finally, while we believe that the proposed sensitivity can be achieved in the requested running time, even a result a factor 2-5 less than our goal is an extremely sensitive test of models that allow lepton flavor violation and would represent a tremendous improvement over current experiments.

### 3.12 Estimated Mecos Costs

We here summarize the expected cost of the MECO beam and apparatus, including engineering and design, construction or purchase, and installation. These cost estimates are preliminary and a baseline cost will be established following a technical review of the Project. At this stage, few of the items are costed with a bottoms-up algorithm and contingency has been included in the estimates either implicitly or explicitly. Some costs have changed from the budget presented to the Department of Energy in March 1999, and we discuss the reason for the significant changes at the end of this section. The costs are summarized in Tables 17 - 19.

The Project includes modifications to the AGS, modifications to the primary proton beam-line and construction of a muon beam-line, the experimental apparatus, and the associated infrastructure (shielding, counting room, etc.). Design costs include salaries of engineering personnel. The design may be done by a third party (for example the National High Magnetic Field Laboratory or a private company), by CAD personnel, or somebody at a collaborating Institution. Cost of purchased items includes components or parts of components. In some cases fabrication costs are separately broken out; they include the salaries of technical personnel hired for the specific purpose of constructing MECO apparatus. The cost of installation includes materials and supplies needed for the installation and the costs of personnel specifically hired by collaborating institutions (including BNL) for this purpose.

In general, salaries of physicists (faculty, postdocs, research physicists and graduate students) are not included in the costs (with the exception of the Project Manager). Some salary support for BNL physicists who are not collaborators but have specific design or oversight duties with respect to items being built at BNL are included. Salary costs are estimated including fringe benefits and applicable indirect charges. In the case of items built at BNL, indirect charges are also included on materials and supplies at a rate that averages about 30%. Significant cost savings may be realized by purchasing materials and supplies (parts of equipment) through our University groups.

Costs currently assumed to be spent at BNL are for items associated with AGS improvements, the primary proton beam-line, and installation costs for parts of the experiment. They are summarized in Table 17.

The only modification to the AGS required for MECO is the addition of the *internal kickers* in the AGS ring for the purpose of improving the extinction. This is a set of pulsed magnetic kickers with an associated power supply and control system. Their cost is estimated by RF experts in the CAD.

The *external kicker* in the proton beam-line is used to improve and allow measurements of the extinction. It consists of a resonantly driven (with a single 0.74 MHz sine wave activation and a Q of 2-300) magnetic kicker with a maximum transverse momentum kick of  $\pm 14$  MeV/c. The costs are estimated by CAD personnel. Costs to refurbish a *septum magnet* to further divert the beam between pulses is also included.

The *proton beam-line* requires several modifications. Included are refurbishing or replacing beam-line magnets, refurbishing the vacuum system, extending the beam-line to the new target station, constructing new beam line instrumentation, and new shielding. Costs associated with dismantling equipment currently occupying the new MECO area are included in this item, as are costs of refurbishing an existing  $\sim 2000$  square foot counting house.



Table 17: A summary of the estimated MECO costs for AGS improvements, primary proton beam, and some installation costs. The basis for the estimates is discussed in the text.

Item	Sub-item	Cost (\$/1000)	Cost (\$/1000)
Internal kicker	Design	100	942
	Purchased items	633	
	Fabrication and Installation	173	
	Contingency	36	
External kicker	Design	348	1906
	Purchased items	696	
	Fabrication and Installation	620	
	Contingency	242	
Septum magnet	Design	85	384
	Purchased items	194	
	Fabrication and Installation	29	
	Contingency	76	
Proton beam-line	Design	762	3239
	Purchased items	1007	
	Fabrication and installation	822	
	Contingency	648	
Muon production target	Design	43	81
	Purchased items	17	
	Installation	5	
	Contingency	16	
Muon beam dump	Design	10	105
	Purchased items	72	
	Installation	2	
	Contingency	21	
CR concrete shield	Design	50	1007
	Purchased items	750	
	Installation	6	
	Contingency	201	
Total			7664

The *muon production target* is a radiation cooled tungsten cylinder of diameter 0.8 cm and length 16 cm. Design costs are for the target and support structure, including studies of surface preparations for improved emissivity and other means of reducing the operating temperature. The *muon beam dump* consists of copper and polyethylene in which muons that don't stop in the stopping target are absorbed. The *CR concrete shield* costs are for concrete shielding and preparation and installation of steel and concrete shielding around the detector solenoid. It is assumed that no shielding will be available for reuse.

Approximately half of the cost of this experiment is in the muon beam-line. These costs are summarized in Table 18.

The largest item is the system of *super-conducting solenoids*. We have used the estimate of the NHMFL for these items. For the coils, quotes were obtained by NHMFL from industry; we have taken the mean of these estimates for a 3.3 T maximum field, scaled it up to the cost of a 5.0 T maximum field by the stored energy and taken a 30% contingency. The *cryostat* and *assembly* cost is based on the NHMFL design and assembly procedure. An estimate was obtained by NHMFL from a company experienced in the assembly of large, complicated vacuum vessels. The estimate includes "industrial contingency" applied by the company. The design cost is estimated at  $\sim 10\%$  of the coil and cryostat cost. The total cost (coil, cryostat, design) is somewhat higher (when corrected for inflation) than a cost estimate based on scaling relationships [103] between the amount of stored energy and the cost. These scaling relationships were derived for thin coil magnets (typically spectrometer magnets). The system proposed is in some ways simpler (no need for thin coils) and in other ways more complex (with axially graded fields and sections of a torus). In any event, the estimate is within the range of systems of similar size that were used to derive the cost scaling relationships. Since the magnets are fully assembled in the cryostat before shipping to BNL, cost of the final *installation* at BNL is rather modest.

The cost of the *refrigerator system* is estimated by NHMFL from contacts with experts at Thomas Jefferson Laboratory. It is dominated by the cost of the cold box and compressors. *Assembly and installation* costs are also estimated by these experts.

The *heat shield* is a cylindrical shell of copper and tungsten that is used to protect the production solenoid from particle spray. It is designed to reduce radiation and heat loads on this solenoid to safe levels for operation over the lifetime of the experiment. Also included in this category are the *muon beam collimators* that are integrated into the transport solenoid and the *muon beam vacuum*.

The last broad cost category is the system of particle detectors and related items; these costs are summarized in Table 19. Contingency has been taken at levels from 0-30%, averaging 18%.

The *extinction monitor* includes relatively straightforward charged particle detectors and counting electronics that is required to monitor the primary beam flux between pulses. The estimate includes the detectors and associated electronics. The *muon stopping target* is the set of thin aluminum target disks in which muons stop. The *detector solenoid proton shield* is the set of absorbers designed to attenuate protons that exit the stopping target and that would otherwise impinge on the tracking detectors. We estimate the cost of *magnet mapping* equipment that would be used to measure the field map in the region of the tracking solenoid and also measure the axial component of the field along the transport solenoid.

Detector costs have been estimated with varying degrees of sophistication; essentially all

Table 18: A summary of the estimated MECO costs for the super-conducting solenoids and related equipment. The basis for the estimates is discussed in the text.

Item	Sub-item	Cost (\$/1000)	Cost (\$/1000)
Super-conducting solenoids	Design	1300	16600
	Coils	5100	
	Cryostats, coil supports	8000	
	Assembly	2000	
	Installation	200	
Refrigerator system	Design	350	5120
	Purchased items	3500	
	Assembly and installation	500	
	Contingency	770	
Power supply, quench protection	Purchased items	500	600
	Contingency	100	
Heat shield	Purchased items	700	900
	Contingency	200	
Muon beam collimators	Design	30	120
	Purchased items	40	
	Fabrication	20	
	Contingency	30	
Muon beam vacuum	Design	20	240
	Purchased items	150	
	Fabrication	20	
	Installation	10	
	Contingency	40	
Total			23580

of them are based on costs of systems with similar requirements, size and complexity. None of the individual items is beyond the state of the art in either particle detector or electronics technology. In general, costs include design, materials, and fabrication. In essentially all cases there will be contributions to the design, construction, and testing of the apparatus from physicists in the collaboration and the salaries of these personnel are not included in the costs. Design costs are based on estimated engineering salaries of a person to be employed at a collaborating Institution and are taken at \$120k per year including benefits and indirect charges. Installation is costed separately. We separate out the cost of detector components

Table 19: A summary of the estimated MECO costs for the experimental equipment and related items. The basis for the estimates is discussed in the text.

Item	Sub-item	Cost (\$/1000)	Cost (\$/1000)
Extinction monitor			80
Muon stopping target			35
	Design	20	
	Parts and fabrication	10	
	Contingency	5	
Detector solenoid $p$ shield			80
	Design	30	
	Purchased items	50	
Magnet mapping			150
	Design	30	
	Parts and fabrication	120	
Tracking detector			560
	Design	240	
	Purchased items	240	
	Fabrication	80	
Tracking electronics			2440
	Design	240	
	Purchased items	2200	
Electron calorimeter			2120
	Design	120	
	Purchased items	1900	
	Fabrication	100	
Electron calorimeter electronics			300
	Design	120	
	Purchased items	180	
Cosmic ray passive shield steel			705
Cosmic ray active shield			310
	Design	60	
	Purchased items	200	
	Fabrication	50	
CR active shield electronics			135
	Design	60	
	Purchased items	75	
Trigger electronics			200
	Design	120	
	Purchased items	80	
Data acquisition system			270
	Design	120	
	Purchased items	150	
Online computing			300
	Design		
	Purchased items	300	
Project manager			360
Installation costs			200
Contingency			1370
Total			9615

(including the photo-detectors) from that of the electronics. The latter includes costs of cabling, front end, and digitizing electronics.

The *tracking detector* costs are loosely based on those of the E871 straw tracking system. There are fewer channels in the current system, but the straws are longer and their operation in vacuum and the requirement of low mass end fittings will increase costs per channel. We assume 2 man-years of engineering will be required for the design of the straw system, its mounting hardware, and the gas control system.

We have costed the *tracking electronics* based on using multi-hit TDC's on each anode signal and flash ADC's on both the anode signals and the pads. We assume a total system cost of \$100 (plus 30% contingency) per signal. The total channel count is  $\sim 6000$  for the  $\sim 3000$  anode signals and  $\sim 16000$  for the pad readout. Hits will be recorded for  $\sim 150$  ns. The requirements on the precision of both the time and charge measurements are very modest. We assume 2 person-years of engineering for the design of these electronics. Similar electronics systems have been used in many experiments with trigger rates and bandwidth requirements similar to that of MECO.

The *electron calorimeter* cost is very dependent on the technology chosen. In the case of a plastic scintillation counter trigger, costs are dominated by the scintillator and the photo-detectors and we have based the cost on quotes from vendors for the materials. Table 19 gives the cost of the crystal calorimeter and electronics. It is dominated by the crystal cost. The difference in cost of the two systems (including electronics) is  $\sim \$1.5$ M. The choice of device to be built will follow more R&D including better simulations of the neutron flux and means of reducing that flux and further understanding of the benefits of and need for the improved energy resolution provided by the crystal calorimeter. The *electron calorimeter electronics* is costed at \$100 per channel plus contingency.

The *cosmic ray passive shield steel* cost is for steel shielding. Installation costs are budgeted separately. The *cosmic ray active shield* cost is estimated based on information from MINOS, which will use similar large area planar scintillator arrays with WLS fiber readout. We include the cost of the scintillator modules, support structure, and photo-detectors. The *CR active shield electronics* will have time and pulse-height measurements on each channel and we have used the same cost per channel as for the electron calorimeter electronics. We assume the design will largely overlap with that of the electronics for the electron calorimeter.

The *trigger electronics* will include custom and commercial fast electronics to form energy sums and trigger signals. This item does not include any data acquisition or higher level trigger system that uses computers.

The *data acquisition system* cost include that of the bus system in which the ADC's and TDC's are housed, the controls, buffer memories, etc. It is anticipated that this system will be rather straightforward, since even in the worst case the data rates are rather low. We separately include costs of *online computing* that is likely to be integrated with the data acquisition system.

*Installation costs* include charges for rigging and other personnel to aid the collaboration in the installation of the detectors. This does not include costs of installation of the cosmic ray passive shield. The salary of a *Project Manager* is included. This person could be employed either at a University or at the Laboratory. This is a full time position with responsibilities only associated with the MECO Project Management.

This current cost estimate is somewhat larger than that presented in March 1999 to the

Department of Energy. The net change can be nearly completely accounted for in terms of inclusion of a number of small items previously omitted, not reusing some accelerator related items, different assumptions about recapturing manpower costs from operating, and rescoping to improve the experiment. The changes that account for the cost differences are itemized below.

In the primary beam-line, the biggest change is in the cost of the kickers, where we now cost both an internal kicker and an external kicker and septum magnet. The cost of the internal kicker has gone down by \$1.7M after engineering costing. We currently cost both an internal and external kicker, and the net change is (+\$0.6M). There are likely to be further cost savings on this, since no cost optimization has been done in purchased items. For example, the cost of broad-band RF power amplifiers has been used, and contacts with amplifier manufacturers indicate that the narrow band amplifiers we need should be significantly less expensive. The total cosmic ray shielding cost has increased significantly since it is now assumed that all new material will be used (+\$1.0M) and a substantial cost savings could be realized if shielding is reused. Other items are essentially unchanged with the exception that all labor costs are now charged; previously some charges had been recaptured from operating (+\$1.6M).

In the secondary muon beam, the cost of the solenoids and installation has gone up (+\$2.6M) based on estimate from the NHMFL. The base cost is up, but with a larger maximum field in the production solenoid and no need for a return yoke except for the steel in the cosmic ray shield. We carry similar contingency. We now cost a new refrigerator of larger capacity, but that cost has gone down (-\$0.4M) and has a smaller contingency (20% vs 25%). We are informed that a large capacity (>4 kW) refrigerator, surplus from SSC, is at BNL and we are exploring the possibility of using it, which would probably result in significant savings. The heat shield cost has increased (+\$1M) due to including some tungsten to reduce the heat and radiation load on the cold mass. We have added the cost of collimators in the muon beam (+\$0.1M) and the muon beam vacuum cost is slightly reduced.

For the detector section, we now explicitly include the salary of a Project Manager (+\$0.36M). The largest change is that the baseline electron calorimeter now uses crystals rather than plastic scintillator (+\$1.6M). As discussed above, the choice of calorimeter technology has not been made and this cost savings may ensue. An equally large change is in the tracking electronics, where the cost has nearly doubled (+\$1.5M). This is due to a slightly lengthened tracker (25% longer) resulting in more pads, and the inclusion of electronics for pads on both sides of the vanes and octagon. The need for this redundancy in the axial coordinate readout is still under study and a cost savings of ~\$1.4M may ensue if only one layer of pads is instrumented. A third change is an increase in the cost of data acquisition and online computing (+\$0.25M). Increased online computing power will result in less off-line load and reduced analysis time. Finally, six items that did not appear in the earlier budget are now explicitly costed – the extinction monitor (+\$0.1M), the stopping target (+\$0.04M), the detector solenoid proton shield (+\$0.1M), the magnet mapping devices (+\$0.18M), the muon beam dump (+\$0.1M), and costs for installing experimental equipment (+\$0.2M).

The net change in total project cost is an increase of very close to \$10M. Of that, ~\$4.7M is scope change: adding a secondary extinction device, using a higher quality electron calorimeter, increasing the tracking detector electronic channel count, and increasing the strength of the production solenoid magnetic field. The need for and cost of the secondary

extinction device require some beam tests to quantify and we believe that cost will go down significantly. We believe the experiment would succeed with only slightly reduced sensitivity (or slightly increased running time) without the other three scope changes; they largely buy increased conservatism in background rejection and improved sensitivity per running time. The remaining \$5.3M increase in project cost derives largely from different assumptions about reusing shielding ( $\sim \$1.0\text{M}$ ), recapture of labor from operating budgets ( $\sim \$1.6\text{M}$ ), and increase in the solenoid cost other than that due to the increased field ( $\sim \$1.6\text{M}$ ) and savings may still ensue on at least some of these items.

Additional savings be realized by purchasing items or parts of items that are normally purchased at the laboratory (shielding, beam line devices, etc.) through the collaborating Universities and saving BNL indirect charges on materials and supplies that total more than \$1M.

### 3.13 MECO Schedule

There is a widely held and, in our view, correct impression that advances in sensitivity by orders of magnitude take a long time, perhaps 10 or more years. We first review the history of the MECO project till the present and then discuss the proposed schedule for completing it. We believe an aggressive schedule of R&D, construction and data taking will allow the MECO collaboration to have sufficient data in hand by the end of FY2006 to achieve the goals of the experiment.

The MECO project began in 1995 with preliminary calculations of the sensitivity that could be achieved in a  $\mu^- N \rightarrow e^- N$  experiment if a new muon beam and detector were built. A Letter of Intent was submitted to BNL and discussed by the Physics Advisory Committee in autumn 1996. A full proposal was submitted and approved by the Associated Laboratory Director for High Energy and Nuclear Physics in October 1997. The preparation of the proposal involved very extensive calculations and simulations of the expected performance of the experiment. In the two years since then, work has continued on these calculations and simulations along with intensive efforts to secure funding for the construction and running of the experiment. In addition, R&D on detectors, beam-lines, and accelerator operations was begun. These efforts were severely restricted by our inability to secure R&D funds and accelerator test time.

If this proposal is approved, we believe an additional 7 years will be required to complete the experiment through the stage of data taking. Our experience with similar experiments (E871 for example) leads us to believe that final results could be published within two years of completing data taking and possibly earlier. We anticipate that results at lesser sensitivity, but still representing a significant improvement on current experiments, would be published earlier. This schedule includes 2 years of engineering development beginning in spring 2000, 2.5 years of construction beginning in fall 2001, and 2.5 years of data taking beginning in spring 2004. This schedule meshes well with current plans for AGS operations for High Energy Physics, which are currently approved by the DOE through the end of FY03. This schedule is also consistent with DOE guidance on potential future support by DHEP for AGS operations, which discourages efforts requiring extended or open-ended running schedules.

To realize this schedule, it will be necessary to do most of the engineering development prior to FY02. We propose to do it by using resources from Collaboration operating grants, forward funding through Collaborating Institutions, and forward funding of R&D by the NSF. We estimate the total engineering manpower (in addition to physicists in the collaboration) required for detector R&D at 9 person-years or  $\sim \$1.1\text{M}$ . The design work for the solenoids and refrigerators is estimated at  $\$1.4\text{M}$  and for the various proton beam-line and AGS elements at 10 person-years or about  $\$1.8\text{M}$ . Much of that will be required in FY00 and FY01 and the Collaboration will pursue aggressively funds to support it as soon as this proposal is approved. We have already begun design work on the system of super-conducting solenoids using collaboration funds and we have the resources to continue that design work on a limited basis. We have had preliminary discussions between Collaboration group leaders and their Institution administrations and have identified  $\sim \$2\text{M}$  in forward funding that could be released as soon as the Project is approved. Our current guidance from the NSF is that they can forward fund R&D prior to the October 2001 formal start date of this Grant. Hence, we propose a schedule that assumes funds for R&D and construction will be available



when required, beginning as early as spring 2000.

In the beam line, we believe the critical path item is the system of super-conducting solenoids. National High Magnetic Field Laboratory personnel have estimated that the complete design work to produce engineering drawings for this system could be completed in 24 months given sufficient manpower, and pieces of it would be finished sooner. Presuming that work begins in April 2000, it could be completed by April 2002. NHMFL personnel have also estimated that an aggressive construction schedule could have the system of solenoids assembled and ready to begin commissioning 2.5 years after starting construction, by April 2004, assuming a construction start date of October 2001. This construction schedule would be less aggressive if some long lead-time items (the super-conducting cable, for example) could be ordered prior to October 2001.

The other potentially long lead time items in the beam-line are the internal and external kickers to improve the proton beam extinction. Early accelerator R&D is required to fully specify the requirements for these devices, and we will work to get that accelerator R&D time. Again, we will pursue opportunities for early funding of the design work for these devices.

For the detector, the part that is technically most challenging is the straw tracking detector with pad readout of the axial coordinate and operating in vacuum. The electronics for that system, including the cabling from the detector to the electronics is also challenging, given the necessity of low mass, reliable operation, and operation of parts of the electronics in vacuum. We believe it is very important to get the development of that system started as soon as possible. The detector component that currently has the largest cost uncertainty is the electron calorimeter. We anticipate a choice between the possible technologies could be made within 6 months of proposal approval, which would leave ample time for development. Construction time for the crystal version of this device will depend on delivery time for the crystals. We will explore whether detectors that will be decommissioned in the next year could provide crystals.

Beam-line and detector installation could be a potential critical path item. Again, the intent is to front-load as much of the rigging and assembly as possible, for example the reconfiguration of the primary beam-line and its shielding, the cosmic ray shield surrounding the detector solenoid, and clearing the space for the new beam-line. Since the proposed location of the experiment uses a beam-line in there are no experiments planned between now and the start of construction, some forward-funding of the costs of these items would yield significant benefit, and we will work to get that funding.

A final important issue is that of the collaboration strength. We believe it is critical to strengthen the collaboration by adding additional strong University groups into it. We have been hampered in this respect by the uncertain future of the HEP program at BNL, which has also made it difficult for current collaboration members to commit resources to the experiment. Approval of this proposal should have a significant positive influence on our efforts in this regard.

## References

- [1] M. Roco and P. Grannis, Higgs Boson Discovery Prospects at the Tevatron, FERMILAB-Conf-99/118-E, 1999.
- [2] J. Konigsberg, Top and Higgs at the Tevatron: Measurements, Searches and Prospects, FERMILAB-Conf-99/129-E, 1999.
- [3] S. Holmes, Tevatron Performance Goals for the Coming Decade, FERMILAB-Conf-99/091-E, 1999.
- [4] L. Hall, The Heavy Top Quark and Supersymmetry, LBL-38110, hep-ph/9605258, 1996.
- [5] Y. Fukuda *et al.*, Phys. Lett. B **436**, 33 (1998).
- [6] Y. Fukuda *et al.*, Phys. Lett. B **433**, 9 (1998).
- [7] Y. Fukuda *et al.*, Phys. Rev. Lett. **81**, 1562 (1998).
- [8] Y. Fukuda *et al.*, Phys. Rev. Lett. **82**, 2644 (1999).
- [9] R. Barbieri and L. J. Hall, Phys. Lett. **B338**, 212 (1994).
- [10] R. Barbieri, L. Hall, and A. Strumia, Nucl. Phys. **B445**, 219 (1995).
- [11] J. Hisano *et al.*, Phys. Lett. **B391**, 341 (1997).
- [12] S. Dimopoulos and L. Hall, LBL 36269, 1994.
- [13] E. Commins *et al.*, Phys. Rev. **A50**, 2960 (1994).
- [14] R. N. Cahn and H. Harari, Nucl. Phys. **B176**, 135 (1980).
- [15] D. Ambrose *et al.*, Phys. Rev. Lett. **81**, 5734 (1998).
- [16] K. Arisaka *et al.*, Phys. Rev. Lett. **70**, 1049 (1993).
- [17] T. Akagi *et al.*, Phys. Rev. Lett. **67**, 2614 (1991).
- [18] P. Krolak *et al.*, Phys. Lett. B **320**, 407 (1994).
- [19] A. M. Lee *et al.*, Phys. Rev. Lett. **64**, 165 (1990).
- [20] U. Bellgardt *et al.*, Nucl. Phys. **B299**, 1 (1988).
- [21] M. L. Brooks *et al.*, *New limit for the family number nonconserving decay  $\mu^+ \rightarrow e^+ \gamma$* , Los Alamos preprint LA-UR-99-2268, submitted to Phys. Rev. Lett., 1999.
- [22] F. Riepenhausen, in *Proceedings of the Sixth Conference on the Intersections of Particle and Nuclear Physics*, edited by T. Donnelly (American Institute of Physics, New York, 1997), p. 34.

- [23] J. Steinberger and H. Wolfe, Phys. Rev. **100**, 1490 (1955).
- [24] M. Conversi *et al.*, Phys. Rev. **D122**, 687 (1961).
- [25] R. Sard *et al.*, Phys. Rev. **121**, 619 (1961).
- [26] G. Conforto *et al.*, Nuovo Cimento **26**, 261 (1962).
- [27] J. Bartley *et al.*, Phys. Lett. **13**, 258 (1964).
- [28] D. Bryman *et al.*, Phys.Rev. Lett. **28**, 1469 (1972).
- [29] A. Badertscher *et al.*, Nucl. Phys. **A377**, 406 (1979).
- [30] S. Ahmad *et al.*, Phys. Rev. **D38**, 2102 (1988).
- [31] C. Dohmen *et al.*, Phys. Lett. **B317**, 631 (1993).
- [32] G. Feinberg, Phys. Rev. 1482 (1958).
- [33] S. Weinberg and G. Feinberg, Phys. Rev. Lett. **3**, 111 (1959).
- [34] W. Marciano and A. Sanda, Phys. Rev. Lett. **38**, 1512 (1977).
- [35] M. Dine *et al.*, Phys. Rev. **D48**, 4269 (1993).
- [36] R. Djilkibaev and V. M. Lobashev, Sov. J. Nucl. Phys. **49(2)**, 384 (1989).
- [37] V. S. Abadjev *et al.*, *MELC Experiment to Search for the  $\mu^- A \rightarrow e^- A$  Process*, INR preprint 786/92, 1992.
- [38] M. Bachman *et al.*, *A Search for  $\mu^- N \rightarrow e^- N$  with Sensitivity Below  $10^{-16}$* , BNL AGS Proposal 940, 1997.
- [39] L. Barkov *et al.*, *Search for  $\mu^+ \rightarrow e^+ \gamma$  down to  $10^{-14}$  branching ration*, Research Proposal to Paul Scherrer Institut, 1999.
- [40] A. Badertscher *et al.*, Phys.Rev. Lett. **39**, 1385 (1977).
- [41] O. Shankar, Phys. Rev. **D20**, 1608 (1979).
- [42] A. Czarnecki, W. Marciano, and K. Melnikov, in *Workshop on Physics at the First Muon Collider and at the Front End of the Muon Collider*, edited by S. H. Geer and R. Raja (American Institute of Physics, Woodbury, N.Y., 1998), p. 409.
- [43] H. Herzog and K. Alder, Helvetica Physica Acta **53**, 53 (1980).
- [44] O. Shanker, Phys. Rev. D **25**, 1847 (1982).
- [45] T. Liu, meco- 038, University of California, Irvine (unpublished).
- [46] A. Frischknecht *et al.*, Phys. Rev. **C32**, 1506 (1985).

- [47] T. Stoudl *et al.*, Nucl. Phys. **A91**, 520 (1967).
- [48] R. Eramzhyan *et al.*, Nucl. Phys. **A290**, 294 (1977).
- [49] T. J. Liu, meco- 026, University of California, Irvine (unpublished).
- [50] O. Benhar, A. Fabrocini, S. Fantoni, and I. Sick, Nucl. Phys. **A579**, 493 (1994).
- [51] B. Cork *et al.*, Phys. Rev. **107**, 248 (1957).
- [52] A.Vaisenberg *et al.*, JETP Lett. **29**, 661 (1979).
- [53] B.Kopeliovich and F.Niedermayer, Phys. Lett. **B151**, 437 (1985).
- [54] R. Armenteros *et al.*, Phys. Rev. **119**, 2068 (1960).
- [55] G. J. Marmer *et al.*, Phys. Rev. **179**, 1294 (1969).
- [56] T. J. Liu, meco- 029, University of California, Irvine (unpublished).
- [57] M. Overlin, meco- 014, University of California, Irvine (unpublished).
- [58] R. Lee, meco- 017, University of California, Irvine (unpublished).
- [59] J. Sculli, meco- 039, New York University (unpublished).
- [60] W. Molzon, meco 006, University of California, Irvine (unpublished).
- [61] J. C. Gallardo, in *Beam dynamics and technology issues for mu+ mu- colliders. Proceedings, 9th Advanced ICFA Beam Dynamics Workshop, Montauk, USA, October 15-20, 1995* (American Institute of Physics, Woodbury, N.Y., 1996), p. 372.
- [62] R. Palmer *et al.*, Nucl. Phys. Proc. Suppl. **51A**, 61 (1996).
- [63] D. Armutliiski *et al.*, Hadron spectra in hadron - nucleus collisions, Prepring JINR P1-91-191, 1991.
- [64] R. Djilkibaev, meco- 009, University of California, Irvine (unpublished).
- [65] M. Bachman and R. Lim, meco- 016, University of California, Irvine (unpublished).
- [66] W. Molzon, meco- 008, University of California, Irvine (unpublished).
- [67] R. Brun *et al.*, *GEANT3*, 1984.
- [68] A. N. Zalikman and L. S. Nikitin, *Tungsten* (Moscow Press, ADDRESS, 1978).
- [69] W. Molzon, meco- 018, University of California, Irvine (unpublished).
- [70] T. J. Liu, W. Molzon, and R. Ostroumov, meco- 031, University of California, Irvine (unpublished).

- [71] S. VanSciver *et al.*, meco- 040, National High Magnetic Field Laboratory (unpublished).
- [72] S. VanSciver *et al.*, meco- 042, National High Magnetic Field Laboratory (unpublished).
- [73] N. Mukhopadhyay, Rep. Prog. Phys. **30**, 1 (1977).
- [74] T. Kozlowski, Nucl. Phys. **A436**, 717 (1985).
- [75] V. Balashov and R. Eramzhyan, Atomic Energy Reviews **5**, (1967).
- [76] Y.G.Budyashov, Soviet Physics JETP **33**, 11 (1971).
- [77] P.Singer, Springer tracks in Modern Physics **71**, 39 (1974).
- [78] S.Sobottka and E.L.Wolls, Phys. Rev. Lett. **20**, 596 (1967).
- [79] L.Vilgelmova *et al.*, Sov. J. Nucl. Phys. **13**, 310 (1971).
- [80] A. Wyttenbach *et al.*, Helv. Phys. Acta. **49**, 776 (1976).
- [81] D. Ambrose *et al.*, Phys. Rev. Lett. **81**, 4309 (1998).
- [82] A. S. Oh and W. Robertson, Nucl. Instrum. Meth. **A309**, 368 (1991).
- [83] L. Benussi *et al.*, Nucl. Instrum. Meth. **A419**, 648 (1998).
- [84] R. Cizeron *et al.*, Nucl. Instrum. Meth. **A307**, 286 (1991).
- [85] E. Barbarito *et al.*, Nucl. Instrum. Meth. **A381**, 39 (1996).
- [86] T. S. Shin *et al.*, Nucl. Instrum. Meth. **A332**, 469 (1993).
- [87] S. Majewski *et al.*, Nucl. Instrum. Meth. **348**, 307 (1994).
- [88] T. J. Liu, meco- 004, University of California, Irvine (unpublished).
- [89] S. Carabello and D. Koltick, meco- 015, Purdue University (unpublished).
- [90] S. Aota *et al.*, Nucl. Instrum. Meth. **A352**, 557 (1995).
- [91] A. Antonelli *et al.*, Nucl. Instrum. Meth. **A354**, 352 (1995).
- [92] G. M. E. Lorenz and H. Vogel, Nucl. Instrum. Meth. **A249**, 235 (1986).
- [93] Y. Kubota *et al.*, Nucl. Instrum. Meth. **A320**, 66 (1992).
- [94] R. J. Barlow *et al.*, Results from the BaBar Electromagnetic Calorimeter Beam Test, July 1998, sLAC-PUB-7887.
- [95] Silicon Photodiodes and Charge Sensitive Amplifiers for Scintillation Counting and High Energy Physics, 1997, hamamatsu Catalog.

- [96] J. Weber and R. Monchamp, Appl. Phys. **44**, 5495 (1973).
- [97] K. H. Kampert *et al.*, Nucl. Instrum. Meth. **A349**, 81 (1994).
- [98] T. B. Collaboration, Technical Design Report for the BaBar Detector, 1995.
- [99] K. Ueno *et al.*, *Detection of Minimum-Ionizing Particles and Nuclear Counter Effect with Pure BGO and BSO Crystals with Photodiode Read-out*, 1997, hep-ph/9704013.
- [100] G. Blamar *et al.*, Nucl. Instrum. Meth. **203**, 213 (1982).
- [101] R. Watanabe *et al.*, Atomic and Nuclear Data Tables **54**, 165 (1993).
- [102] O. Allkofer *et al.*, Phys. Lett. B **36B**, 425 (1971).
- [103] M. A. Green, R. A. Byrns, and S. J. S. Lorant, Adv. in Cry. Eng. **37**, (1992).

### 3.14 MECO Appendix 1 – NHMFL Magnet Design

Contract: New York University

meco-042

---

## Conceptual Design of the Muon-Electron Conversion Project (MECO) Magnet System Phase II, Final Report

*Steve Van Sciver*

[ynsciver@magnet.fsu.edu](mailto:ynsciver@magnet.fsu.edu)

*Søren Prestemon*

[Soren@magnet.fsu.edu](mailto:Soren@magnet.fsu.edu)

*Danny Crook*

[crook@magnet.fsu.edu](mailto:crook@magnet.fsu.edu)

*Yehia Eyssa*

[Eyssa@magnet.fsu.edu](mailto:Eyssa@magnet.fsu.edu)

## 1. Introduction

The National High Magnetic Field Laboratory has concluded a design study for the Muon-Electron Conversion Experiment (MECO) magnet system (see Figure 1). We present results for Phase II of the project, which include the following:

- A review of the magnetic field analysis together with an estimate of the influence of fabrication tolerances on the field profile and a discussion of possible winding techniques.
- A discussion detailing all key structural components, along with associated drawings. This includes magnet bobbins, cryostats, warm to cold links, and external support structures. The design allows for regular maintenance to the production and detector solenoids.
- An estimate of the thermal loads. Conduction and radiation loads are estimated for the complete structure, as well as refrigeration requirements for cooldown.
- A budget estimate, based on itemized material quantities and current industry prices.

The design is based on consideration of magnetic field quality and total system cost. We anticipate that the major cost associated with the project lies with the cryostat and support structure; the design we propose attempts to address the structural issues without compromising the field quality.

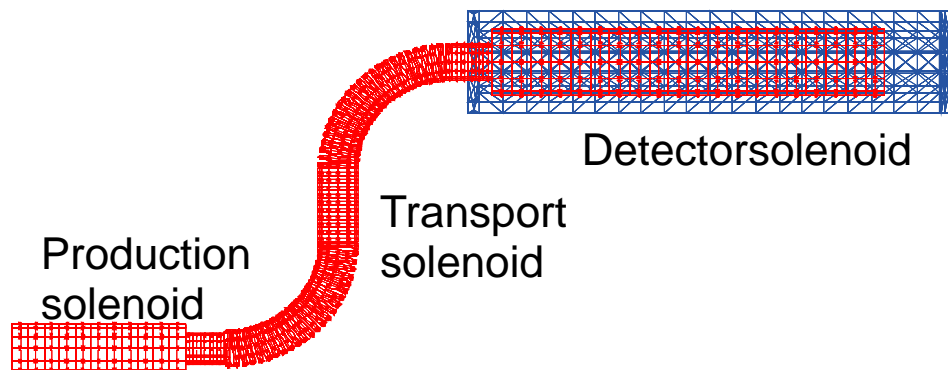


Figure 1. System of magnets with iron shielding around the detector, from the Vector Field model.



## 2. Magnetic Field Analysis and Coil Design

The phase I report shows that an iron neck on the cosmic ray shield would require a large number of trim coils to compensate for the local field influence. By replacing the neck with non-magnetic steel, the field-profile difficulty disappears, and the number of discrete coils proposed in that report is sufficient to yield the required profile along the complete beam path (see Figure 1 and Figure 4).

The winding method is different for each solenoid system. The transport coils will be individually wound, with the inner diameter and total Amp-turns stipulated at a fixed current for each coil so that they can be run in series. The radial builds of the magnets, assuming a current density of  $100 \text{ A/mm}^2$ , are shown in Figure 2. Coils that deviate dramatically from their neighbors in radial build imply that a finer discretization is required. Each of these coils will be replaced either by two or more thin coils, or a base coil accompanied by low-current trim coils.

We have estimated the design tolerance for radial and axial errors (see Figure 5); in our view they are not particularly stringent, which will keep the fabrication costs low. The production and detector solenoids will probably be wound directly on their cases, which we anticipate being of composite material to reduce weight and cost. There is some concern that radiation may damage epoxy in the composites in the production solenoid. The bobbin in that section could be made of aluminum or stainless steel, but every effort should be made to reduce the radiation impinging on the magnets. The total Amp-meters will be stipulated as a function of length along the solenoid in each case; the vendor will be free to choose the most economical means of actually winding the magnet. We feel that the production and detector solenoids must be wound directly on their cases due to their long lengths and large diameters. Individual magnets would need to be slipped over the case over large distances, resulting in tight fabrication tolerances and therefore a higher cost.

Calculations of the hoop stresses in the magnets show that no external structure is needed to support the windings. The calculation is based on a peak field of 3.3 T in the production solenoid, although we have also considered a 5 T scenario. Calculations with a peak field of 5 T show that some additional external structural support would probably be required. However we find that no significant complications arise from the higher field scenario.

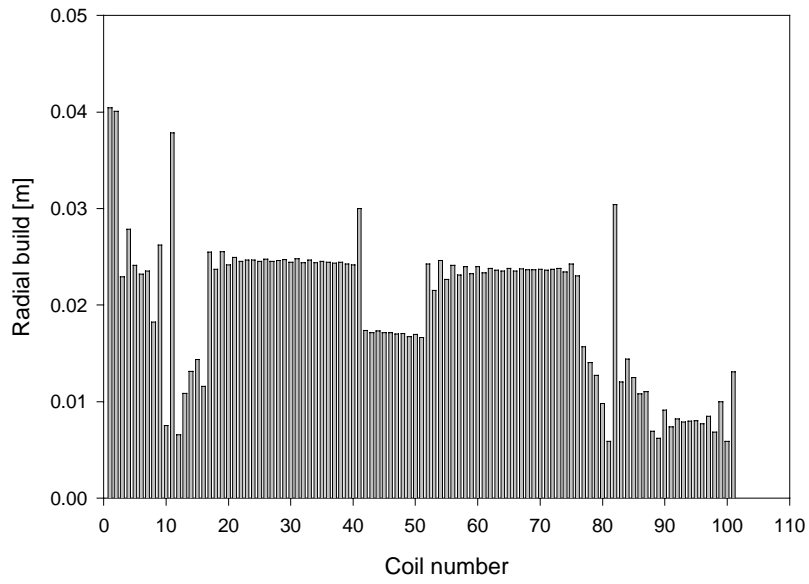


**Figure 2. Radial build of the magnets, based on a current density of 100 A/mm<sup>2</sup>.**

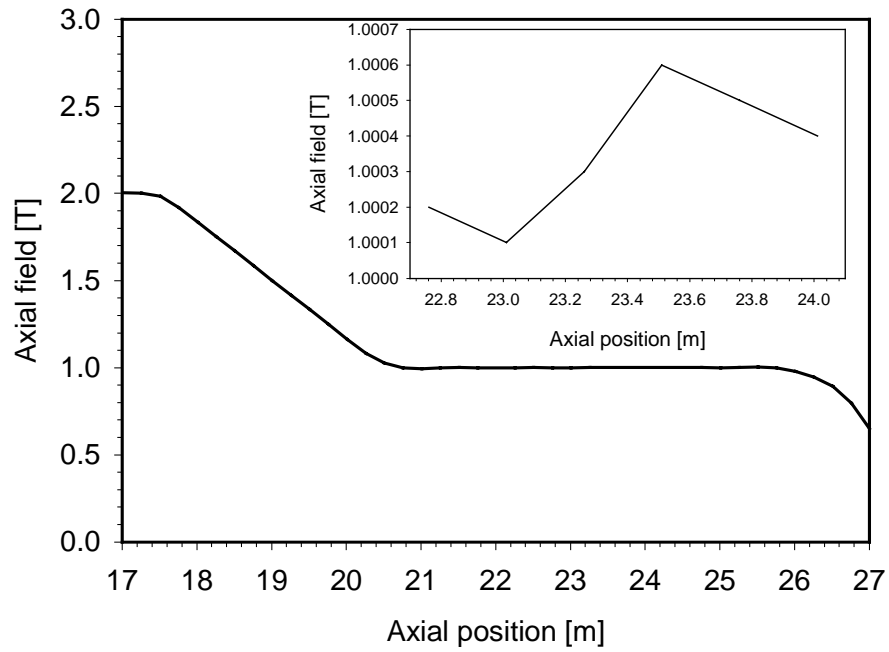


**Figure 3. Field quality in the detector solenoid.**

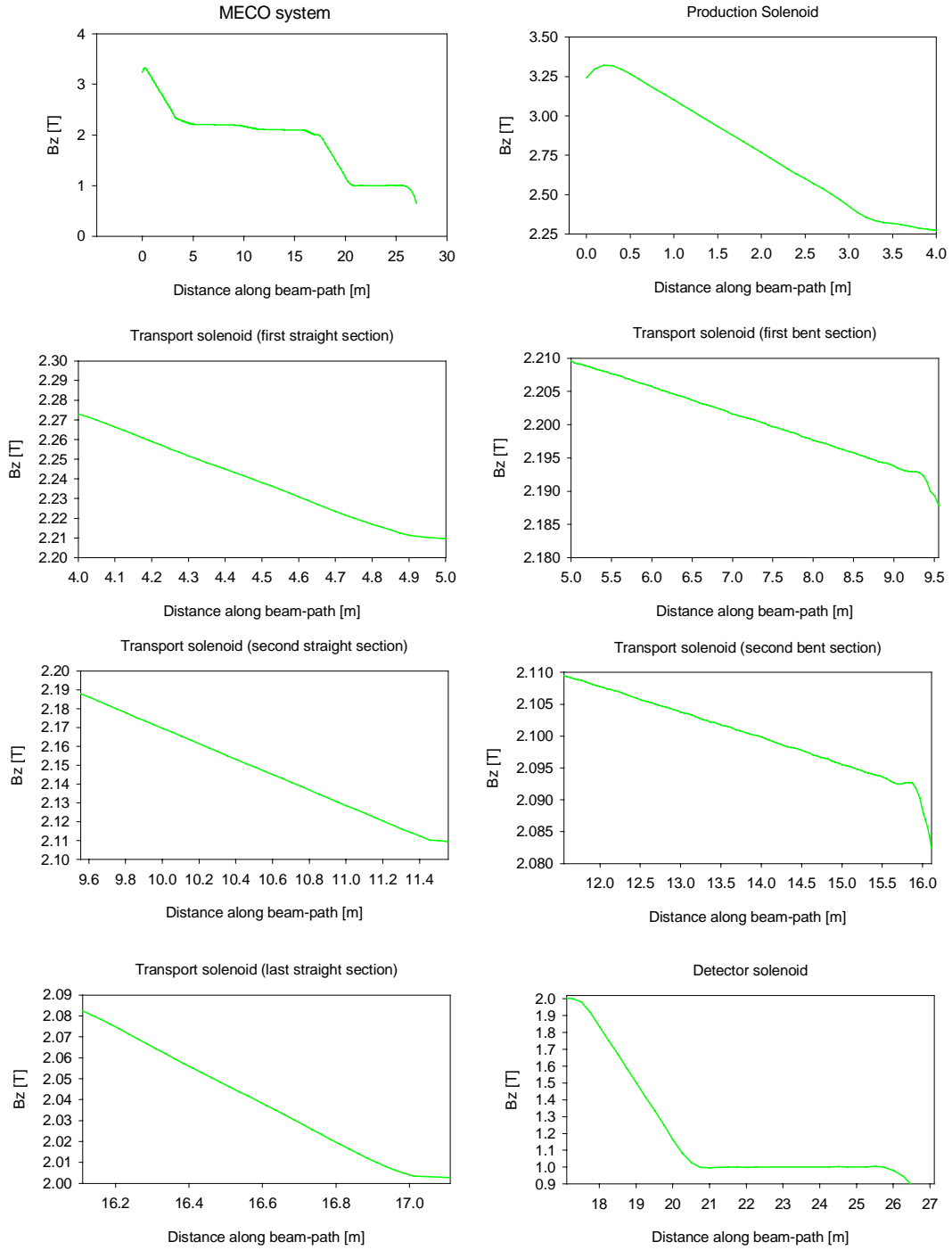


**Figure 4. Axial field along the beampath.**

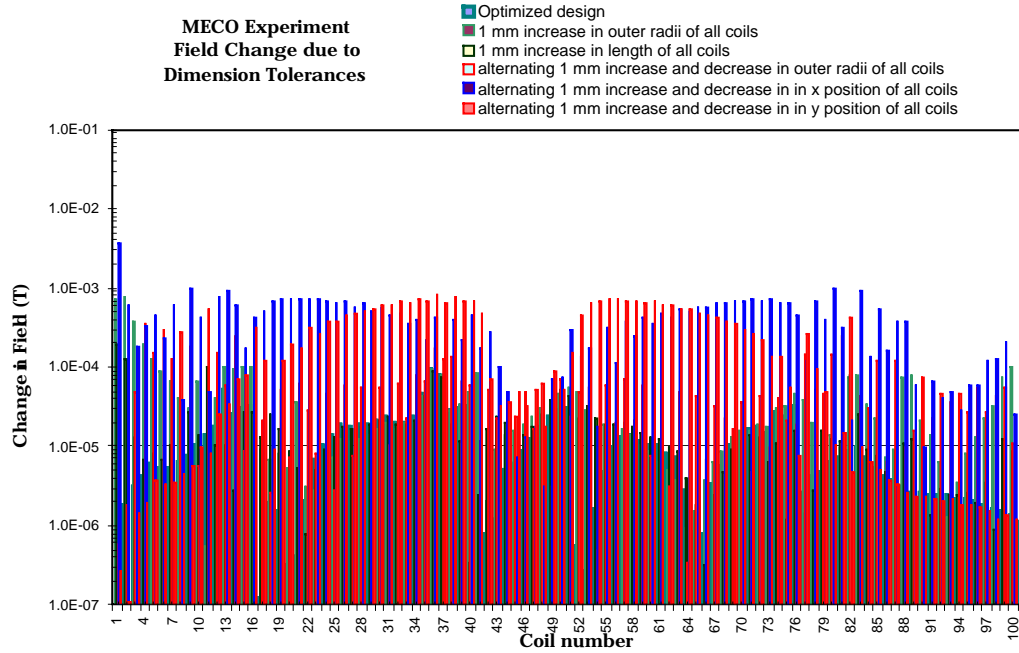
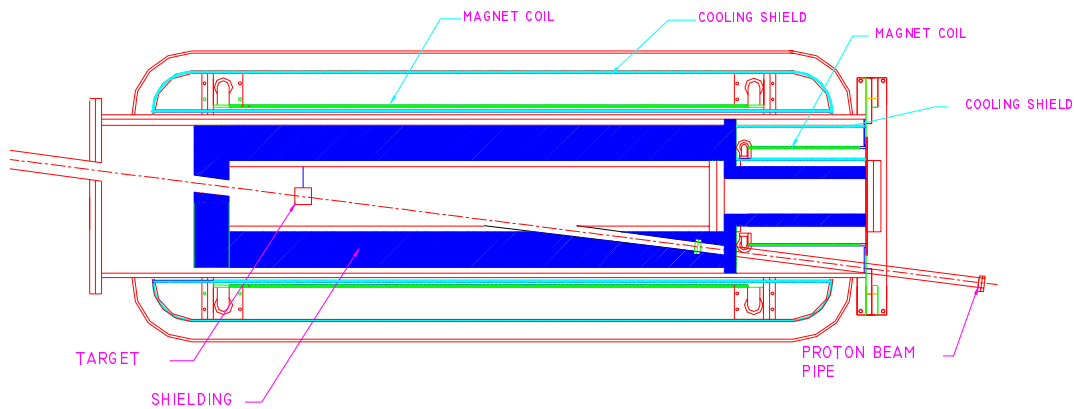


Figure 5. Effect of dimensional errors on field quality.

### 3. Structural considerations

The axial field profile is the critical design issue, and renders the project rather complex from a structural design perspective. Although the forces on the magnets (both from the Lorentz forces and weight) are not particularly large, numerous other elements must be supported inside the solenoid bores. The production solenoid must contain the 29 metric ton radiation shield. The transport solenoid contains collimators in each of the straight sections, and the detector solenoid contains the stopping target as well as the detector itself. Finally, throughout the whole system the uninterrupted warm vacuum tube must be supported.

The main difficulty from a structural design perspective is that no significant axial separation can be allowed between coils, or even between sections. The jumps in coil radii from one section to the next allow, however, for the introduction of warm structural supports without the introduction of axial spacings. The only coil separations that occur are in the bent sections. A view of the production solenoid is shown in Figure 6. Note the proton beam entering from the lower right; the tungsten target is located at the point where the proton beam crosses the axis of the production solenoid. Access to the target is from the front (left) via a flange. A cross sectional view is provided in Figure 7. The load transfer from the inner vacuum vessel and the radiation shield to the outer vacuum vessel is rather straightforward on the left. On the right, the load can also be brought out by the inner cryostat vacuum wall, since sufficient space exists between the inner bore of the



**Figure 6. The production solenoid, with the radiation shield, magnet, and cryostat. The proton beam enters from the bottom right and exits to the upper left. The transport solenoid attaches to the right.**

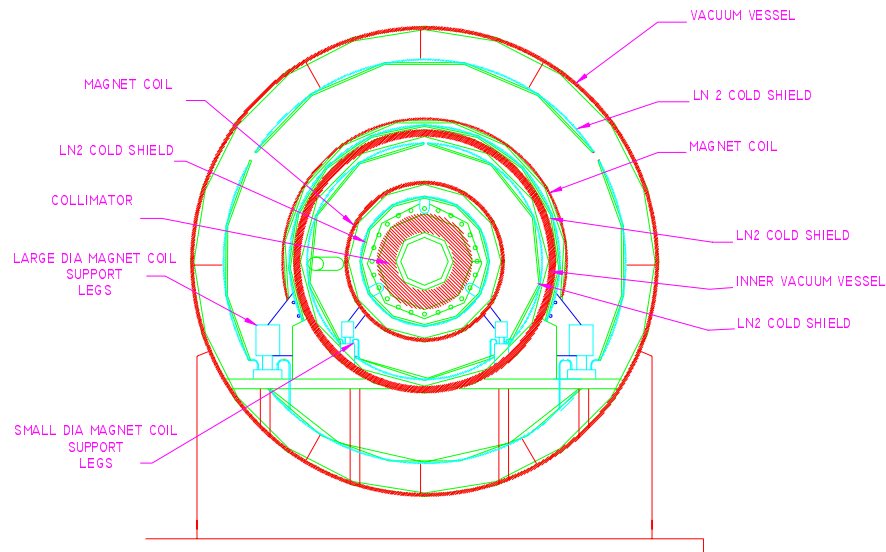


**Figure 7. Section of the production solenoid and coupling to the transport solenoid.**

production solenoid and the outer bore of the transport solenoid for two distinct cryostats. The weight of the cold materials (coils and their supports) as well as the Lorentz forces, which in the production solenoid act largely to the right (essentially in the direction of the detection solenoid), are transferred to the outer vacuum vessel through G10 supports.

The fact that the coils in the bent sections fan out implies that space is available for structural components to pass from the inner vacuum tube to the outer vacuum vessel without direct contact to cold members. Since the first straight section in the transport solenoid is rather short, the inner vacuum tube, as well as the collimator located within it,

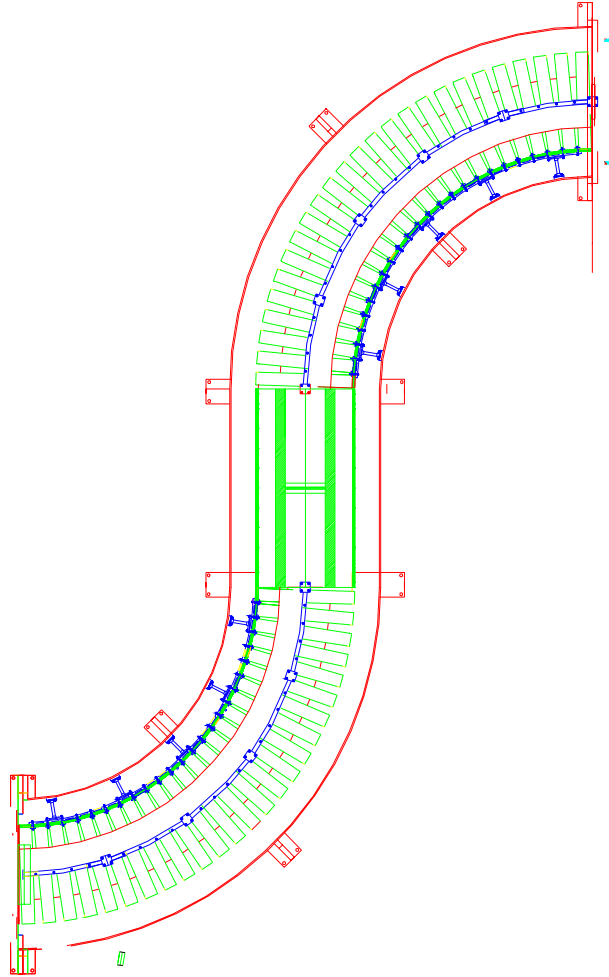


**Figure 8. Top view of the transport solenoid, with a 90° cutout.**

can be supported on the left by structure connecting it to the inner cryostat wall of the production solenoid, and on the right by the structural components in the bent section (see Figure 7 and 8). Similarly, the inner vacuum vessel and collimator in the center straight section of the transport solenoid are supported by the nearest structural supports in the bent solenoid sections.

The detector solenoid poses a structural problem due to its sheer size, and the fact that the coils must be adjacent to one another throughout its length due to field quality requirements. As in the production solenoid, the weight of the inner vacuum vessel and the detectors must therefore be carried from the ends (see Figure 9). All cold structure will be secured using direct warm-cold links on the left, with all degrees of freedom secured in order to minimize the transmission of Lorentz-forces from the detector solenoid to the transport solenoid. On the right, the axial degree of freedom is not fixed;

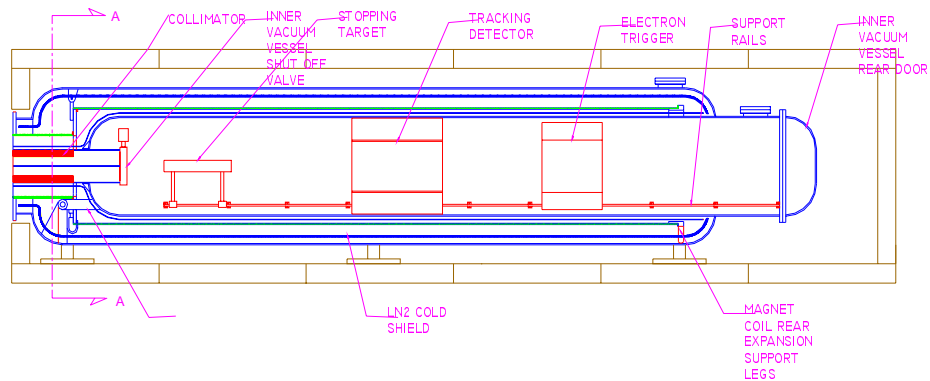


**Figure 9. Side view of the detector solenoid.**

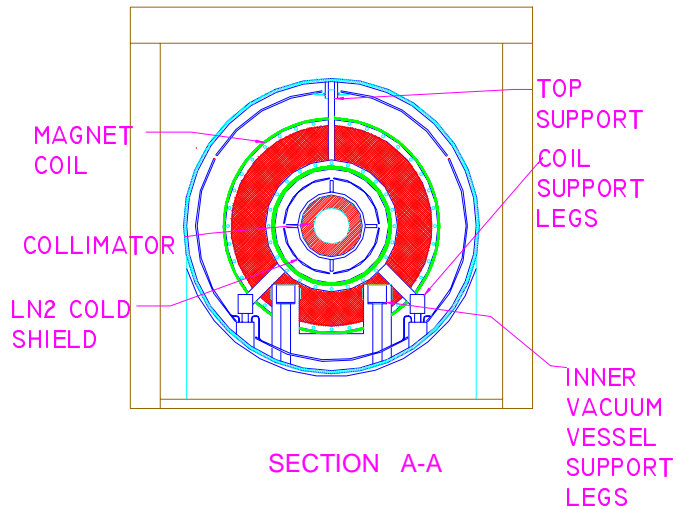


**Figure 10. Cross-section of the coupling from the transport solenoid to the detector solenoid.**

during cooldown the cold structure will contract, with the right end of the cold mass shifting by as much as 4 cm to the left. The use of a composite coil form has the double advantage of reducing weight while allowing us to tailor the thermal coefficient of expansion to yield cooldown deformation similar to that of the magnets. The transmission of forces and the coupling of the detector solenoid to the transport solenoid is clarified in Figure 9.

#### **4. Refrigeration requirements**

Heat loads due to conduction through the warm-to-cold links are estimated to be quite small, at 3 W at 4.2 K and 170 W at 80 K. Radiation loads are more significant, with 110 W at 4.2 K and 2300 W at 80 K. The internal energy associated with cooling the entire structure is calculated to be 8.3 GJ. Based on these estimates, we project that a refrigerator capacity of 1.2 kW at 4.2 K should be sufficient for a cooldown in less than 30 days, and would be quite capable of sustaining the system during operation.

#### **5. Cost estimation**

The cost of the entire system components is itemized as follows.

- For the cryostat structure, the material masses were estimated and \$/kg prices associated to them based on quotes from industry. Composite material (e.g. G10) are calculated at a rate of \$55/kg. Stainless steel is priced at \$35/kg. These values are scaled to take into account material and fabrication costs. The cryostat cost is estimated at 3.0 M\$.
- The magnet cost is based on quotes from industry as well as experience gained from other large magnet projects and scaled according to the project dimensions. We estimate the cost of the magnets to be 7 M\$. In the case of a peak field of 5 T in the production solenoid, the increase in magnet size and structural complexity leads to a scaled magnet cost of 8.5 M\$.
- The power system, including power supplies and protection systems, is estimated to total \$500,000.
- The refrigerator system, together with controls, is estimated at 3 M\$.

The total base estimate (3.3 T scenario) for the MECO system is 13.5 M\$. A 20% contingency yields a final system estimate of 16.2 M\$. The estimate covers the material and manufacture cost of the complete system as itemized above. It does not include installation costs at Brookhaven National Laboratory, nor does it include costs associated with engineering design.



## 4 KOPIO - a search for $K^0 \rightarrow \pi^0 \nu \bar{\nu}$

I-H. Chiang, J.W. Glenn, V. Jain, D. Lazarus, K. Li,  
L. Littenberg<sup>2</sup>, G. Redlinger, R. Strand  
Brookhaven National Laboratory

K. Kinoshita  
University of Cincinnati

G. Atoyan, M. Grigoriev, V. Issakov, A. Ivashkin, M. Khabibullin,  
A. Khotjanzev, Y. Kudenko, O. Mineev, A. Poblaguev  
INR, Moscow

T. Nomura, N. Sasao  
Kyoto University

M. Blecher, M. Pitt, B. Vogelaar  
Virginia Polytechnic Institute & State University

B. Bassalleck, N. Bruner, D.E. Fields, J. Lowe, T.L. Thomas  
University of New Mexico

M. Ito  
Thomas Jefferson National Accelerator Facility

E. Blackmore, D. Bryman<sup>2</sup>, M. Hasinoff, A. Konaka,  
J. Macdonald, T. Numao, R. Poutissou, G. Smith  
TRIUMF/UBC

S.K. Dhawan, H. Kaspar, S. Pislak, M.E. Zeller<sup>2</sup>  
Yale University

P. Truöl  
University of Zurich

---

<sup>2</sup>co-spokesperson

## 4.1 Introduction

At the present time CP violation is recognized to be one of the most important outstanding issues in the study of elementary particle physics. It is being vigorously attacked in the  $B$  sector by existing experiments such as CDF at the Fermilab Tevatron Collider and new ones constructed specifically for this purpose, including BaBar at SLAC's PEP-II, BELLE at KEKB, and HERA-B at DESY. The KOPIO component of the RSVP project proposes to add a new dimension to this world wide effort: a measurement of direct CP violation in the  $K$  sector via the decay  $K_L^0 \rightarrow \pi^0 \nu \bar{\nu}$ .

The single most incisive measurement in the study of CP violation is that of the branching ratio for  $K_L^0 \rightarrow \pi^0 \nu \bar{\nu}$  ( $B(K_L^0 \rightarrow \pi^0 \nu \bar{\nu})$ ). Using current estimates for Standard Model (SM) parameters, it is expected to lie in the range  $(3.1 \pm 1.3) \times 10^{-11}$  [1]. In the SM this branching ratio is unique in that it directly measures the area of the CKM unitarity triangle, i.e. the physical parameter that characterizes CP violation.

The  $\pi^0 \nu \bar{\nu}$  decay mode is also unique in that it is completely dominated by direct CP violation [2] and is entirely governed by short-distance physics involving the top quark. Theoretical uncertainties are extremely small because hadronic effects can be extracted from the well measured decay  $K^+ \rightarrow \pi^0 e^+ \nu$ . Thus its measurement will provide the standard against which all other measurements of CP violation will be compared, and even small deviations from the expectation derived from other SM measurements will unambiguously signal the presence of new physics.

The experimental aspects of measuring  $B(K_L^0 \rightarrow \pi^0 \nu \bar{\nu})$  are quite challenging. The mode is a three body decay where only a  $\pi^0$  is observed. There are competing decay modes which also yield  $\pi^0$ s, but whose branching ratios are millions of times larger. And observing a decay mode with a branching ratio on the order of  $3 \times 10^{-11}$  requires a prodigious number of kaons in order to achieve the desired sensitivity. Because the measurement is so challenging a detection technique must be developed that provides maximum possible redundancy for this kinematically unconstrained decay, that has an optimum system for insuring that the observed  $\pi^0$  is the only observable particle emanating from the  $K_L^0$  decay, and that has multiple handles for identifying possible small backgrounds that might simulate the desired decay mode. It is with these issues in mind that the KOPIO experiment has been designed.

The KOPIO technique employs a low energy, time structured  $K_L^0$  beam to allow determination of the incident kaon momentum. This intense beam, with its special characteristics, can be provided by the BNL AGS. Utilizing low momentum also permits a detection system for the  $\pi^0$  decay photons that yields a fully constrained reconstruction of the  $\pi^0$ 's mass, energy, and, momentum. As is shown in this proposal, these features provide the necessary redundancy and checks mentioned above. The system for vetoing extra particles is also well understood since it is based on experience with a previous experiment, BNL E787, which successfully contended with particles in the same energy domain.

The goal of KOPIO is to obtain about 60 events with a signal to background ratio of 2:1. This will yield a statistical uncertainty in the measurement of the area of the CKM unitarity triangle of less than 10%.

In what follows, the theoretical motivation (Section 4.2), experimental overview (Section 4.3), accelerator and beam (Sections 4.4 and 4.5), detector (Sections 4.6 to 4.11), background and sensitivity (Sections 4.12 to 4.14), R&D (Section 4.15), and costs (Section 4.16) are

presented.

## 4.2 $K_L^0 \rightarrow \pi^0 \nu \bar{\nu}$ – Theoretical Motivation

### 4.2.1 Standard Model

Understanding the phenomenology of quark mixing and CP violation is currently one of the central goals of particle physics. Examining the CKM ansatz of the Standard Model (SM) through precise determination of its basic parameters, several of which are poorly known at present, is crucial. To assure a clear interpretation of experimental results, the ideal observable must not only be sensitive to fundamental parameters, but must also be calculable with little theoretical ambiguity.

The rare decay  $K_L^0 \rightarrow \pi^0 \nu \bar{\nu}$  is unique among potential SM observables; it is dominated by direct CP violation [2] and is entirely governed by short-distance physics involving the top quark (for general reviews see [3, 4]). Long distance effects have been shown to be negligible [5]. Theoretical uncertainties are extremely small because the hadronic matrix element can be extracted from the well measured decay  $K^+ \rightarrow \pi^0 e^+ \nu$ , where small isospin breaking effects have been calculated. Since the dominant uncertainty due to renormalization scale dependence has been practically eliminated by including next-to-leading QCD corrections, the remaining theoretical uncertainty for  $B(K_L^0 \rightarrow \pi^0 \nu \bar{\nu})$  is reduced to  $O(1\%)$ .

$K_L^0 \rightarrow \pi^0 \nu \bar{\nu}$  is a flavor-changing neutral current (FCNC) process that is induced through loop effects in the Standard Model. The leading electroweak diagrams are shown in fig. 1. The expression for the  $K_L^0 \rightarrow \pi^0 \nu \bar{\nu}$  branching ratio can be written as

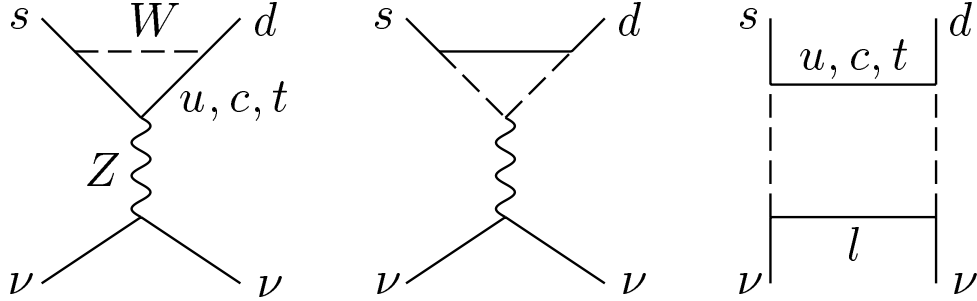


Figure 1: The leading electroweak diagrams inducing  $K_L^0 \rightarrow \pi^0 \nu \bar{\nu}$ .

$$B(K_L^0 \rightarrow \pi^0 \nu \bar{\nu}) = r_{IB} \frac{B(K^+ \rightarrow \pi^0 e^+ \nu)}{|V_{us}|^2} \frac{\tau(K_L^0)}{\tau(K^+)} \frac{3\alpha^2}{2\pi^2 \sin^4 \Theta_W} [Im(V_{ts}^* V_{td}) X(x_t)]^2 \quad (3)$$

where

$$X(x) \equiv \eta_X \cdot \frac{x}{8} \left[ \frac{x+2}{x-1} + \frac{3x-6}{(x-1)^2} \ln x \right] \quad \eta_X = 0.985 \quad (4)$$

and  $x_t = m_t^2/M_W^2$ . Here the appropriate top quark mass to be used is the running  $\overline{MS}$  mass,  $m_t \equiv \bar{m}_t(m_t)$ , which is related by  $\bar{m}_t(m_t) = m_t^*(1 - 4/3 \cdot \alpha_s(m_t)/\pi)$  to the pole mass  $m_t^*$  measured in collider experiments. With this choice of mass definition the QCD correction factor is given by  $\eta_X = 0.985$  and is essentially independent of  $m_t$  [6]. The coefficient

$r_{IB} = 0.944$  summarizes the leading isospin breaking corrections in relating  $K_L^0 \rightarrow \pi^0 \nu \bar{\nu}$  to  $K^+ \rightarrow \pi^0 e^+ \nu$  [7].

$K_L^0 \rightarrow \pi^0 \nu \bar{\nu}$  is driven by direct CP violation due to the CP properties of  $K_L$ ,  $\pi^0$  and the relevant short-distance hadronic transition current. Since  $K_L^0$  is predominantly a coherent, CP odd superposition of  $K^0$  and  $\bar{K}^0$ , only the imaginary part of  $V_{ts}^* V_{td}$  survives in the amplitude. Since the value of the sine of the Cabibbo angle is well known ( $|V_{us}| = \lambda = 0.2205$ ), this quantity is equivalent to the Jarlskog invariant,  $\mathcal{J} \equiv -\text{Im}(V_{ts}^* V_{td} V_{us}^* V_{ud}) = -\lambda(1 - \frac{\lambda^2}{2})\text{Im}(V_{ts}^* V_{td})$ .  $\mathcal{J}$ , in turn, is equal to twice the area of any of the six possible unitarity triangles[8]. A comparison of the area of any unitarity triangle obtained indirectly through studies of the  $B$  system or otherwise with the same quantity obtained directly from  $K_L^0 \rightarrow \pi^0 \nu \bar{\nu}$  is then a critical test of the SM explanation of CP violation.

To facilitate the SM prediction of  $B(K_L^0 \rightarrow \pi^0 \nu \bar{\nu})$  and exhibit its relation to other measurements, we employ the Wolfenstein parametrization ( $\lambda, A, \varrho, \eta$ ) of the CKM matrix, which allows a display of unitarity in a transparent way. In this representation, Eqn. 3 can be recast as

$$B(K_L^0 \rightarrow \pi^0 \nu \bar{\nu}) = 1.8 \cdot 10^{-10} \eta^2 A^4 X^2(x_t) \quad (5)$$

Inserting the current estimates for SM parameters into Eqn. 5, the branching ratio for  $K_L^0 \rightarrow \pi^0 \nu \bar{\nu}$  is expected to lie in the range  $(3.1 \pm 1.3) \cdot 10^{-11}$ [1]. The unitarity relation

$$1 + \frac{V_{td} V_{tb}^*}{V_{cd} V_{cb}^*} = -\frac{V_{ud} V_{ub}^*}{V_{cd} V_{cb}^*} \equiv \bar{\varrho} + i\bar{\eta} \quad (6)$$

determines the most commonly discussed triangle in the  $(\bar{\varrho}, \bar{\eta})$  plane. Here  $\bar{\varrho} = \varrho(1 - \lambda^2/2)$  and  $\bar{\eta} = \eta(1 - \lambda^2/2)$ . This unitarity triangle is illustrated in fig. 2. A clean measure of its height is provided by the  $K_L^0 \rightarrow \pi^0 \nu \bar{\nu}$  branching ratio. We note that, all other parameters being known, Eqn. 5 implies that the relative error on  $\eta$  is half that on  $B(K_L^0 \rightarrow \pi^0 \nu \bar{\nu})$ . Thus, for example, a 15% measurement of  $B(K_L^0 \rightarrow \pi^0 \nu \bar{\nu})$  can in principle determine  $\eta$  to 7.5%.

To construct the complete unitarity triangle in the  $K$  system, the charged mode  $K^+ \rightarrow \pi^+ \nu \bar{\nu}$  which is closely related to  $K_L^0 \rightarrow \pi^0 \nu \bar{\nu}$  is also needed. However,  $K^+ \rightarrow \pi^+ \nu \bar{\nu}$  is not CP violating and receives a non-negligible charm contribution leading to a slightly higher theoretical uncertainty (about 5%) [9]. Measurement of  $B(K^+ \rightarrow \pi^+ \nu \bar{\nu})$  allows the extraction of  $|V_{td}|$  with the least theoretical uncertainty. The first evidence for  $K^+ \rightarrow \pi^+ \nu \bar{\nu}$  was recently reported by E787 [10], at a branching ratio,  $B(K^+ \rightarrow \pi^+ \nu \bar{\nu}) = 4.2_{-3.5}^{+9.7} \times 10^{-10}$ , that is several times higher than the central SM prediction (although statistically consistent with it). Analysis of substantial additional data is ongoing [11] and will indicate whether there is consistency with the SM prediction. Together with  $B(K_L^0 \rightarrow \pi^0 \nu \bar{\nu})$  the unitarity triangle is completely determined as shown in fig. 2. Only a few other possible SM observables (*e.g.*  $x_s/x_d$ ,  $B \rightarrow l^+ l^-$  or certain CP asymmetries in  $B$  decays) provide similar opportunities for unambiguously revealing SM effects.

The pure  $B$ -system alternative to obtaining  $\bar{\varrho}$  and  $\bar{\eta}$  from  $K \rightarrow \pi \nu \bar{\nu}$  discussed most frequently requires measuring  $B^0$  or  $\bar{B}^0 \rightarrow \pi\pi$  and  $B^0$  or  $\bar{B}^0 \rightarrow J/\psi K_S^0$ . At  $B$  factories or hadronic colliders, the time-dependent asymmetry in the rate between  $B^0$  and  $\bar{B}^0$  must be measured in both cases. These CP violating asymmetries measure  $\sin 2\alpha$  and  $\sin 2\beta$ , respectively, and could in principle be used to infer  $\bar{\varrho}$  and  $\bar{\eta}$  (fig. 2), completing the CKM

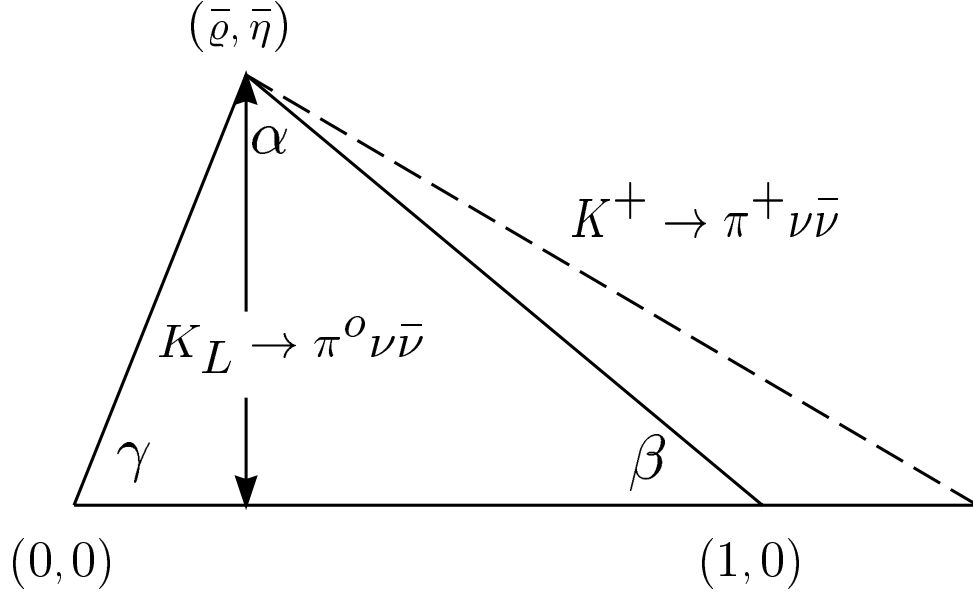


Figure 2: The unitarity triangle.

determination. However, the extraction of  $\sin 2\alpha$  from  $B \rightarrow \pi\pi$  is complicated by the presence of penguin contributions. If only the channel  $B_d \rightarrow \pi^+\pi^-$  is used, these contributions introduce potentially sizable theoretical uncertainties [12]. On the other hand, avoiding penguin effects requires a careful isospin analysis and a combination of several modes, including the challenging decay  $B_d \rightarrow \pi^0\pi^0$ . Also, inferring  $\bar{\rho}$  and  $\bar{\eta}$  from  $\sin 2\alpha$  and  $\sin 2\beta$  involves discrete ambiguities, so that some additional information (*e.g.* on the size of  $V_{ub}$ ) is necessary to single out a unique solution. The CKM analysis for  $K \rightarrow \pi\nu\bar{\nu}$  is less complicated, which could turn out to be of advantage in the unitarity triangle determination.

Alternatively, results from the CP violation experiments in  $B$  physics and a  $K_L^0 \rightarrow \pi^0\nu\bar{\nu}$  measurement could also be combined for high precision determinations of the CKM matrix. One could complete a CKM matrix determination that is essentially free of hadronic uncertainties[13]. The method could become particularly interesting when CP asymmetries in  $B$  decays are measured with improved precision at the LHC. Such a precise determination of the independent CKM parameters, in which  $K_L^0 \rightarrow \pi^0\nu\bar{\nu}$  plays a crucial role, would provide an ideal basis for comparison with other observables sensitive to mixing angles, like  $K^+ \rightarrow \pi^+\nu\bar{\nu}$ ,  $B \rightarrow \pi l\nu$ ,  $x_s/x_d$  or  $V_{cb}$  from  $b \rightarrow c$  transitions. Any additional, independent determination of CKM parameters would then constitute a test of the Standard Model. Any significant deviation would point to new physics.

Additional strategies for combining and comparing information from the rare  $K$  and the  $B$  sector are described in Ref. [4]. Finally, it should be emphasized that it is very desirable that such fundamental quantities as  $\rho$  and  $\eta$  be measured redundantly via methods that do not share the same systematic errors.

### 4.2.2 Non-standard Models

Extensions of the Standard Model can in principle modify the physics discussed above in many ways. Usually extended models introduce a variety of new degrees of freedom and *a priori* unknown parameters, and it is therefore difficult to obtain definite predictions. However one can make a few general remarks relevant for  $K_L^0 \rightarrow \pi^0 \nu \bar{\nu}$  and the comparison with information from the  $B$  system. For a review of CP violation in  $B$  physics beyond the SM see [14, 15].

A clean SM test is provided by comparing  $\eta$  from  $K_L^0 \rightarrow \pi^0 \nu \bar{\nu}$  with that triangulated from measurements of  $|V_{ub}/V_{cb}|$  and  $x_d/x_s$ . Similarly, if  $B(K^+ \rightarrow \pi^+ \nu \bar{\nu})$  is measured, a very clean test is to compare the value of  $\sin 2\beta$  obtained from the two kaon decays with that determined from the CP-asymmetry in  $B \rightarrow J/\psi K_S^0$ . Other incisive tests involve comparisons of the of the Jarlskog invariant obtained from  $B(K_L^0 \rightarrow \pi^0 \nu \bar{\nu})$  with indirect determinations of the same quantity from the  $B$  system. Any discrepancy would clearly indicate new physics. The more theoretically precise the observables under discussion, the smaller the deviation that could be detected.

In some new physics scenarios, such as multi-Higgs doublet models[16, 17] or minimal SUSY in which the CKM matrix remains the sole source of CP violation, the extraction of  $\sin 2\alpha$  and  $\sin 2\beta$  from CP asymmetries in  $B$  decays would be unaffected. Such effects might then show up in a comparison with  $K_L^0 \rightarrow \pi^0 \nu \bar{\nu}$ , where e.g. charged Higgs contributions modify the top quark dependent function  $X(x_t)$  in (3).

In other new physics scenarios, such as supersymmetric flavor models[18], the effects in  $K \rightarrow \pi \nu \bar{\nu}$  tend to be small, while there can be large effects in the  $B$  (and also the  $D$ ) system. In these models the rare  $K$  decays are the only clean way to measure the true CKM parameters.

Examples for new physics scenarios that show drastic deviations from the Standard Model are provided by some of the extended Higgs models discussed in [17], in topcolor-assisted technicolor models [19], in left-right symmetric models [20], in models with extra quarks in vector-like representations[21], lepto-quark exchange [21], and in 4-generation models [22].

In the past year, attention has been focussed on the contributions of flavor-changing  $Z$ -penguin diagrams in generic low-energy supersymmetric extensions of the Standard Model [18, 23, 24, 25, 26]. Such diagrams can interfere with the weak penguins of the Standard Model, and either raise or reduce the predicted  $B(K_L^0 \rightarrow \pi^0 \nu \bar{\nu})$  by considerable factors. Although there is still some controversy about this mechanism, it appears that very large effects are possible, possibly even more than an order of magnitude.

The E787 result on  $K^+ \rightarrow \pi^+ \nu \bar{\nu}$  and recent confirmation of a large value for  $\epsilon'/\epsilon$ [27, 28] have focussed much attention on rare  $K$  decays. Many of the BSM effects mentioned above could lead to a considerable enhancement of  $B(K^+ \rightarrow \pi^+ \nu \bar{\nu})$  over the SM prediction. The same type of flavor-changing  $Z$ -penguin diagrams that can contribute to rare  $K$  decays can affect  $\epsilon'/\epsilon$  [25]. If  $\epsilon'/\epsilon$  is dominated by such new physics,  $B(K_L^0 \rightarrow \pi^0 \nu \bar{\nu})$  can be more than 20 times higher than the central Standard Model prediction[25, 29]. It is also possible for such effects to suppress  $B(K_L^0 \rightarrow \pi^0 \nu \bar{\nu})$  significantly. We stress, however, that as opposed to the case of  $\epsilon'/\epsilon$ , deviations from the predicted value of  $B(K_L^0 \rightarrow \pi^0 \nu \bar{\nu})$  unambiguously indicate the presence of new physics.

### 4.2.3 Theoretical summary

As a consequence of unprecedented theoretical precision and anticipated experimental accessibility, a measurement of  $K_L^0 \rightarrow \pi^0 \nu \bar{\nu}$  can unambiguously test the SM origin of CP violation, directly measure the area of the unitarity triangle, and ultimately yield the most accurate determination of the CKM CP violating phase  $\eta$ . This rare decay mode therefore provides a unique opportunity for making significant progress in our understanding of flavor-dynamics and CP violation. It is competitive with and complementary to future measurements in the  $B$  meson system. If new physics is manifesting itself in  $K^+ \rightarrow \pi^+ \nu \bar{\nu}$  and  $\epsilon'/\epsilon$ , it is virtually certain to show up in an unambiguous way in a measurement of  $K_L^0 \rightarrow \pi^0 \nu \bar{\nu}$  at the SM-predicted level. Absence of  $K_L^0 \rightarrow \pi^0 \nu \bar{\nu}$  within the range of about  $(3 \pm 2) \times 10^{-11}$  or a conflict with other CKM determinations would certainly indicate new physics.



### 4.3 Overview of the $K_L^0 \rightarrow \pi^0 \nu \bar{\nu}$ measurement technique

Along with the challenge of obtaining sufficient detection sensitivity, one of the main issues in measuring an ultra-rare process is the control of systematic uncertainties in estimating tiny levels of backgrounds. In general Monte Carlo calculations are of limited value in assessing minute problems or low level physics processes which can simulate the signal. The only reliable recourse is to use data to systematically study the backgrounds. This is feasible when there is enough experimental information for each event so that the signal can be securely grasped, the backgrounds confidently rejected, and the background levels independently measured in spite of limited statistics. Only with reliable background determinations at a level well below the experiment's sensitivity can observation of an extremely small signal be firmly established. The KOPIO experiment has been designed with this approach in mind.

The complete experimental signature for the  $K_L^0 \rightarrow \pi^0 \nu \bar{\nu}$  decay mode consists of exactly two photons with the invariant mass of a  $\pi^0$ , and nothing else. The experimental challenge arises from the 34% probability that a  $K_L^0$  will emit at least one  $\pi^0$  in comparison with the expected decay probability for  $K_L^0 \rightarrow \pi^0 \nu \bar{\nu}$  which is ten orders of magnitude smaller. Compounding the difficulty, interactions between neutrons and kaons in the neutral beam with residual gas in the decay volume can also result in emission of single  $\pi^0$ s, as can the decays of hyperons which might occur in the decay region, *e.g.*  $\Lambda \rightarrow \pi^0 n$ . The current experimental limit  $B(K_L^0 \rightarrow \pi^0 \nu \bar{\nu}) < 5.9 \times 10^{-7}$  [30] comes from an auxiliary Fermilab experiment which employed the Dalitz decay  $\pi^0 \rightarrow \gamma e^+ e^-$ . Further improvement in sensitivity by perhaps an order of magnitude may be expected during the next few years. Thus, an experimental improvement in sensitivity of more than four orders of magnitude is required to obtain the signal for  $K_L^0 \rightarrow \pi^0 \nu \bar{\nu}$  at the SM level of  $B(K_L^0 \rightarrow \pi^0 \nu \bar{\nu}) = 3 \times 10^{-11}$ .

For any experiment seeking to measure  $K_L^0 \rightarrow \pi^0 \nu \bar{\nu}$  the most important means of eliminating unwanted events is to determine that nothing other than one  $\pi^0$  was emitted in the decay, *i.e.* to veto any extra particles. The most difficult mode to suppress in this manner is  $K_L^0 \rightarrow \pi^0 \pi^0$  ( $K_{\pi^2}^0$ ). If this were the only defense against unwanted events, however, an extremely high (perhaps unachievable) photon veto detection efficiency would be required. Thus, to increase the probability that the source of an observed signal is truly  $K_L^0 \rightarrow \pi^0 \nu \bar{\nu}$ , another handle is needed.

That handle is provided by measurement of the  $K_L^0$  momentum via time-of-flight (TOF). Copious low energy kaons can be produced at the AGS in an appropriately time structured beam. From knowledge of the decaying  $K_L^0$  momentum the  $\pi^0$  can be transformed to the  $K_L^0$  center-of-mass frame and kinematic constraints can be imposed on an event-by-event basis. This technique facilitates rejection of bogus kaon decays and suppression of all other potential backgrounds, including otherwise extremely problematic ones such as hyperon decays and beam neutron and photon interactions.

The background suppression is achieved using a combination of hermetic high sensitivity photon vetoing and full reconstruction of each observed photon through measurements of position, angle and energy. Events originating in the two-body decay  $K_L^0 \rightarrow \pi^0 \pi^0$  identify themselves when reconstructed in the  $K_L^0$  center-of-mass system. Furthermore, those events with missing low energy photons, the most difficult to detect, can be identified and eliminated. With the two independent criteria based on precise kinematic measurements and demonstrated photon veto levels, not only is there enough experimental information so that

$K_L^0 \rightarrow \pi^0 \pi^0$  can be suppressed to the level of an order of magnitude below the expected signal, but the background level can also be measured directly from data.

The beam and detectors for KOPIO employ well known technologies. Important aspects of the system are based on previously established measurement techniques and new aspects have been studied in beam measurements and with prototypes and simulations. Figure 3 shows a simplified representation of the beam and detector concept and fig. 4 gives a schematic layout of the entire apparatus. The 24 GeV primary proton beam is presented to the kaon production target in 200 ps wide pulses at a rate of 25 MHz giving a microbunch separation of 40 ns. A 500  $\mu$ sr solid angle neutral beam is extracted at  $\sim 40^\circ$  to produce a “soft”  $K_L$  spectrum peaked at 0.65 GeV/c; kaons in the range from about 0.4 GeV/c to 1.3 GeV/c are used. The vertical acceptance of the beam (0.005 r) is kept much smaller than the horizontal acceptance (0.1 r) so that effective collimation can be obtained to severely limit beam halos and to obtain another constraint on the decay vertex position. Downstream of the final beam collimator is a 4 m long decay region which is surrounded by the main detector. Approximately 16% of the kaons decay yielding a decay rate of about 14 MHz. The beam region is evacuated to a level of  $10^{-7}$  Torr to suppress neutron-induced  $\pi^0$  production. The decay region is surrounded by an efficient Pb/scintillator photon veto detector (“barrel veto”). In order to simplify triggering and offline analysis, only events with the signature of a single kaon decay producing two photons occurring within the period between microbunches are accepted.

Photons from  $K_L^0 \rightarrow \pi^0 \nu \bar{\nu}$  decay are observed in a two-stage endcap detector comprised of a fine-grained preradiator followed by an 18 radiation length ( $X_0$ ) electromagnetic calorimeter. The preradiator obtains the times, positions and angles of the interacting photons from  $\pi^0$  decay by determining the initial trajectories of the first  $e^+e^-$  pairs. The preradiator consists of 60 0.034  $X_0$ -thick layers, each with plastic scintillator, converter and dual coordinate drift chamber. The preradiator has a total effective thickness of 2  $X_0$  and functions to measure the photon positions and directions accurately in order to allow reconstruction of the  $K_L$  decay vertex while also contributing to the achievement of sufficient energy resolution.

The calorimeter located behind the preradiator consists of “Shashlyk” tower modules, roughly 10 cm by 10 cm in cross section and 18  $X_0$  in depth. A Shashlyk calorimeter module consists of a stack of square tiles with alternating layers of Pb and plastic scintillator read out by penetrating WLS fibers. The preradiator-calorimeter combination is expected to have an energy resolution of  $\sigma_E/E \simeq 0.033/\sqrt{E}$ . Shashlyk is a proven technique which has been used effectively in BNL experiment E865 and is presently the main element in the PHENIX calorimeter at RHIC.

Suppression of most backgrounds is provided by a hermetic high efficiency charged particle and photon detector system surrounding the decay volume. The system includes scintillators inside the vacuum chamber, decay volume photon veto detectors and detectors downstream of the main decay volume. The barrel veto detectors are constructed as Pb/scintillator sandwiches providing about 18  $X_0$  for photon conversion and detection. The detection efficiency for photons has been extensively studied with a similar system in BNL experiment E787. The downstream section of the veto system is needed to reject events where photons or charged particles leave the decay volume through the beam hole. It consists of a sweeping magnet with a horizontal field, scintillators to detect charged particles deflected out of the beam, and photon veto modules. A special group of counters - collectively, the “catcher”

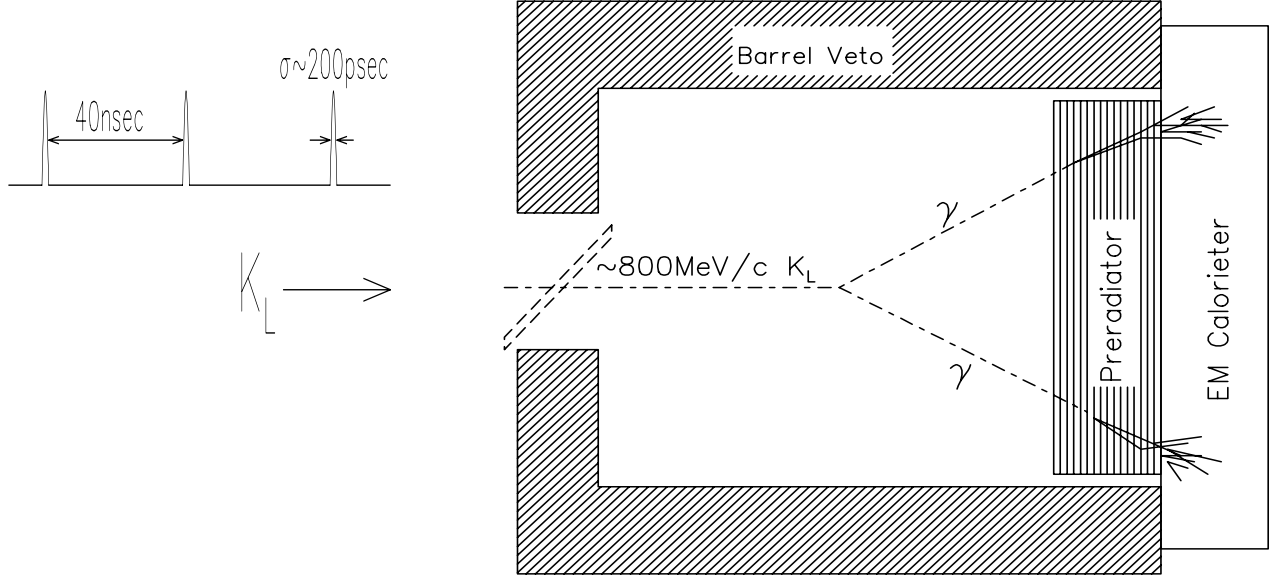


Figure 3: Elements of the KOPIO concept : a pulsed primary beam produces low energy kaons whose time-of-flight reveals their momentum when the  $\pi^0$  from  $K_L^0 \rightarrow \pi^0 \nu \bar{\nu}$  decay is reconstructed.

- vetoes particles that leave the decay volume but remain in the beam phase space. This system takes advantage of the low energy nature of our environment to provide the requisite veto efficiency while being blind to the vast majority of neutrons and  $K^0$ s in the beam. The catcher uses Cerenkov radiators read out with phototubes.

The KOPIO system described above will clearly identify the  $K_L^0 \rightarrow \pi^0 \nu \bar{\nu}$  decay signal and effectively reject all backgrounds using a combination of kinematic measurements and photon vetos. Fig. 5 illustrates KOPIO's extensive arsenal of weapons including the measured quantities and constraints available. Reference values for the resolutions in the measured quantities are given in Table 1.

To illustrate how KOPIO will function to reject backgrounds, we consider bogus events originating with  $K_{\pi_2}^0$  decays. The two types of  $K_{\pi_2}^0$  background are the “even pairing” cases when the two observed photons come from one  $\pi^0$  and the odd pairing cases when each photon originates from a different  $\pi^0$ . The odd pairing events will generally not reconstruct to the  $\pi^0$  mass and are also suppressed by kinematic constraints as will be discussed below. Fig. 6 shows the  $\pi^0$  energy distribution to be detected in the  $K_L$  center of mass frame ( $E_{\pi_0}^*$ ) for the  $K_L \rightarrow \pi^0 \nu \bar{\nu}$  and  $K_L \rightarrow \pi^0 \pi^0$  ( $K_{\pi_2}^0$ ) decays and fig. 7 gives the 2-gamma mass spectrum  $M_{\gamma\gamma}$  for the signal ( $M_{\gamma\gamma} = M_\pi$ ) and for the odd-pairing gammas.

By tagging the  $K_L$  momentum as well as determining the energy and direction of  $\gamma$ s, one can fully reconstruct the kinematics in 2-body decays. In the case where one  $\pi^0$  is missing from a  $K_{\pi_2}^0$  decay (“even pairing”), a kinematic cut on the monochromatic center of mass energy  $E_{\pi_0}^*$  is effective, as shown in fig. 6. In the case where one photon from each  $\pi^0$  is missed (“odd pairing”), a  $\pi^0$  mass requirement ( $m_{\gamma\gamma}$ ) is effective as shown in fig. 7. Additional photon energy cuts on  $E_{\pi_0}^*$  vs.  $|E_{\gamma_1}^* - E_{\gamma_2}^*|$ , where  $E_{\gamma_1}^*$  and  $E_{\gamma_2}^*$  are the energies of  $\gamma$ s in the  $K_L$  center of mass system, are especially effective in further suppressing the  $K_{\pi_2}^0$  background. This is illustrated in fig. 8 which shows distributions of  $E_{\pi_0}^*$  vs.  $|E_{\gamma_1}^* - E_{\gamma_2}^*|$  (using the

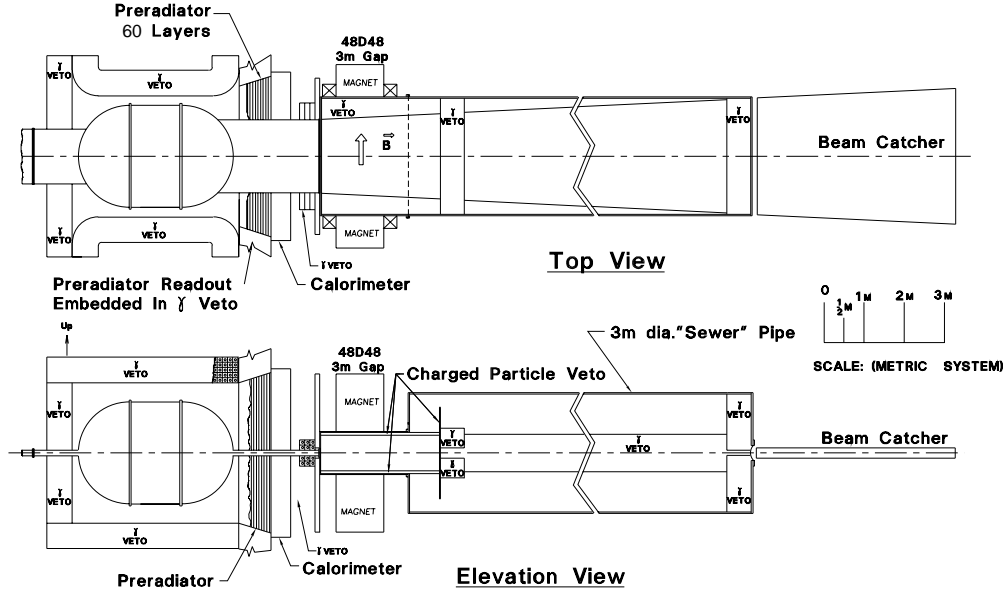


Figure 4: Plan and elevation views of KOPIO detector.

energy resolution indicated in Table 1 and after the  $\pi^0$  mass requirement was imposed) for the  $K_L \rightarrow \pi^0 \pi^0$  (left plot) and for the  $K_L^0 \rightarrow \pi^0 \nu \bar{\nu}$  signal (right plot). The band in the left hand figure at  $E_{\pi^0}^* = 249 \text{ MeV}$  corresponds to the even pairing background, which is suppressed by a  $E_{\pi^0}^*$  cut at  $225 \text{ MeV}/c$  as discussed above. The remaining band corresponds to the odd pairing background, which is confined to a region constrained by the  $\pi^0$  mass. The solid lines show the signal regions in both plots for nominal cuts<sup>3</sup>. Further background suppression can be had at the cost of modest acceptance loss providing a certain margin of safety. When reasonable photon veto efficiency values based on E787 measurements are also assumed, the added capability of full kinematic reconstruction leads to the  $K_{\pi_2}^0$  background being suppressed to a level well below the anticipated signal. A more complete discussion of the potential backgrounds is given below.

Evaluation of the KOPIO system leads to the expectation that a signal of about 60  $K_L^0 \rightarrow \pi^0 \nu \bar{\nu}$  events will be collected if the SM prediction holds. In the following sections, we provide details on the KOPIO beam, detection apparatus, sensitivity and backgrounds along with cost and schedule estimates.

<sup>3</sup>The signal region in Fig. 8 appears low in  $E_{\pi^0}^*$ . This is because the photon veto, which is not applied to the events shown in this figure, is especially effective at eliminating those odd-pairing events which appear in the signal box.

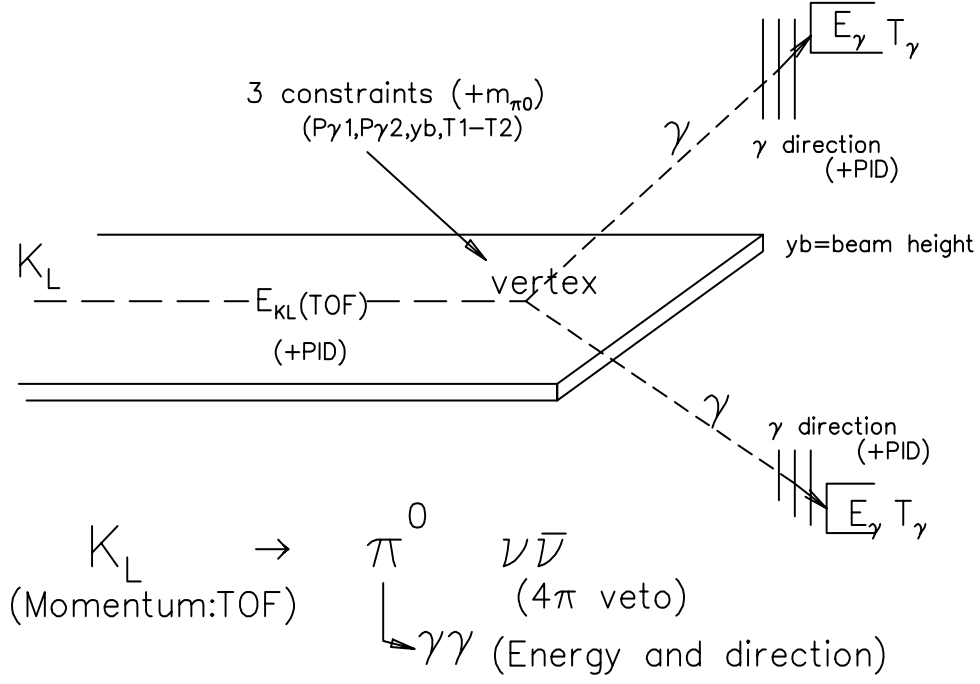


Figure 5: An illustration of quantities measured and constraints available in the KOPIO experiment. Measurements include the  $K_L$  energy, and the gamma energies, directions and times. Particle identification (PID) is also available. Constraints include the  $\pi^0$  mass ( $M_{\pi}^0$ ), the beam vertical extent ( $y_b$ ) and relative timing of the photons.

Table 1: Parameters and nominal resolutions ( $\sigma$ 's) for photon energy ( $E$ ), angles ( $\theta_{xz}, \theta_{yz}$ ), conversion positions ( $x, y$ ), and timing ( $t$ ) anticipated for KOPIO. In simulations, each measured quantity is smeared by adding a quantity  $G\sigma$  where  $G$  is a random value chosen from a normal distribution with zero mean and unit variance, and  $\sigma$  is given in the table.

Quantity	Nominal value	$\sigma$ used in smearing
$E$	$C_E$ (0.033 GeV <sup>1/2</sup> )	$C_E/\sqrt{E}$
$\theta_{xz}$	$\sigma_{\theta_{xz}}$ (8.2mrad·GeV <sup>0.7</sup> )	$\sigma_{\theta_{xz}} \cdot E^{-0.7}$ (96%) $3.6 \cdot \sigma_{\theta_{xz}} \cdot E^{-0.7}$ (4%)
$\theta_{yz}$	$\sigma_{\theta_{yz}}$ (8.2mrad·GeV <sup>0.7</sup> )	$\sigma_{\theta_{yz}} \cdot E^{-0.7}$ (96%) $3.6 \cdot \sigma_{\theta_{yz}} \cdot E^{-0.7}$ (4%)
$x$	$C_x$ (0.45 cm·GeV <sup>1/2</sup> )	$C_x/\sqrt{E}$
$y$	$C_y$ (0.45 cm·GeV <sup>1/2</sup> )	$C_y/\sqrt{E}$
$t$	$\sigma_t$ (0.2 ns)	$\sigma_t$

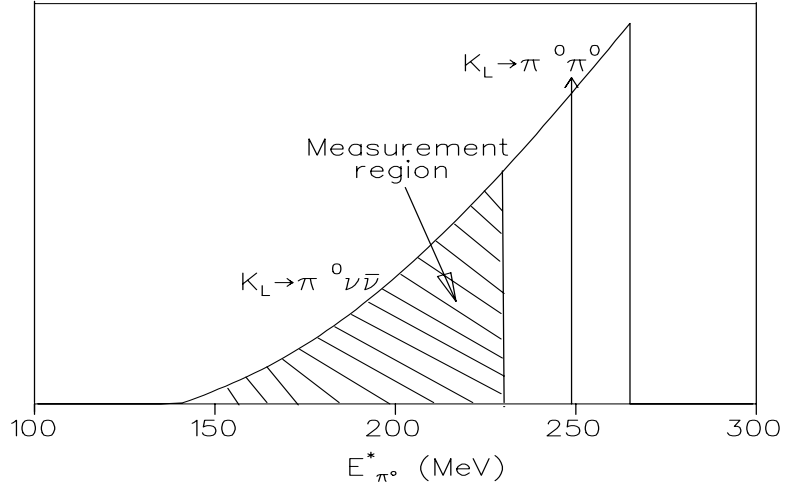


Figure 6: Energy spectrum of  $\pi^0$  in the  $K_L$  center of mass frame (left).

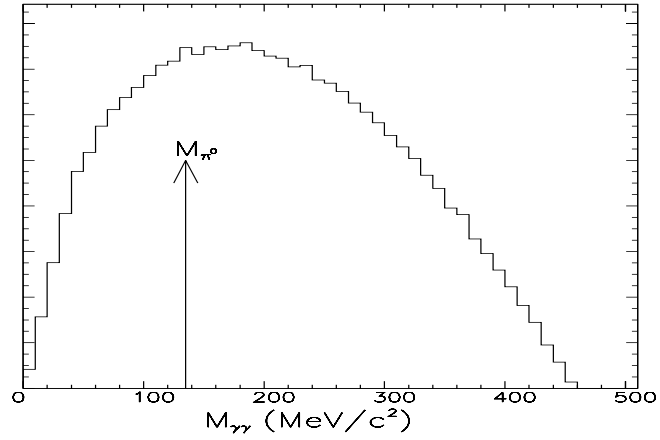


Figure 7: The 2-gamma mass spectrum ( $M_{\gamma\gamma}$ ) for "odd-pairing" gammas in  $K_{\pi 2}$  decays.

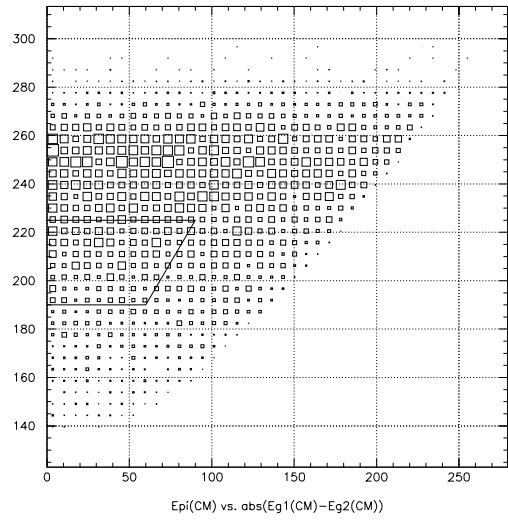
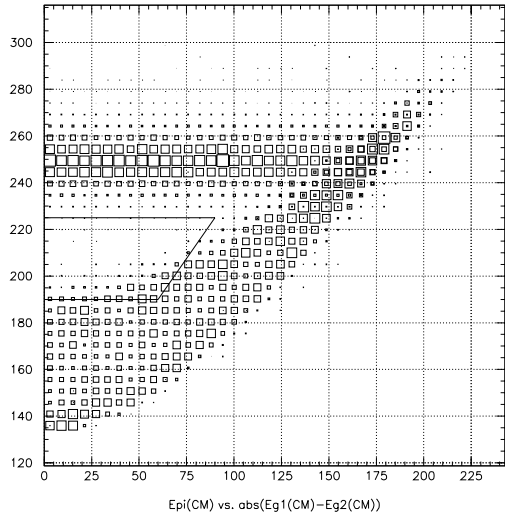


Figure 8: Distributions of  $E_{\pi^0}^*$  vs.  $|E_{\gamma_1}^* - E_{\gamma_2}^*|$  after  $\pi^0$  mass requirement for the  $K_L \rightarrow \pi^0 \pi^0$  (left) and for the signal (right). The solid line encloses the signal region.

## 4.4 AGS

### 4.4.1 Primary beam luminosity

In recent years the AGS has achieved new records of intensity for synchrotrons. The present SEB peak extraction current has reached  $> 7 \times 10^{13}$  protons/pulse. Further improvements are expected to bring this intensity to  $10^{14}$ [31]. For estimates here we will assume this entire intensity will be available for  $K_L$  production. Coupled with a high current micro-bunched beam, good duty factor and extended availability during the RHIC era,<sup>4</sup> the AGS is the ideal accelerator site for rare neutral kaon decay experiments employing time-of-flight.

### 4.4.2 Bunched beam

Short ( $\sim 200$ ps) bunches of protons on the kaon production target are desired so that the time-of-flight measurements can result in a few % momentum resolution in the experimental configuration described above. The straightforward expedient of keeping the beam bunched in RF buckets and compressing them would require excessive voltage to make the bunches this short. The method[32, 33] chosen here involves the following three steps: 1) With constant field in the main guide magnets, power an RF cavity that creates a string of empty RF longitudinal buckets around the AGS at a radius outside a de-bunched, coasting beam; 2) Set the radius of the extraction transverse resonance at the radius of these empty buckets; and 3) Force the protons in the coasting beam between these buckets by slowly reducing the main guide field. As extraction occurs where the beam is being forced between the separatrix lines of the empty buckets at the point at which they are closest, the extracted beam has the desired structure.

This concept has been tested at the AGS, exploiting a VHF acceleration cavity that is normally used to dilute the beam in longitudinal space. It operates at about 93 MHz with  $\sim 30$  KV across the gap. For bunched extraction it is powered after the beam is accelerated to full energy and the main field is fixed. This creates 251 empty buckets, every 3.35 m around the AGS, with an energy width of 20 MeV. The guide field is then reduced at a rate of about 0.4%/sec. The resultant stable phase angle is  $0.5^\circ$  and the gap between buckets is  $15^\circ$  or 0.5 ns. The frequency of the cavity is also ramped down, since the momentum of the extracted protons is falling with guide field (this frequency change is  $\sim 1$  part in  $10^5$ ). The motion through this gap is highly non-linear; tracking of particles in simulations[33] indicate the RMS width of a bunch forced between buckets with this configuration should be  $\sim 160$  ps.

During the 1995-7 SEB runs, initial tests of this concept were carried out using a number of different beam and detector configurations. Secondary particles were timed against the RF acceleration voltage, and the frequency was adjusted to minimize bunch width. Fig 9 shows the distribution of particle times from the most recent test. A Gaussian fit extracts an RMS width of  $\sim 280$  ps.

Widths are still somewhat larger than expected, but the present results are extremely encouraging. Further progress is expected as the instrumentation and feedback circuitry is improved. For use in the proposed experiment, a new cavity with a lower frequency will

---

<sup>4</sup>RHIC is projected to operate for 30 to 40 weeks per year and requires injection from the AGS for  $\sim 2$  hours/day. Thus, approximately 22 hours/day are available for AGS proton operation.



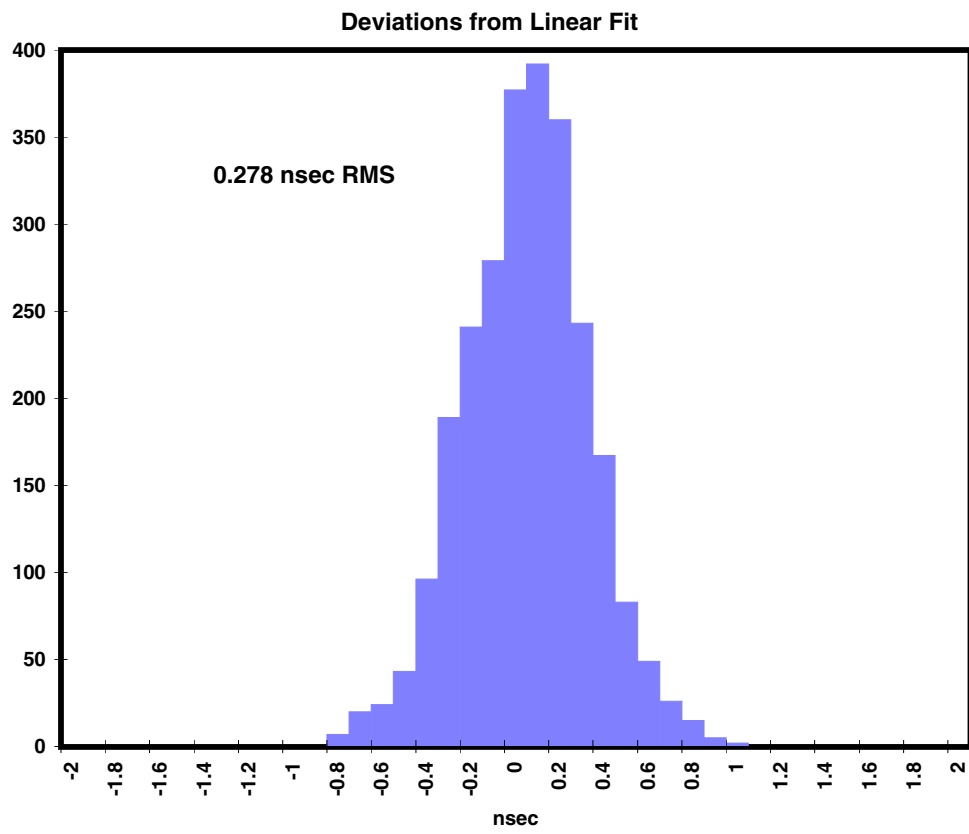


Figure 9: Time in E864 beam Čerenkov with respect to RF timing.

be built. Since the minimum RMS bunch width goes as  $\sim V^{-\frac{1}{2}}$ , we propose to commission a 100 KV, 20 MHz cavity. This is well within the reach of current technology and can be expected to reach a level of  $< 150$  ps which would be more than adequate for our purposes.

## 4.5 Beam

KOPIO requires a copious source of  $K_L^0$  of momentum 700 MeV/c. Ideally the spectrum should be peaked around this value with outlying tails as small as possible. A reasonable approximation to such a spectrum can be obtained from a 24 GeV/c primary proton beam if the neutral channel is taken off at a large angle ( $\sim 40^\circ - 45^\circ$ ). Such a beam also has the advantage of a very low rate of surviving hyperons (potentially a serious source of background). However because there are a lot of neutrons in this kind of beam, care has to be taken in the design of collimation and vacuum systems.

### 4.5.1 Particle production

#### $K_L$ production

There is relatively little data on particle production in the region of interest, and the programs and parameterizations that address it tend to disagree significantly among themselves. Fortunately, there does exist a relatively recent, high-quality measurement of  $K^\pm$  production by 14.6 GeV/c protons at angles from  $5^\circ$  to  $58^\circ$ [34]. These measurements were taken with thin nuclear targets (Be, Al, Cu, and Au). Since KOPIO envisions running at 24 GeV/c and using a 10.6 cm Pt target, these results require correction for the increased primary energy (+30%), and for the  $1.2\lambda_I$  target. The latter correction arises from three effects: the extinction of the beam, absorption of  $K^+$  in the target, and secondary  $K$  production. As will be discussed below, these effects tend to cancel, and the residual is about the same size as that of the primary energy correction, but of opposite sign. We assume that the  $K_L^0$  cross section can be satisfactorily approximated by the average of the  $K^+$  and  $K^-$  cross sections, and that production off Au and off Pt do not differ significantly.

The extrapolation in primary energy is done in four steps[35]. (1) Invariant  $K^\pm$  cross sections from  $pp$  collisions are fit to the phenomenological form[36, 37]:

$$E_{K^\pm} \frac{d\sigma(pp \rightarrow K^\pm X)}{d\mathbf{p}_{K^\pm}} = B(s)(1 - x_R)^{n(s)} e^{b - \sqrt{b^2 + c^2(s)} p_T^2} \quad (7)$$

(2) Assuming that in the interaction of protons with light nuclei, kaon production is dominated by single inelastic interactions of the primary proton with the nucleons, the  $pp$  cross sections are multiplied by a phenomenologically determined function of  $\mu(p_K) \equiv \sigma_{Kp}^{inel}(p_K)Z + \sigma_{Kn}^{inel}(p_K)N$  and  $\mu(p_0) \equiv \sigma_{pp}^{inel}(p_0)Z + \sigma_{pn}^{inel}(p_0)N$  to obtain the cross sections off Be. (3) The results of (2) are multiplied by a factor  $(A_{Pt}/A_{Be})^{\alpha(x_F)}$  to get predicted cross sections off Pt. (4) The predictions are rescaled by comparison with data taken in the forward direction at 23.1 GeV/c[38].

The predictions are then compared with the Au data of Abbott *et al.* for  $K^\pm$  production. Fig. 10 shows the data for  $K^+$  production for  $\theta = 40^\circ$  and  $45^\circ$  and the corresponding predictions from the above procedure. Fig 11 show similar plots for  $K^-$  production.

We are now in a position to confidently extrapolate to 24 GeV/c. For  $\theta \sim 40^\circ$ , for example, this correction turns out to be about 30% on average (it is a function of  $p_K$ ). The extrapolated  $K^+$  and  $K^-$  cross sections are averaged, giving the results of Fig. 12.

To obtain yields, these cross sections must be integrated over the beam aperture and corrected for finite target effects. Beam attenuation in the target results in an effective

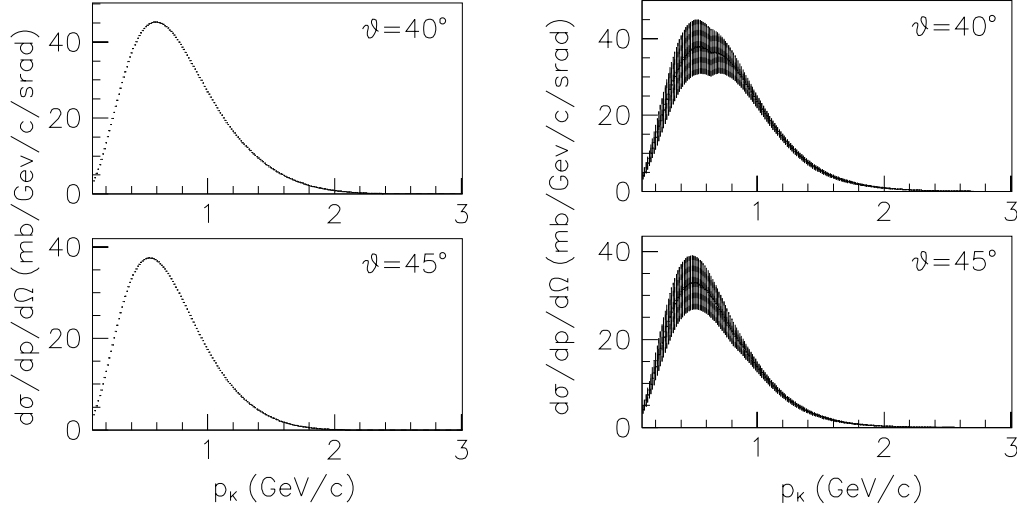


Figure 10: The right hand graphs are double differential inclusive cross sections for  $K^+$  production by 14.6 GeV/c protons on Au at  $\theta = 40^\circ$  and  $45^\circ$ . The error bars show statistical uncertainties only. The left hand graphs are predictions from the procedure described in the text.

target thickness of  $(1 - e^{-10.6/8.8})8.8 \text{ cm} = 6.2 \text{ cm}$ . This represents an effective reduction factor of 0.58 with respect to thin target results. The effect of  $K^+$  and secondary production in the long target was calculated via GEANT. Although we don't trust this program to yield reliable absolute yields, it should give a reasonable estimate of the thick target effects. GEANT runs on 0.5 cm and 10.6 cm targets were made[39]. The resultant correction factors varied significantly with production angle, but were very weak functions of  $p_K$ . For  $\theta = 40^\circ$ , this factor equals 1.32. For  $\theta = 45^\circ$ , it is = 1.36. Thus the product of all corrections is very close to 1 in the region of interest.

After applying all corrections, the yield and production spectrum of  $K_L^0$  are obtained. For  $10^{14}$  protons incident on the target, a total of  $6.6 \times 10^8$   $K_L^0$  are produced into a  $500 \mu\text{sr}$  solid angle centered at spoiler discussed below and the loss due to decays in flight,  $2.6 \times 10^8$   $K_L^0$  arrive at the detector 10m downstream of the production target with the momentum spectrum shown in Fig. 13.

### Neutron production

Simulations and data on neutron production at large angles are also problematical. Therefore a new measurement was made [40] in the B1 beam line at the AGS. Fig. 14 shows a sketch of the set-up used in the measurement of the neutral particles: the beam counter arrangement, TOF scintillator wall and BaF<sub>2</sub> detector.

A small fraction of the 24 GeV/c AGS primary proton beam was extracted into the B1 line. A 10 cm long by  $4 \times 4 \text{ mm}^2$  cross section platinum production target was placed at the apex of the E802 spectrometer [41]. A beam spot of  $3 \times 3 \text{ mm}^2$  was determined by a small plastic counter (finger counter) placed very close to the front of the target. The TOF1 and TOF2 counters located upstream of the target, the finger and steering counters defined the

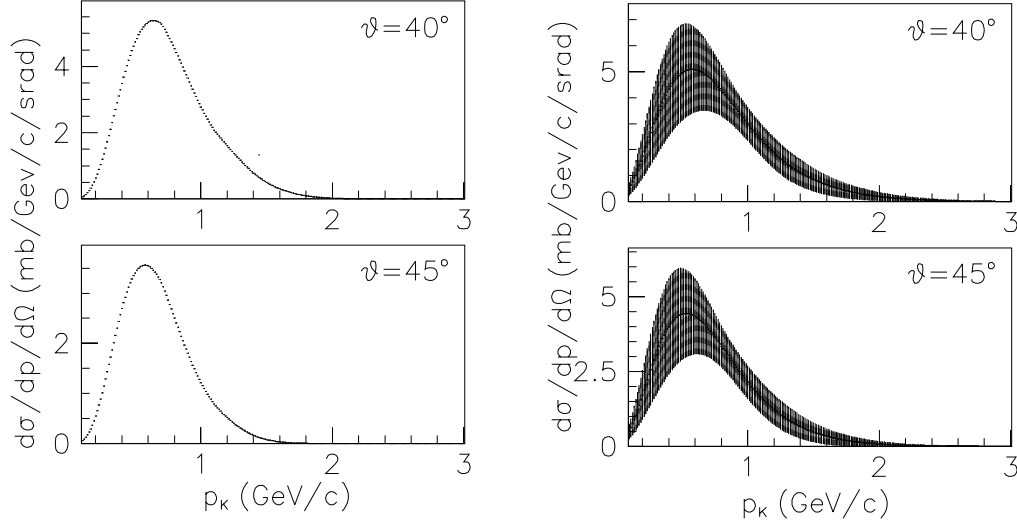


Figure 11: The right hand graphs are double differential inclusive cross sections for  $K^-$  production by 14.6 GeV/c protons on Au at  $\theta = 40^\circ$  and  $45^\circ$ . The error bars show statistical uncertainties only. The left hand graphs are predictions from the procedure described in the text.

geometry of the proton beam.

An array of 36 modules of BaF<sub>2</sub> was used to detect neutrons and photons. The detector was assembled to form a 6x6 array. Each module had a 3.5 cm x 3.5 cm cross section and was 35 cm in length. Each crystal was coupled directly to a fast phototube. The array was placed at a distance of 7.4 m from the target at the rotating spectrometer platform behind the plastic time-of-flight (TOF) wall, as shown in Fig. 14. The BaF<sub>2</sub> detector covered the area of about 440 cm<sup>2</sup>, or approximately  $6.4 \times 10^{-5}$  of  $4\pi$  solid angle.

To reject charged particles which hit the BaF<sub>2</sub> detector, and to form a neutral trigger two veto counters were used: a) a large counter (Int) behind the target (about 0.5 m), b) a veto counter ( $V_{BaF_2}$ ) in front of the BaF<sub>2</sub> array.

The neutral trigger (NT) required a single beam particle to pass through the beam counters with no particles in the veto counters plus a signal in the BaF<sub>2</sub> detector during the time window of about 200 ns. The neutral trigger was formed as

$$NT = TOF_1 \times TOF_2 \times \text{Finger} \times \overline{Int} \times \overline{V_{BaF_2}} \times BaF_2$$

A time-zero signal used in the off-line analysis is obtained from the two photomultipliers of TOF<sub>2</sub> as

$$T_{start} = 1/2(TOF_{21} + TOF_{22}).$$

The number of protons on the Pt target was calculated as a triple coincidence:

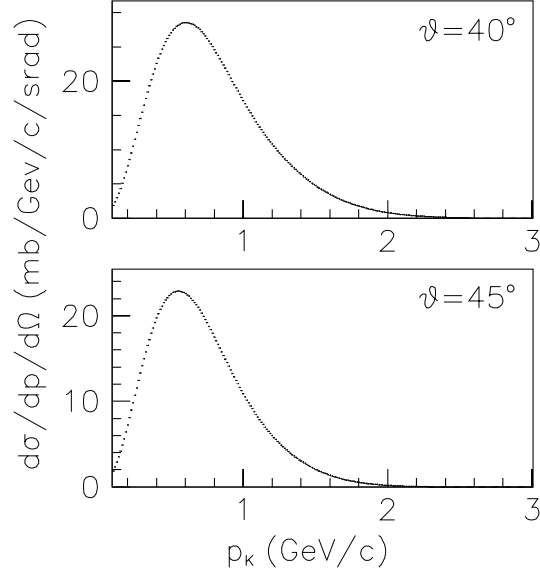


Figure 12: Calculated double differential inclusive cross sections for  $K_L^0$  production at  $40^\circ$  and  $45^\circ$  by 24 GeV/c protons on Pt.

TOF1×TOF2×Finger.

The timing in the BaF<sub>2</sub> detector was defined as the TDC time of the crystal which had the maximum energy deposit. The TDC scale (resolution of 50 ps/channel) allowed us to measure a time interval of 200 ns, corresponding to neutron energy of less than 10 MeV. The timing shifts between the photon prompt peaks for different crystals were corrected in an off-line analysis. The timing resolution of BaF<sub>2</sub> varies from 200 to 400 psec ( $\sigma$ ) and depended on the type of the PMT used (two types were used). There is also some contribution to the time resolution from the beam counters. After applying a time-amplitude correction in the off-line analysis, a time resolution of 0.55 ns ( $\sigma$ ) was achieved for the whole BaF<sub>2</sub> assembly.

Deposited energy was calibrated via tracks identified as minimum ionizing by the TOF wall. Time calibration was based on the position of the prompt photon signal.

Fig. 15 shows a typical energy vs TOF spectrum. The prompt peak position corresponds to the photon time-of-flight from the target to the BaF<sub>2</sub>. Neutrons with higher energies (closest to prompt peak) have larger energy deposits in the BaF<sub>2</sub> detector, as seen in Fig. 15. However since the BaF<sub>2</sub> array is only a fraction of an interaction length deep, deposited energy is not a very good estimator of the true neutron energy (although it is fine for photons). Therefore the neutron energy was calculated from time-of-flight information. To get final neutron energy spectra, a flat background was subtracted from the TOF spectra, determined from the hits that precede the prompt peak. Spectra so derived for the  $\theta = 38.5^\circ$  and  $46.5^\circ$  settings are shown in Fig. 16.

To obtain the true neutron flux, the absolute efficiency of the BaF<sub>2</sub> detector for detection of fast neutrons is needed. Such an efficiency was measured in Refs. [42, 43]. For  $E_n \geq 100$  MeV Ref. [43] gives a neutron efficiency  $\epsilon_n \sim$  of 0.25 - 0.3 for 25cm thick crystals. For neutron energy below 40 MeV the efficiency is less than 0.2 and falls to about zero for

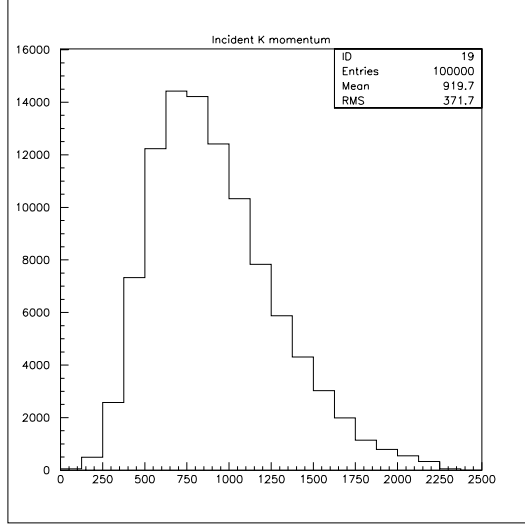


Figure 13:  $K_L^0$  spectrum incident on KOPIO decay volume.

neutron energy of  $\leq 15$  MeV [42]. The uncertainty in the  $\text{BaF}_2$  efficiency limits the accuracy of the measurement of neutron flux, especially at low energies, but it is good enough for our purposes. Since our crystals are 35cm deep, we must correct the above efficiencies upward, by a factor  $(1 - e^{-35/L_{int}})/(1 - e^{-25/L_{int}})$ . The Particle Data Book[44] gives 29.6 cm for  $L_{int}$ , which implies a correction factor of 1.22.

The photon yields are more straightforward to extract. The photons are selected by timing and the calibrated energy is used directly. The extracted neutron and photon yields measured at  $38.5^\circ$  and  $46.5^\circ$  are given in Tables 2 and 3. The results on neutrons agree reasonably well in total yield with the predictions of GEANT/GCALOR, but the observed spectra are somewhat harder than those of the simulation.

Table 2: Neutron and photon yield at  $38.5^\circ$ . The total number of protons on target is  $20.6 \times 10^6$ . Corrections for DAQ dead time (16 %) and  $\text{BaF}_2$  efficiency have been made.

Threshold, MeV	10	50	100	300	830
n/p	$2.03 \times 10^{-3}$	$1.69 \times 10^{-3}$	$1.46 \times 10^{-3}$	$0.89 \times 10^{-3}$	$0.35 \times 10^{-3}$
n/ $\gamma$	2.18	3.43	4.08	4.05	3.88

Table 4 recasts the above results in a normalized form. One can use this table to estimate the neutron and photon (pre-spoiler) fluxes in KOPIO. In fact the solid angle coverage of the  $\text{BaF}_2$  is only about 60% larger than that of the KOPIO beam. For a proton beam intensity of  $10^{14}$  protons/pulse on target, at  $38.5^\circ$ , the neutron flux above 10 MeV is  $1.26 \times 10^{11}$ /pulse. For  $46.5^\circ$ , the corresponding number is  $8.3 \times 10^{10}$ . For neutron energy above 830 MeV, the flux decreases by a factor 20 – 30 at  $46.5^\circ$  and by a factor 5 – 6 at  $38.5^\circ$ . For photons, the flux above 10 MeV is  $5.75 \times 10^{10}$ /pulse at  $38.5^\circ$  and  $2 \times 10^{10}$ /pulse at  $46.5^\circ$ . As we discuss

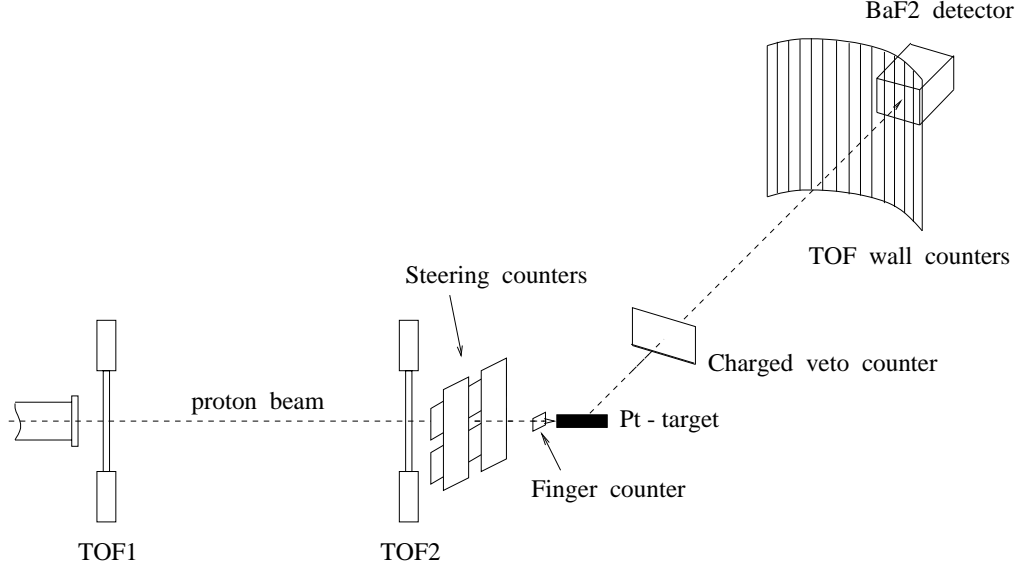


Figure 14: The configuration of beam counters, TOF wall and BaF<sub>2</sub> array. The charged veto counter is referred to as “Int” in the text.  $V_{BaF_2}$  is not shown.

Table 3: Neutron and photon yield at 46.5°. The total number of protons (p) on a target is  $60.5 \times 10^6$ . Corrections for DAQ dead time (16 %) and BaF<sub>2</sub> efficiency have been made.

Threshold, MeV	10	50	100	300	830
n/p	$1.35 \times 10^{-3}$	$1.02 \times 10^{-3}$	$7.96 \times 10^{-4}$	$3.09 \times 10^{-4}$	$0.52 \times 10^{-4}$
n/ $\gamma$	4.19	4.88	4.98	3.98	3.06

below, this can be greatly reduced by an appropriate photon spoiler system. The neutron flux will also be reduced, although only by a factor  $\leq 2$ , by such a spoiler.

#### 4.5.2 Beam design simulation

Beamline design for KOPIO has several objectives. Charged particles emanating from the production target must be swept out, the photon component of the beam must be highly suppressed and beam neutron halo must be kept well below  $10^{-3}$ . A number of Monte Carlo studies using GEANT3/GCALOR have been performed to optimize a design to meet these objectives.

The geometry of the beam line (the target, proton beam direction and the collimator are shown in Fig. 17. For the purposes of this study the target was taken to be 2mm square in cross-section and 10 cm long. A series of precision collimators (Fig. 17) are used to define the asymmetric neutral beam of solid angle 5.2 mr (V) x 96 mr (H) = 500  $\mu$ sr. (Early studies were done with collimation directed at producing a 4 mr vertical by 125 mr horizontal beam cross-section.) The horizontal and vertical apexes of the collimator coincided. Studies with



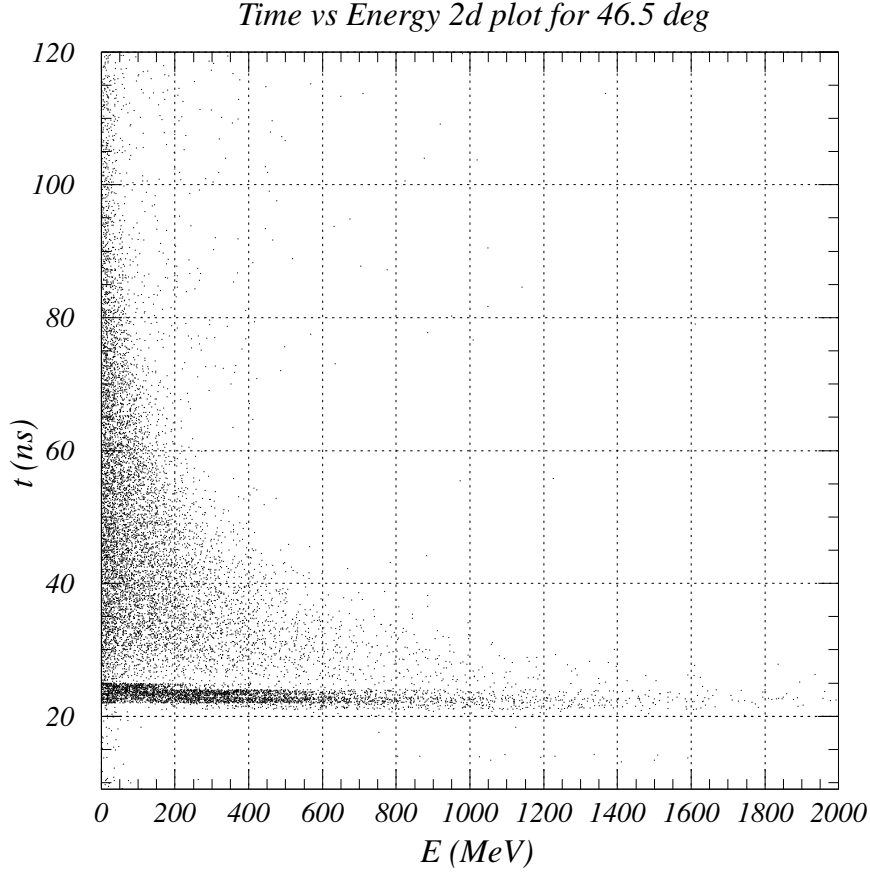


Figure 15: Time vs energy for  $\theta = 46.5^\circ$  setting.

both tungsten and lead as collimator material were done. Herein we report on results with an all-lead collimator. This leaves scope for further improvement through the use of tungsten at critical points. The beamline was simulated by GEANT3/GCALOR. To save computer time the simulation of the neutron production was separated from that of its propagation. Two types of calculations were made. (1) Primary proton interactions were generated by GEANT3/GCALOR and the resulting neutron and proton spectra determined. Neutrons and protons were selected from these distributions and followed into the beamline. (2) Neutrons were generated according to our measured spectra and followed into the beamline. In both cases the subsequent history of the particles was followed by GEANT.

To reduce the high flux of beam photons a lead filter (“spoiler”) was installed in the collimator. The filter is a stack of 50 (70) Pb foils 1 mm thick and 2 (or 3) cm apart. It completely covers the beam hole in the collimator. The first foil is located at 1 m from the target, and the total length of the filter varies from 1 m to 2.1 m. To remove positrons and electrons from the beam aperture a vertical magnetic field was applied. The field is envisioned

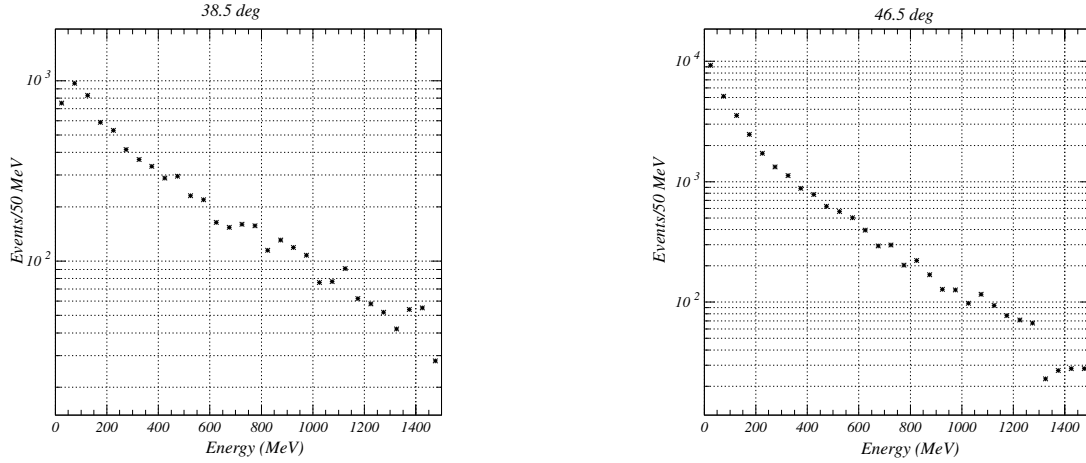


Figure 16: Extracted neutron energy spectrum at  $38.5^\circ$  (left) and  $46.5^\circ$  (right). The bin size is 50 MeV.

Table 4: Normalized neutron and photon yield.

Angle	Particle	Threshold, MeV	Flux ( $\text{p}^{-1}\mu\text{sr}^{-1}$ )
$38.5^\circ$	neutron	10	$2.52 \times 10^{-6}$
	neutron	100	$1.78 \times 10^{-6}$
	photon	10	$1.15 \times 10^{-6}$
$46.5^\circ$	neutron	10	$1.66 \times 10^{-6}$
	neutron	100	$1.04 \times 10^{-6}$
	photon	10	$0.40 \times 10^{-6}$

as beginning at the upstream edge of the first collimator and extending downstream for 2m. (Point 1 to Point 2 on Fig. 17). The dependence of photon intensity in the beam catcher on magnetic field is shown in Fig. 18 for lead thickness of 5 cm and 7 cm. A reduction of the photon flux by a factor of 150-200 is possible for 7 cm of lead with  $B = 1.5\text{T}$ . One gains very slowly with  $B$  beyond this point. Moreover the photon spectra becomes much softer after the filter, as seen in Fig. 19. The ratios of neutral kaon decays with and without the filter are 0.70 for 5 cm of lead and 0.62 for 7 cm. The corresponding factors for beam neutrons are 0.72 and 0.65. Unlike the photon case, neither the neutron nor the kaon spectra are much affected by the presence of the filter.

Neutron halo studies were made by both methods described above. Nucleons were started in the target within a solid angle of 30 mrad (vertical) x 280 mrad (horizontal) that is much wider than collimator-defined acceptance and allowed to hit the the collimator front face. We ran  $10^7$  neutrons from the target to the collimator in each run. A low energy cutoff parameter of 10 MeV was used, i.e. a neutron was stopped at the point where its energy was reduced to  $\leq 10$  MeV. The resulting distributions at various points along the beam were used to optimize the collimator design. This is a continuing process, but results thus far are

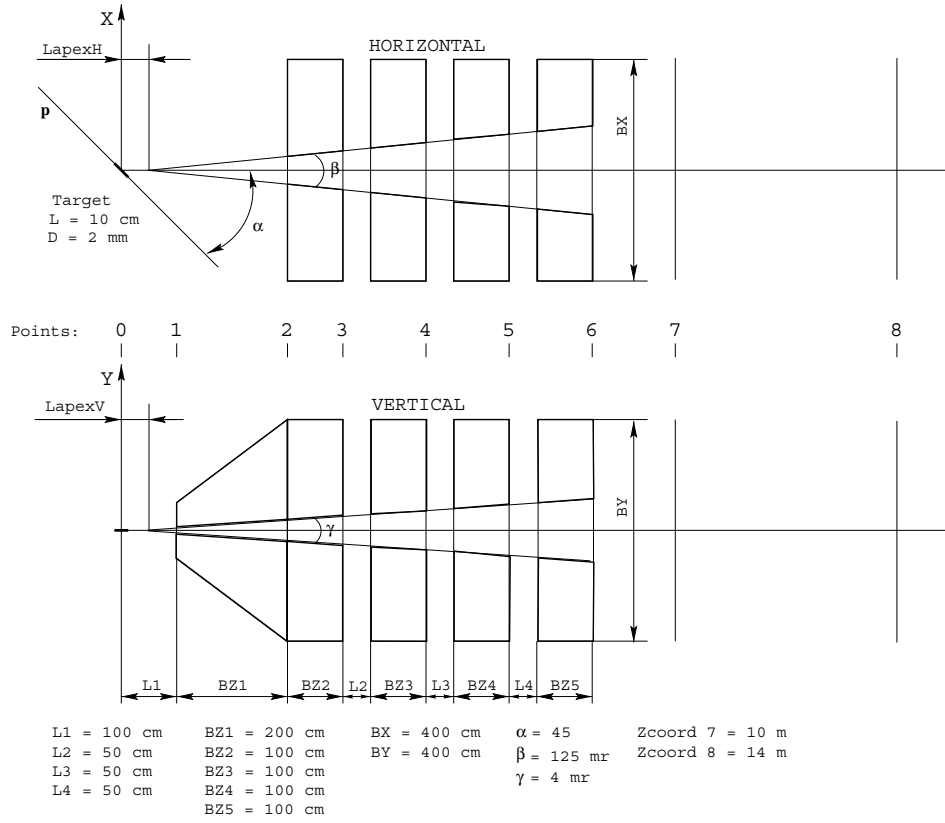


Figure 17: Schematic view of the neutral beam line. The baseline calculations are for  $\text{LapexH} = \text{LapexV} = 0$ .

very encouraging. Fig. 20 shows the x and y projections of the neutron beam at a point 14m downstream of the production target in the type (1) calculation. The fraction of neutrons in the halo, defined as the region more than 1 cm vertically and 3 cm horizontally out of the beam profile, is  $4.8 \times 10^{-4}$ .

Fig. 21 gives the corresponding results for the type (2) calculation. Here the fraction of halo neutrons is  $5.0 \times 10^{-4}$ , very similar to the type (1) calculation. However it must be corrected for the contribution of protons. The correction factor can be determined in type (1) calculations where the fractional proton contribution is observed to be only a few percent. Assuming that this ratio is only a weak function of the nucleon momentum, the total halo in the type (2) calculation is only slightly higher than in the type (1) calculation. The beam halo fraction at  $40^\circ$  is about a factor two higher than that at  $45^\circ$ .

Beam optimization continues. The addition of an extra 0.5m of Pb shielding reduces the halo fraction at  $40^\circ$  to  $3.9 \times 10^{-4}$ , which is already very promising. To meet our trigger rate goals, another factor  $\sim 2$  will be needed. Calculations with a 4 mr x 105 mr beam aperture yield a factor 2.5 smaller halo at the cost of roughly 20% in beam flux. Moving the target 20cm upstream of the apex of the collimators reduces the halo by a factor 2 at the cost of

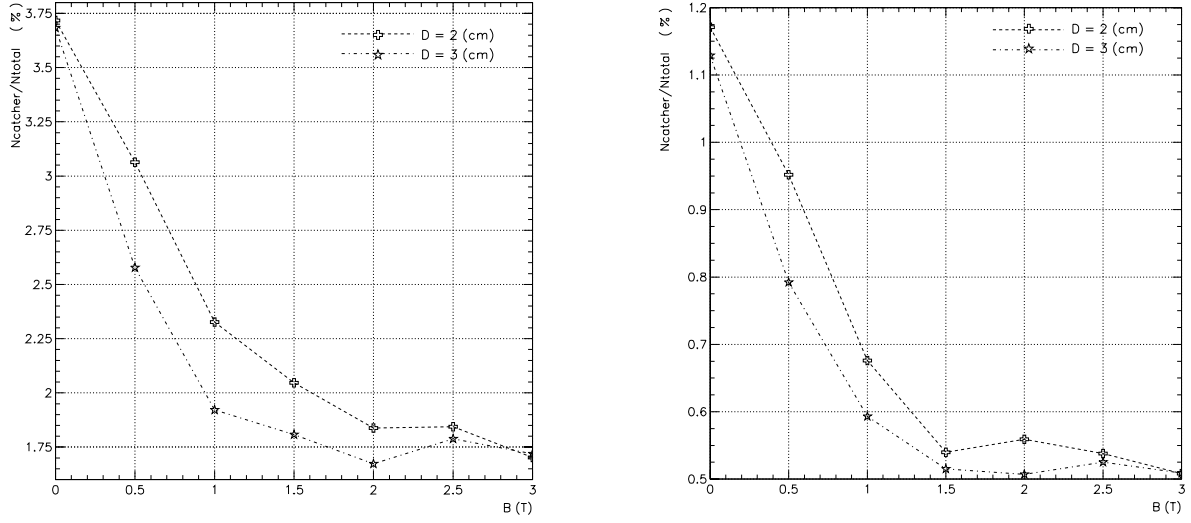


Figure 18: Fraction of photons penetrating filter, versus sweeping magnetic field. Cases of 2 and 3 cm foil separation are shown. Left graph is for the case of a total Pb thickness of 5cm. Right graph is for 7 cm.

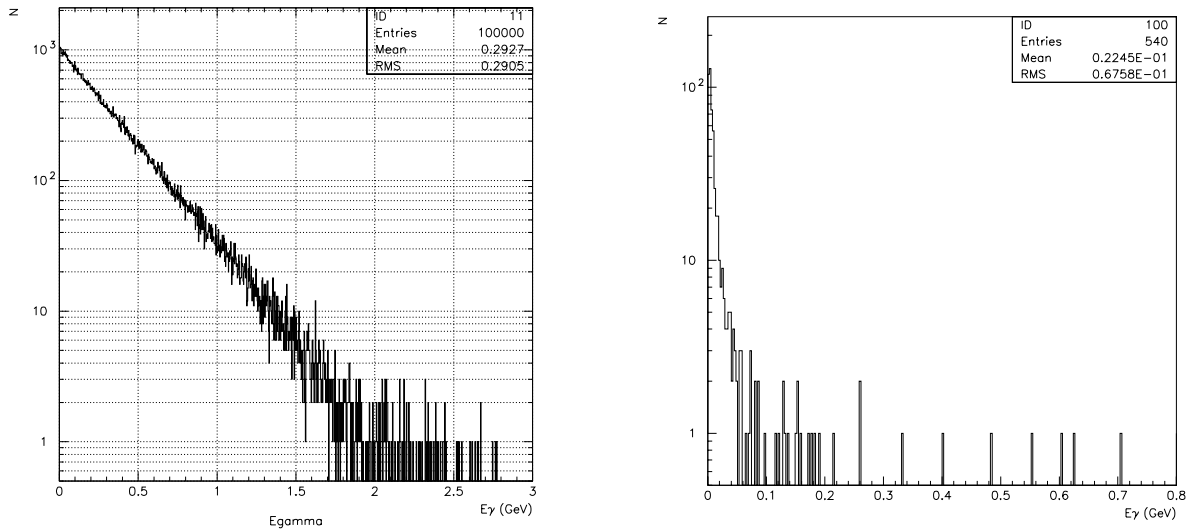


Figure 19: Photon spectra in the collimator-defined aperture before (left) and after (right) a 7 cm Pb filter with  $B = 1.7$  T.

13% of beam intensity. Substitution of tungsten for lead in critical regions yields a 15-20% benefit. Based on these studies, we expect to be able to achieve  $10^{-4}$  integral halo at  $40^\circ$ .

As a test of our methods, the AGS-791/871 beamline [45] was also simulated, and the halo profiles obtained matched available data [46].

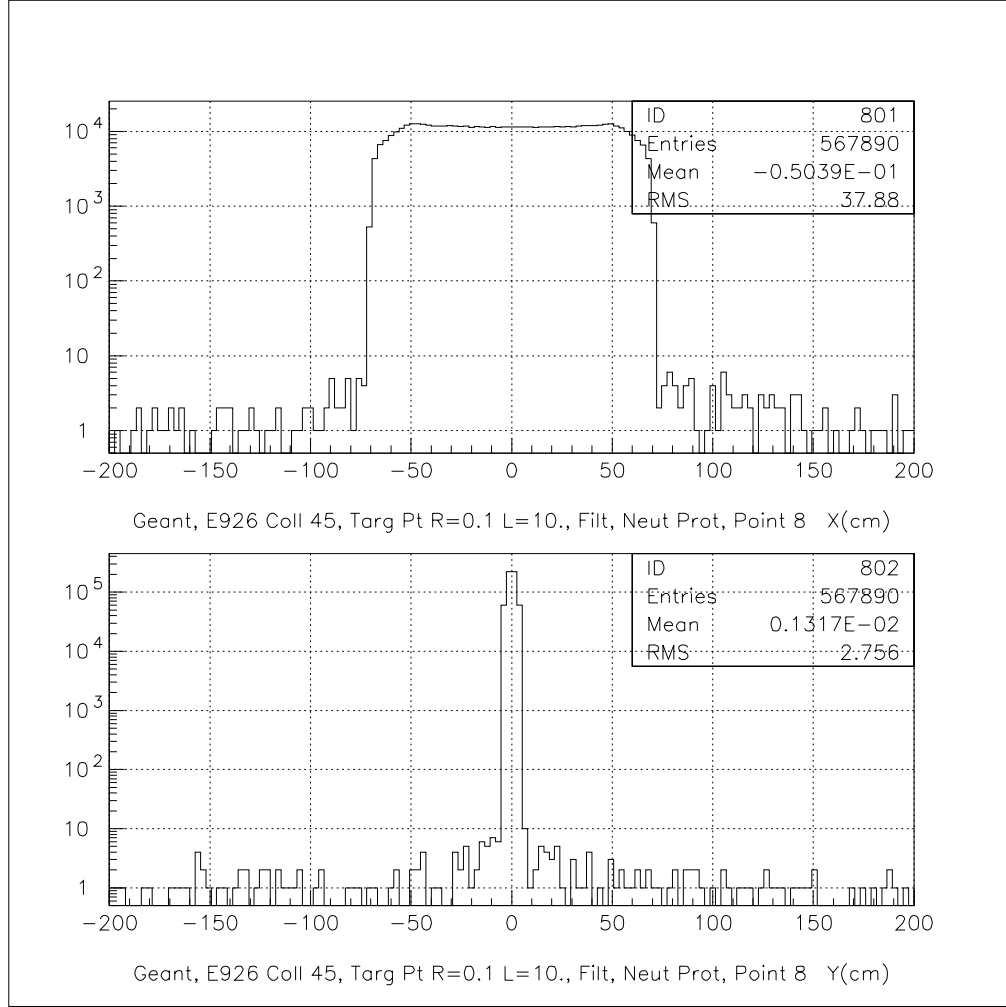
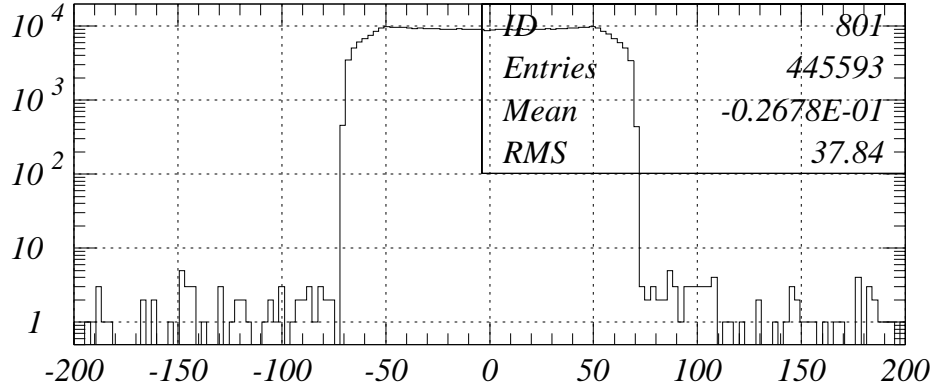
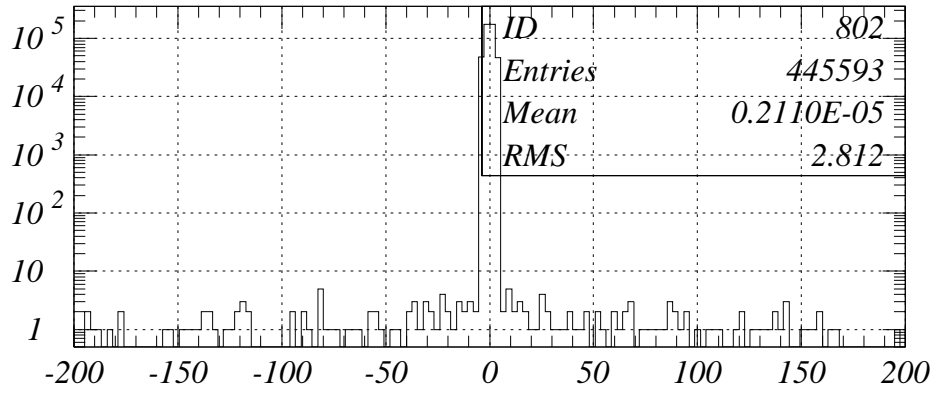


Figure 20: The x (top) and y (bottom) projections of the neutron distribution 14m downstream of the production target for  $\theta = 46.5^\circ$ . Gamma filter = 7cm, B= 1.5T. Calculation begins with neutron and proton distributions from GEANT3/GCALOR.

99/10/01 14.52



*Spect, E926 Coll 46.5, Targ Pt R=0.1 L=10., Filt, Neut, Point 8 X(cm)*



*Spect, E926 Coll 46.5, Targ Pt R=0.1 L=10., Filt, Neut, Point 8 Y(cm)*

Figure 21: The x (top) and y (bottom) projections of the neutron distribution 14m downstream of the production target for  $\theta = 46.5^\circ$ . Gamma filter = 7cm, B= 1.5T. Calculation begins with measured neutron distributions.

## 4.6 Vacuum and Mechanical considerations.

Figure 22 shows the basic vacuum elements of the apparatus in the experimental area. The beam is in vacuum all the way from the target to the left of the drawing to the exit of the downstream pipe in front of the “catcher” to the right.

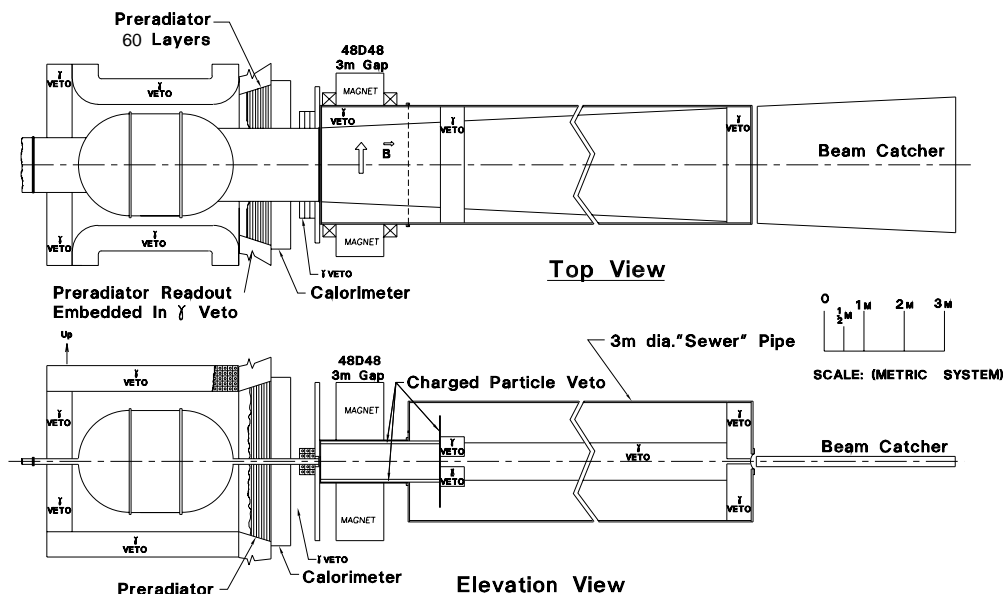


Figure 22: Plan and elevation views of the experimental apparatus. The beam enters from the left in a vacuum system that begins at the target.

### 4.6.1 Vacuum in the decay region.

The decay volume and the entire beam path within the view of the detector must be at high vacuum ( $\sim 10^{-7}$  torr) in order to suppress background from neutron and  $K^0$  interactions with the residual gas. The walls of the vacuum containment must also be of minimal material ( $\leq 5\% X_0$ ) in order to reduce photon conversions and photon production from charged particles, for example in  $K_{e3}$  decays. Coupled to the fact that the beam has a high aspect ratio ( $\sim 1$  m horizontally by  $\sim 5$  cm vertically), these constraints provide a challenge to designing the vacuum containment in the decay region.

The vacuum vessel is shown in fig. 23. An engineering report on its design, including a finite element stress analysis, is presented in a KOPIO technote [47]. Possible vendors have been found to manufacture the vessel as described below.

The material from which the vessel is formed is a Graphite/epoxy laminate (Mitsubishi K137/954-3 or Amoco P75/954-3) which is about 1.3 cm thick, or about  $5\% X_0$ . The central region consists of two hemispherical shells 2.5 m in diameter joined by Graphite/epoxy composite material flanges to a central cylinder. The flanges also serve as tie points for carbon fiber wires which support the vessel from above and provide stability from below (not shown in fig. 23).



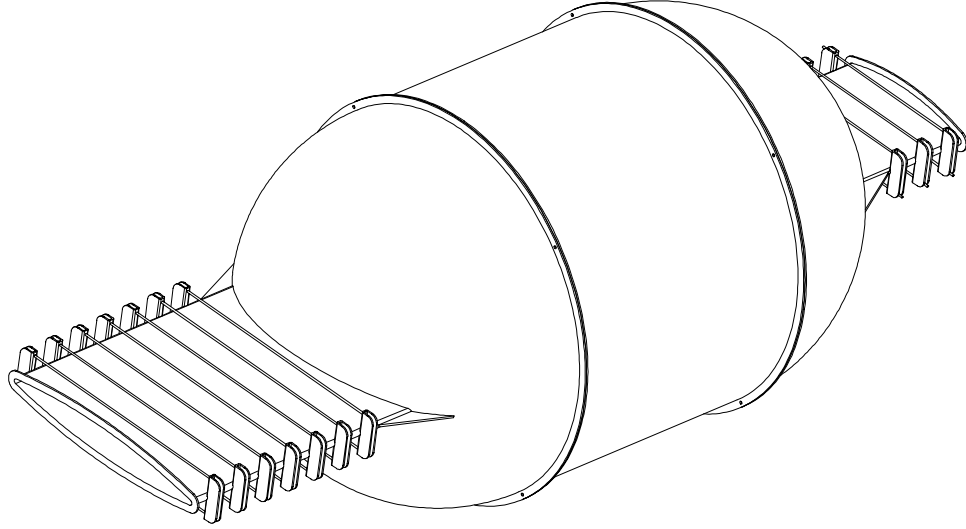


Figure 23: Drawing of the decay region vacuum vessel.

The beam pipes on either end of the hemispheres are connected to vacuum pipes upstream and downstream of the decay volume. These, in turn, are anchored to the floor. Thus, the large stresses on the vessel where the beam pipes join the hemispheres are taken up by the floor.

In order to provide sufficiently high vacuum, the inside of the vessel must be lined with metal. This can be accomplished by placing aluminum foil on the mandrels used for forming the vessel components before the graphite/epoxy material is applied, and curing the system in vacuum.

Directly upstream of the upstream  $\gamma$  vetos in fig. 22 is the pumping station for the decay volume vacuum. It is separated from the beam (dirty) vacuum upstream by a thin window. It consists of a box containing the necessary pumps plus an optical feed-through through which the fibers for the charged particle veto (housed inside the vacuum vessel) pass.

Because of the large horizontal to vertical aspect of the beam, the beam pipes deserve special consideration. They should be as close to the beam shape as possible to minimize the beam hole in the detectors, but must also be made of thin material (both in size and radiation lengths) to minimize absorption of photons or interactions of neutrons. The concept employed is to construct them as opposing arches with external supports (made of carbon fiber “wires” and carbon fiber material) to resist collapse from atmospheric pressure. This concept is also shown in fig. 23. The downstream end of the beam pipe is 160 cm at its widest extent and 20 cm high in the horizontal center. One of the advantages of using carbon fiber wire supports is that the preradiator panels can be shaped to fit closely to the beam pipe, thus maximizing the acceptance of the detector.

#### **4.6.2 Vacuum and mechanical downstream of the decay region.**

The region downstream of the decay volume (see Fig. 4), and just beyond the end of the calorimeter, the decay volume vacuum vessel ends with a thin window. Its flange is connected to a vacuum box that fills the downstream sweeping magnet. That vacuum box is in turn connected to a 3 m diameter, 13 m long cylindrical pipe which terminates in a 3m diameter end plate with an Al vacuum window that is roughly 280 cm wide by 15 cm high. The box and pipe have appropriate feed throughs for the various veto counters that are housed therein, as well as holes for pumping.

The sweeping magnet is a standard Brookhaven 48D48 with a horizontal 1 kG field and a 200cm gap. Between it and the calorimeter is a 10 cm thick magnetic shield with a 160 cm wide by 15 cm high slit through which the beam passes.

Beyond the vacuum region is the beam catcher which is described elsewhere.

## 4.7 Preradiator

The requirements of the preradiator (PR) include a photon angular resolution of approximately 25 mr, a photon conversion efficiency of about 0.7 ( $2.0 X_0$ ), a good measurement of the deposited energy and as short as possible linear extent so as to limit shower size at the calorimeter. The principle we will employ is to measure the positions and angles of the first  $e^+e^-$  pair following photon conversion in a series of thin converter/detector modules. Each PR module consists of an inactive converter material, a dual coordinate drift chamber and a scintillator. The chambers provide the position measurements and the scintillation counters are used for triggering, timing, and energy loss measurement. To keep multiple Coulomb scattering (MCS) at the 25 mr level the PR modules each contain  $\leq 0.034 X_0$ , are separated by about 1 cm and have position resolution of between 150 and 200  $\mu\text{m}$ . In addition, the energy deposited in the preradiator will be measured with sufficient precision to allow the full energy measurement (including the PR and the calorimeter) to be better than  $3.3\%/\sqrt{E}$

### 4.7.1 Design concept

We are considering two designs for the preradiator sub-elements. One scheme is based on a “honeycomb strip chamber” [48] with integrated scintillators illustrated in fig. 24. The system is based on proportional tubes made from corrugated, metalized kapton and metalized scintillators. The second system under study, shown in fig. 25, consists of flat square cell drift chambers with an extruded Al comb backplane and independent extruded scintillator elements similar to those to be used in the barrel veto detector. In both cases, the primary chamber readout will be done with the induced charge signals from 3 - 5 mm wide cathode strips (CS) strips running perpendicular to the anode wires at a 6 mm pitch. Measurement of the combined induced charge distribution on the CS will allow the best resolution to be obtained on the position of the  $e^+e^-$  pairs. The timing of the anode wire pulses will also be read out yielding the position of the initial track ionization perpendicular to the wire direction. The wire signals will be multiplexed using every other wire joined in groups of three to a single electronics channel. The preradiator modules will be oriented with alternating vertical and horizontal wires (horizontal and vertical CS).

In the honeycomb arrangement, when the three pieces shown in fig. 24 are joined two close packed rows of hexagonal tubes are formed. The cell size of each tube is 7 mm between parallel faces. The central foil has strips on both sides which are electrically connected. An attractive feature of this chamber arrangement is the nearly cylindrical geometry in which the strips cover half the circumference of the tubes yielding a larger induced pulse. Where the scintillators make contact with the foil they are not metalized; otherwise they are metalized and connected to ground. As an integral component of the tubes, the scintillators will be constructed precisely from injection molded plastic panels. The side facing the tubes will be formed to the corrugated shape of the tubes, adding mechanical strength to the tube structure. The opposite side will contain grooves every 10.5 mm into which will be placed wave length shifting (WLS) fibers for reading out the scintillators. The thickness of one module, including metal, foils, and scintillator, will be about 1.5 cm making the preradiator depth 90 cm.

The Al comb chambers may provide a simple compact preradiator with comparable

performance. In this case, the cell size will be 5 mm x 5 mm with a maximum drift time of about 70 ns. The 0.5 mm thick Al strongback supports the wires strung through plastic end-pieces and crimp pins. The thickness of the cell divider fins is specified to be 250  $\mu\text{m}$  and the tolerance on the overall flatness of the structures up to 4 m in length is of order 150  $\mu\text{m}$ . For long horizontal wires, small plastic wire support pieces will be installed about every meter. Thin copper coated G-10 with etched cathode strips will be spaced 2.5 mm from the anode wires. Extruded Al combs have been produced with the specifications indicated in fig. 25 by the Northern State Metal Corp.[49] The combs are mounted on 0.4 mm Cu plates which serve as the photon converter material. The CS foils are read out at the ends as in the honeycomb arrangement. Extruded scintillator of thickness 3 mm with grooves for WLS fibers every 1 cm has been tested to produce 8.5 p.e. for a single minimum ionizing particle. In total the modules are 0.9 cm thick providing 2  $X_0$  in 60 modules of 54 cm in depth.

Prototypes are being constructed of both systems mentioned above for evaluation.

In both cases, the majority of the modules are 4.5 m long, with 30  $\mu\text{m}$  sense wires. Panels of size 4.5m x 4.5m will be constructed using 4.5m long 2.25m wide modules, with accommodation made for the beam slit. The fibers will be grouped into 16 cm sections within a panel. The orientation of the fibers will be, alternating along the beam direction ( $z$ ): horizontal (yielding a  $y$  measurement), vertical (yielding an  $x$  measurement), and at 45° (termed  $v$ ). The fibers will extend through one quadrant and be viewed at the appropriate outside edge. For triggering purposes, and to reduce the influence of phototube noise, four planes of sections with the same view, *i.e.*,  $x$ ,  $y$ , or  $v$ , will be ganged together on a single phototube. The entire preradiator will consist of 60 panels with a total of approximately 50,000 wires (with their readout multiplexed by 3), 50,000 strips with analog readout, and 1700 phototubes.

#### 4.7.2 Readout

The anodes and cathodes from each preradiator panel will be read out and digitized individually at the chamber; only digitized information will be taken from the chamber area. Thus, the readout boards on the chambers will each contain the appropriate preamplifiers, discriminators (for time measurements), track and hold circuits (for analog measurements), multiplexing, and digitization circuitry. Because wire chambers are employed it will take several micropulses to accumulate the data from an event. A local trigger formed from regions of interest for the event defined by the scintillator readout arrangement described above will provide the appropriate gates for the chamber information which is to be passed on to the digitizers. Thus the expensive component of the system, *i.e.* the digitizers, will be heavily multiplexed.

#### 4.7.3 Performance

We show in Fig. 26 the angular resolution of photons as determined by GEANT simulation of the preradiator with 3.4%  $X_0$  per layer and assuming 150  $\mu\text{m}$  position resolution for both the CS measurements of  $e^+e^-$  pairs and drift times of initially detected ionization. The resolutions (sigma) obtained are dominated by MCS and vary from 15 mr at  $E_\gamma = 450$  MeV to 33 mr at  $E_\gamma = 150$  MeV. Using position resolutions up to 350  $\mu\text{m}$  worsened the angular

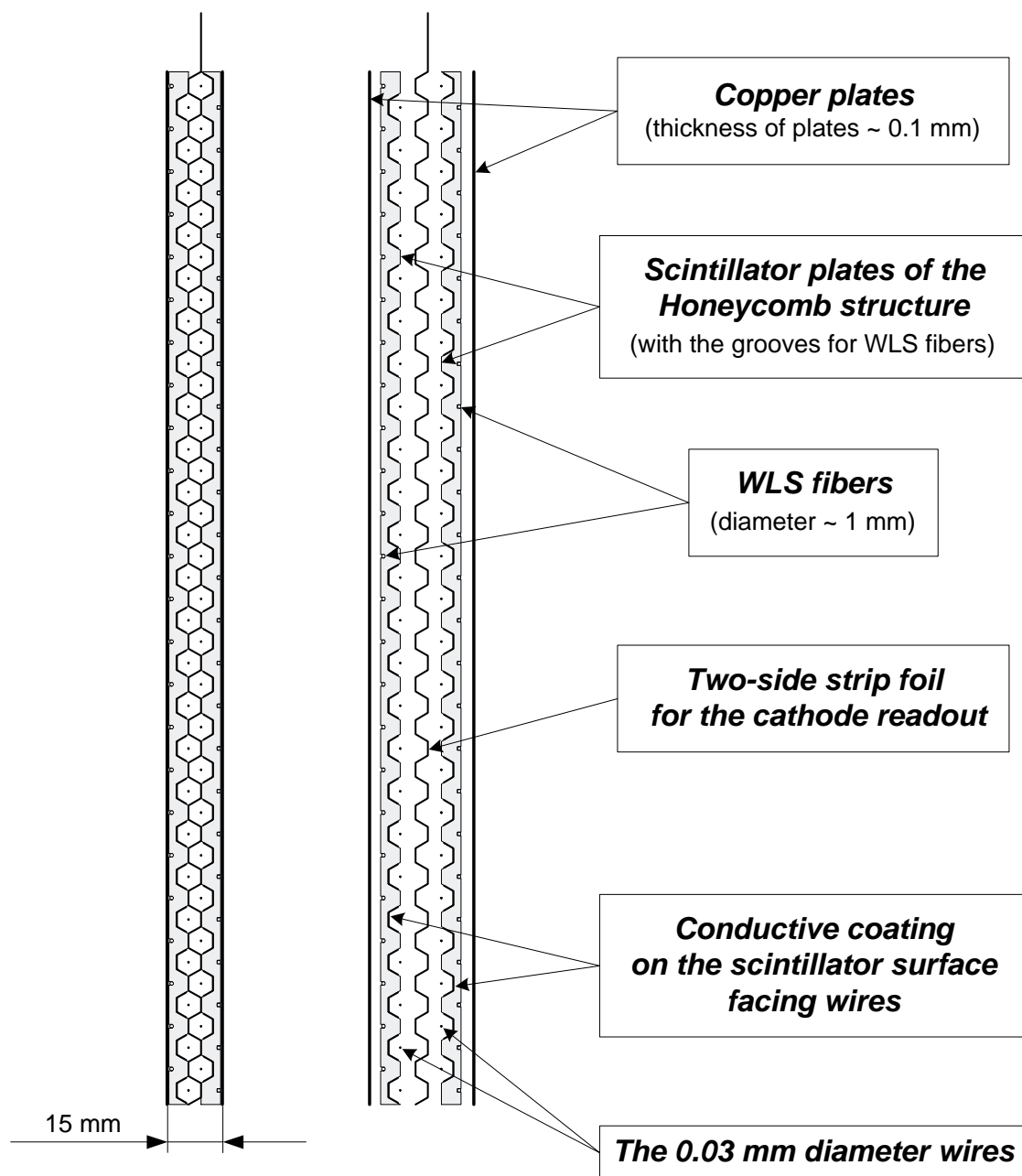


Figure 24: End view of the hexcell preradiator.

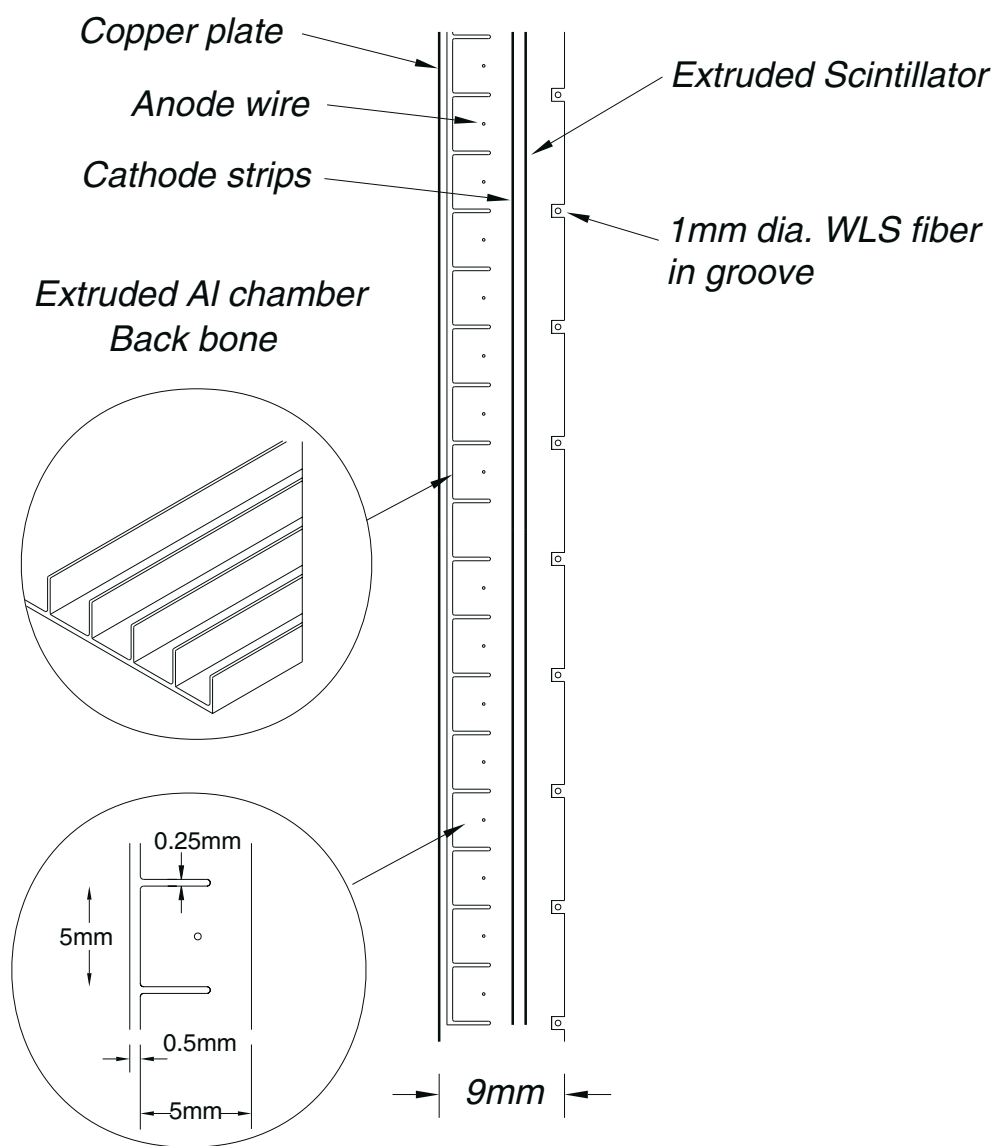


Figure 25: End view of the Al-backbone preradiator.

resolutions by about 10 %. The case shown uses anode drift time information from the first chamber struck by the  $e^+e^-$  pair and averaged position measurements from the CS of the second and fourth chambers hit. Subsequent evaluations of signal and backgrounds described in this report use preradiator resolutions generated in this manner.

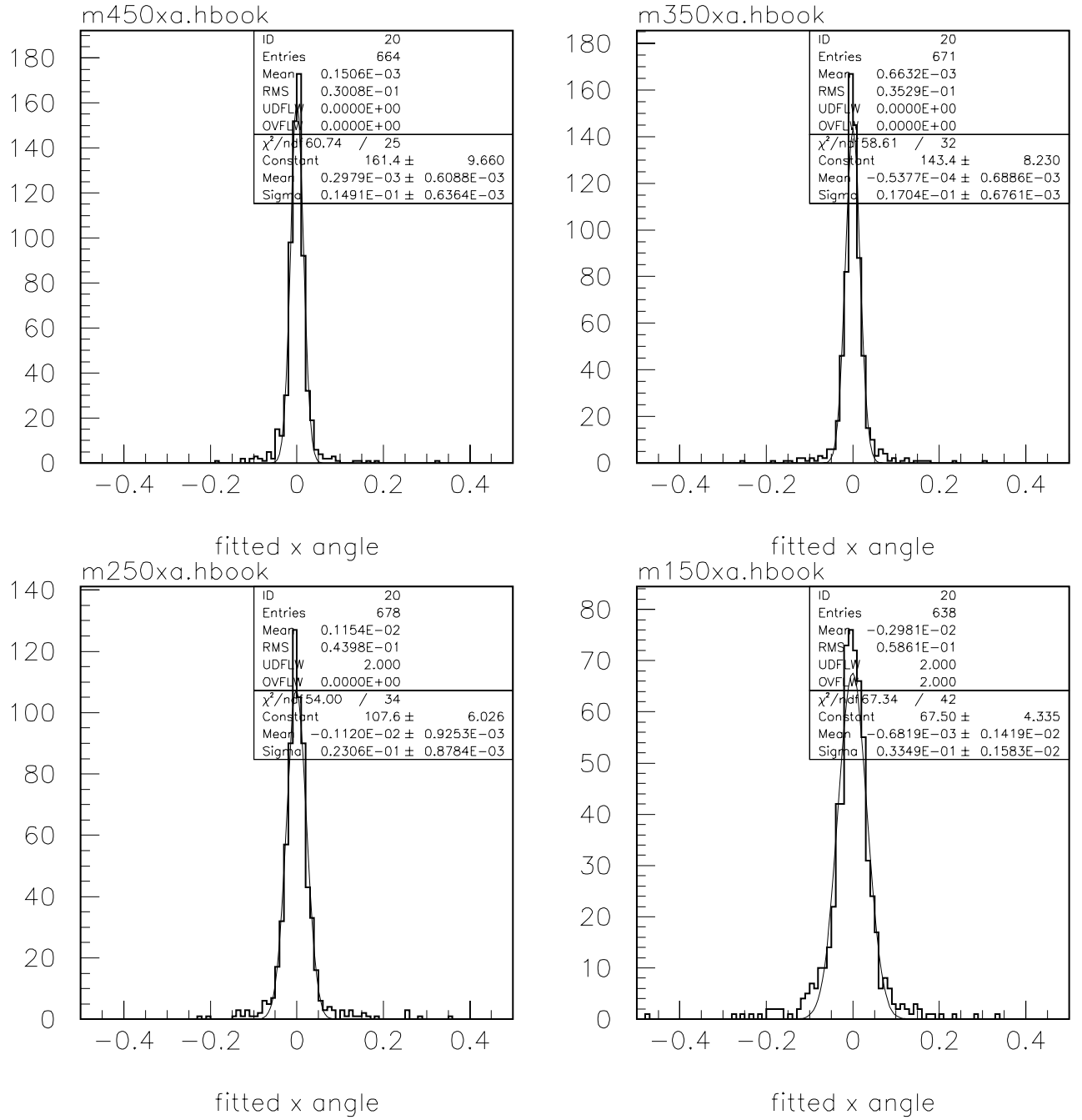


Figure 26: Preradiator angular resolution for various photon energies. GEANT results are shown for  $E_\gamma = 450$  (top left), 350 (top right), 250 (bottom left) and 150 MeV (bottom right).



## 4.8 Calorimeter

In the KOPIO experimental configuration the endcap calorimeter occupies an area of 5.2x5.2 m<sup>2</sup> behind the preradiator. The optimization study described above and other considerations lead to the following requirements for the calorimeter:

1. Time resolution approximately 60 ps/  $\sqrt{E(GeV)}$ ,
2. Energy resolution 3-3.5%/  $\sqrt{E(GeV)}$ ,
3. Granularity 10 cm.

To meet the specified requirements in an economical way we have chosen a Shashlyk based calorimeter. Such a calorimeter is composed of Shashlyk modules which are lead-scintillator sandwiches read out by means of wave length shifting (WLS) fibers passing through holes in the scintillator and lead. While we propose a module with significantly improved performance over previous incarnations, the technique is well proven, *e.g.*, E865 at Brookhaven [50], and has been adopted or is being considered by other experiments, *e.g.*, the PHENIX RHIC detector [51], the HERA-B detector at DESY [52], and the LHCb detector at CERN [53].

We have significant experience with the E865 calorimeter which is composed of 600 such modules and ran reliably in a higher rate environment than that expected in the KOPIO experiment. It is from that experience, and improvements which have been prototyped and simulated, that we draw our confidence that the design goals can be reached.

The E865 Shashlyk module has an energy resolution of 8%/  $\sqrt{E}$ . A new prototype module has been constructed, studied in a test beam, and measured to have a resolution of 4%/  $\sqrt{E}$ . Using this experimental study as a reference point for tuning Monte Carlo simulations, mechanisms for further improvements to achieve the desired performance have been determined and are described below. Details of measurements and calculations can be found in KOPIO technical note [54].

### 4.8.1 Prototype module

The design of a prototype module is shown in Fig. 27. Ten such modules were produced at TECHNOPLAST (Vladimir, Russia). The module is a sandwich of alternating perforated stamped lead and injection molded polystyrene-based scintillator plates. The cross-sectional size of module is 110 × 110 mm<sup>2</sup>; the thickness of plates are 0.35 mm for lead and 1.5 mm for scintillator. Each plate has 144 equidistant holes in a 12 × 12 matrix, with the spacing between the holes being 9.5 mm. The diameter of the holes is 1.5 mm in the lead plates, while the holes in the scintillator have a conical shape with diameter ranging from 1.4 to 1.5 mm. 72 WLS fibers are inserted into these holes. Each fiber is looped at the front of the module, so that both ends of a fiber are viewed by the PMT. Such a loop (radius ~ 3 cm) may be considered as a mirror with reflection coefficient of about 90%. The fiber ends are collected in one bunch, glued, cut and polished, and connected to a 1" diameter PMT.

To increase light collection 60 μm perforated white reflecting paper is interleaved between lead and scintillator plates, and edges of scintillator plates are aluminized. The complete

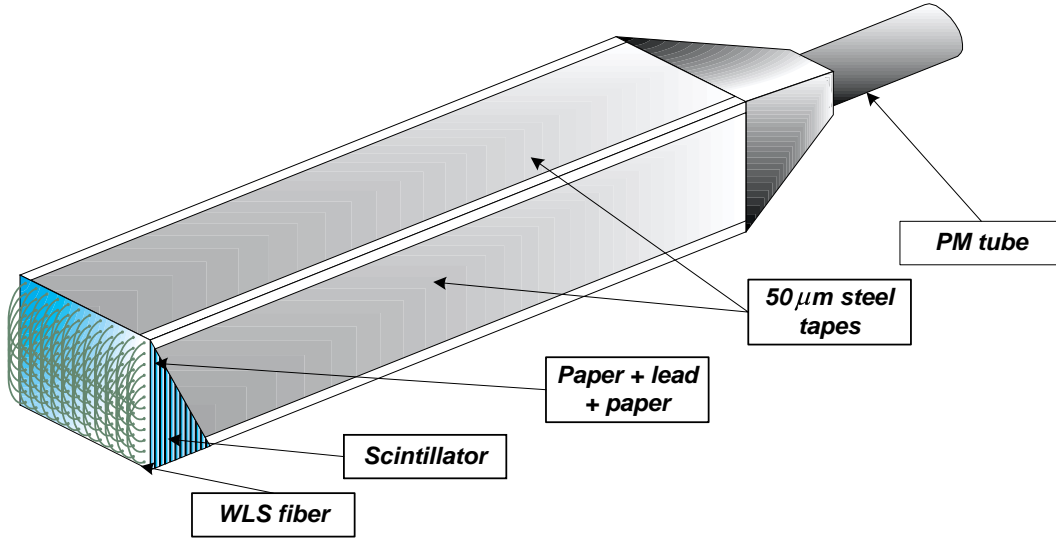


Figure 27: Shashlyk module design

stack of all plates is held in compression by the four  $50 \mu\text{m}$  stainless steel side strips that are pretensioned and welded to both front and back special endcaps.

Parameters of module are summarized in Table 5. The KOPIO calorimeter will contain 2209 such modules.

#### 4.8.2 Experimental study of the prototype module

The characteristics of the modules were studied on B2 test beam at the AGS with 0.5 - 2 GeV/c electrons and pions during the Spring and Fall of 1998. The prototype calorimeter consisted of  $3 \times 3$  modules. The tests examined the response to tagged electrons of different energies and the uniformity of response as a function of incident position of the beam. Three different photomultiplier tubes (FEU85, FEU115, and EMI - 9903B) and three different WLS fibers (KURARY:Y11(200)M-DC, BICRON: BCF-99-29A-SC and BCF-92-SC) were examined.

The results of resolution measurements ( $\sigma_E/E$ ) for various configurations, as well as fits to these data (where  $\sigma_E/E$  is parameterised as  $\sqrt{p_1^2 + p_2^2/E}$ ) are shown in fig. 28. Also shown is a GEANT calculation of resolution in the limit of sampling and geometry alone. One sees from these results that Shashlyk with the Kuraray fiber and EMI tube yield a resolution of  $3.8\%/\sqrt{E}$ .

GEANT simulations are in good agreement with the data of fig. 28 when sampling, leakage, holes, light attenuation, photostatistics, and noise are included in the calculation. The measurements were not sensitive to uniformity of light collection.

Energy resolution depending on the level of details of Monte-Carlo simulation is shown on Table 6.

Table 5: Properties of Shashlyk module.

<i>Item</i>	<i>Dimension</i>
Lateral segmentation	110 mm x 110 mm
Absorber layers	240
Scintillator thickness	Analog NE110, 1.5 mm
Absorber thickness	Pb, 0.35 mm
Reflective material thickness	TYVEK paper, 0.06 mm x 2
Effective $X_0$	31.5 mm
Effective $R_M$	54.9 mm
Number of WLS fibers per module	72
Fiber spacing	9.5 mm
Holes diameter in Scintillator/Lead	1.4 mm/1.5 mm
Diameter fiber	1.0 mm (1.2mm)
Fiber bundle diameter	14 mm (17 mm)
Effective density	2.75 g/cm <sup>3</sup>
Active depth	473 mm (15.9 $X_0$ )
Total depth (without PMT)	610 mm

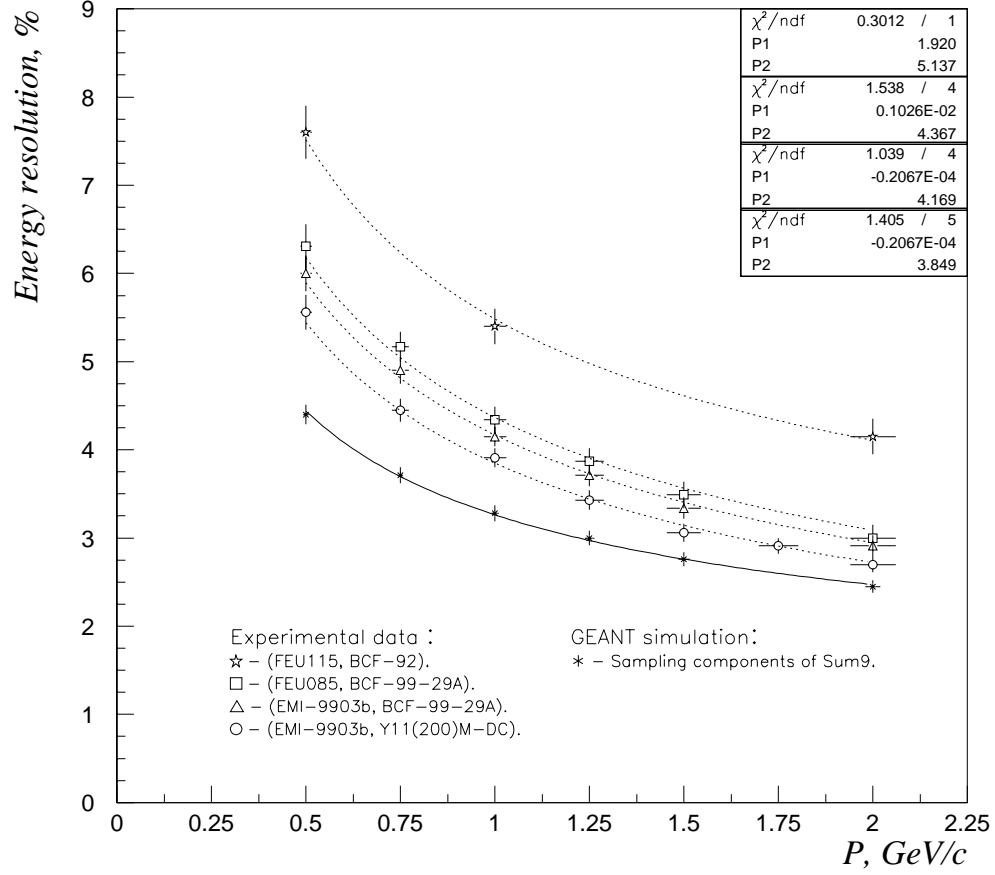


Figure 28: The energy resolution of the nonet of modules versus momentum of the electron beam. The measurements were made for four types of light collection systems (see text). The results of the fit for the different configurations are given in the figure. A GEANT calculation in the limit of sampling and geometry alone is also shown.

Table 6: Energy resolution of uniformly exposed prototype module depending on the level of detail of Monte-Carlo simulation

	$\sigma_E/\sqrt{E}$ (%)
Sampling only	2.69
+ 240 layers	2.84
+ Holes and steel strips	3.04
+ Attenuation in fiber	3.01
+ Photostatistics	3.65
+ $3 \times 3$ modules	<b>3.84</b>
+ Nonuniformity of light collection	4.27

#### 4.8.3 Improving the energy resolution

Sampling constitutes the main contribution to the energy resolution. However, it is less than the combined contribution of other factors, 3.3% (added in quadrature). Among these contributions the most significant are photostatistics, 2.1%, and uniformity of light collection, 1.8%.

The possibilities of improving the sampling contribution are limited. Decreasing the thickness of lead plates or increasing of thickness of scintillator plates increases the effective radiation length of the module, and as a result resolution deteriorates due to longitudinal fluctuations of electromagnetic shower and due to an increased transverse leakage (increased Molière radius). Simultaneously decreasing the thickness of lead and scintillator plates will lower photostatistics. Decreasing lead and/or scintillator plates may also cause technical problems for module production.

Within these limitations we consider 3 possible improved samplings shown in Table 7:

To improve the uniformity of light collection we propose using a chemical modification of a scintillator surface (CMSS) [55] on the edges of the scintillator plates, which produces thin (50-100  $\mu\text{m}$ ) white foam layer with a diffuse reflection efficiency of about 93%. This coating also increases total light output (photostatistics). Monte-Carlo distributions of light output as a function of the distance from the center of modules with and without this coating are shown on Fig. 29

In addition to increasing scintillator plate thickness and fiber diameter, light output may be also increased by establishing optical contact between fiber and scintillator. This may be accomplished by gluing fibers within scintillator holes. Direct measurements on a single plate confirmed this concept. Results of calculations for the 3 versions of modules with the above described improvements is presented in Table 7.

One can see that improvements in mechanical and optical construction of modules can yield an energy resolution of about  $3.2\%/\sqrt{E}$ . There is almost no difference between the expected resolution for versions 1 and 3. Larger longitudinal leakage fluctuations in the case of version 3 can be compensated by a better sampling term. Increasing of the number of modules to capture a larger fraction of visible energy is limited by a greater noise contribution. If fibers are not glued, resolution will be increased by  $0.1\%/\sqrt{E}$ .

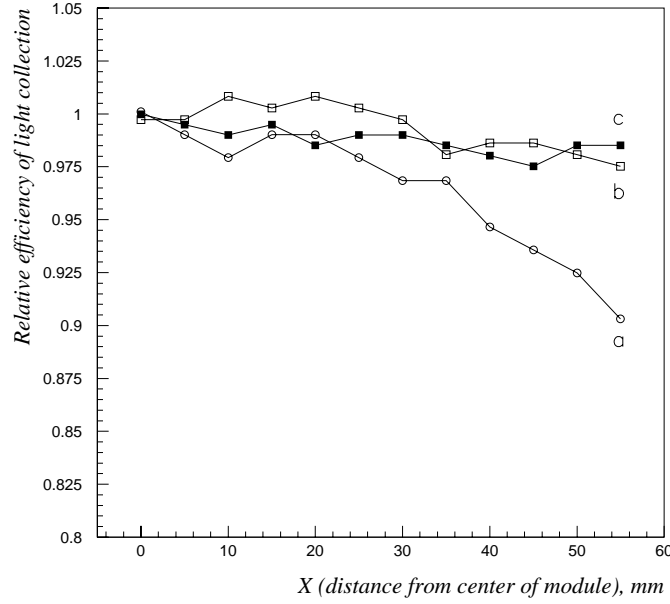


Figure 29: Monte-Carlo dependence of light output on distance from center of module for (a) existing prototype of module, (b) suggested module totally covered by CMSS, and (c) module with CMSS only on edges. Data normalized to 1 at center of plate.

Table 7: Energy resolution ( $\sigma_E/\sqrt{E}$ ) in a module, uniformly exposed by 250 MeV photons, depending on the level of detail of the Monte-Carlo simulation. Statistical accuracy of the calculations is 2%

Module version	1	2	3
Number of layers	400	300	300
Lead thickness (mm)	0.25	0.35	0.25
Scint. thickness (mm)	1.5	2.0	2.0
Fiber diameter (mm)	1.2	1.2	1.2
Sampling only	2.14	2.50	1.91
+ Finite number of layers	2.12	2.54	2.13
+ Holes and steel strips	2.34	2.68	2.31
+ Attenuation in fiber	2.53	2.88	2.57
+ Photostatistics	2.82	3.09	2.75
+ Nonuniformity of light collection	2.87	3.15	2.84
+ 3 × 3 modules	3.17	3.42	3.23
– gluing of fiber	3.28	3.53	3.16

#### 4.8.4 Time resolution

Detailed time resolution studies of Shashlyk modules were performed by the PHENIX collaboration [51]. The results of those studies show that, for 1 GeV electrons, the time resolution for their modules was 100 psec and the light yield was 1200 photoelectrons. The experimental light yield for the prototype module described above was 3100 photoelectrons at 1 GeV, and the anticipated improvement on this is a factor of 2.2. Since time resolution is inversely proportional to the square root of the light yield, we can anticipate a resolution of  $\sim 50 \text{ ps}/\sqrt{E(\text{GeV})}$  for the improved modules. We note that the average photon energy for the experiment is about 250 MeV/c, so our time measurements will have a time resolution on the order of 100 ps.

#### 4.8.5 Summary

Modules for a Shashlyk calorimeter with energy resolution about  $4\%/\sqrt{E}$  have been constructed and experimentally tested. Monte-Carlo simulation based on this experimental data indicates that this resolution can be improved to about  $3.3\%/\sqrt{E}$  with a time resolution better than  $60 \text{ ps}/\sqrt{E}$ . These realizable parameters well meet the design goals of the KOPIO experiment.

## 4.9 Veto detectors

Suppression of most backgrounds is provided by a hermetic high efficiency photon and charged particle detector system. This system divides itself into two sections: the region around the decay volume and the region downstream of the decay volume including the beam catcher. The preradiator/calorimeter also acts as a veto system, thus the decay region is thoroughly enclosed. Figure 4 shows the layout of the various components of the veto system.

### 4.9.1 Decay region veto detectors

Around the decay region the basic element of the photon veto system is a Pb scintillator sandwich consisting of 23 7 mm thick, 15 cm wide scintillator plates interspersed with 1 mm of Pb, see fig.30. The length of each element depends on its specific location in the apparatus, with the longest element being 4 m. The scintillators are extruded, with 1 mm grooves placed 10 mm apart running their full length, see fig. 31. Readout is accomplished with wave length shifting (WLS) fibers placed in the grooves and viewed from each end of the element. In most locations four elements are stacked perpendicularly to the photon direction of flight, providing about 18  $X_0$  of thickness of conversion and detection thickness.

The WLS fiber used is BCF99-29 which has a decay time of about 3.3 ns and an attenuation length of more than 4 m. The fibers are viewed with FEU-115M phototubes at either end. The FEU-115M, produced in Russia, has a photocathode sensitivity extended into the green region, as appropriate for detecting WLS fiber light. Details of construction, testing, and performance of such modules can be found in a KOPIO technical note [57].

From the tests, a single plate of scintillator as described above has a light yield of 17 photoelectrons for minimum ionizing particles. The summed output of phototubes reading out both ends of the fibers shows less than a 10% variation over the length of the scintillator. The light yield corresponds to 12 photoelectrons per MeV of energy loss in the scintillator. This results in about 1300 photoelectrons for minimum ionizing particles passing through the total thickness of a stack, which can be compared with 750 photoelectrons for the photon veto counters in E787. Comparison with E787's results is important since it is the performance of that veto system which is well documented [58], and with which we make our veto efficiency estimates.

The method of stacking the veto modules around the decay volume is depicted in figure 4. The nature of the modules allows their ends to be curved, thus facilitating the construction of the hermetic enclosure. Straight modules span the roof, floor, and upstream parts of the enclosure, while curved modules make up the sides. The modules spanning the 3.5m width of the top of the enclosure are supported by an external truss structure via thin ( $\sim 100\mu\text{m}$ ) straps extending down from the external support beams, see fig. 32. For the side walls the modules will be mounted in shelves which support their weight.

Because backward going photons have low energies, the scintillator to lead ratio and the number of WLS fibers per plate will both be increased for the upstream modules.



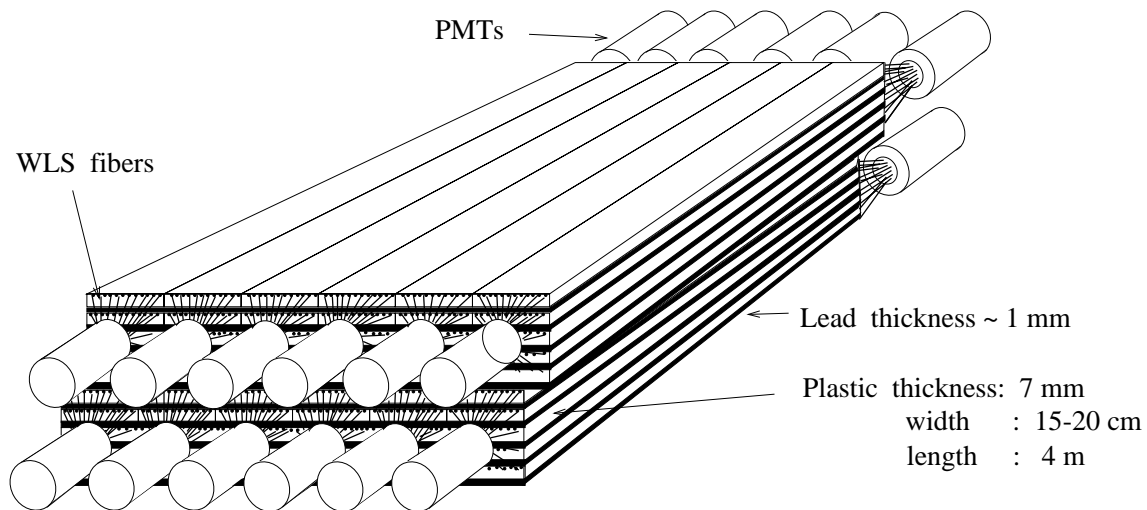


Figure 30: Isometric schematic view of twelve veto elements.

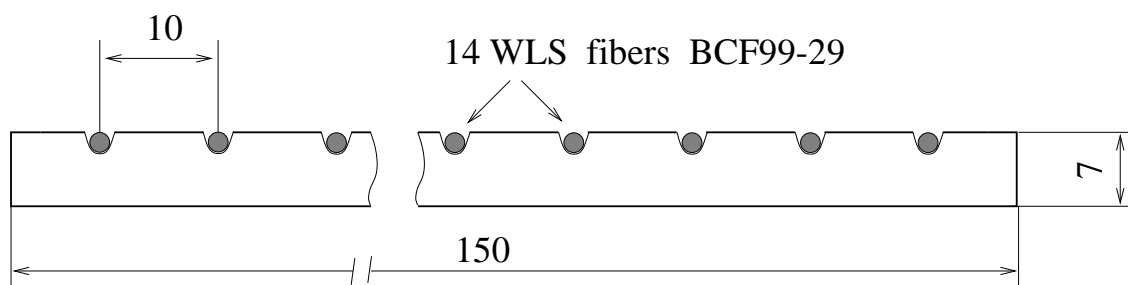


Figure 31: End view of a scintillator plate.

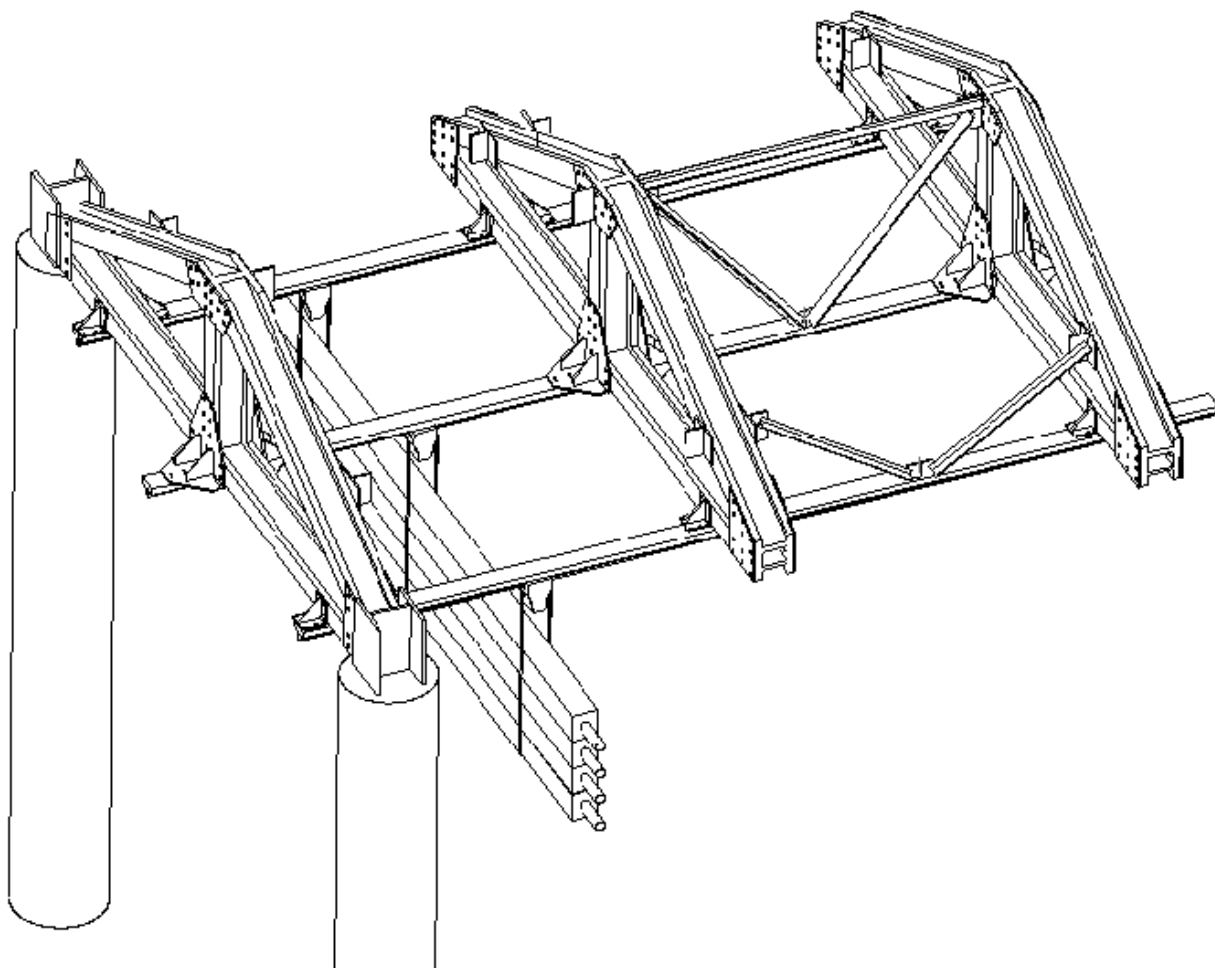


Figure 32: Support structure for the roof veto counters.

### 4.9.2 Charged particle and downstream veto detectors

Vetoing charged particles is important for suppressing background modes such as  $\pi^+\pi^-\pi^0$  and  $K_{e3}$ , and for reducing the trigger rate. The most dangerous mode is the former, and after kinematic suppression must be suppressed by a factor of  $10^9$  to yield a  $\pi^+\pi^-\pi^0/\pi^0\nu\bar{\nu}$  ratio of less than 0.1.

To achieve the required high veto efficiency we will have two levels of detection for charged particles. In the decay region, scintillator inside the vacuum vessel forms the first line of defense. The vessel will be lined with 7 mm of scintillator which will be read out with embedded WLS fibers running longitudinally. For readout, the fibers will run upstream along the walls of the upstream beam pipe of the vacuum vessel, and exit the vacuum through the pumping station box upstream of the detector. The second detection of charged particles in the decay region will be with the photon veto system where the first plate in each element is a scintillator plate. This method has the added advantage of also detecting photons which might result from charge exchange of  $\pi^-$ s coming from  $K^0$  decays.

In the downstream beam hole direction beyond the calorimeter, charged particles will be swept out of the neutral beam with the bending magnet, seen in fig. 4, and into veto scintillators. By and large these counters will also be backed by photon veto counters.

Photon vetoing downstream of the calorimeter will be accomplished with counters whose construction is essentially as described above. Because of the large angles of photon trajectories in the horizontal plane, the downstream beam pipe will be lined in its median plane with similar detectors.

### 4.9.3 Beam catcher

The requirement of high veto efficiency is true for all directions of flight of the extra photons, including the region occupied by the beam. This presents a challenge since the beam region contains as many as  $10^{11}$  neutrons per 100 TP machine pulse, as well as  $1.7 \times 10^8 K_L^0$  per pulse. Fortunately, however, only a few times  $10^{-3}$  of the undesirable events send their photon into the beam region 15 m downstream from the decay region, and most of those photons have energies above 100 MeV. Thus, the detector that must operate in the beam region, termed the catcher, need only have a detection efficiency of about 99% to achieve the required background suppression.

#### Catcher Designs

##### **Pb-Lucite Sandwich Catcher**

At present we are considering two catcher designs. One is the detector based on Pb-Lucite sandwiches viewed on edge by means of total internally reflected Cerenkov light. It is blind to low energy protons and charged pions due to Cerenkov threshold or total reflection threshold, and thus is expected to be blind to neutrons.

Based on this design, a prototype counter has been constructed and tested in three kinds of beams, 100–400 MeV photons, 200–400 MeV neutrons, and 200–1200 MeV protons. A module is composed of 8 layers of 2mm-thick lead sheets and 9 layers of 10mm-thick Lucite sheets stacked alternately, viewed by two 5-inch photomultipliers from both (up and down) ends of Lucite sheets. Four identical modules are placed in series along the beam direction,

and the total thickness is equivalent to  $12 X_0$ .

In a photon beam at INS (KEK-Tanashi), its inefficiency has been measured with various photon energies and threshold values, as shown in Fig. 33. We have found that the distribution

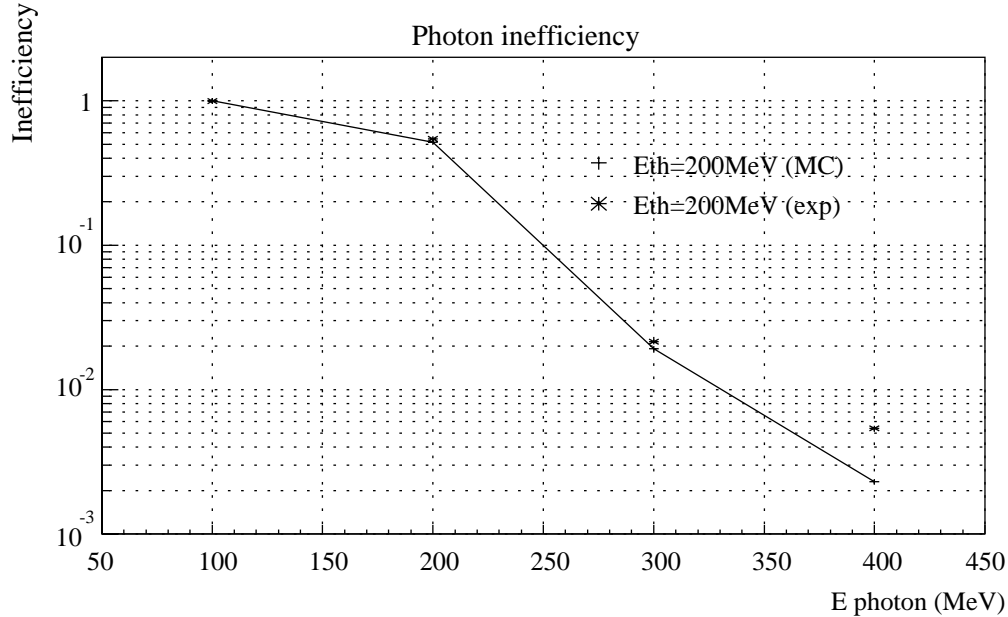


Figure 33: Photon inefficiencies as a function of incident energy with energy threshold of 200 MeV.

is well reproduced by MC simulation so far as 0.5% level.

As for the neutron efficiency, we have performed two measurements. In a low energy region around  $\pi^0$  production threshold, we have measured the neutron efficiency directly using the neutron TOF beam line at RCNP (Osaka). In a high energy region where a neutron might come within the event time window, i.e. above 1500 MeV/c ( $E_{n,kin}=830$  MeV), we have measured the efficiency for protons (instead of neutrons) and compared it with a MC simulation to verify the validity of the nuclear interaction part in the simulation. Even though detailed analysis of these measurements is still proceeding, the simulation says that if we set the energy threshold at 200 MeV, we can obtain 98% photon efficiency above 300 MeV, while the neutron efficiency can be kept as low as 1% level at 1500 MeV/c, as shown in Fig. 34

Studies are continuing to improve the low energy detection efficiency and to reduce the neutron efficiency by other cuts. This design and the results of the tests are presented in a KOPIO technical note [56].

### Aerogel Distributed Catcher

The other design [59] takes advantage of the low energy of the beam to produce inefficiency in neutron and beam kaon detection without sacrificing photon detection efficiency. This is possible since the photons we wish to veto are coming directly down the beam line, while the particles to which we wish to be blind arise from low energy  $\pi^0$  decays and knock-

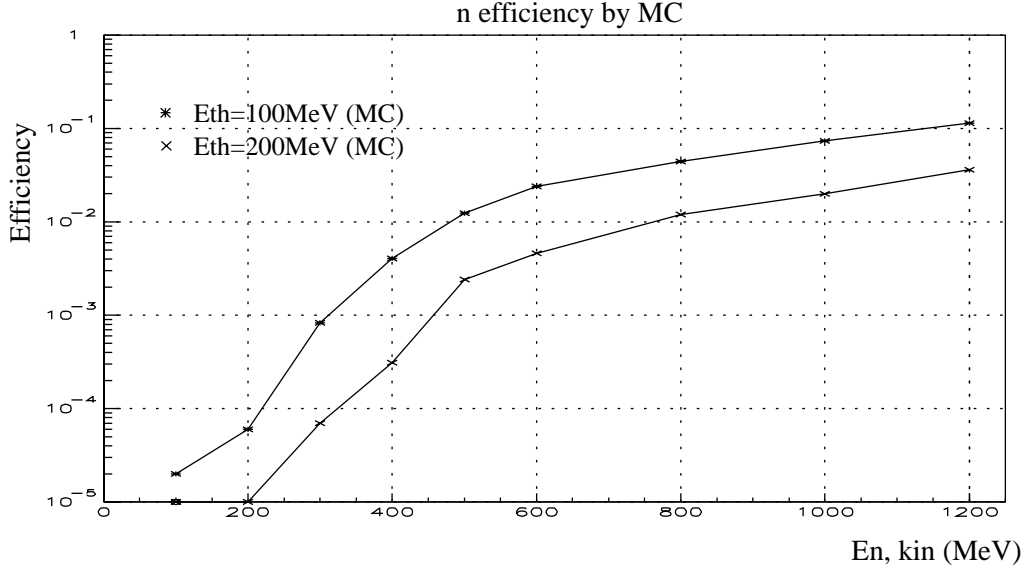


Figure 34: Simulated neutron efficiencies as a function of incident energy, with thresholds of 100 MeV and 200 MeV.

on proton recoils which are produced over a wide range of angles with respect to the beam. The basic concept is to convert the photons, detect the resulting electron/positrons through Cerenkov radiation, and veto those which are traveling in the beam direction.

The catcher consists of 600 modules of the design shown in fig. 35. The modules are arrayed in 25 rows (transverse to the beam) of 24 modules, with the rows separated by 25 cm. The radiators are 5 cm thick aerogel with index of refraction about 1.03. Such a radiator raises the threshold velocity of charged particles high enough so that knock-on protons produced by beam neutrons make no light. That aerogel can be reliably used in this application has been demonstrated by the HERMES collaboration [60]. The HERMES group notes that new production techniques now yield very transparent hydrophobic aerogel with indices of refraction in the range 1.01 to 1.1. We choose 1.03 since the HERMES group performed their beam tests with this material and were able to obtain more than 20 photoelectrons from a 5 cm thick radiator.

Each module segment contains  $1/3 X_0$  of material. Along the beam there are 25 segments for a total of  $8.3 X_0$  over a distance of 6.3 m. The modules in a row are staggered laterally by half a module width from those in the following and preceding rows. Vetoing will occur if there is coincidence between the module in which the photon converts and either of the modules directly in back of it in the next row.

The unscattered Cerenkov light emerging from the downstream end of each aerogel slab will be focussed and reflected by a section of spherical mirror with its axis tilted vertically at  $45^\circ$  to the horizontal. Such light can be focussed onto a 5 cm PMT mounted vertically over, and pointed at the mirror. That a sufficient amount of such unscattered light can be captured has been demonstrated in the HERMES R&D program.

We have performed a GEANT Monte Carlo calculation which simulates three types

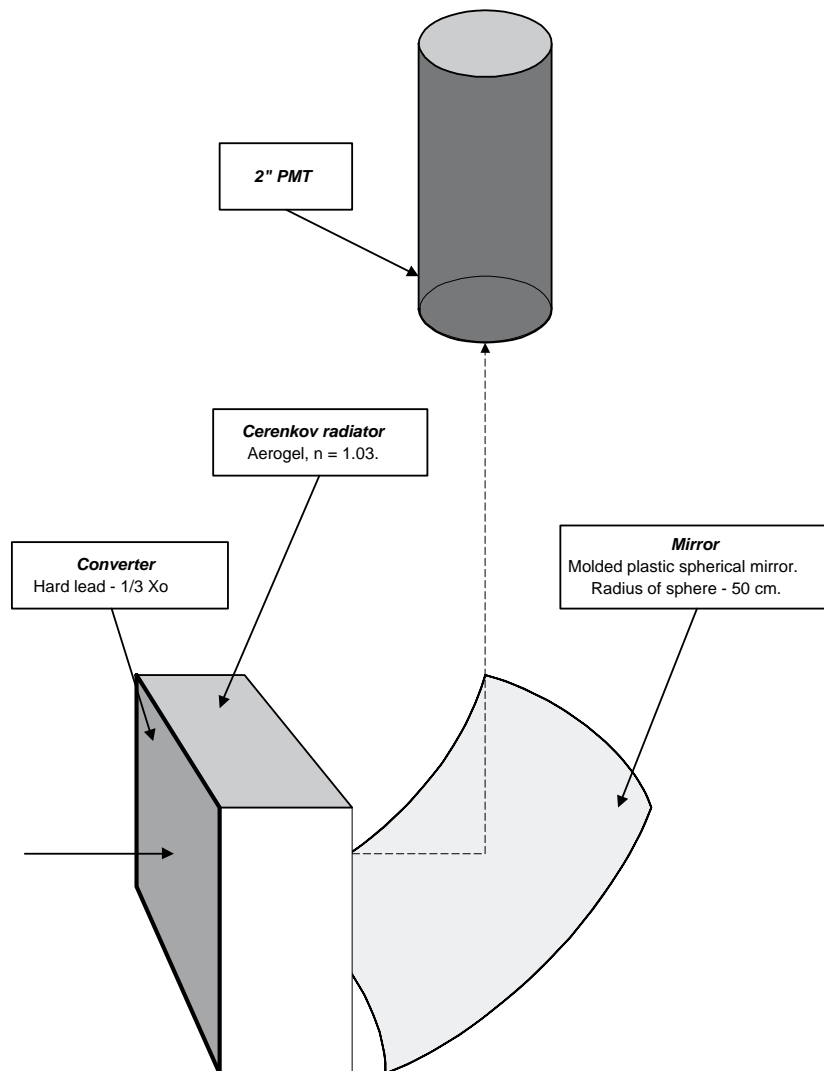


Figure 35: A catcher module.

Table 8: Efficiency of the catcher for various incident particles.

Mode	Momentum (MeV/c)	Efficiency (%)
Decay photons	100.	89.
	200.	95.
	500.	98.5
Beam neutrons	1500.	0.34
	3000.	4.
Beam $K_L^0$	750.	3.4

of events: photons coming from the beam region of the decay volume; neutrons in the beam; and  $K_L^0$ s in the beam. The momenta of the kaons were chosen from a Gaussian distribution centered on 750 MeV/c with a standard deviation of 250 MeV/c. Table 8 shows the efficiencies for detecting these types of particles, where the efficiency is for detection of light in two longitudinally contiguous segments.

From our Monte Carlo calculations  $K_L^0 \rightarrow \pi^0 \pi^0$  events with a photon in the catcher will result in about a 20% addition to the background, and an accidental veto probability due to neutrons of about 10%.

One must also consider the blindness probability, *i.e.* the probability of having any member of a set of counters destined to veto an event being blinded by another hit within, say, 10 ns of the event. Due to the high granularity of the catcher this is reduced to less than a percent for hadronic interactions. Another source of blindness, however, is the prompt photons associated with the beam. These show up at the catcher 4-7 ns before those we wish to veto, thus they will not cause accidental vetos. But they will illuminate the catcher and possibly cause blindness. We calculate the probability of this occurring to be less than  $8 \times 10^{-3}$ . Improving the pulse pair resolution of the detectors to better than 4 ns can significantly reduce this probability, and we are undertaking an R&D program to this end. We expect to instrument each catcher phototube with a transient digitizer operating at 0.5-1.0 GHz.

## 4.10 Trigger

The basic idea of the trigger is quite simple: two and only two photons appearing in the forward detector and no other particles appearing anywhere else in the veto system.

### 4.10.1 Trigger scheme

There will be about  $4.2 \times 10^7$  kaon decays per 3-s machine pulse in the detector volume, corresponding to a decay rate of  $\sim 14$  MHz. With a micro pulse frequency of 25 MHz, the probabilities of zero, one and two or more  $K_L^0$  decays within a micro pulse are about 60%, 30% and 10%, respectively. Because the decay volume is 4 m long, the time between photon conversions in the forward detector and particles interacting in the veto counters ranges from zero to 12 ns. Since the RMS spread in kaon decay times within a micro pulse is comparable, about 15 ns, we cannot reliably veto one  $K_L^0$  decay and accept another within the same micro pulse. We thus choose at the outset to trigger only on those micro pulses with single decay in which exactly two photons are present in the forward detector, and no veto counters fire. Although this costs about 40% of the possible  $K$  decays, it greatly simplifies the trigger scheme and allows a reasonable trigger rate.

The Level-0 trigger requires the presence of activity in the pre-radiator, no energy deposited in the barrel region (with a threshold of 5–10 MeV), no charged particles observed, and minimum and maximum numbers of hits in the pre-radiator scintillators and calorimeter. Another fast effective logic scheme will require cuts on the average hit positions in the  $x$  and  $y$  projections (a very crude form of transverse momentum balance). Two-dimensional cluster counting in the  $x - y$ ,  $x - z$  and  $y - z$  planes will also be applied at this level.

In order to recognize two and only two conversions in the forward detector system we group the scintillators in the preradiator to form three dimensional “cells”. Each plane of the preradiator will be divided into quadrants, and the fibers of each quadrant grouped into 16 cm units. The orientations of the fibers in contiguous planes along the beam ( $z$ ) direction are horizontal ( $x$ ), vertical ( $y$ ), and at  $45^\circ$  ( $v$ ). This pattern is repeated along the length of the preradiator. Because each scintillator yields a relatively small number of photoelectrons (about 7) and to reduce the influence of phototube noise in the photon energy measurement, we group four planes of fiber units together, *i.e.*, four  $x$ ’s, four  $y$ ’s and four  $v$ ’s. One cell has a volume roughly 18 cm in  $z$  and 16 cm in  $x$  and  $y$ . (The redundant  $v$  plane is present to remove (off-line) the combinatorics in  $x - y$  that would occur with two conversions in the same quadrant at the same depth. This information is not used at Level-0.) The numbers of clusters of cells in the  $x - y$ ,  $x - z$  and  $y - z$  planes, after projecting hits onto each plane, are obtained using fast logic based on gate array chips or memory lookup units. There are five cell-planes in the  $z$  direction and the calorimeter is treated as the sixth column element in the  $x - z$  or  $y - z$  matrix. As presently conceived this approach is about 97% efficient at recognizing  $\pi^0$ s from  $\pi^0\nu\bar{\nu}$  events. Roughly 5% of  $\pi^0\pi^0$  events fail to be rejected due to overlapping photons.

Most veto counters will be viewed from both ends and mean-timed. They will be appropriately delayed to compensate for hit positions along the beam, *i.e.*, upstream, in the barrel, or at points along the downstream regions. With the time of veto counter hits so adjusted, the number within a given micro pulse can be determined. This process will be



“pipelined”, so it imposes no dead time.

Once this level of trigger (L0) is satisfied, the time and analog information from all counters and from the appropriate channels of the preradiator will be digitized and read out. The delay of the trigger is constrained to be on the order of 150-200 ns since that is the evolution time for the analog information from the strips in the preradiator chambers.

#### 4.10.2 L0 Trigger rates

To determine the rates of the Level-0 trigger output, Monte Carlo simulations were done. Events were generated for various decay modes, and the Level-0 trigger logic was applied. A photon veto threshold for the barrel region was set at 5 MeV (visible energy). The charged particle detection inefficiency was conservatively assumed to be 1 %. Table 9 summarizes the number of Level-0 triggers per machine cycle for the various modes for which significant numbers of triggers are expected.

Table 9: Number of L0 triggers per machine cycle for various decay modes.

Mode	B.R.	Triggers
$\pi^\pm(\mu + e)^\mp\nu$	0.66	200
$\pi^0\pi^0\pi^0$	0.21	600
$\pi^+\pi^-\pi^0$	0.13	20
$\pi^0\pi^0$	$10^{-3}$	100
$\gamma\gamma$	$6 \times 10^{-4}$	900
Accidentals		2000
Total		3820

#### 4.10.3 Higher level trigger rates

Although the present Level-0 estimate reduces the data flow to a manageable level, we are considering several schemes of higher level triggers based on the fast digitized information available on energy and time to further reduce the data volume before events are fully read out. These include requirements of unbalanced sums of observed energies and transverse momenta, and cuts based on refined timing information and tracking. As an example consider  $K_L \rightarrow \gamma\gamma$  events. Given that the full rest mass energy of the  $K_L^0$  goes into the photon energies in  $K_L \rightarrow \gamma\gamma$  decays while only a fraction goes into those of  $K_L \rightarrow \pi^0\nu\bar{\nu}$  decays, the total laboratory energy of the photons in the former is usually greater than that in the latter. That this is true can be seen in fig. 36. Forming a correctly compensated analog sum of the total energy seen in the forward detector allows one to cut high energy ( $2\gamma$ ) events while having a small impact on the desired  $\pi^0\nu\bar{\nu}$  events. The MC simulation indicates an additional suppression factor of 5. Similar suppression factors are obtained for other “energy conserving” decay modes such as  $K_L^0 \rightarrow \pi^0\pi^0\pi^0$ . This logic scheme can be further improved by combining it with the time-of-flight information, which compensates for the variation in the incident  $K_L$  energy.

Another example is the reduction of accidental events by employing tighter timing, and hit patterns and energies of struck cells available from digitized information.

The Level-1 scheme with a decision time of  $\sim 10\mu s$  is based on a combination of highly multiplexed fast ADC's for triggering, memory lookup units for providing energy calibration, and arithmetic units for energy summing or energy-weighted hit-position determination. The read-out process will be aborted (with the additional deadtime of  $\sim 1\mu s$ ) if it fails the logic. The DAQ system reads out the data from the detectors, most notably the preradiator chambers, at a rate of  $10^3$  events per  $\sim 3$  second machine spill. This will require one level of buffering in order to keep the dead time below a few percent. As described in the DAQ section, such a system will be straightforward to implement using present technology.

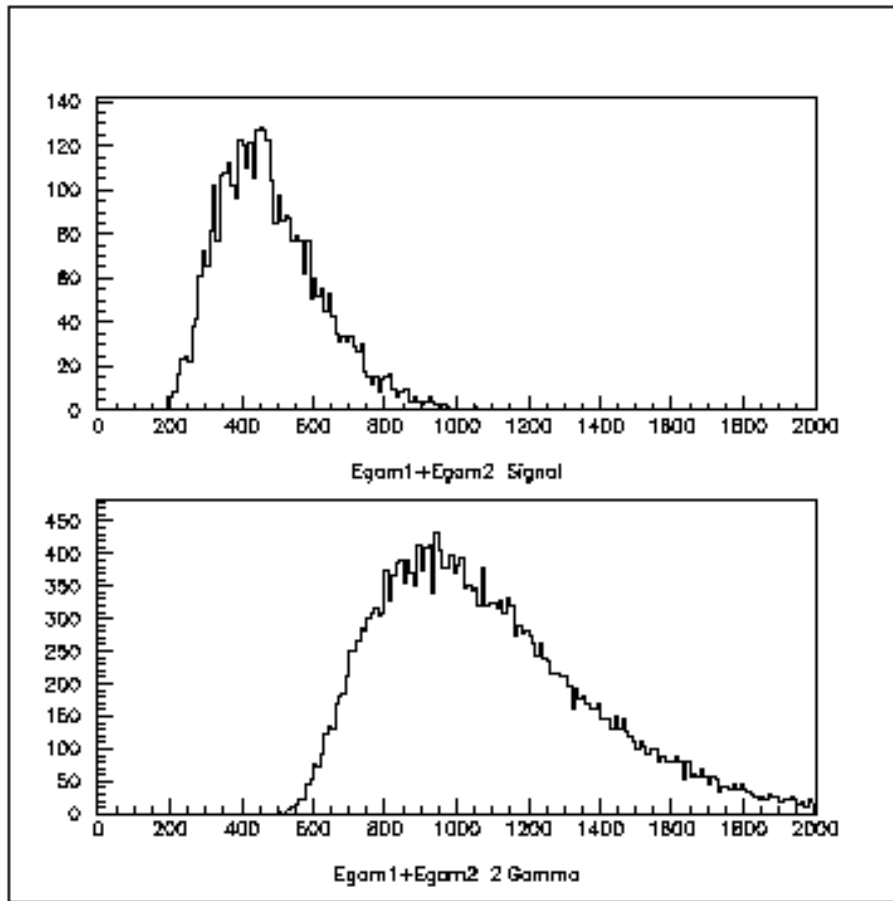


Figure 36: Total 2 photon laboratory energy of  $\pi^0\nu\bar{\nu}$  signal events (top), and of  $2\gamma$  events (bottom).

## 4.11 Data Acquisition

After the hardware trigger Level 1, the data acquisition system receives the following information:

- analog signals from phototubes ( 4000 ch) are fed into either switched capacitor arrays SCA, transient digitizers, or ADC/TDCs readout into buffer modules located in a VME-P crate. ADCs in other formats will be read via a custom interface into similar buffer modules. It is assumed that the density of modules achieved will be 256 channels per crate for a total of sixteen crates; and,
- digitized data from chambers that gets stored into large memories located in a VME-P crate. Each VME-P crate has enough storage to keep events from one given spill. In the inter-spill, the data is moved over Fast or Gigabit Ethernet through a network switch. A 16 processor farm receives the data for Level 3 processing and data reduction. Commodity CPU's without monitors will be used to keep costs down. A large CPU host collects the events from the farm and data is written to disks and logged to tape in the background

Table 10: A summary of data rates.

Modes	# of $\gamma$ /ev	Data /ev / K Bytes	Trig./spill After L2	Data/spill K Bytes
$\pi^\pm(\mu + e)^\mp\nu$	2	2.7	200	540
$\pi^0\pi^0\pi^0$	6	7.1	120	852
$\pi^+\pi^-\pi^0$	4	2.7	20	54
$\pi^0\pi^0$	4	4.9	20	98
$\gamma\gamma$	2	2.7	180	486
Accidentals		2.7	1000	2700
All				4730

Data rates have been estimated assuming the following: each  $\gamma$  will generate 8 phototube pulses and 35 layers of chamber hits in the preradiator and 9 phototube pulses in the calorimeters. Each phototube pulse is sampled (8 bit samples) at 500 MHz for 50 ns for an average of 32 Bytes/pulse<sup>5</sup> and each layer of chamber hits is digitized in 16 Bytes. This adds up to a total of 1.1 KB/ $\gamma$ . Extra overhead from header data and randoms in the veto counters is estimated at 0.5 KB/ev

Although the signature of the trigger will be the presence of two gammas, some of the backgrounds really contain more gammas. These events will trigger when pairs of gammas are located in the same area. Data produced by such a pair will have more data than a clean gamma and thus we have calculated the rates based on the number of gammas in

---

<sup>5</sup>Data rates are estimated assuming all pmt pulses are transient digitized at 500 MHz.

each trigger. Assuming trigger rates as described in the previous section and the results of preliminary Monte Carlo calculations, we estimate data rates shown in Table 10.

The estimated total data rate of  $< 5$  MB/spill can be handled easily by two DLT7000's. Monitoring and calibration triggers are accounted for by raising this rate to 7 MB/spill. Such a data acquisition system collects data at a rate less than that presently handled in the E787 experiment.

## 4.12 Simulations

We simulated the performance of the KOPIO detector in order to estimate the acceptance for  $K_L^0 \rightarrow \pi^0 \nu \bar{\nu}$  and the suppression of backgrounds. Since the KOPIO neutral beam is planar as indicated in Fig. 5 (see Overview Section), the decay vertex is obtained from the preradiator measurement of each photon conversion position and direction extrapolated to the beam plane. The position and direction of the other photon, the time difference between the two photons (i.e. the path length difference between the photons and the vertex), and the  $\pi^0$  mass provides up to four additional constraints. These extra constraints are effective in removing non-Gaussian tails, particularly in the preradiator angular measurements. The  $K_L$  energy is measured by time-of-flight and its direction is obtained by connecting the production target position and the decay vertex.

Figure 26 [in Sec 4.7] shows the simulated preradiator angular resolution distributions obtained for several photon energies. The angular resolution function is parameterized by two Gaussians, one of which represents the core and the other accounts for the tail due to large angle scattering of the electron or positron. Table 1 lists the resolution parameters used in the simulations including effects of the energy dependence of the angular resolution. Typically 200k Monte Carlo events were generated for each mode used to study the acceptance and background rejection. Up to 100M events were generated to examine the rarest cases such as photons missing in the beam holes.

The analysis of the Monte Carlo data was performed in 2 steps. First a 3C constrained least square kinematic fit was performed without using the  $\pi^0$  mass constraint. This fit provided the two-photon invariant mass  $m_{\gamma\gamma}$ . Fig 37(a) shows the  $\gamma\gamma$  mass distribution for signal events with  $m_\pi^0$  resolution (RMS) approximately 10 MeV. In the second step, a full

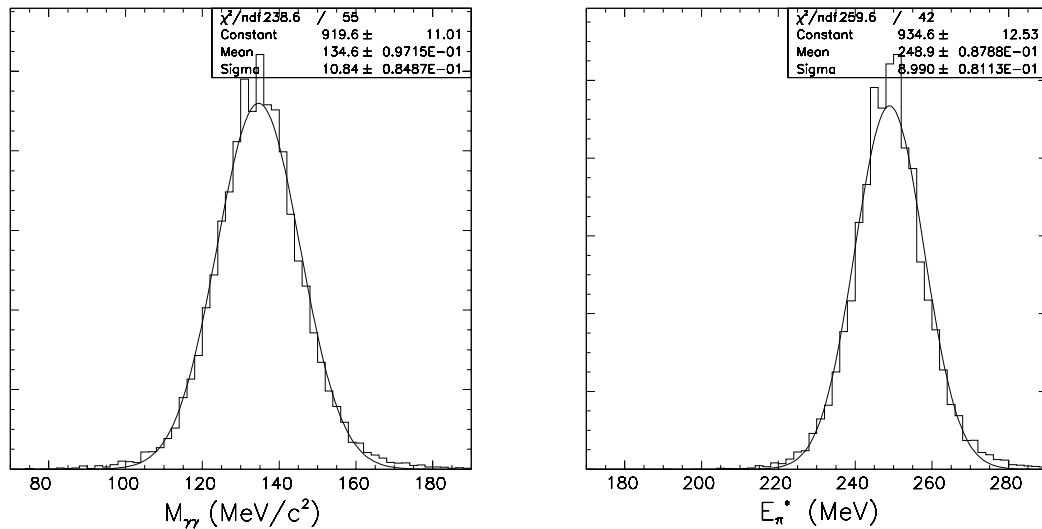


Figure 37: Reconstructed  $\gamma\gamma$  mass and  $E_\pi^*$  from the detector simulation for the  $K_{\pi_2}^0$  even paring events.

4C constrained fit was performed including the  $\pi^0$  mass constraint to achieve the best vertex and energy resolutions. Fig 37(b) shows the reconstructed  $E_\pi^*$  distribution for the  $K_{\pi_2}^0$  even paring events, and Fig 38 shows the reconstructed  $K_L$  decay vertex resolution distributions with  $\sigma_x = 7$  cm,  $\sigma_y = 1.3$  cm, and  $\sigma_z = 14.6$  cm.

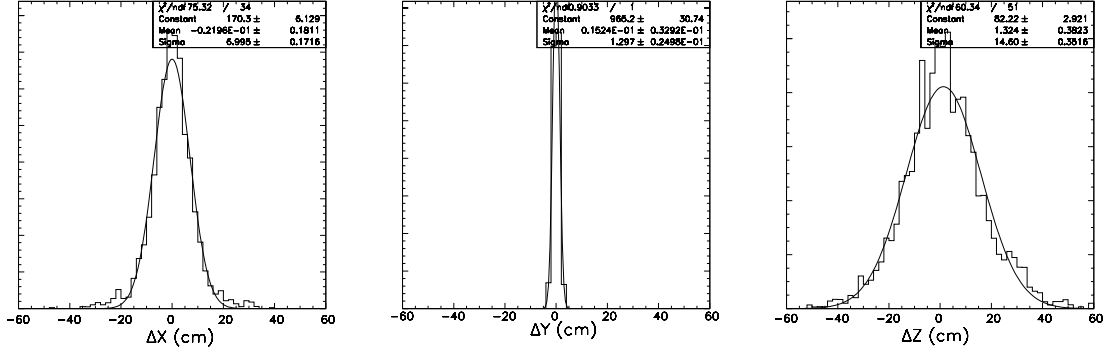


Figure 38: Reconstructed  $K_L$  decay vertex resolutions.

## 4.13 Background Rejection

### 4.13.1 Photon veto

High detection efficiencies for additional photons and charged particles are the primary defenses against backgrounds in the  $K_L^0 \rightarrow \pi^0 \nu \bar{\nu}$  measurement. However, there are barriers to achieving unlimited efficiency such as photo-nuclear interactions in which the photon energy is transferred entirely to neutrons to which we are mostly blind. In the following we deal with the limits of photon detection efficiency, the KOPIO kinematic method of suppressing the most dangerous background with extra photons due to  $K_{\pi 2}^0$ , and the problems of photons escaping detection in beam holes and within the showers of other photons.

Charged particle detection efficiencies are also relevant to the suppression of backgrounds like  $K_{e3}$  and  $K_L^0 \rightarrow \pi^+ \pi^- \pi^0$ . The detection efficiency for pions and electrons will be discussed in the context of the background estimates for these modes presented in the next section.

#### Photon Detection Efficiency

E787 has achieved a  $\pi^0$  detection inefficiency of  $< 10^{-6}$  for 200 MeV/c  $\pi^0$  decays which yield photons between 20 and 225 MeV. The detector employs lead/scintillator calorimetry similar to that proposed for KOPIO. The central E787 photon detector consisted of about 1 radiation length ( $X_0$ ) of plastic scintillator (range stack) followed by multiple layers of 1 mm thick lead and 5 mm thick scintillator (barrel veto) for a total of about 15  $X_0$ . The greatest inefficiency, 1%, occurs for photon energies  $\leq 20$  MeV due to sampling fluctuations. The inefficiency for higher energy photons was  $10^{-4}$  and appeared to be limited by sampling fluctuations, shower escape and photo-nuclear reactions which may be contributing at comparable levels.

Progress on the limits of photon detection has been made in a beam test at INS (Japan)[61] where the efficiency for detection of photon-induced events with photo-nuclear interactions (i.e. those in which soft neutrons were also detected) was made in the energy range from 185 MeV to 1 GeV. Single photon inefficiencies as low as  $10^{-6}$  for 1 GeV photons could be inferred from these measurements under the assumption that no events occur in which high energy neutrons carry off all the missing energy. If this assumption were valid, the efficiencies quoted below for higher energy photons would be considerably improved with the consequences of much reduced backgrounds and higher acceptance for KOPIO. However, in order to determine the true photon veto inefficiency at higher energies than covered by E787, construction of a full  $4\pi$  spectrometer like that needed for a  $K \rightarrow \pi \nu \bar{\nu}$  experiment will be required. Thus, due to the uncertainties in the validity of the inefficiencies inferred in Ref. [61], we will use only the levels already demonstrated by E787 in our estimates below. Uncertainties in the level of photon detection efficiency achievable are actually largest for the region  $E_\gamma \leq 20$  MeV which is preferentially populated by higher energy  $\pi^0$  decays due to Lorenz boosting. For these photons, the detection efficiency is minimal at best and additional measures must be taken.

#### Suppression of photons in $K_{\pi 2}^0$ decays

In order to fully suppress  $K_{\pi 2}^0$  backgrounds, a  $\pi^0$  detection inefficiency of  $10^{-8}$  is required. This is a realistic goal in KOPIO where both “missing” photons from  $K_{\pi 2}^0$  decay can be required to be in the higher energy range of the E787 measurements because we

have kinematic handles available to suppress those configurations with low energy missing photons.

Some improvements in the photon detection inefficiency for lower energy photons may also be possible (until the photo-nuclear limit is reached) by using a finer sampling calorimeter, especially at the front of the barrel veto. The photon detection efficiency for higher energy photons may also be improved by a small factor by implementing more radiation lengths to block remaining shower escape. In the KOPIO experiment, we will increase the average thickness to  $18 X_0$ . Figure 39 shows the photon detection inefficiency assumed in KOPIO background estimates.

Due to the requirement of a single  $K_L$  decay per micro-bunch in the KOPIO decay volume, accidental losses associated with photon vetoing are expected to be small.<sup>6</sup>

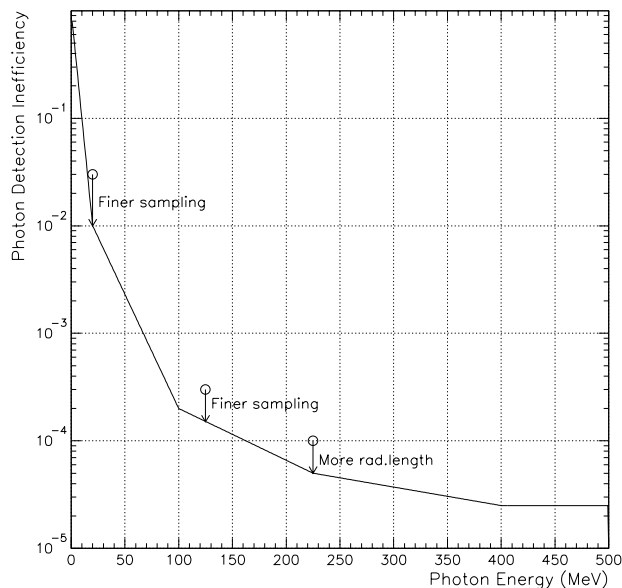


Figure 39: Photon detection inefficiency used in this proposal(solid line). The open circles are the E787 results.

### **Photon loss in beam holes and within overlapping showers.**

100 million events were generated to study the effect of the beam holes. Backgrounds due to photons escaping towards the upstream beam hole were found to be negligible. However, the photons exiting towards the downstream beam hole were found to cause significant backgrounds if not dealt with. The primary defense against this effect is the system of downstream photon detectors, in particular, the catcher described above. Figure 40 shows the energy distribution of  $K_{\pi 2}^0$  photons hitting the catcher. The  $K_{\pi 2}^0$  background is dominated by the odd pairing case with energies above 300 MeV. Having a detector which is 99% efficient for photon energies above 300 MeV is sufficient to bring events exiting through the beam

---

<sup>6</sup>The single decay per micro-bunch provides a quieter environment than found in E787 where the photon veto accidental losses were in the neighborhood of 20%.



hole under control. At a 300 MeV threshold, we expect accidental losses due to the catcher to be  $< 10\%$ .

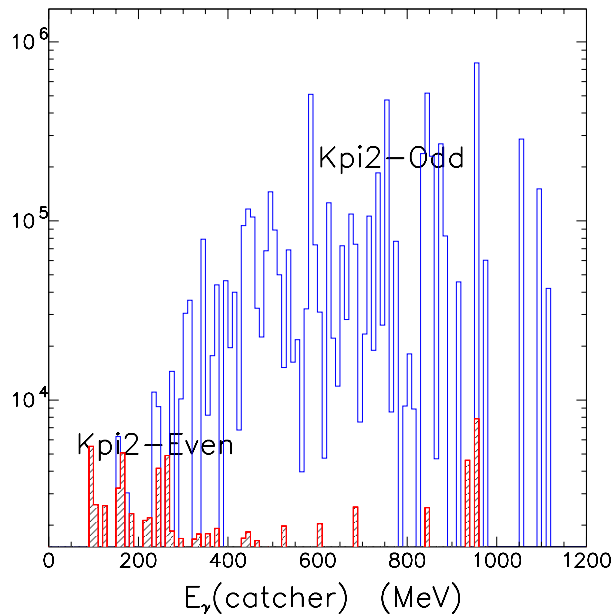


Figure 40: Energy distribution of photons in the beam hole for  $K_{\pi_2}^0$  even (hatched) and  $K_{\pi_2}^0$  odd type events. Absolute normalization of vertical scale is arbitrary.

Although the detection of decay photons traveling out the beam hole seems feasible with the present catcher design, the KOPIO experiment could even proceed without such a detector. As indicated above, we use kinematics to reconstruct the direction and energy of missing  $K_{\pi_2}^0$  photons in order to eliminate potential background events. Figure 41 shows the reconstructed position of the  $K_{\pi_2}^0$  photons exiting the beam hole obtained from the two photons detected in the preradiator (dots) for the odd pairing case. The  $K_L^0 \rightarrow \pi^0 \nu \bar{\nu}$  signal event distribution, when a  $K_{\pi_2}^0$  hypothesis is assumed, is also shown (boxes). At a cost of 20% (33%) of the acceptance, an additional factor of 25 (50) rejection could be provided to suppress these events. The backgrounds associated with lost photons in the beam hole are then below the nominal  $K_{\pi_2}^0$  background due to the detection inefficiencies discussed above<sup>7</sup>.

Photons can also hide in the showers of other detected photons but we expect that the consequent inefficiency will be smaller than the effects described above. These overlapping photons occur a few per cent of the time in  $K_{\pi_2}^0$  events for distances between the two photons at the calorimeter less than 50 cm (about 6 Moliere radii). For separation distances  $\leq 20$  cm, the probability is  $< 1\%$  for  $K_{\pi_2}^0$  decays. When the distance between two photons is between 20 and 50 cm, we identify the overlapping photons by comparing the shower center of gravity in the calorimeter (position resolution  $\sigma \sim 3$  cm) to the expected position from the preradiator. With an estimated inefficiency of  $10^{-3}$  for the center of gravity method

<sup>7</sup>However, the signal to noise ratio (S/N) would be worsened by about 25% if the catcher information were not used.

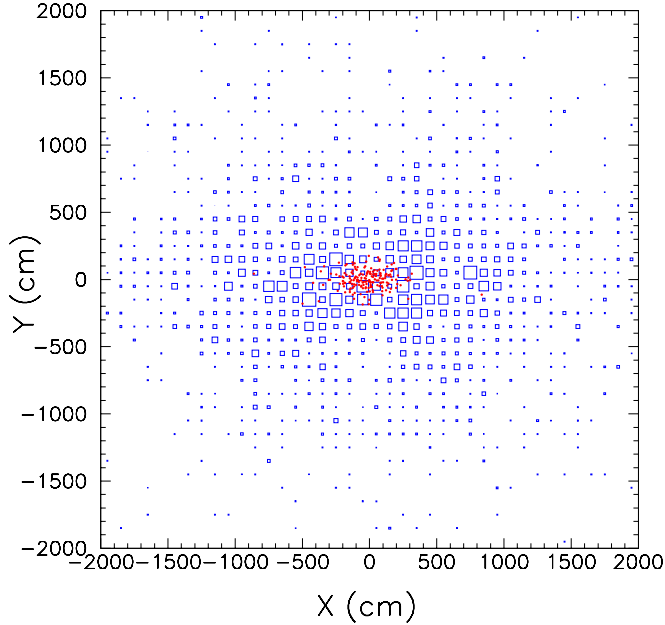


Figure 41: The reconstructed x-y distribution at the catcher position for  $K_{\pi 2}$  photons which exit through the beam hole (dots), and for signal events (boxes) interpreted as  $K_{\pi 2}$  decays.

and including the probability of the conversion of the extra photon in the preradiator, the inefficiency due to overlapping photons is  $10^{-5}$ . When the separation is less than 20 cm and the overlapping photons merge, the invariant mass of the photons becomes much larger than the  $\pi^0$  mass and the missing energy and mass are small. The inefficiency of this invariant mass cut is limited by the photonuclear reaction probability (a few times  $10^{-3}$ ) of the overlapped photon. Again, taking into account the photon non-conversion probability, the photon detection inefficiency due to overlap in the region of separation  $< 20$  cm is also estimated to be  $10^{-5}$ . We have also found that the loss of acceptance due to cuts aimed at eliminating overlapping photons is only a few percent.

#### 4.13.2 Background Estimates

##### Methodology

The energy and direction measurements of photons by the KOPIO preradiator/calorimeter arrangement along with momentum tagging of the  $K_L$  by time-of-flight provide powerful kinematic constraints for suppressing backgrounds. Among the most effective constraints are the mass of the two photons ( $m_{\gamma\gamma}$ ), and the center of mass energy of the  $\pi^0$  ( $E_{\pi^0}^*$ ). Vertex restrictions from photon tracking help in rejecting accidentals and particles produced near the surface of the detector by the beam halo. The tight vertical collimation of the beam reduces the beam halo and provides an extra vertex constraint. In the horizontal direction, we apply tighter cuts on the photon reconstruction algorithms to suppress backgrounds. In addition, we construct constraints to avoid backgrounds coming from earlier timing micro-bunches and require that there was only one  $K_L^0$  decay in the micro-bunch of interest for

$K_L^0 \rightarrow \pi^0 \nu \bar{\nu}$  candidates. The  $4\pi$  coverage of the photon veto ( $\overline{\gamma}$ ) and charged particle veto ( $\overline{charge}$ ) are effective in suppressing other  $K_L$  decays. The entire decay volume is evacuated to suppress production of particles in the decay region. Since the KOPIO technique provides complete information on each decay mode, we expect to be able to use data to accurately measure the levels of backgrounds.

In addition to  $K_{\pi 2}^0$  decays, potential sources of background include neutron production of  $\pi^0$ 's in the fiducial region vacuum, other  $K_L$  decays like  $K_{\pi 3}$ ,  $K_{e3}$  and  $K_L \rightarrow \gamma\gamma$  and  $\Lambda \rightarrow n\pi^0$  decays. Suppression of most backgrounds is accomplished by the high efficiency hermetic photon detector along with kinematic constraints. In the following, we discuss the nominal background levels anticipated for each of the potential sources for the entire proposed exposure of  $10^{14}$  protons on target.

### $K_L \rightarrow \pi^0 \pi^0$

The dominant background  $K_{\pi 2}^0$  has a branching ratio of  $9 \times 10^{-4}$ . In the  $K_{\pi 2}^0$  background studies, each Monte Carlo event was weighted with an energy dependent veto efficiency and a photon direction reconstruction efficiency in order to study the rejection and acceptance. The kinematic information was primarily used to suppress  $K_{\pi 2}^0$  background through the use of a cut on the pion c.m. energy  $E_{\pi^0}^*$  for the even paring background events, and a cut on the reconstructed pion mass  $m_{\gamma\gamma}$  for odd paring background events. The full kinematic information was found to allow a range of  $K_{\pi 2}^0$  rejections and treatment of rare pathologies such as bucket-to-bucket wrap-around events and events in which photons escape through the beam hole. These constraints were also found to effective in the simulations for suppressing other decay modes such as  $K_{\pi 3}$  and  $K_{e3}$  decay modes discussed below.

Dealing with low energy  $K_{\pi 2}^0$  photons (where the inefficiency is greatest) is particularly important. The energy of the missing photons in  $K_{\pi 2}^0$  events can be obtained by subtracting the measured energies of the two observed photons from the  $K_L$  energy. Requiring significant total missing energy (i.e.  $(E(K_L) - E_{\gamma 1} - E_{\gamma 2})$ ) as is generally the case for  $K_L^0 \rightarrow \pi^0 \nu \bar{\nu}$  events suppresses most potential background events that contain lower energy missing photons. However, in unusual cases when one of the missing photons has very high energy and one has very low energy an additional cut on missing mass (i.e.  $\sqrt{(E(K_L) - E_{\gamma 1} - E_{\gamma 2})^2 - (\mathbf{P}(K_L) - \mathbf{P}_{\gamma 1} - \mathbf{P}_{\gamma 2})^2)}$ ) is effective. Because the missing mass in  $K_{\pi 2}^0$  events is proportional to  $\sqrt{E_{miss1} * E_{miss2}}$ , where  $E_{miss}$  is the energy of a missing photon, the missing mass also becomes small for the case of asymmetric energy sharing. Figure 42 shows the missing mass vs. missing energy distribution of photons for  $K_{\pi 2}^0$  and  $K_L^0 \rightarrow \pi^0 \nu \bar{\nu}$  events. After removing the low missing mass and low missing energy region, we can suppress the low energy photons to achieve  $10^{-8}$  overall detection inefficiency for the two missing photons in  $K_{\pi 2}^0$  events.

The effect of eliminating events with small missing mass can be seen more directly by comparing  $E_{\pi^0}^*$  distributions before and after the photon veto cut for the  $K_{\pi 2}^0$  odd background events where one photon from each  $\pi^0$  is missed (Figure 43). The peak above  $E_{\pi^0}^* = 230$  MeV after the photon veto cut corresponds to the small missing mass region<sup>8</sup>. This is one of the main reasons why the phase space below the  $K_{\pi 2}^0$  peak,  $E_{\pi^0}^* < 249$  MeV, is used for the

---

<sup>8</sup>There is a one-to-one correspondence between  $E_{\pi^0}^*$  and missing mass:  $E_{\pi^0}^* = \frac{m_K^2 + m_{\pi^0}^2 - m_{miss}^2}{2m_K}$ . For small missing mass,  $E_{\pi^0}^*$  is large.

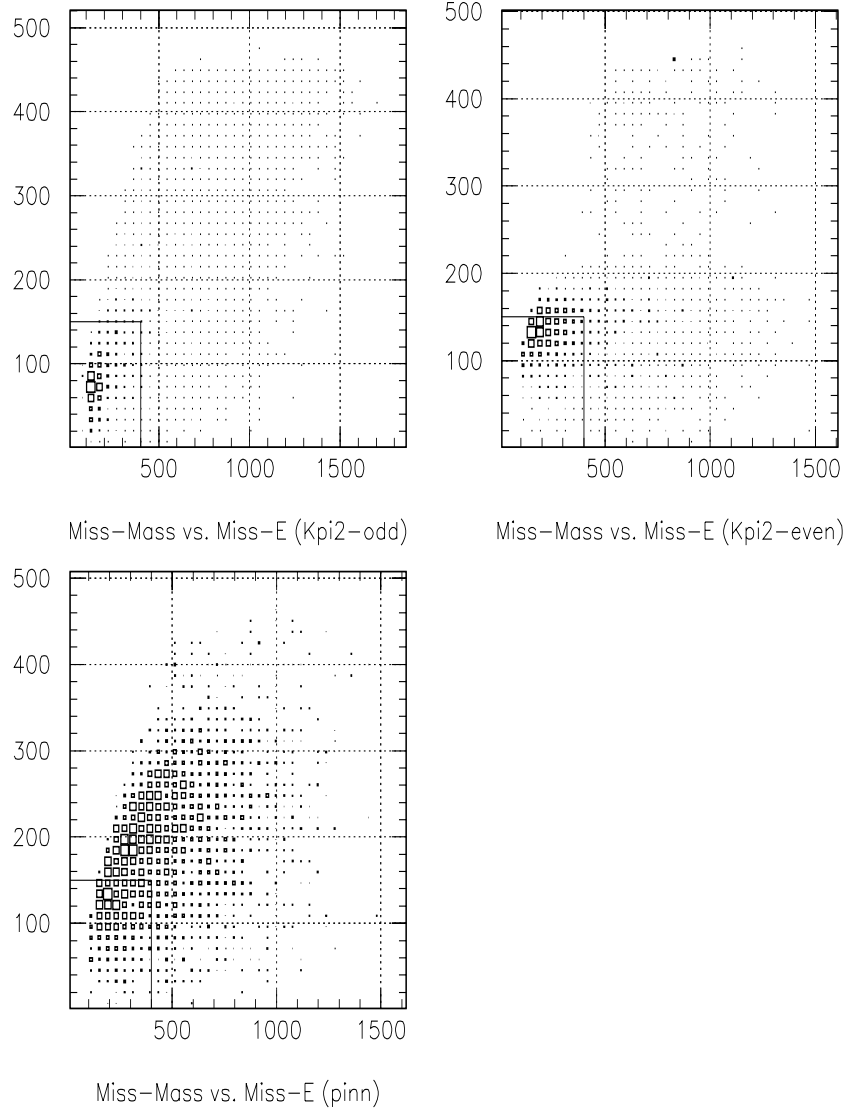


Figure 42: Missing mass vs. missing energy distribution of photons for  $K_{\pi 2}^0$  odd,  $K_{\pi 2}^0$  even and  $K_L^0 \rightarrow \pi^0 \nu \bar{\nu}$  events.

KOPIO measurement.

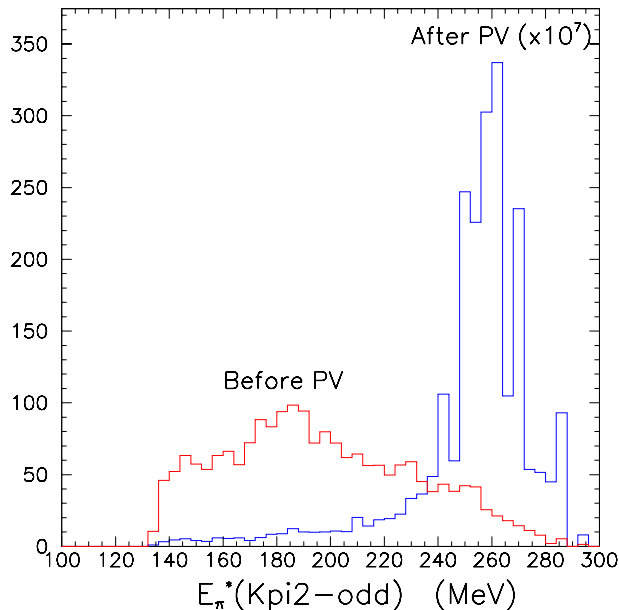


Figure 43:  $\pi^0$  energy distribution in the  $K_L$  center of mass system ( $E_{\pi^0}^*$ ) for  $K_{\pi_2}^0$  odd events before and after photon veto cuts.

The  $K_{\pi_2}^0$  even background arising from the previous timing micro-bunch (“wrap-around” events) can cause a serious problem because the  $E_{\pi}^*$  cut as well as the missing energy cut to suppress low energy missing photons may fail. Figure 44 shows  $E_{\pi}^*$  assuming that the particle is coming from the previous bunch versus the longitudinal  $\pi^0$  momentum of the signal (box) and the wrap-around  $K_{\pi_2}^0$  background. This background is suppressed by cutting on these quantities as indicated in the figure.

Table 11 gives the estimated acceptance factors for the  $K_{\pi_2}^0$  backgrounds, including all combinations of 2 missing photons out of the 4 photons when both observed photons convert in the preradiator. Multiplying the total  $K_{\pi_2}^0$  acceptance by the branching ratio and the number of  $K_L^0$  decays, we expect 13 events from this source split evenly the between the odd and even pairing types. When we include those cases where one photon converts in the preradiator and one in the calorimeter, and account for accidental losses (see below) the total  $K_{\pi_2}^0$  background expected is 15 events.

$$\underline{K_L \rightarrow \pi^+ \pi^- \pi^0}$$

Since the  $K_{\pi_3}$  decay contains a  $\pi^0$  in the lower momentum range of  $K_L^0 \rightarrow \pi^0 \nu \bar{\nu}$ , this mode is suppressed by a combination of charged particle vetos and additional c.m. energy cuts ( $E_{\pi}^*$ ). Charged pions can disappear by detector inefficiency (e.g. insufficient light output from the charged veto scintillators) or via nuclear interactions.

Using 1 cm thick plastic scintillation counters and a threshold of 1MeV, Inagaki et al.[62] found inefficiencies for 1 GeV/c particles to be  $3.2 \times 10^{-4}$  for  $e^+$ ,  $6 \times 10^{-4}$  for  $\pi^-$ ,  $< 1.6 \times 10^{-5}$  for  $\pi^+$  and  $< 1.3 \times 10^{-4}$  for  $e^-$ . In KOPIO, when the  $\pi^-$  reacts via charge exchange

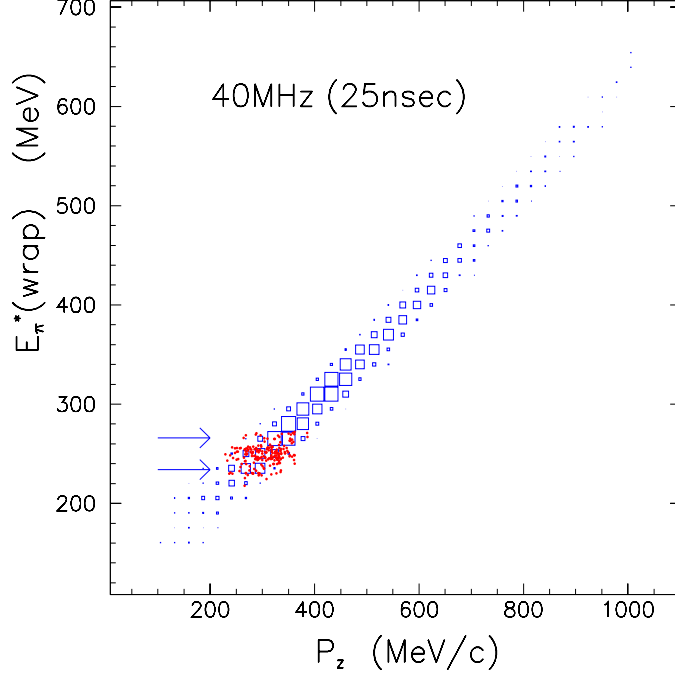


Figure 44:  $E_{\pi}^*$  assuming that the particle is coming from the previous bunch versus longitudinal  $\pi^0$  momentum for the signal (boxes) and background events from wrap-around  $K_{\pi 2}^0$  (even) decays (dots). The arrows indicate the cut values use to suppress the background.

$\pi^- p \rightarrow \pi^0 n$  or  $\pi^- p \rightarrow \gamma n$  before being detected by the charged particle veto system, photon energy will be present elsewhere to reduce the overall inefficiency. However, the influence of the 3-3 resonance causes the interaction cross sections for pions to be large at KOPIO energies. Ultimately, pion reactions producing only neutrons will represent an irreducible level of efficiency. In order to make estimates for such processes, we have employed cross section measurements[63] on reactions of the type  $\pi^+ + C \rightarrow p + p$  in the energy region appropriate for KOPIO and, assuming isospin symmetry, obtain values for  $\pi^- + C \rightarrow n + n$  reactions (including those with larger numbers of neutrons). Then, taking into account the measurements of Inagaki et al. mentioned above, we estimated the overall charged pion inefficiencies for the  $K_{\pi 3}$  background to be  $\leq 10^{-4}$  for  $\pi^-$  and  $\leq 10^{-5}$  for  $\pi^+$  resulting in a suppression factor of  $\leq 10^{-9}$ .

The unusual case where a  $\pi^+$  gets a very small energy and stops in a veto counter without depositing much energy is potentially problematic because the charged veto rejection for  $\pi^+$  is not available. However, these events are concentrated in a particular phase space region in  $E_{\pi^0}^*$  vs. missing energy as shown in Fig. 45 and can easily be rejected with little acceptance loss.

Figure 46 shows a plot of  $E_{\pi^0}^*$  vs.  $|E_{\gamma 1}^* - E_{\gamma 2}^*|$  for the  $K_{\pi 3}$  background. A cut in  $E_{\pi^0}^* < 190$  MeV is very effective, and is compatible with the odd paring cuts. Putting all the cuts together gives an estimated 6 events (including 4 with two photons converted in the preradiator and 2 with one) from  $K_{\pi 3}$ .

Table 11: Acceptance factors for the  $K_{\pi 2}^0$  even and odd pairing backgrounds (two photons converting in the preradiator).

Requirement	Even Pairing	Odd Pairing
No. $\gamma$ Combinations	2	4
Z fiducial region and $P_K$	0.57	0.59
Solid angle	0.34	0.29
Preradiator Conversion Probability	0.50	0.50
$m_{\gamma\gamma} = m_\pi$	0.73	0.09
Wrap- $K_{\pi 3}$ low energy	0.68	0.78
$E_\pi^*$	0.016	0.27
Photon veto	$8.3 \times 10^{-8}$	$2.9 \times 10^{-8}$
Missing Energy	0.57	0.84
$E_\pi^*$ vs. $ E_{\gamma 1}^* - E_{\gamma 2}^* $	0.82	0.53
Acceptance	$5.8 \times 10^{-11}$	$8.1 \times 10^{-11}$
Total $K_{\pi 2}^0$ Acceptance	$1.4 \times 10^{-10}$	

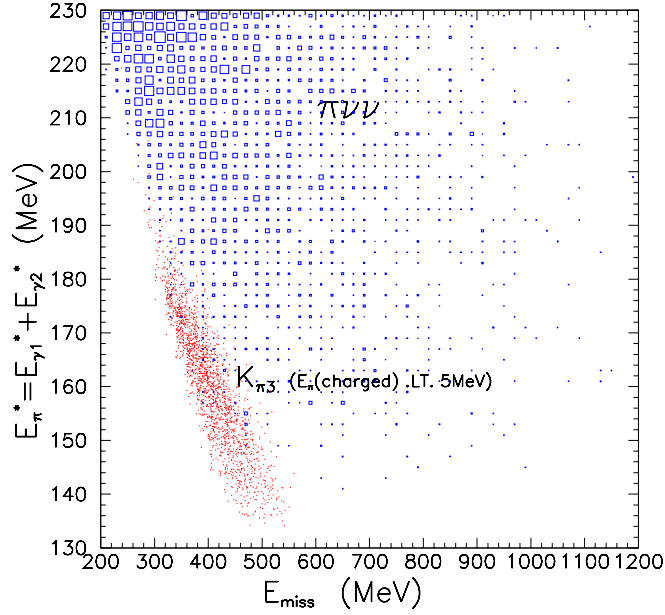


Figure 45:  $E_{\pi 0}^*$  versus missing energy for the  $K_{\pi 3}$  background when  $\pi^+$  kinetic energy is less than 5MeV.

#### $K_L \rightarrow \pi^- e^+ \nu$ ( $K_{e3}$ )

The  $K_{e3}$  background can arise when the  $\pi^-$  and  $e^+$  react via charge exchange before they are detected and two photon clusters (each with one or two photons) remain. In making background estimates for KOPIO, we will use the inefficiencies for electrons and positrons

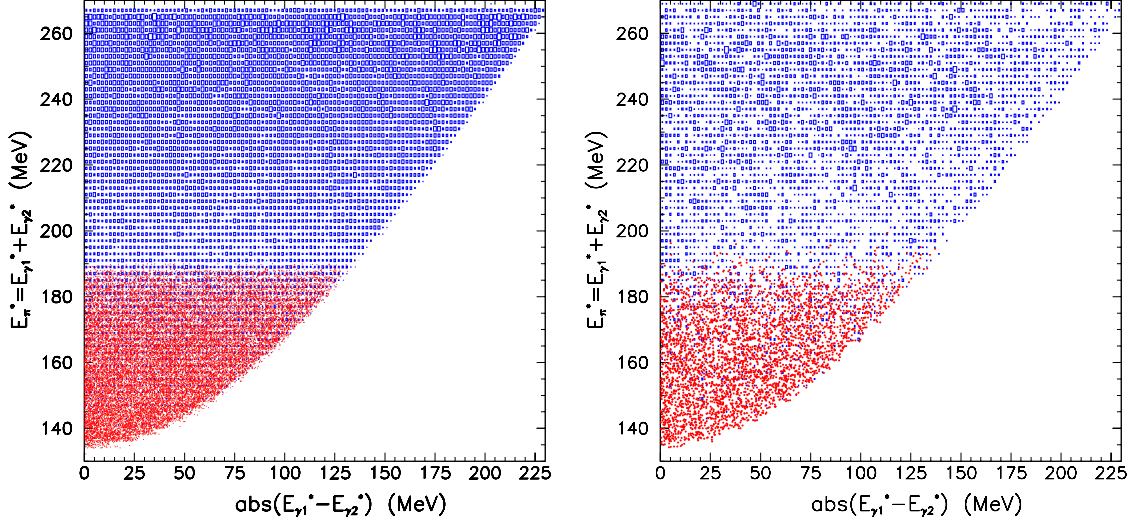


Figure 46:  $E_{\pi^0}^*$  versus  $|E_{\gamma_1}^* - E_{\gamma_2}^*|$  plot for  $K_{\pi 3}$  background (red dots) and signal (blue squares). Left plot shows the case of perfect resolution and right that of expected resolution.

measured by Inagaki et al. along with estimates of the pion charge exchange cross sections.

Fortunately, there are two extra kinematic handles on the  $K_{e3}$  background: the two photon mass ( $m_{\gamma\gamma}$ ), which tends to be much larger than  $m_{\pi^0}$  and the c. m. energy of the two photons ( $E_{\pi^0}^*$ ) which tends to be at the end point of the phase space. Due to the use of a low energy beam, the photons from  $\pi^- p \rightarrow n\pi^0$  can be identified as two photon clusters, which provides the extra rejection power needed to suppress this mode.

Figure 47(a) shows the  $\pi^0$  momentum distribution produced by the  $\pi^- p \rightarrow n\pi^0$  reaction for the  $K_{e3}$  background. Here, we conservatively assume that only those events below 250 MeV/c can be rejected by the photon clustering cut. Figure 47(b) and (c) show  $m_{\gamma\gamma}$  and  $E_{\pi^0}^*$  distributions for the signal and  $K_{e3}$  background. Selecting the phase space region below the  $K_{\pi 2}$  peak in the  $E_{\pi^0}^*$  distribution is particularly effective.

Overall, the  $K_L \rightarrow \pi^- e^+ \nu$  background is expected to be 0.06 events.

### $K_L \rightarrow \gamma\gamma$

$K_L \rightarrow \gamma\gamma$  is very tightly constrained by kinematics. For example, by knowing the direction of one photon, one obtains the energies of both photons and the direction of the other photon. Cutting on the monochromatic photon energies in c.m. system ( $E_{\gamma}^*$ ) using an invariant mass cut on 2 photons ( $m_{\gamma\gamma}$ ) and the CM energy of the 2 photons ( $E_{\pi^0}^*$ ), brings this process under control. We expect 0.04 events from this background source.

### $\Lambda \rightarrow \pi^0 n$

Because of the large angle of the neutral beam used here, the cross section for producing  $\Lambda$ s is low and they decay completely before reaching the decay volume. Backgrounds could arise from  $\Lambda$ 's produced by halo neutrons and  $K_L$ 's. Again, the production cross section of  $\Lambda$ s by the beam halo is low because the beam is soft and it is hard for  $\Lambda$ s to reach the



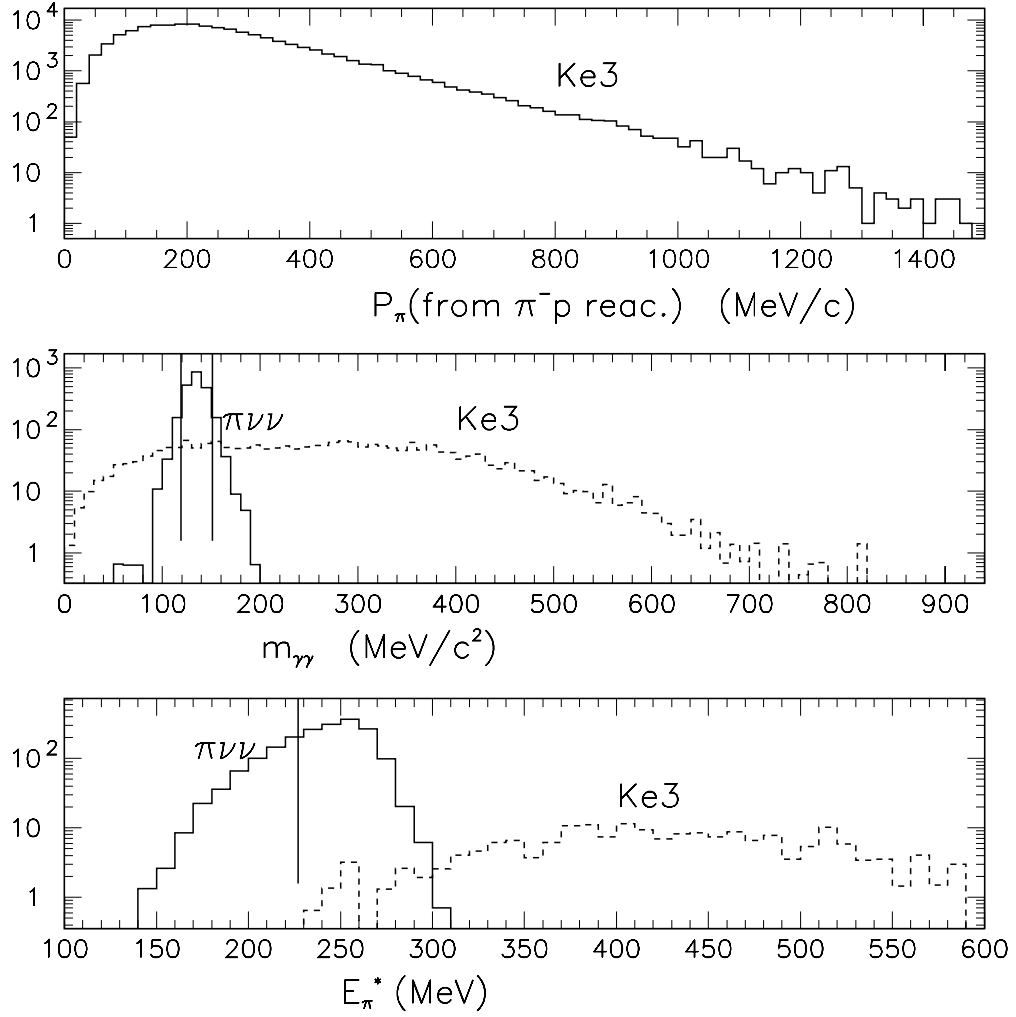


Figure 47: (a) Momentum of  $\pi^0$ , (b) invariant mass of 2 “photon” energy clusters ( $m_{\gamma\gamma}$ ) and the (c) the center of mass energy of the two photons ( $E_{\pi^0}^*$ ) of the  $K_{e3}$  background.

fiducial decay volume from the interaction point. Good collimation of the beam as well as a vertex cut to eliminate events produced near the surface of the last collimator suppresses this background to a negligible level of 0.2 events.

#### $nA \rightarrow \pi^0 A$

Neutrons interacting with the residual gas in the decay volume can produce single  $\pi^0$ s without any other easily detectable activity. This background is primarily suppressed by having an excellent vacuum ( $10^{-7}$  torr) and by the reduced number of neutrons above the  $\pi^0$  production threshold (800 MeV/c) at the 40 degree production angle. The micro-bunching of the beam provides further suppression of the neutrons as illustrated in Fig. 48 which shows the arrival time of  $K_L$ 's and neutrons with respect to photons at 10m from the production

target. Neutrons with momenta between 1 and 2.4 GeV/c fall into our arrival time of interest (i.e.  $K_L$  with momenta between 0.5 and 1.3 GeV/c). Within this time window, the neutron to  $K_L$  ratio is improved by a factor of 5. Despite the fact that a low energy beam is used here, the effective  $n/K_L$  ratio is as good as or better than in higher energy experiments. This background is further suppressed by the kinematic cuts used for  $K_{\pi 2}^0$  because it includes a large unphysical kinematical phase space due to the miss-assignment of an incoming neutron as a  $K_L$ . We expect 0.5 events from this background source.

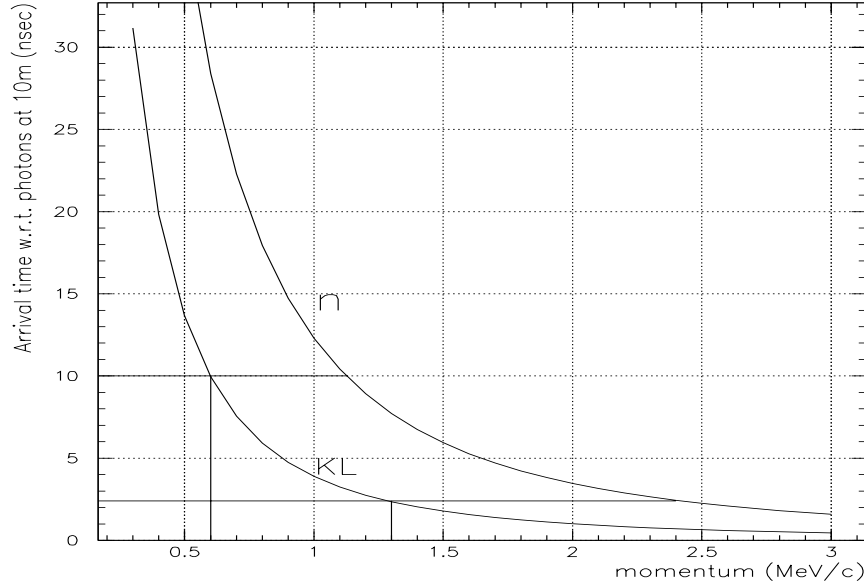


Figure 48: Arrival time of  $K_L$ 's and neutrons with respect to photons at 10m downstream from the production target.

### Accidentals

Accidental backgrounds are caused by beam halo neutrons, photons and  $K_L$ 's which are scattered from the last collimator and get into the detector. Multiple stages of collimation of the narrow vertical beam should provide good collimation. From our measurements and GEANT calculations of our beam, confirmed by our correct simulation of the E791 beam, we would expect to bring the neutrons, kaons and gammas scattered into the detector down to  $\sim 1$  MHz, 100 KHz, and 10 KHz, respectively. Requiring the converted track in the preradiator further suppresses neutrons and  $K_L$ s because they show different track characteristics from photon conversions in the preradiator. Finally, photon tracking allows us to reject those photons coming from the upstream collimators. Assuming the signal event coincidence timing window of 1 ns, the rate of the accidental background is estimated to be  $\sim 1$  event.

## 4.14 Sensitivity and Measurement Precision.

Our estimates of sensitivity for  $K_L^0 \rightarrow \pi^0 \nu \bar{\nu}$  decay are tightly coupled to the cuts required for background suppression, particularly for the  $K_{\pi^2}^0$  and  $K_{\pi^3}$  backgrounds. Fig. 49 illustrates the KOPIO methodology based on kinematic reconstruction in the  $K_L$  c.m. system. On the left is a pure kinematic scatter-plot of c.m. pion energy ( $E_{\pi^0}^*$ ) vs. the difference of gamma energies in the c.m. system ( $|E_{\gamma_1}^* - E_{\gamma_2}^*|$ ), for the  $K_{\pi^2}$  background (blue dots) and  $K_L^0 \rightarrow \pi^0 \nu \bar{\nu}$  (red dots). Regions 1, 2 and 3 are free of background. Now, even when the resolution and acceptance effects are included in the simulations, Regions 1 and 2 remain virtually background free as indicated on the right hand plot in fig. 49.

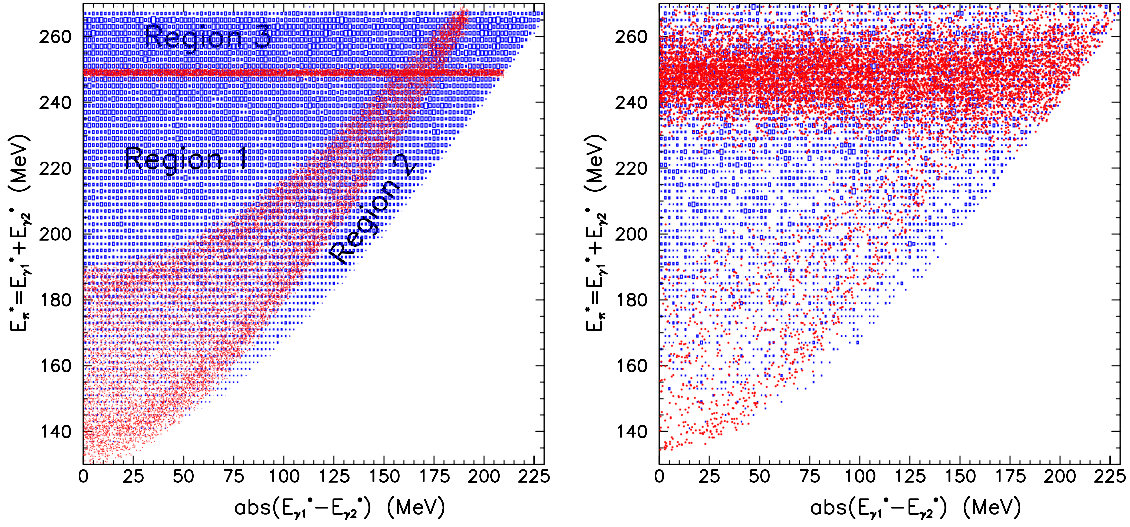


Figure 49:  $E_{\pi^0}^*$  vs.  $|E_{\gamma_1}^* - E_{\gamma_2}^*|$  for the  $K_{\pi^2}$  background (red dots) and signal (blue boxes). The left hand figure shows the pure kinematic effects while the right hand figure includes experimental resolution effects.

Table 12 gives the breakdown leading to the estimated 1.0% acceptance for  $K_L^0 \rightarrow \pi^0 \nu \bar{\nu}$  with two photons converting in the preradiator. The list includes factors for the 3 m long Z fiducial region and the  $K_L$  momentum cut ( $0.4 \text{ GeV}/c < P_K < 1.4 \text{ GeV}/c$ ), the solid angle acceptance, the conversion and reconstruction of two photons in the preradiator, and the accessible  $K_L^0 \rightarrow \pi^0 \nu \bar{\nu}$  phase space ( $E_{\pi^0}^*$ ) acceptance. In addition, there are cuts on missing energy and mass and on photon energy sharing. The inefficiency due accidental spoiling of good events is estimated to be  $\leq 10\%$  for a threshold of a few MeV in the preradiator, calorimeter and barrel veto, 300 MeV in the catcher, and a timing window of 2 ns. Taking the estimated accidental loss (due to accidental hits spoiling otherwise acceptable events) of 10%, the overall detection efficiency becomes 0.0114. Accepting the cases where one photon converts in the preradiator and one in the calorimeter increases the overall acceptance to  $\epsilon = 0.015$ .

The acceptance can be estimated for a variety of cut selections and levels of S/N. For the

Table 12: Acceptance factors for  $K_L^0 \rightarrow \pi^0 \nu \bar{\nu}$  (two photons converting in the preradiator).

Requirement	Acceptance factor
Z fiducial region and $P_K$	0.58
Solid angle	0.33
Preradiator Conversion Probability	0.50
$m_{\gamma\gamma} = m_\pi$	0.73
Wrap-around/ $K_{\pi 3}$ low energy	0.73
$E_\pi^*$	0.31
Photon veto	1.000
Missing Energy	0.91
$E_\pi^*$ vs. $ E_{\gamma 1}^* - E_{\gamma 2}^* $	0.9
Acceptance	0.0126

nominal  $K_L^0 \rightarrow \pi^0 \nu \bar{\nu}$  and background acceptance estimates given above, we have included events in which at least one of the photons converts in the preradiator. Of all such  $K_L^0 \rightarrow \pi^0 \nu \bar{\nu}$  events, about 50% have both photons converting and 50% have one photon converted in the preradiator and one in the calorimeter. Since there are additional constraints available when the angles of both photons are measured, this category contributes about 75% of the events for a given level of S/N. The signal yield is calculated as follows:

$$\begin{aligned}
N_K &= (4.2 \times 10^7 \text{ } K_L \text{ decays/pulse}) \cdot 0.57(\text{single decay}) \cdot (6.1 \times 10^6 \text{ pulses}) \\
&= 1.47 \times 10^{14} \text{ } K_L \text{ decays} \\
N_{\pi \nu \bar{\nu}} &= N_K \cdot \epsilon \cdot B \\
&= (1.47 \times 10^{14}) \cdot (0.015) \cdot (3 \times 10^{-11}) \\
&= 65 \text{ events}
\end{aligned}$$

where  $B = 3 \times 10^{-11}$  is the SM central value for the branching ratio. The figure 0.57 is the fraction of unaccompanied  $K_L^0$  decays assuming a 25 MHz microbunching frequency and a 3 second spill. A total AGS cycle time of 5.3 seconds is assumed. We expect to measure 65  $K_L^0 \rightarrow \pi^0 \nu \bar{\nu}$  events in 9000 hours of beam at  $1 \times 10^{14}$  protons/spill. The single event sensitivity of the experiment would be approximately  $6 \times 10^{-13}$  if not limited by background. A summary of the signal and background estimates is given in Table 13. For the nominal cuts scenario, the signal would exceed the background by about a factor of 2.

Since we expect that the actual background levels will be determined reliably from the data, it will be feasible to select the cuts in order to optimize the precision of the extraction of the  $K_L^0 \rightarrow \pi^0 \nu \bar{\nu}$  branching ratio, and to demonstrate the stability of the result at varying levels of background suppression. For example, by tightening the cut on  $E_\pi^*$  vs.  $|E_{\gamma 1}^* - E_{\gamma 2}^*|$  (see Table 13) the number of events could be reduced from 65 to 48 while the S/N ratio would increase from 2 to 3. Table 14 shows several other examples of the numbers of events obtainable with various S/N ratios and also the precisions obtainable on  $B(K_L^0 \rightarrow \pi^0 \nu \bar{\nu})$ , at the SM central value. If the other relevant CKM parameters were known well, it would then

Table 13: Estimated event levels for signal and backgrounds.

Process	Modes	Main source	Events
$K_L^0 \rightarrow \pi^0 \nu \bar{\nu}$			65
$K_L$ decays ( $\bar{\gamma}$ )	$\pi^0 \pi^0, \pi^0 \pi^0 \pi^0, \pi^0 \gamma \gamma$	$\pi^0 \pi^0$	24
$K_L \rightarrow \pi^+ \pi^- \pi^0$			9
$K_L \rightarrow \gamma \gamma$			0.04
$K_L$ decays ( $\overline{charge}$ )	$\pi^\pm e^\mp \nu, \pi^\pm \mu^\mp \nu, \pi^+ \pi^-$	$\pi^- e^+ \nu$	0.06
$K_L$ decays ( $\bar{\gamma}, \overline{charge}$ )	$\pi^\pm l^\mp \nu \gamma, \pi^\pm l^\mp \nu \pi^0, \pi^+ \pi^- \gamma$		0.1
Other particle decays	$\Lambda \rightarrow \pi^0 n, K^- \rightarrow \pi^- \pi^0, \Sigma^+ \rightarrow \pi^0 p$	$\Lambda \rightarrow \pi^0 n$	0.03
Interactions	n, $K_L, \gamma$	$n \rightarrow \pi^0$	0.5
Accidentals	n, $K_L, \gamma$	n, $K_L, \gamma$	1.5
Total Background			35

be possible to extract  $\eta$  with a precision of approximately 10% from the KOPIO measurement of  $K_L^0 \rightarrow \pi^0 \nu \bar{\nu}$ .

Table 14: Signal/Noise, numbers of  $K_L^0 \rightarrow \pi^0 \nu \bar{\nu}$  events and the precision of the  $B(K_L^0 \rightarrow \pi^0 \nu \bar{\nu})$  measurement.

S/N	$K_L^0 \rightarrow \pi^0 \nu \bar{\nu}$ Signal	$B(K_L^0 \rightarrow \pi^0 \nu \bar{\nu})$ Precision
1	94	0.15
2	65	0.15
3	48	0.17
5	32	0.20

## 4.15 The KOPIO R&D program and Schedule

From our experience with rare kaon decay experiments (AGS E865 searching for  $K^+ \rightarrow \pi^+ \mu^+ e^-$  at a level below  $10^{-11}$ , and AGS E787 measuring the branching ratio for  $K^+ \rightarrow \pi^+ \nu \bar{\nu}$  at a level  $\sim 10^{-10}$ ) we understand the difficulty of the KOPIO undertaking. Therefore to insure success as efficiently and in as timely a manner as possible we have designed an R&D program which will test and optimize each component of the detection system, including the beam, before we commit to large investments of accelerator beam time. Much of this testing will be performed in a low energy tagged photon beam at the the BNL NSLS LEGS facility, and at the TRIUMF cyclotron facility's pion, muon, and " $\pi^0$ " beams. Some of the testing and development, most notably that of the neutral beam itself, will occur at the AGS.

Below we give an outline of this R&D program.

1. We propose building the neutral beamline as early as possible so that shielding and particle rates can be optimized. The constructed beam would then allow various detector components to be tested and perfected under "battle" conditions.<sup>9</sup>
2. Prototypes of the preradiator designs described in Section 4.7 are being constructed. Stacks of prototype modules will be tested at the LEGS facility, and perfected to insure the resolution and efficiency as predicted in our GEANT calculations. Full size prototype modules will be constructed to test and perfect the mechanical engineering concepts and to perfect constructional techniques.
3. A prototype lucite-Pb catcher described in Section 4.9 has been built and tested in Japan; results can be found in KOPIO technical note TN013. Prototypes of the aerogel-based catcher modules will be constructed and tested in both photon and neutron beams at facilities mentioned above. Sufficient aerogel for this purpose is currently on hand and mirror design has been proceeding.
4. Elements of barrel veto modules, with full 4 m length wls fiber readout, have been tested for light output in Russia. Construction of prototype modules of full depth and at least 1m length is well underway at the moment. They too will be tested at the LEGS facility. Subsequently we will make and test a full-length prototype before beginning production.
5. As described in 4.8 we have constructed and tested Shashlyk modules and achieved  $4\%/\sqrt{E}$  resolution. We are currently constructing modules with the improvements prescribed by our calculations that should yield  $\sim 3.3\%$  resolution. These will be tested for photon efficiency, energy and timing resolution, and for sensitivity to neutrons at the afore mentioned facilities.
6. We have been investigating existing designs for the preradiator analog and timing electronics. There are several extant devices used in HEP and heavy ion experiments which

---

<sup>9</sup>We note that the AGS will be running as an injector for RHIC for the foreseeable future, and has a program of external beam experiments during the time before construction of the KOPIO detector will be complete. Small periods of beam delivered to the KOPIO beamline will be sufficient to thoroughly develop the beam and test pieces of apparatus in the beam environment.

look promising. During this R&D phase we will adapt those which are appropriate, and design and build prototypes which will be incorporated into, and used with the prototype preradiators

7. Engineering studies of the vacuum vessel continue. As part of our R&D program, and before committing to build the full scale vessel, we will build and test a scale model.
8. Further R&D for beam bunching will build on that which has already been carried out at the AGS. It is desirable to acquire the beam bunching RF cavity as soon as possible so that operation of the AGS in this mode can be fully understood.

Since each item in the above list involves a proven technology, we have confidence that the R&D program can be successfully completed in at most two years. If the beam can be constructed on the same time scale, we should be able to have a significant engineering run with a partially constructed detector in the third year, and a run with the full detector in the fourth. These two runs, each only a few weeks long, will allow us sufficient time to fully test the apparatus.

During the next, and subsequent runs physics quality data collection will occur, and each run will break new ground in the measurement of  $B(K_L^0 \rightarrow \pi^0 \nu \bar{\nu})$ . When the system is operating at full capacity, a 15 week run at full intensity should yield about 10 SM  $K_L^0 \rightarrow \pi^0 \nu \bar{\nu}$  events with a signal to background ratio of 2, and permit a measurement of  $\eta$  to about 18%.

To summarize, we feel it is reasonable for us to be ready to take physics quality data in FY 2005. How long it will take to complete the experiment after that time will be a matter of how much beam time is available to us.

## 4.16 Costs

We summarize here the expected cost of KOPIO, including the AGS modifications, beamline construction and modification, and detector fabrication. These estimates are preliminary, although they have been costed via a bottoms-up algorithm. A more accurate baseline cost will be established following a technical review of the project.

The accelerator and beamline capital costs for this experiment have been estimated by the BNL Collider Accelerator Department (CAD). These include AGS equipment such as the bunching RF cavity, the design and construction of the neutral beam, and of a counting house for experimental equipment. These costs include contingencies averaging around 20% and total \$5.812M.

Detector costs have been estimated by the KOPIO collaborators including a uniform 30% contingency. Preliminary engineering estimates are derived mainly from experience and engineering knowledge, but not from thorough engineering analysis. Where possible bid or catalog prices for various components have been used. In other cases the costs of similar items or systems in current experiments were used.

The calorimeter modules will be built in Russia. The costs are based on Russian estimates which have been reliable in the past for similar systems built in Russia, *i.e.*, modules for the E865 and the Phenix calorimeters, and recent prototype modules. Cost estimate for WLS fibers is the current price. The electronics costs of this system are based on quoted prices for commercial modules and on the incremental cost of transient digitizers (TDs) recently built at TRIUMF. The total cost of the calorimeter system is \$4.318M.

The preradiator system incorporates chambers and scintillation counters. The chamber materials and construction costs are based on preliminary engineering estimates and past experience in constructing similar devices. The pmts are in hand from a previous experiment. The electronics costs are preliminary estimates by an electrical engineer. They are based on schematic designs employing existing components and standard construction techniques. The injection molded scintillator costs includes materials, mold making, and production estimates. The WLS fiber estimate is based on the current price. The pmt electronics costs are commercial plus TD costs as discussed above. The total cost of the preradiator system is \$6.440M.

For the most part, we envision building the veto counters in Russia. Costs are based on Russian estimates (see discussion of calorimeter costs above). The electronics costs are based on commercial prices and on the incremental costs of TDs mentioned above. The total cost of the veto system is \$2.654M.

The aerogel version of the catcher is costed here. It is likely this system will be built in Japan. The bulk of the cost is for the aerogel and the photomultiplier tubes and bases. We have a recent quote for the former and the latter cost is based on catalog prices. The cost of other components is based on recent experience with similar systems. The total cost for the catcher is \$1.576M.

The cost of the vacuum system is a preliminary engineering estimate based on a similar system. The cost estimate of the vacuum vessel is a recent commercial bid. The total cost of the vacuum and mechanical support system is \$1.256M.

We estimate the cost for electronic infrastructure (racks, crates, power supplies, A/C, etc.) on the basis of commercial prices and recent experience. It is envisioned as being



handled by the BNL group. The total cost is \$1.303M.

DAQ is also envisioned as handled by the BNL group. Very little needs to be home-made. Costing is done on the basis of current commercial prices, but of course we expect to buy equivalent products available at the time the project is funded. Costs of DAQ equipment for a given capacity historically go down with time. The total cost is presently estimated to be \$0.688M.

The gain monitoring system is costed by experience with the E787 end cap monitoring system. It will probably be constructed in Japan. The total comes to \$0.247M.

We have allotted a total of \$0.260M for our residual R&D program. Details of this program are given in Sec. 4.15.

The Yale group will hire a physicist to act as project manager and also a project engineer for the three-year duration of the construction project. The cost of this will be \$0.787M.

Total detector costs are then estimated to be \$19.529M. The cost of the project as a whole is \$25.341M. Fig. 50 is a breakdown of the cost by system. Details of both the AGS and detector costs at one wbs level below that of Fig. 50 are to be found at <http://pubweb.bnl.gov/people/e926/costs.html>.

WBS #	Title	Units	Unit cost (\$)	Material		Total (\$)	tech FT Cost (man-mo)	Labor		EDIA FT Cost (man-mo)	Burden (\$)	Burden (\$)	Contingency (\$)	Total (\$)	BY1	BY2	BY3
1				Cost (\$)	Burden (\$)			Cost (\$)	Burden (\$)								
	Project total			15356.27	1031.96	16388.23	88.78	1320.02	501.68	21.72	621.91	369.01	5495.38	25341.40	10862.10	9920.96	4558.34
1.2.1	Detector Systems			13131.27	410.58	13541.84	88.78	557.92	92.56	21.72	146.32	43.51	4502.01	19529.35	9290.66	8627.70	3610.99
1.2.1.1	Calorimeter			3238.16	5.00	3243.16	10.16	65.00	3.25	1.56	10.00	0.50	996.57	4318.48	2159.24	1295.54	863.70
1.2.1.2	Preradiator			4633.69	206.48	4840.18	15.24	97.50	4.87	2.34	15.00	0.75	1481.30	6439.61	2575.84	2575.84	1287.92
1.2.1.3	Veto			1878.15	6.25	1884.40	19.54	125.00	6.25	3.91	25.00	1.25	612.57	2654.47	1327.23	1061.79	265.45
1.2.1.4	Catcher			1153.10	0.35	1153.45	2.03	13.00	0.65	0.78	5.00	0.25	363.71	1576.06	630.42	630.42	315.21
1.2.1.5	Vacuum			770.00	38.50	808.50	20.32	130.00	6.50	3.13	20.00	1.00	289.80	1255.80	1130.22	125.58	0.00
1.2.1.6	Electronics Infra.			772.61	73.72	846.33	16.90	100.16	55.84	0.00	0.00	0.00	300.70	1303.04	903.46	371.98	27.60
1.2.1.7	DAQ			295.55	80.27	375.82	4.60	27.26	15.20	10.00	71.32	39.76	158.81	688.17	117.89	115.80	454.48
1.2.1.8	Gain Monitor			190.00	0.00	190.00	0.00	0.00	0.00	0.00	0.00	0.00	57.00	247.00	24.70	123.50	98.80
1.2.1.9	R&D			200.00	0.00	200.00	0.00	0.00	0.00	0.00	0.00	0.00	60.00	260.00	169.00	65.00	26.00
1.2.1.10	Project Management			0.00	0.00	0.00	72.00	467.32	137.86	0.00	0.00	0.00	181.55	786.73	252.64	262.24	271.84
1.2.2	Beam			2,225.00	621.38	2,846.38		762.10	409.11		475.59	325.50	993.36	5812.05	1,571.44	3,293.26	947.35

Figure 50: KOPIO project cost summary.

# References

- [1] G. Buchalla and A.J. Buras, *Nucl. Phys.* **B548**, 309 (1999) hep-ph/9901288.
- [2] M.K. Gaillard and B.W. Lee, *Phys. Rev.* **D10**, 897 (1974); J. Ellis, M.K. Gaillard and D.V. Nanopoulos, *Nucl. Phys.* **B109**, 213 (1976); L. Littenberg, *Phys. Rev.* **D39**, 3322 (1989).
- [3] L. Littenberg and G. Valencia, *Ann. Rev. Nucl. Part. Sci.* **43**, 729 (1993); B. Winstein and L. Wolfenstein, *Rev. Mod. Phys.* **65**, 1113 (1993); J.L. Ritchie and S.G. Wojcicki, *Rev. Mod. Phys.* **65**, 1149 (1993); G. Buchalla, A.J. Buras and M.E. Lautenbacher, *Rev. Mod. Phys.* **68**, 1125 (1996).
- [4] A.J. Buras and R. Fleischer, in *Heavy Flavours II*, World Scientific, eds. A.J. Buras and M. Linder, 65-238 (1997).
- [5] D. Rein and L.M. Sehgal, *Phys. Rev.* **D39**, 3325 (1989); G. Buchalla and G. Isidori, *Phys. Lett.* **B440**, 170 (1998).
- [6] G. Buchalla and A.J. Buras, *Nucl. Phys.* **B400**, 225 (1993).
- [7] W.J. Marciano and Z. Parsa, *Phys. Rev.* **D53**, R1 (1996).
- [8] C. Jarlskog and R. Stora, *Phys. Lett.* **B 208**, 268 (1988).
- [9] G. Buchalla and A.J. Buras, *Nucl. Phys.* **B412**, 106 (1994).
- [10] S. Adler *et al.*, *Phys. Rev. Lett.* **79**, 2204 (1997).
- [11] G. Redlinger, KAON-99 Conference, June 1999.
- [12] M. Gronau, *Phys. Lett.* **B300**, 163 (1993).
- [13] A.J. Buras, *Phys. Lett.* **B333**, 476 (1994).
- [14] C. Dib, D. London and Y. Nir, *Int. J. Mod. Phys.* **A6**, 1253 (1991).
- [15] Y. Grossman, Y. Nir, and R. Rattazzi, in *Heavy Flavours II*, eds. A.J. Buras and M. Lindner, World Scientific Publishing Co., Singapore, 755-794 (1997) hep-ph/9701231.
- [16] G. Bélanger, C.G. Geng and P. Turcotte, *Phys. Rev.* **D46**, 2950 (1992).
- [17] C.E. Carlson, G.D. Dorata and M. Sher, *Phys. Rev.* **D54**, 4393 (1996) hep-ph/9606269.
- [18] Y. Nir and M. Worah, *Phys. Lett.* **B423**, 319 (1998).
- [19] Z. Xiao, C. Li and K. Chao, *Eur. Phys. J.* **C10**, 51 (1999) hep-ph/9903348.
- [20] Y. Kiyo, T. Morozumi, P. Parada, M.N. Rebelo, and M. Tanimoto, *Prog. Theor. Phys.* **101**, 671 (1999) hep-ph/9809333.

- [21] Y. Grossman and Y. Nir, *Phys. Lett.* **B398**, 163 (1997).
- [22] T. Hattori, T. Hasuike, and S. Wakaizumi, hep-ph/9908447v2 (1999).
- [23] A.J. Buras, A. Romanino, and L.Silvestrini, *Nucl. Phys.* **B520**, 3 (1998).
- [24] G. Colangelo and G. Isidori, *JHEP* **09**, 009 (1998) hep-ph/9808487 (1998).
- [25] A.J. Buras and L.Silvestrini, *Nucl. Phys.* **B546**, 299 (1999) hep-ph/9811471.
- [26] A.J. Buras, G. Colangelo, G. Isidori, A. Romanino and L. Silvestrini, hep-ph/9908371.
- [27] A. Alavi-Harati *et al.* [KTeV Collaboration], *Phys. Rev. Lett.* **83**, 22 (1999) hep-ex/9905060.
- [28] V. Fanti *et al.*[NA48 Collaboration], CERN-EP/99-114, hep-ex/9909022.
- [29] S. Bosch, A.J. Buras, M. Gorbahn, S. Jager, M. Jamin, M.E. Lautenbacher, and L. Silvestrini, TUM-HEP-347-99, Apr 1999, hep-ph/9904408.
- [30] A. Alavi-Harati *et al.*, hep-ex/9907014.
- [31] T. Roser, private communication.
- [32] R. Cappi and C. Steinbach, CERN-PS-OP-81-10, *Particle Accelerator Conference 1981*, 2806.
- [33] J. W. Glenn, AGS/AD Technote 426 (1996); J. W. Glenn, *et al.*, **Proc. Particle Accelerator Conference** (in press), BNL-63890, May 1997.
- [34] T. Abbott *al.* [E802 Collaboration], *Phys. Rev.* **D45**, 3906 (1992).
- [35] P. Kapinos, E926 Technical Note 5, Aug 1997.
- [36] S.V. Efremov, M.V. Kazarnovsky, E. Ya. Paryev, *Zeit. Phys.* **A344**, 181 (1992).
- [37] S.V. Efremov, E. Ya. Paryev, *Zeit. Phys.* **A348**, 217 (1994).
- [38] D. Dekkers *et al.*, *Phys. Rev.* **137**, B952 (1965).
- [39] L. Littenberg, E926 Technical Note 11, Aug 1998.
- [40] M. Grigoriev, Yu. Kudenko, O. Mineev, E926 Technical Note 7, April 1998.
- [41] T. Abbott *al.* [E802 Collaboration], *Nuc. Instr. Meth.* **A290**, 41 (1990).
- [42] R.A. Kryger *et al.*, “Efficiency of a BaF<sub>2</sub> scintillator detector for 15-150 MeV neutrons” *Nucl. Instr. Meth.* **A346** 544 (1994).
- [43] V. Wagner *et al.*, “Detection of relativistic neutrons by BaF<sub>2</sub> scintillators” *Nucl. Instr. Meth.* **A394** 332 (1997).

- [44] C. Caso, *et al.*, *Eur. Phys. Jour.* **C3** 1 (1998).
- [45] S.D. Worm, UTA thesis, UTEXAS-RHIP-95-1, UTEXAS-HEP-95-21, KL-243, Aug 1995.
- [46] M. Hebert, private communication.
- [47] W.T. Emmet, “Design and Manufacturing Considerations for the KOPIO Vacuum Vessel”, KOPIO Technote TN012, (1998).
- [48] H. van der Graaf, *et al.*, NIM in Phys. Res. A307 (1991), 220-230.
- [49] Northern State Metal Corp.
- [50] G.S. Atoyan, *et al.*, “Lead-scintillator electromagnetic calorimeter with wave length shifting fiber readout”, NIM, **A320**, 144 (1992)
- [51] G. David, *et al.*, “Performance of the PHENIX EM Calorimeter”, PHENIX Technote 236 (1996).
- [52] A. Golutvin, “Electromagnetic calorimeter for HERA-B”, HERA-B Tech. Note 94-073 (1994).
- [53] Technical Proposal, CERN LHCC 98-4, LHCC/P4, 20Feb. 1998.
- [54] G.S. Atoyan, *et. al.*, “Preliminary Research of Shashlyk Calorimeter for E926”, E926 Technote (1999).
- [55] V.K. Semenov, private communication.
- [56] T. Nomura, *et al.*, “Studies of a Prototype Photon Catcher”, KOPIO Technote TN013 (1998).
- [57] Y. Kudenko and O. Mineev, “Extruded grooved scintillator with WLS fiber readout”, KOPIO TN008 (1998).
- [58] S. Adler, *et al.*, Phys. Rev. Lett. **79** 2204 (1997).
- [59] M. Blecher, L. Littenberg, and M. Zeller, “A Catcher Design for KOPIO”, KOPIO TN016 (1999).
- [60] E. Cisbani, *et al.*, “Proposal for a Dual Radiator RICH for HERMES”, HERMES Technical note (1997).
- [61] S. Ajmura *et al.*, KEK preprint 97-243.
- [62] T. Inagaki *et al.*, NIM A359 (1995) 478.
- [63] R. D. Ransome, *et al.*, Phys. Rev. C 46 (1992) 273.



## 5 RSVP Organization and Management

The success of each of the Projects in this Proposal depends on the performance of the Collaboration, which is designing and will build and operate the experiment (including appropriate parts of secondary beamlines) and analyze data from it, the BNL Collider Accelerator Department (CAD) which will upgrade and operate the AGS and appropriate primary and/or secondary beamlines, the NSF, which is proposed to provide the funds for the Projects' construction, and the Department of Energy, which is anticipated to provide the funds for the operation of the accelerator and experiments. We believe it is important to have a clear plan for the management of each of the Projects that encompasses the construction of each experiment, its beam-line, and the associated accelerator improvements.

Since there are two Projects in this Proposal, we model the management plan on that of the NSF portion of the funding of the U.S. ATLAS and U.S. CMS Projects.

A Construction Schedule and Funding Plan for each Project will be established and tracked with a Work Breakdown Structure (WBS) system. Each Construction Schedule will include Project Milestones at various WBS levels. Each Funding Plan will contain budgets at various WBS levels and carry appropriate contingency at each level. It is anticipated that the NSF will supply funds to the Grant-holding Institution or Institutions (subsequently referred to as Grant-holder) each fiscal year according to the established Funding Profile for each Project. The Grant-holder for each Project will disburse funds to each organization within that Project consistent with Memoranda of Understanding with that organization, and subject to the approval process put in place for each Project. Contingency will be held by each Project and allocated within that Project consistent with the change control procedures established by each Project. The Grant-holder will be responsible for ensuring that funds are disbursed consistent with the Funding Plan put in place by each Project.

We propose four parts to the management structure of the Projects in this Proposal, each with specific responsibilities and authority.

- A Joint Oversight Committee (JOC) will consist of personnel from the High Energy Physics Division of the Department of Energy and the Physics Division of the National Science Foundation. Members will be appointed by the Assistant Director of Math and Physical Sciences for the NSF and the Director of the Office of High Energy and Nuclear Physics for the DOE. Its role will be to oversee progress on the construction Projects and to ensure that agency goals for cost, schedule and technical performance are being met in a satisfactory manner. It will review the execution of the Projects. The JOC will also embody the authority to approve high-level changes to the scope and funding of each Project. The co-chairs (one each from the NSF and DOE) of the JOC will represent the two agencies for all project issues. This committee has the sole authority to approve changes to each of the Project's baseline cost and funding profile. The JOC also has the responsibility to approve an Accelerator run plan; this is discussed in Section 7.
- A Laboratory Oversight Committee (LOC) will consist of physicists and other experts from outside BNL, chaired by the BNL Associate Laboratory Director for High Energy and Nuclear Physics. The LOC Chair will have the responsibility to provide assurance

to the Agencies that the Projects are properly managed and receive appropriate attention and support by the Laboratory to reach their goals in a timely manner. He or she will conduct periodic reviews of each Project's performance. Approval of the LOC Chair is required to allocate contingency within each Project above a certain dollar amount, to make changes to each Project's scope above some WBS level, and to modify Project Milestones over a time threshold established in the project management plan. Memoranda of Understanding between Collaborating Institutions or the Laboratory and the Project Management require LOC Chair approval. Approval of each Project's Construction Schedule and Funding Plan by the LOC Chair is required. The LOC and its chair also have responsibility for recommending to the Joint Oversight Committee an Accelerator Running Plan; this is discussed in section 7.

- Each Collaboration will perform the scientific work of the experiment, including design, contributions to the construction, data collection and analysis, and publication of results. Each Collaboration will establish a mechanism for selecting a Spokes-person or Spokes-persons that will head the Collaboration. Each Collaboration may have one or more Deputy Spokes-persons and a Collaboration Council that will ensure appropriate representation of all Collaborating Institutions in the decision making process of the Collaboration. The Spokes-person(s) of each project will work jointly with the respective Project Manager to effect the successful construction of the Project. Approval of the Spokes-person(s) is required to allocate contingency above a certain dollar amount and to reallocate contingency between subsystems, to make changes to the Project scope above some WBS level, and to change Project Milestones above some WBS level. Memoranda of Understanding between Collaborating Institutions or the Laboratory and the Project Management require Spokes-person approval. Appointment of Subsystem Managers requires Spokes-person approval. Approval of each Project's Construction Schedule and Funding Profile by the respective Spokes-person(s) is required.
- The Project Management Group for each Project will be headed by a Project Manager who will be responsible for managing the overall construction Project and its cost, schedule, and technical performance. Each Project Manager will be appointed by the Collaboration Spokes-person, subject to the approval of the LOC Chair. The Project Manager will have the responsibility to prepare the Funding Plan and the Construction Schedule and prepare the Memoranda of Understanding that capture the roles and work plans for each Collaborating Institution and the Laboratory. The Project Manager will also prepare annual work and funding plans. The Project Manager will be responsible for preparing annual Project performance reports to the Funding Agencies and will track costs and progress with periodic reports to the Spokes-person and the LOC Chair. He or she will have the authority to approve contingency usage below a certain dollar level and approve Project Milestone changes below a certain WBS level. The Project Manager will appoint subsystem managers as needed with the concurrence of the Spokes-person.

Subsystem Managers will have the responsibility to produce an acceptable baseline cost estimate and a plan and schedule for the design and construction of the subsystem.



They will prepare annual work plans and budgets for each subsystem. The Subsystem Managers will have the responsibility to track and report the work of the subsystem and to allocate contingency among the subsystem's project elements. Subsystem contingency assignment authority is subject to Project Manager and/or Spokes-person and LOC Chair approval above some dollar threshold. Change of subsystem milestones above some WBS level requires Project Manager and/or Spokes-person and LOC Chair approval.

The accelerator and beam-line improvements represent a special situation that requires close cooperation with CAD personnel. A Memorandum of Understanding with the BNL CAD will capture the work and funding plan. An Accelerator/Beam-line Manager for each Project will work closely with the respective Project Manager and with CAD management and will have the responsibility to produce an acceptable baseline cost estimate and a plan and schedule for the design and construction of the accelerator and primary beam-line improvements and/or construction for that Project. He or she will also prepare annual work plans and budgets for the accelerator/beam-line work. Accelerator/Beam-line milestone changes and contingency allocation will require the same approval as that of Project subsystems.

Upon approval of this proposal, each of the Collaborations' Spokes-person(s) and the LOC Chair will establish a plan for the development of accelerator operations for each Project's accelerator operating parameters. This plan will include accelerator development time prior to completing the Project to ensure that data taking can begin promptly after Project completion. Each Collaboration Spokes-persons and the LOC Chair will also prepare an Operations Plan for the experiments that will include adequate allocations of running time and operations personnel to support the running of the experiments. This Operations Plan will be subject to Joint Oversight Committee approval.



## 6 AGS Operations to Support RSVP Experiments

We discuss here the cost of AGS slow extracted beam (SEB) operations to support the RSVP experiments. These costs have been estimated by CAD personnel. The operations plan is predicated on a model discussed below, with the caveat that costs are based on only High Energy Physics (HEP) experiments running during each fiscal year. Should Nuclear Physics (NP) experiments run in parallel with HEP experiments, then significant cost sharing would ensue for both programs, largely due to shared salary costs. This incremental and cost sharing model had been the case at the AGS, for the period of 1986-1999, when both HEP and NP experiments were run.

- HEP slow extracted beam (SEB) operations will run concurrently with RHIC collider operations. RHIC operations will require two beam fills every 10 hours. It is expected that initially each fill will take 2 hours to accomplish. During RHIC injection all other machine operations will cease, so as to allow full attention to this process. We expect this filling time to reduce as one gains experience with the operation.
- The HEP program operations are calculated as an incremental cost to the base NP support of RHIC injector operations.
- HEP will incrementally support the power costs for SEB, beam transport and experimental area operations. The standby AGS power consumption of 7 MW is billed to RHIC operations. The additional flat-top, extraction system, beam transport and experiment power is billed to HEP.
- The accelerator manpower is covered by RHIC operations. Main control room operations is sufficient to cover SEB operations during RHIC collision operations. There are no manpower charges to accelerator operations except for a small incremental effort to support the SEB extraction system.
- The RHIC program does not support any manpower for AGS experiments. NP has not budgeted test beam support for its own program. All experimental area manpower support will be billed to HEP. The manpower costs that are shown below consist of a base manpower level that supports the extraction system, switch-yard transport, primary proton transport and the primary target area. The incremental manpower cost for an experiment is explicitly identified. The additional HEP manpower is matrixed into the Collider Accelerator Department staff, mostly into the Experimental Support and Facilities Division.
- The incremental accelerator materials and purchases costs to support HEP operations will be billed to HEP. The experimental area materials and purchases will be fully billed to HEP. These costs are based upon past SEB operations expenses. There is a base cost to support the extraction system, switch-yard transport, primary proton beam transport and the primary target area. The incremental material and purchase costs for each experiment is explicitly identified.

- Any capital construction costs are fully borne by the HEP program office. Should the experiment subsequently (after Project completion) require modifications to either the accelerators or beam lines, these costs would be borne by the HEP program.

The RHIC machine is expected to be funded to operate 37 weeks per year for ion - ion, proton - ion and polarized proton - polarized proton operations. None of these modes preclude an independent AGS fixed target operation. The accelerator complex operates in a rapid context-switching mode. The switch from ion to proton operations will not exceed 30 minutes for each cycle. The working assumption is that AGS fixed target operations would

Table 1: The manpower and materials costs associated with the base AGS operations and the incremental operation of the RSVP experiments.

Item	Sub-item	Cost [ \$M ]	Cost [ \$M ]
Accelerator Operations			1.8
	Power (7 MW base)	1.0	
	Material, purchases	0.8	
Experimental Areas Common Base			2.3
	Manpower (16 FTE)	2.0	
	Material, purchases	0.3	
KOPIO Stand-alone Incremental (15 weeks)			5.2
	Manpower (6 FTE)	0.7	
	Power ( +1 MW)	0.1	
	Material, purchases	0.3	
MECO Stand-alone Incremental (15 weeks)			5.2
	Manpower (8 FTE)	1.0	
	Power (-4 MW)	-0.5	
	Material, purchases	0.6	
KOPIO+MECO Combined Incremental (30 weeks)			7.8

be available for 20 hours per day and 7 days per week (except for scheduled maintenance periods). The majority of RHIC operations would entail ion - ion operations. For any RHIC running with protons, the standby linac power costs would be subtracted from the SEB cost to HEP. The estimated costs are based upon 15 week per year SEB operation. If the running were to be increased by an additional 5 weeks, the power would scale accordingly, the materials and purchases would have a small increase, and the manpower cost, except for shift differentials, would remain fixed. The costs (fully burdened) for 15 weeks operations are given in Table 1, broken down into the costs for accelerator operations, experimental area base cost, stand-alone KOPIO (E926) and MECO (E940) costs, and combined KOPIO and MECO

shared operations cost. KOPIO (24 GeV) and MECO (8 GeV) cannot run concurrently. Two consecutive runs of 15 weeks in a given year would cost \$7.8M. The reduction in concurrent running costs is due to shared manpower between the two experiments.

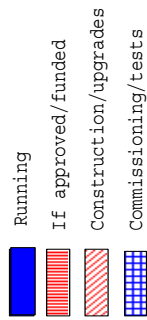
The manpower required to run the external beam-lines for the RSVP experiments has been estimated by CAD personnel and is summarized in Table 2. The requirements are broken down into the base operations for the running of the areas common to the two experiments and the specific requirements for each of the experiments. These estimates are preliminary. For example, in the case of MECO, NHMFL personnel estimate the manpower requirements for operating the system of refrigerators and super-conducting solenoids may be significantly less than the estimates given below. In addition, savings may result from shared operations with other programs.

Table 2: The table gives manpower requirements for the base operations of the experimental areas and for the operations of equipment specific to each of the experiments.

Item	Sub-item	FTE	FTE
Base operations			16.0
	Physicist	1.0	
	Engineering (mechanical, electrical)	1.0	
	Controls	.5	
	Instrumentation	1.0	
	Vacuum systems	.5	
	Magnet systems	1.5	
	Power supplies	1.5	
	Utilities (power, water, AC)	2.0	
	Extraction systems	1.0	
	ES&H, QA, administration., training	1.0	
	Shift operations	5.0	
KOPIO support			6.0
	Physicist, engineering	1.0	
	RF systems (micro-bunch)	2.0	
	Technicians (instrumentation, vacuum, magnet, etc.)	3.0	
MECO support			8.0
	Physicist, engineering	1.0	
	Cryogenic engineering, technicians	4.0	
	Technicians (instrumentation, vacuum, magnet etc.)	3.0	

A sample construction and running schedule is shown in Fig 1. The actual schedule will be decided based on available funding and direction from the Laboratory Oversight Committee and Joint Oversight Committees as discussed in Sections 5 and 7.

# Possible AGS Operations Plan - FY00-06



**DRAFT**

Program Element	Experiment	FY00	FY01	FY02	FY03	FY04	FY05	FY06
<i>RHIC Operation</i>		Running	Running	Running	Running	Running	Running	Running
<i>AGS SEB Operations</i>								
♦ E949 [Bryan,Kettel,Sugimoto]	$\kappa^+ \rightarrow \pi^+ \nu \bar{\nu}$	Construction/upgrades	Commissioning/tests	Running				
♦ E926 [Bryan,Littenberg,Zeller]	$\kappa^0 \rightarrow \pi^0 \nu \bar{\nu}$	R&D	R&D	Construction/upgrades	Construction/upgrades	Construction/upgrades	Construction/upgrades	Construction/upgrades
♦ E940 [Molzon]	$\mu^- \bar{N} \rightarrow e^- \bar{N}$	R&D	R&D	Construction/upgrades	Construction/upgrades	Construction/upgrades	Construction/upgrades	Construction/upgrades
♦ Test Runs [R&D for E926/E940]		Running	Running	Running	Running	Running	Running	Running
♦ * E930 [Tamura]	Hypernuclear $\gamma$ 's	Construction/upgrades	Construction/upgrades					
♦ * E931 [Dehnhard,Hungerford,Zeps]	$\Delta I = 1/2$ Rule	Construction/upgrades	Construction/upgrades					
<i>AGS FEB Operations</i>								
♦ E821 [Hughes,Morse,Roberts]	$\mu^- g-2$	Running	Running					
♦ E951 [McDonald]	$\mu\mu$ collider	Construction/upgrades	Construction/upgrades	Construction/upgrades	Construction/upgrades	Construction/upgrades	Construction/upgrades	Construction/upgrades
<i>Radiobiology</i>								
♦ AGS		Running	Running	Running	Running	Running	Running	Running
♦ BAF		Construction/upgrades	Construction/upgrades	Construction/upgrades	Construction/upgrades	Construction/upgrades	Construction/upgrades	Construction/upgrades

\* Medium Energy Experiments

Figure 1: Sample schedule.

## 7 Establishing the RSVP Accelerator Running Plan

The MECO and KOPIO experiments cannot be run simultaneously since they require different values for the proton energy and different time structure for the extracted beam. Accelerator time will be required for each experiment during both its construction phase and its commissioning and data taking phase. We specify below the procedure for establishing an Accelerator Running Plan.

During the construction phases of the two experiments, accelerator R&D time will be needed to establish the operating parameters of the AGS and the primary beam-lines. The guiding principle for allocating test time during this period is that the two experiments will get equal time, averaged over a period long enough to make efficient use of the AGS. The BNL Associate Laboratory Director for High Energy and Nuclear Physics will work to acquire the necessary operating resources to provide sufficient accelerator R&D time to commission the accelerator and primary beam prior to each Project's construction completion date.

During the running phase, when either of the experiments has completed its construction phase and is ready to commission the detector or take data, a similar guiding principle applies. If only one experiment is completed, that experiment will be run. When both experiments are able to use beam for either commissioning or taking data, time will be divided equally between the experiments, averaged over any two consecutive fiscal years, consistent with efficient use of beam time and efficient accelerator operations. When the proposed running time for MECO is complete the Laboratory Oversight Committee will review and recommend to the LOC chair action on any request for additional running time. Otherwise, the accelerator will be run for KOPIO.

The Laboratory Oversight Committee will periodically hear presentations from and review the progress of the MECO and KOPIO Projects during both the construction and operations phases of RSVP. Following these reviews and on the advice of the LOC, the LOC Chair will recommend to the JOC and sponsoring agencies a running plan consistent with the principles stated above.





## 8 Summary of Educational Outreach Programs

The MECO and KOPIO experiments will provide excellent training for graduate and post-doctoral students in particle physics. There are strong University groups in these experiments and the time scale for designing and constructing the apparatus and for collecting and analyzing data is sufficiently short that these students can receive broad training in both particle detector hardware techniques and in analysis. Many of the collaborating groups have also involved undergraduates in their research, and this is expected to continue.

In addition to this traditional educational mission of the University faculty involved in these projects, many of these faculty and researchers and their home Institutions have been involved in outreach programs to secondary school students and faculty. These outreach programs will benefit from interacting with the scientists involved in the MECO and KOPIO projects. In this section, we discuss the outline of a number of outreach programs that we propose to develop. Full descriptions of the programs will be given in separate document that will be developed in the coming month.

### 8.1 The UCI Program

UCI is preparing a proposal that will be submitted separately to the NSF to support an outreach program associated with the UCI MECO group. We here outline the proposed program, which builds on successful outreach programs in place at UCI.

UCI's Center For Educational Partnerships (CFEP) has a strong history of successful educational partnerships with target secondary schools that have high minority and economically disadvantaged populations. There currently exists a demonstrated need to increase the representation of economically disadvantaged in the sciences. For example, in Santa Ana Unified School District (SAUSD), a large urban district adjacent to Irvine, over 85% of the graduates are Hispanic or African American and the majority of the population qualifies for free or reduced cost lunch. Less than 3% of the Hispanic and African American graduates from SAUSD matriculate in the UC system each year, a system designed to accept the top 12.5% of graduates. In particular, only 25 of the 1,895 SAUSD graduates in 1998 enrolled at UCI and only 9 of these 25 entered majoring in science or engineering. Similar situations exist for Anaheim Union High School District and Garden Grove Unified School District, two other nearby districts with which UCI is building partnerships.

Recently, the Science Outreach Center (SOC) was established, funded by the State of California, to capitalize on partnerships between UCI and these target secondary schools to develop and expand programs that enhance the academic achievement and increase the college matriculation rates of underrepresented minorities and economically disadvantaged students. Current partnerships and programs, including a summer residential program in Biology and informational outreach and tutoring assistance programs, have resulted in increased enrollment in elective third year science courses throughout SAUSD. In addition, the SOC outreach programs have assisted three high schools to offer Advanced Placement Biology for the first time this fall.

Through the partnerships and programs such as those described below, our goal is to double the number of under-represented minority high school graduates from our partner schools that matriculate at the University of California in the sciences by the year 2003.

We will propose to develop a series of outreach activities associated with this project in three stages:

1. A team of three middle school teachers, three high school teachers, SOC staff and members of the UCI MECO group will design a curriculum for a summer residential program for high school and middle school students. The goal of the course of study is to generate student interest and excitement in current academic research in physics and more broadly, in the methods and technology of modern research in the physical sciences. This curriculum will include hands-on activities using the tools of the trade of particle physics, including working with particle detectors and state of the art computers. The middle and high school teachers will be paid a stipend to encourage their participation.
2. A ten-day residential summer AP Physics preparation program will be instituted to encourage approximately 20 students from each of three area high schools to enroll in newly offered AP Physics classes at their schools. A five-day residential physics program will bring 60 middle school students to the University to introduce them to the excitement of science, mathematics and University life. This program will be run jointly by SOC staff, the middle and high school teachers, and researchers from MECO. Students' living expenses on Campus will be supported by the program and the middle and high school teachers will receive a stipend.

UCI's CFEP and SOC staff have experience developing and implementing such residential programs. In the summer of 1999, 58 incoming 7th and 8th grade students completed a 12-day residential program in Chemistry, and the AP Biology and AP Calculus Summer Institutes each hosted 30 students from partner schools for an 11-day stay on campus.

3. Saturday adjunct courses in high school AP physics and middle school general science and mathematics will be offered to build upon the summer experiences of the middle school students and continue the interaction of the high school students who have enrolled in AP courses and are preparing for AP examinations. An after-school seminar series will be presented jointly by Saturday Academy students, teachers, SOC staff and scientists from the UCI MECO group with the goal of disseminating teaching material and program information to other teachers and students. This series will serve to expand the program beyond the initial set of three high schools and three middle schools.

This three-pronged approach will be continued for three years during this project. The success of the program will be measured by the extent to which new AP Physics courses are offered and the success of students in these courses, the matriculation rate of the participants in the UC system, and the enrollment in elective science courses by the middle school students that attend the program.

The proposal will include a request for the resources needed to bring students onto campus for the residential program, funds for stipends for the high school and middle school teachers, and funds for partial salary support for a Program Director who will be dedicated to the organization and implementation of the summer and school year programs.

This Physics Summer/Saturday Program will serve as a model for the expansion of AP Chemistry, AP Computer Science and other AP science programs that target schools can provide to their students. It is an action-oriented model driven by numerical goals. Integrating both school-centered and student-centered approaches, it increases student and teacher content knowledge as well as lifts the standards of performance expectation.

## **8.2 The New York University Program**

The proposed MECO project can build on existing programs at NYU that reach out to science-education majors as well as classroom teachers, a group whose improved appreciation of science can affect large numbers of elementary and secondary school students. For example, the NYU School of Education Department of Teaching and Learning runs the TOC (Teacher Opportunity Core Program) and MSTEP (Math Science Technology Enhancement Program) programs funded by the New York State Department of Education and a Dwight D. Eisenhower grant. As part of these programs, in-service teachers spend a summer doing research with some scientific group, including ones at Brookhaven National Laboratory. Alan Mincer has been regularly teaching a course for this program since the fall of 1993. He has also been involved in the NSF funded New York City Science and Math Collaborative for Excellence in Teacher Preparation that links NYU Faculty of Arts and Science and the School of Education with five senior colleges of the City University of New York and local schools to develop a model training program for elementary and secondary school teachers, including new courses for prospective teachers, placement of undergraduates as "teacher scholars" in local public schools, and summer internships for high school teachers in faculty laboratories.

The NYU group will have ongoing laboratory work for MECO at NYU; this will be a natural place for teachers in this program to do research not only in the summer but, due to their proximity to the School of Education, also during the school year.

## **8.3 The University of Houston Program**

Various members of the faculty of the University of Houston have been engaged in outreach programs with secondary schools in the Houston area. These programs primarily involve 4-6 week summer courses for 9th grade science and physics teachers, helping them develop course materials and demonstrations for their classes. In addition the Physics Department brings a well known scientist, usually a Nobel Laureate, to campus once a year to offer an open house and lecture for high school students as well as a public lecture on some topic of general interest. The MECO collaborators from the University of Houston group participate actively in this program.

Aside from participation in the above departmental programs, the Houston Medium Energy Physics group that collaborates on MECO is involved in outreach through Houston Community College System (HCCS), which has a large representation of minority and economically disadvantaged students. A teacher at HCCS is supported to conduct research with the UH group under a part time appointment as a research scientist. This adds a research dimension to the HCCS experience which would otherwise be absent. The UH group has

a proposal pending for state funds to expand this program in order to include support for undergraduate students from HCCS in their research.

The planned UH outreach program would include developing interactions with science teachers, in order to help prepare lesson plans for science instruction in physics, and introducing students as early as possible to the excitement of science. In addition, the group would expand its interactions with HCCS, involving their undergraduates in the MECO research program.

## 8.4 The University of New Mexico Program

The University of New Mexico (UNM), is located in a part of the US with one of the largest relative representations of minorities (Hispanics and Native Americans) and economically disadvantaged students. In fact, UNM is considered a “minority institution”, *i.e.* an institution in which more than about one third of the enrolled students are from those minority groups. As such the problems and obstacles faced by minority students (in high schools as well as at the university) have to be addressed on a daily basis. For example, part of the state lottery proceeds are used to allow qualified minority undergraduates to attend UNM tuition-free.

The KOPIO collaborators will be able to rely on various existing programs at UNM that reach out to underrepresented groups. Examples include MESA (Math, Engineering, Science Achievement), a successful program to recruit minority high school students, and the NASA-sponsored PURSUE program (Preparation for University Research of Students in Undergraduate Education). UNM and collaborating higher education institutions in the state have been funded by NASA to enhance the quality of the Math, Science, Engineering, and Technology (MSET) education. The specific objectives of these programs are to increase the production of students, especially those underrepresented in MSET fields, in scientific and technical fields who are competitively trained and have discipline-related work experience; integrate cutting-edge science and technology concepts and practices into relevant areas of the undergraduate curriculum; increase participation by faculty and students in projects that both foster collaborative inquiry and that promote broad and significant improvements to undergraduate teaching and learning, especially of the techniques and methodologies associated with the conduct of research; create models for the development of excellence in MSET academic infrastructure, undergraduate preparation, and student research training. Within these programs undergraduate students typically work in teams, supervised and mentored by faculty members and/or selected postdocs as well as graduate students.

Independent of these university- and department-wide programs, the UNM group has participated in local outreach programs in primary and secondary schools by giving talks and mentoring high schools students. This year (like several times in the past) the group is sponsoring and coaching a group of local high school students in a science project as part of the New Mexico Supercomputing Challenge. For several years NSF REU (Research Experience for Undergraduates) students have participated in summer research throughout the department at UNM. This past summer two high school students were employed by the group and gained valuable hands-on experience in a research lab environment. A recent undergraduate success story is a very talented female Hispanic student who worked with the group for several years (summers and during the semesters). She is now a graduate student

at UC San Diego. In fact, undergraduate students have been continually employed (at least part-time) in research activities for quite a few years now.

The UNM group has been fully participating in AGS Experiment 865, has played an important role in the writing of this proposal, and will be one of the leading groups in the KOPIO experiment. Apart from the obvious Ph.D. dissertation topics within KOPIO the group plans to vigorously continue its outreach to local secondary schools (where connections have now been established at several high schools) and to pursue the very successful integration of undergraduate students into this exciting research.

## **8.5 The Virginia Polytechnic Institute and State University Program**

The Physics Department has an on-going NSF-funded program known as the Distance and Service-Learning Project which is a partnership between the Department and science programs at high schools throughout Southwest Virginia. The project is piloted with Floyd County High School. The goals of the Project are to: increase the level of science literacy among the general (rural) student population at Floyd County High School; lead to the creation of an Advanced Placement Physics course; improve the oral, written, and electronic communication skills of physics majors at Virginia Tech; and to introduce physics majors to new applications of their discipline, including careers in teaching.

The Virginia Tech faculty collaborating on the KOPIO component of RSVP will adapt the Project to involve local high school students in cutting edge experimental physics. In addition the experiment will provide many opportunities for participation by undergraduates in building equipment and in analysis of data. The Virginia Tech physics department has a long history of involving undergraduate majors in state-of-the-art research and was recently recognized as an “outstanding department” in this area by the university.

## **8.6 The Yale Program**

One of the great advantages of KOPIO, in comparison to other elementary particle experiments, is its modest size. While we will be developing new techniques for instrumentation in the low energy particle physics field, for example, angle and energy measurement of photons with energies in the 50 to 1000 MeV domain, this will be done in a small group environment with much of the development being done at Yale. This activity will provide ample opportunity for students at almost any level of education, graduate, undergraduate, or secondary, to become seriously involved in the inner workings of the project. This involvement will cover the full gamut of the art and science of experimental particle physics - from apparatus simulation, through detector development and testing and operation, to data acquisition hardware and software. The “hands on” experience that KOPIO can give to students is rare in the current environment of large particle physics experiments.

The Yale group has much experience involving students of various levels of development. Of course there are the many Ph.D. degree recipients that have come from the recent experiments performed by the collaborating groups. But there have also been many undergraduate students working both at Yale during the school year and at Brookhaven during the summer, as well as teachers from secondary schools, who have had the opportunity to participate in

our experiments. This activity will continue and can be expanded with the construction and operation of KOPIO.

The internet allows projects such as KOPIO to tell their stories to the scientific community and to the world at large. Yale will maintain a web site which will contain a section describing the scientific goals, the techniques involved, and the progress of the experiment at a level understandable by high school students. We intend to establish links to the local high schools through the Yale-New Haven Teachers Institute and other Yale connections. The site will be interactive and we will encourage conversation between such students and the collaborators on the experiment. We believe this will be a “positively fed-back” activity in that once the conversations start their number will grow through word of mouth (or rather, word of computer).

We have given several lectures over the past few years to local teachers at all levels, from 4th grade through 12th. They have been very well received but there has been no mechanism to continue the interaction once the lectures are over. A dynamic web site can provide such an opportunity.

## **8.7 The Brookhaven National Laboratory Program**

Brookhaven National Laboratory’s educational outreach activities associated with the RSVP initiative will be described in greater detail in a separate outreach proposal to be submitted to the National Science Foundation. What these activities will involve is summarized below:

The Laboratory’s educational outreach will focus on mathematics, science and technology (MST) education at upper elementary levels, in response to demonstrated needs. Elementary teachers will provide a leverage point for the efforts of BNL researchers.

To help improve student performance in MST, New York State K-12 education standards now place greater emphasis on students’ ability to solve problems or reach conclusions through observation and reasoning, rather than simply recalling facts.

Teachers are being called on to provide this focus through activities in which the students carry out their own experiments or design projects; the teacher serves more as a facilitator than a lecturer. However, if teachers do not elucidate underlying content principles as an end point in this process, student problem-solving or inquiry can become simple trial-and-error, whose results cannot be generalized. Insight will be missing, and with it a basis for reasoning. While this might be obvious to a researcher, it can present a challenge to teachers - particularly elementary teachers who are not mathematics, science or technology specialists.

Thus, to support current strategies to improve student performance in MST there exists a need to provide elementary teachers - and their students - with an idea of how inquiries are conducted in mathematics, science and technology, and a grasp of how basic principles are extracted from these inquiries and then applied.

Scientists and engineers can help meet this need by first sharing their knowledge of MST process and principles with elementary teachers. Once teacher enhancement is completed, researchers can then support teachers in applying their experience to their classrooms.

BNL researchers will first work with science education specialists from SUNY Stony Brook and master teachers to design innovative and affordable classroom demonstrations and experiments, embodying MST process and basic principles. While derived from actual

research, concepts will also be relevant to the experience of elementary students: topics such as acceleration, collisions, symmetry etc., will form the basis of the activities. Examples already exist in BNL's Science Museum and Office of Educational Programs.

The activities will form the curriculum of a seminar program serving about thirty upper level elementary teachers annually over three years, in collaboration with local school districts. The seminar program, called "Insights," will consist of about twenty three-hour sessions during the school year. "Insights" sessions will be conducted by Laboratory researchers, assisted by educators. Each session will call on teachers to conduct experiments, demonstrations etc., and interpret the results - as far as possible - in terms of basic principles. Academic or in-service credit will be available.

After teachers have completed the seminar series, transfer of their knowledge to students will be supported by continuing interactions with Laboratory scientists, follow-on awards, and development of special BNL resources - including actual laboratory data and onsite facilities, and possibly offering analytic services in support of student experiments.

Here, particular emphasis will be placed on determining the impact of the "Insights" program and follow-on activities on student performance, and the extent to which the model might usefully be generalized. As experience is gained, a website will be developed to make selected activities and resources more widely available to students and teachers.





## 9 Diversity Goals

An important part of the National Science Foundation mission is the successful engagement of under-represented groups in the scientific activities supported by the Agency. In NSF sponsored research activity, there are always opportunities for promoting and advancing this goal. The RSVP proponents will pursue these goals under the general rubric of 'Diversity Emphasis'. By diversity emphasis, we mean actively seeking the involvement of groups that are under-represented in scientific research. Examples of the characteristics that define such groups are gender (more female participants still need to be attracted into the sciences), ethnicity (African-Americans and Hispanics continue to be under-represented in the scientific community) and disability (more disabled workers can be involved in basic research).

Given the wide geographic and institutional distribution of the participants in the RSVP experiments, our approach to addressing the diversity goals stated above is to make use of approaches that are already instituted and active at the participating institutions. We will adopt a vigorous pursuit of the goals and programs extant at our participating institutions that are geared to addressing diversity issues. At BNL, for example, the head of the Laboratory's Diversity Office now reports directly to the Laboratory Director in order to raise the priority and visibility of this important function. Many other RSVP institutions have similarly strengthened and renewed their commitment to the diversity issue in recent years.

When the RSVP proposal has been approved by NSF, and the Management Plans for MECO and KOPIO are being created, there will be appropriate diversity goals and milestones incorporated in those Plans.